Transformer models for electromagnetic transient studies with particular reference to HVdc transmission

Wade G. Enright

A thesis presented for the degree of
Doctor of Philosophy
in
Electrical and Electronic Engineering
at the
University of Canterbury,
Christchurch, New Zealand.

February 1996

To my wife Jodi,

thanks for the encouragement.

ABSTRACT

In this thesis a formulation for incorporating general magnetic equivalent circuits in electromagnetic transient programs is presented. The formulation is applied to create new single-phase, and the first three-limb three-phase PSCAD-EMTDC program transformer models. The new models proposed are validated with laboratory, factory, and field data.

Problems associated with magnetically independent phase representations of three-limb three-phase transformers are discussed. Considerable differences are shown in the behaviour of three-phase bank and three-limb three-phase transformers, particularly for the case of in-rush studies.

The new transformer models are applied to: the first intervalidation of the Harmonic Domain Analysis program with the widely accepted PSCAD-EMTDC program, investigating the division of magnetising current harmonics between transformer windings, and the development of a new means to reduce HVdc converter dc side harmonics; the smoothing transformer.

The first set of field measurements from a group connected generator HVdc converter station are presented. A PSCAD-EMTDC model for the group connection is validated with the field data and used to investigate the transient behaviour of three-phase bank and three-limb three-phase converter transformers. Considerable differences are shown in the case of a single-phase ground fault.

LIST OF PUBLICATIONS

Publications associated with this research work:

MACDONALD, S.J., ENRIGHT, W., ARRILLAGA, J. AND O'BRIEN, M.T. 'Test results from Benmore HVdc station with generators operating in group connected mode'. Paper presented to the CIGRE Joint working group 11/14-09, August 1994.

LISBOA, M.L.V., ENRIGHT, W. AND ARRILLAGA, J. (1995), 'Harmonic and time domain simulation of transformer magnetisation non-linearities'. *Proceedings IPENZ annual conference (Innovative technology)*, Vol. 2, February, pp. 72-77.

MACDONALD, S.J., ENRIGHT, W., ARRILLAGA, J. AND O'BRIEN, M.T. 'Harmonic measurements from a group connected generator HVdc converter scheme'. *IEEE Transactions on Power Delivery*, Vol. 10, No. 4, October 1995, pp. 1937-1943.

ENRIGHT, W., ARRILLAGA, J., WOOD, A.R. AND HIDALGO, F.P. 'The smoothing transformer, a new concept in dc side harmonic reduction of HVdc schemes'. Paper presented at the IEEE/PES 1996 Winter meeting, Baltimore, Maryland, January 1996.

ARRILLAGA, J., ENRIGHT, W., WOOD, A.R. AND HIDALGO, F.P. 'DC side harmonic reduction in HVdc converters by direct ripple reinjection'. Paper accepted for presentation at the IEE sixth international conference on AC and DC transmission, London, April-May 1996.

LISBOA, M.L.V., ENRIGHT, W. AND ARRILLAGA, J. 'Improved repesentation of the magnetic non-linearities of multi-limb transformers for use in power system harmonic studies'. Paper accepted for presentation at the 12th PSCC conference, Dresden, Germany, 19-23 August 1996

ENRIGHT, W., ARRILLAGA, J., WOOD, A.R. AND WATSON, N.R. 'Modelling multi-limb transformers with an electromagnetic transient program'. Paper accepted for presentation at ELECTRIMACS 1996, Saint-Nazaire, France, September 1996.

ACKNOWLEDGEMENTS

In this document these paragraphs are the last I write. With both happiness and sadness I leave this work behind. For this thesis and the future prospects I now look forward to, I acknowledge the following people.

To my supervisor Professor J. Arrillaga, I wish to express my sincere thanks for your loyalty, guidance, and friendship. I will not forget your advice Jos. Thank you also to Dr P.S. Bodger, Dr A.R. Wood and Dr S.J. Macdonald for your helpful discussions during the course of this work.

I also wish to acknowledge my mentor, Dr K.S. Turner, I am grateful for your commitment and encouragement. Special recognition is due to K. Devine, N. Frampton, and the Electricity Corporation of New Zealand Ltd for the financial support of this research. To Trans Power New Zealand Ltd thanks are due for technical support, especially the help of P. Thompson.

I acknowledge the practical help and friendship given by Ken Smart. Thank you Ken, Martha, and the boys, for offering me a home away from home.

Finally, to my postgraduate colleagues, family and friends who cared, I offer my warmest thanks. To Tony Enright (senior) your advice throughout my university years has been calming. To Tony Enright (junior) I hope you enjoy your years of research. Charlie Stobert, thanks for being a good friend.

CONTENTS

LIST OF FIGURES

LIST OF TABLES

GLOSSARY

The following are the main symbols used in this thesis:

$\tilde{\theta}$	=	vector of branch mmf
θ'_k	=	magnetic equivalent circuit (MEC) resultant branch magneto motive force (MMF)
θ_{k1}	=	MEC branch MMF drop
θ_{k2}	=	MEC branch forcing MMF
θ_{nk}	=	intercept of branch saturation characteristic tangent with MMF axis
$\tilde{\theta}_{node}$	=	vector of nodal MMF
μ_o	=	permeability of free space
μ_{rk}	=	relative permeability
$\tilde{\phi}$	=	vector of MEC branch flux
ϕ_k	=	MEC branch flux
ϕ_{nk}	=	intercept of branch saturation characteristic tangent with flux axis
$\tilde{\phi}_r$	=	yoke, leakage and zero-sequence flux vector
$\tilde{\phi}_s$	=	winding-limb flux vector
ω_h	=	harmonic voltage source angular frequency
ω_o	=	base angular frequency
ω_R	=	smoothing transformer resonant frequency
$[A]$	=	branch-node connection matrix
$[A]^T$	=	node-branch connection matrix
A_k	=	core cross-sectional area
a	=	transformer ratio
B_k	=	branch flux density
b_1	=	ordinates to the origin of saturation characterisitic asymptote to m_1

b_2	=	ordinates to the origin of saturation characteristic asymptote to m_2
$\mathcal{E}$	=	saturation characteristic correction term
H_k	=	branch magnetising force
$[I]$	=	identity matrix
$\tilde{Im}_{prim}$	=	primary magnetizing current harmonic
$\tilde{Im}_{sec}$	=	secondary magnetizing current harmonic
$\tilde{\tilde{i}}$	=	vector of winding current
i_c	=	capacitor current
i_k	=	MEC winding current
i_l	=	inductor current
i_{m1}	=	red phase magnetising current
i_{m2}	=	yellow phase magnetising current
i_{m3}	=	blue phase magnetising current
i_{nc}	=	capacitor Norton equivalent current source
i_{nl}	=	inductor Norton equivalent current source
$\tilde{\tilde{i}}_{ns}$	=	previous time step transformer equivalent current injection
k	=	smoothing transformer coupling factor
L_k	=	core limb length
L_{11}	=	primary winding self inductance
L_{22}	=	secondary winding self inductance
M_{12}	=	two winding transformer mutual inductance
m_1	=	slope of saturation characteristic unsaturated region
m_2	=	slope of saturation characteristic saturated region
N_k	=	MEC branch turns number
$\mathcal{P}_k$	=	MEC branch incremental permeance
$\mathcal{P}_k^*$	=	UMEC branch actual permeance
$\mathcal{R}_k$	=	MEC branch incremental reluctance
$\mathcal{R}_k^*$	=	UMEC branch actual reluctance
R_{oc}^{*prim}	=	single-phase open-circuit reluctance (primary)
R_{oc}^{*sec}	=	single-phase open-circuit reluctance (secondary)
R_{prim}	=	transformer primary winding resistance
R_{sec}	=	transformer secondary winding resistance
R_{ss}^{*prim}	=	single-phase short-circuit reluctance (primary)
R_{ss}^{*sec}	=	single-phase short-circuit reluctance (secondary)
R_w^*	=	winding-limb reluctance
r_a	=	generator armature resistance
$\tilde{V}_c$	=	capacitor voltage
V_{dc}	=	dc transmission line voltage
V_{dcl}	=	dc transmission line harmonic voltage
$\tilde{V}_h$	=	converter dc side voltage harmonics

V_r = rectifier wall bushing voltage
V_{wbv} = converter wall bushing voltage
$\tilde{V}_1$ = smoothing transformer capacitor side winding voltage
$\tilde{V}_2$ = smoothing transformer dc line side winding voltage
v_k = MEC winding voltage
v_l = inductor voltage
v_1 = primary voltage (red-phase)
v_2 = secondary voltage (red-phase)
v_3 = primary voltage, yellow-phase
v_4 = secondary voltage, yellow-phase
v_5 = primary voltage, blue-phase
v_6 = secondary voltage, blue-phase
Xl_{prim} = transformer primary leakage reactance
Xl_{sec} = transformer secondary leakage reactance
x'' = generator subtransient reactance
Y_c = capacitor Norton equivalent admittance
Y_l = inductor Norton equivalent admittance
$[Y_{ss}]$ = mutually coupled transformer equivalent admittance matrix
$\tilde{Z}_{load}$ = load impedance
$\tilde{Z}_{source}$ = generator impedance

Single-phase MEC

ϕ_c = core flux
ϕ_{l1} = primary winding leakage flux
ϕ_{l2} = secondary winding leakage flux
$\mathcal{P}_c$ = core incremental permeance
y_l = leakage admittance

Three-limb three-phase MEC

$\phi_{1,2,3}$ = winding-limb flux
$\phi_{4,5}$ = yoke flux
$\phi_{6,7,8}$ = zero-sequence flux
$\phi_{l1,l3,l5}$ = primary winding leakage flux
$\phi_{l2,l4,l6}$ = secondary winding leakage flux
$\mathcal{P}_{1,2,3}$ = winding-limb incremental permeance
$\mathcal{P}_{4,5}$ = yoke incremental permeance
$\mathcal{P}_{7,8,9}$ = zero-sequence incremental permeance

y_l = leakage admittance
y'_l = mutual leakage admittance between primary coils
y''_l = mutual leakage admittance between primary and secondary coils on different limbs
y'''_l = mutual leakage admittance between secondary coils

Single-phase UMEC

ϕ_1 = primary winding-limb flux
ϕ_2 = secondary winding-limb flux
ϕ_3 = yoke flux
ϕ_4 = primary winding leakage flux
ϕ_5 = secondary winding leakage flux
$\mathcal{P}_1^*$ = primary winding-limb permeance
$\mathcal{P}_2^*$ = secondary winding-limb permeance
$\mathcal{P}_3^*$ = yoke permeance
$\mathcal{P}_4^*$ = primary winding leakage permeance
$\mathcal{P}_5^*$ = secondary winding leakage permeance

Three-limb three-phase UMEC

$\phi_{1,2,3}$ = primary winding-limb flux
$\phi_{4,5,6}$ = secondary winding-limb flux
$\phi_{7,8,9}$ = primary winding leakage flux
$\phi_{10,11,12}$ = secondary winding leakage flux
$\phi_{13,14}$ = yoke flux
$\phi_{15,16,17}$ = zero-sequence flux
$\mathcal{P}^*_{1,2,3}$ = primary winding-limb permeance
$\mathcal{P}^*_{4,5,6}$ = secondary winding-limb permeance
$\mathcal{P}^*_{7,8,9}$ = primary winding leakage permeance
$\mathcal{P}^*_{10,11,12}$ = secondary winding leakage permeance
$\mathcal{P}^*_{13,14}$ = yoke permeance
$\mathcal{P}^*_{15,16,17}$ = zero-sequence permeance

Chapter 1

INTRODUCTION

Converter transformer models in current use with electromagnetic transient programs are based on the Steinmetz "approximate" equivalent circuit. A uniform flux is assumed throughout the core legs and yokes, individual winding leakages are combined and the magnetising current is placed on one side of the resultant series leakage reactance. Such arbitrary placement of magnetising current and lumped leakage reactance representation is expected to produce inaccurate information of transient behaviour and harmonics, where correct representation of winding flux leakage and division of magnetising current between transformer windings is critical.

In the absence of better information a proposal was made by [Dommel 1975] for using the coil closest to the core to calculate core flux. Considering the complexity of modern transformer designs, the proximity criterion, even when construction details are available, is difficult to implement in power systems programs.

Some HVdc schemes use the three-limb core converter transformer arrangement. However, the Steinmetz equivalent circuits were not initially intended to model the three-limb core and each transformer phase is commonly modelled as a magnetically independent unit.

A three-limb three-phase transformer model has recently been proposed [Stuehm 1993] which derives an electric circuit dual from a magnetic circuit equivalent that includes air and steel flux paths. Although the core leg, yoke and zero-sequence paths are individually represented, the individual winding leakages are lumped together and the question of the subdivision of the magnetising components between the windings is not resolved.

A new transformer model based on the unified magnetic equivalent circuit theory is developed in this thesis which removes the ambiguity of magnetising current subdivision and permits any type of core construction. The influence of the new model on the transient performance of HVdc converters is assessed by comparison with the conventional PSCAD-EMTDC model. The transient behaviour of three-phase bank and three-limb three-phase converter transformers is also compared.

Chapter 2 introduces the electromagnetic transient technique: the capacitor/inductor

Norton equivalents, and the power system nodal admittance matrix representation. The historical development of PSCAD-EMTDC, as a specialised HVdc electromagnetic transient program, is given. The state of the art in PSCAD-EMTDC component models is described, particular attention is given to the magnetically independent transformer phase representation. Present multi-limb multi-phase transformer models are reviewed and a new magnetic equivalent circuit based electromagnetic transformer representation proposed.

In chapter 3 the interphase magnetic coupling representation of the new three-limb three-phase transformer representation is verified with laboratory results. The transient behaviour of the PSCAD-EMTDC single-phase bank, and new magnetic equivalent circuit (MEC) transformer models is compared. The new models are applied to the first rigorous intervalidation of the Harmonic Domain Analysis program with PSCAD-EMTDC. Newton's technique is applied to solve the non-linear three-limb three-phase magnetic equivalent circuit at each time step. Iterative and non-iterative MEC transformer models are compared under steady-state over-voltage operating conditions.

Chapter 4 introduces the unified magnetic equivalent circuit (UMEC). A two winding transformer UMEC is used to investigate the effect of core, and flux leakage paths on short, and open-circuit inductance respectively. Two winding transformer self and mutual inductances are expressed in terms of branch permeance. UMEC model accuracy is verified with laboratory data. A UMEC model of the Benmore valve-group converter transformers is derived. The harmonic flows predicted by the PSCAD-EMTDC and UMEC transformer models are compared in a test system derived from the New Zealand HVdc Benmore converter station. The single-phase UMEC is extended to represent the three-limb three-phase core configuration. A model of the Manapouri three-limb generator transformers is derived and verified with factory test data.

Chapter 5 introduces the group connected generator HVdc converter principle. The first ever set of field measurements for such as scheme in operation are given. A PSCAD-EMTDC model of the New Zealand HVdc group connected scheme at Benmore, inclusive of single-phase UMEC converter transformer representation, is verified with field data.

Chapter 6 presents the smoothing transformer as a new means for reducing HVdc converter dc side harmonics, at characteristic and non-characteristic frequencies, with compact passive components. The smoothing transformer is investigated with a UMEC transformer model, a realistic design is examined in the field data verified test system for the Benmore group connection. The steady-state and transient performance of the smoothing transformer is compared with that of the existing dc smoothing reactor and filter bank.

Chapter 7 derives a UMEC three-limb three-phase converter transformer model that is equivalent to the validated single-phase representations. The responses of the

single-phase bank and three-limb three-phase converter transformers to a single-phase fault are compared. The field data verified PSCAD-EMTDC Benmore test system is again applied and the conventional converter transformer winding configuration is used.

Finally, in chapter 8 the main conclusions to this thesis are given along with directions for future work.

Chapter 2

A PSCAD-EMTDC MULTI-LIMB TRANSFORMER FORMULATION

In this chapter the electromagnetic transient program underlying theory and historical development is presented. The state of the art in individual component models is discussed with reference to the PSCAD-EMTDC program. Transformer models that include core construction details are not presently represented in the PSCAD-EMTDC program. Therefore a new formulation for representing multi-limb multi-phase transformers in an electromagnetic transient program is proposed.

2.1 ELECTROMAGNETIC TRANSIENT PROGRAMS

The electromagnetic transient program is now widely accepted as a tool for the simulation of power system dynamics which are sensitive to relatively fast electromagnetic interactions between components. In addition to transient studies, the increasing number of non-linear controllers and fast switching components place a greater emphasis on the application of electromagnetic transient analysis to the steady-state; here significant waveform distortion results from continuous switching transients.

General reviews emphasising the many techniques categorised as electromagnetic transient analysis, and the accompanying computer programs have recently been documented [Zavahir 1992] [Anderson 1995]. In these theses an electromagnetic transient program was modified to incorporate state variable analysis, and transient stability respectively; detailed technique and computer program historical reviews were necessary to understand exactly why the new hybrid programs improved ac/dc system simulation. The main aim of the present work is to improve modelling of transformer non-linearities in electromagnetic transient programs.

Using as a basis the algorithm proposed by Dommel, in the early 1970's the Bonneville Power Administration produced the ElectroMagnetic Transient Program (EMTP) for the simulation of transient phenomenon in single and multi-phase networks [Dommel 1969]. Trapezoidal integration is used to transform inductive and capacitive differential equations into equivalent admittances and current sources. The inductor

differential equation

$$v_l(t) = L\frac{di_l(t)}{dt} \tag{2.1}$$

becomes

$$i_l(t) = Y_l v_l(t) + i_{nl} \tag{2.2}$$

where

$$Y_l = \frac{\Delta t}{2L}$$

and

$$i_{nl} = i_l(t-\Delta t) + \frac{\Delta t}{2L} v(t-\Delta t)$$

The inductor Norton equivalent is shown in figure 2.1(a).

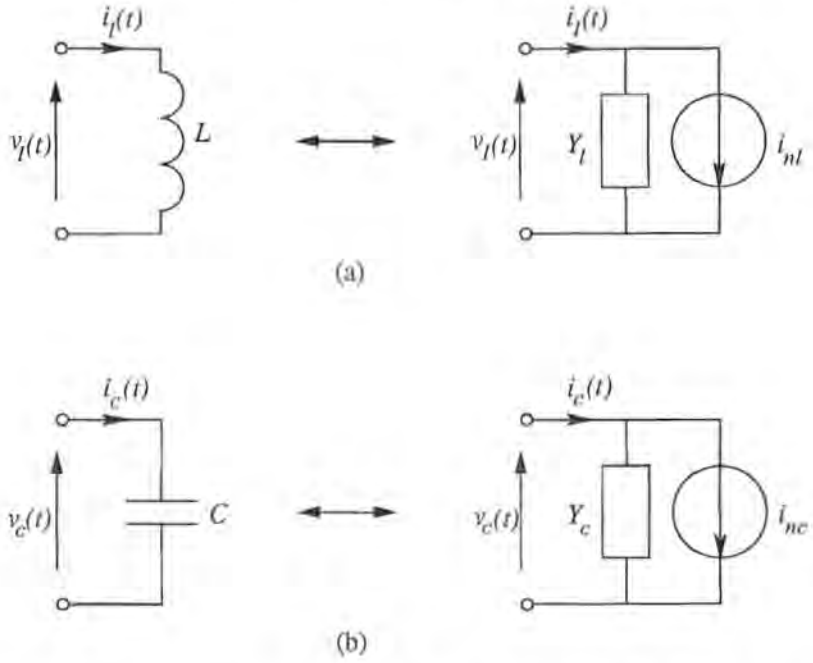

Figure 2.1 Electromagnetic transient program Norton equivalents: (a) Inductor, (b) Capacitor.

The capacitor differential equation

$$i_c(t) = C\frac{dv_c(t)}{dt} \tag{2.3}$$

becomes

$$i_c(t) = Y_c v_c(t) + i_{nc} \tag{2.4}$$

where

$$Y_c = \frac{2C}{\Delta t}$$

and

$$i_{nc} = -i_l(t-\Delta t) - \frac{2C}{\Delta t} v(t-\Delta t)$$

The capacitor Norton equivalent is shown in figure 2.1(b).

Once inductive and capacitive branches are converted to Norton equivalents they are combined with purely resistive branches, and the state of the system at time t is described by the set of linear equations [Dommel 1969]

$$[Y]\tilde{v}(t) = \tilde{i}(t) - \tilde{I} \tag{2.5}$$

where

$[Y]$	=	nodal admittance matrix
$\tilde{v}(t)$	=	node voltage vector
$\tilde{i}(t)$	=	injected node current vector
$\tilde{I}$	=	current source vector

If the vector of node voltages is partitioned into two sets, one with the unknown voltages $\tilde{v}_A(t)$ and another with the known voltages (specified voltage sources) $\tilde{v}_B(t)$, then equation 2.5 can be rewritten

$$\begin{bmatrix} [Y_{AA}] & [Y_{AB}] \\ [Y_{BA}] & [Y_{BB}] \end{bmatrix} \begin{bmatrix} \tilde{v}_A(t) \\ \tilde{v}_B(t) \end{bmatrix} = \begin{bmatrix} \tilde{i}_A(t) \\ \tilde{i}_B(t) \end{bmatrix} - \begin{bmatrix} \tilde{I}_A \\ \tilde{I}_B \end{bmatrix} \tag{2.6}$$

The vector of unknown node voltages is found by solving

$$[Y_{AA}]\tilde{v}_A(t) = \tilde{i}_A(t) - \tilde{I}_A - [Y_{AB}]\tilde{v}_B(t) \tag{2.7}$$

EMTP is well suited for simulating large ac systems where dynamic behaviour follows a small number of network topological changes. The program was not initially applied to frequent and variable switching cases such as ac/dc conversion.

In 1976 Manitoba Hydro began developing the ElectroMagnetic Transient Direct Current program (EMTDC). The resulting specialised HVdc simulation program combined Dommel's technique with valve group and salient pole synchronous machine models [Woodford *et al.* 1983]. A user written interface was included to process and control voltage and current sources, and switch branch elements. Disconnected subnetworks were utilised to maximise the speed of solution. In 1985 Manitoba HVdc Research Center validated EMTDC simulation with transient field data from Bipoles 1 and 2 of the Nelson River dc transmission system [Woodford 1985]. Recently the Power System Computer Aided Design (PSCAD) package was combined with EMTDC, this graphical interface assists the user in setting up, running and analysing simulations [EMTDC models 1994].

The practical applications of the transformer formulations presented in this work are all specific to HVdc transmission. For this reason PSCAD-EMTDC has been selected as the most appropriate program to implement the new models proposed. Figure 2.2 presents a simplified flow diagram for the PSCAD-EMTDC program.

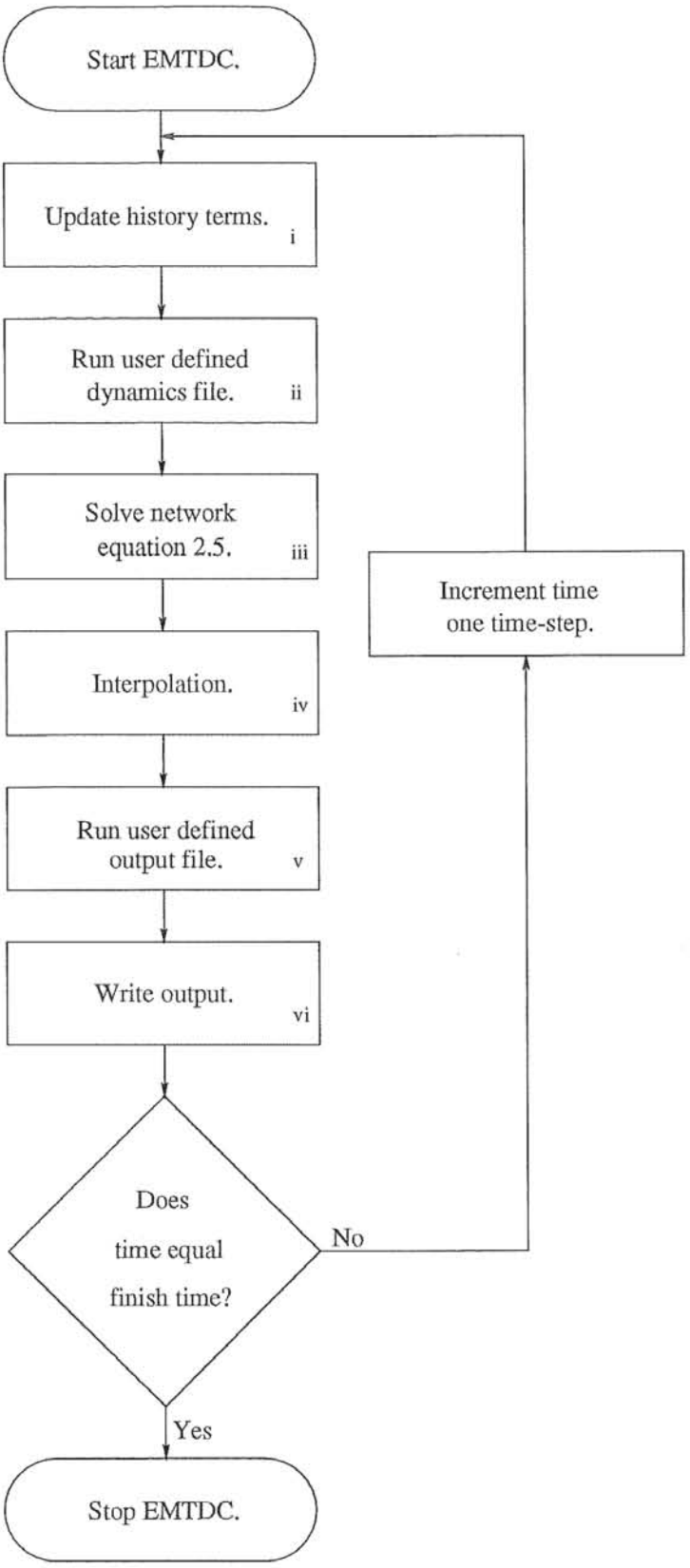

Figure 2.2 Simplified EMTDC main program.

2.2 THE STATE OF THE ART IN PSCAD-EMTDC COMPONENT MODELS

Many individual HVdc components are accurately represented by PSCAD-EMTDC models [EMTDC user 1994]. The Bergeron and frequency-dependent distributed transmission line models are used to represent overhead lines. Conductor properties and unbalanced geometries are included in the transmission line models. The six pulse graetz bridge model uses a phase locked oscillator for the complex co-ordination of valve firing pulses. Time-step interpolation accurately determines individual switching instants. A complete range of HVdc link controllers is available. FACTS devices such as Static var compensators (SVC), thyristor controlled reactors and thyristor switched capacitor models have been added to the library of components.

The SVC, salient pole generator and squirrel cage induction machine models are incorporated in state variable form; a current source and stabilising Norton resistance provide a simple and effective interface with the electromagnetic transient program.

Electric circuits and continuous system modelling functions are interfaced. Metering functions record instantaneous electrical, magnetic and mechanical variables, as well as steady-state information on real and reactive power, phasor magnitude and angle.

In comparison to the precision of other PSCAD-EMTDC component models, the mutually coupled winding representation for transformers is simplistic and can result in a degradation of simulation accuracy. The electrical equations for the two coupled coils in figure 2.3(a) are

$$\begin{bmatrix} v_1(t) \\ v_2(t) \end{bmatrix} = \begin{bmatrix} L_{11} & M_{12} \\ M_{12} & L_{22} \end{bmatrix} \begin{bmatrix} \frac{di_1(t)}{dt} \\ \frac{di_2(t)}{dt} \end{bmatrix} \tag{2.8}$$

If winding resistance is included, equation 2.8 is easily manipulated into the form of the Steinmetz "exact" equivalent circuit shown in figure 2.3(b), where

$$L_1 = L_{11} - aM_{12}$$

and

$$L_2 = a^2 L_{22} - aM_{12}$$

This linear equivalent circuit applies to individual phases only. This approximation is also appropriate for multi-phase banks of single-phase transformers where the individual units are magnetically independent. Moreover in ac fault studies transformers are usually represented with magnetically independent units [Giesner 1971] [The Electricity Council 1981] [Bickford and Heaton 1986] [General Electric Company 1987].

Non-linear magnetising and core-loss components of winding current are incorporated in the PSCAD-EMTDC transformer model with a shunt current source and resistance respectively across one winding. Since the single-phase approximation does

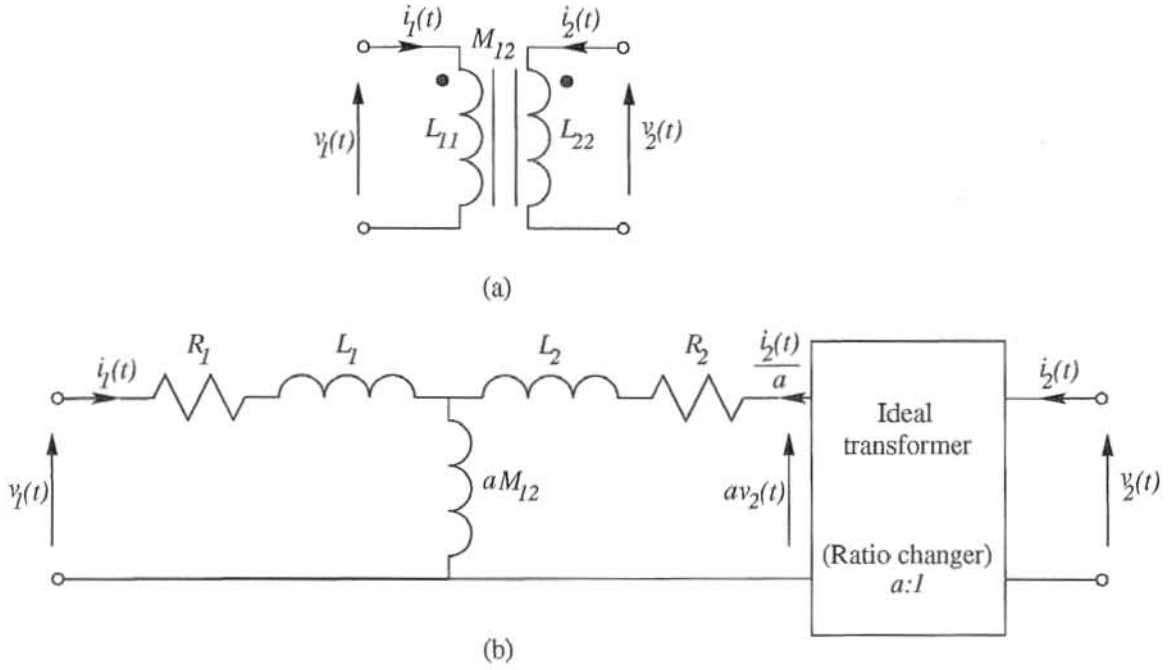

Figure 2.3 PSCAD-EMTDC linear transformer model: (a) Mutually coupled coils, (b) Steinmetz circuit.

not incorporate interphase magnetic coupling, the magnetising current injection is calculated at each time step independent of the other phases.

Accurate simulation of HVdc converter stations with multi-limb converter transformers requires a new PSCAD-EMTDC transformer model. Three-limb converter transformers are present in some existing HVdc schemes, as they can offer financial and operational advantages. The eight converter transformers of the Vindhyachal 500MW back-to-back HVdc converter station (India) are three-limb three-phase units. Although transportation limitations have traditionally restricted the presence of three-limb three-phase transformers in remote HVdc systems, sealed winding site-assembled multi-limb transformers can provide the lowest cost alternative to single-phase banks [Flux 1971]. Moreover three-limb converter transformers have been shown to significantly reduce the detrimental effect of dc excitation caused by geomagnetically induced currents [Takasu *et al.* 1994].

2.3 MODELLING MULTI-LIMB TRANSFORMERS

An important contribution to the modelling of power system transformers was made by [Chen and Dillon 1974]. Although they recognised the influence of the transformer core and flux path leakage, their models were based on linear transformations. Non-linear transformer magnetisation effects were given detailed consideration [Abu Nasser 1981], but only for the case of magnetically independent phases.

The principle of duality has been used [Arturi 1991] [Stuehm 1993] to take into

account the magnetising currents and core configuration when modelling multi-limb transformers with the EMTP program. The duality based equivalents involve a large number of components; for instance twenty-three inductances and nine ideal transformers are required to represent a three-phase three-winding transformer. Recent attempts to validate duality based models [Stuehm 1993] with experimental results for a three-legged stacked core transformer have shown considerable discrepancies (of up to 40%). Moreover the duality method requires the use of true non-linear inductors in series; this is not feasible in the EMTP [Dommelen 1987] and Stuehm adds components to the electric dual to isolate each true non-linear inductor.

Alternative proposals [Hatziargyriou *et al.* 1993] [Chen and Neudorfer 1993], based on an equivalent inductance matrix, reduce the complexity of the equivalent circuit. However, Hatziargyriou's method does not take into account the core non-linearity under transient conditions and Chen's non-linear equivalent inductance matrix requires regular updating during the EMTP solution; such updating reduces the speed of electromagnetic transient programs.

[Leon and Semlyen 1994] have recently proposed a Norton equivalent transformer representation as a simple interface with an electromagnetic transient program; but do not perform direct analysis of the magnetic circuit and select a combination of the duality and leakage inductance representation.

Also based on the Norton equivalent transformer concept this chapter now describes a multi-limb transformer formulation derived directly from magnetic equivalent circuit analysis. This formulation provides a method that allows detailed magnetic equivalent circuits to be easily implemented in electromagnetic transient programs.

2.4 INCREMENTAL PERMEANCE FORMULATION

The representation of the magnetic equivalent circuit branch k, as displayed in figure 2.4, separates the branch reluctance and winding magneto-motive-force (MMF) components. Individual magnetic characteristics can be applied to each branch. Each transformer winding can be modelled as a lumped coil or on a turn to turn bases with single or multiple magnetic equivalent circuit branches respectively.

The non-linear relationship between branch flux and branch reluctance MMF drop must be linearised. This non-linear relationship can be described by

$$\theta_{k1} = r_k(\phi_k) \tag{2.9}$$

The MMF of winding N_k is given by

$$\theta_{k2} = N_k i_k \tag{2.10}$$

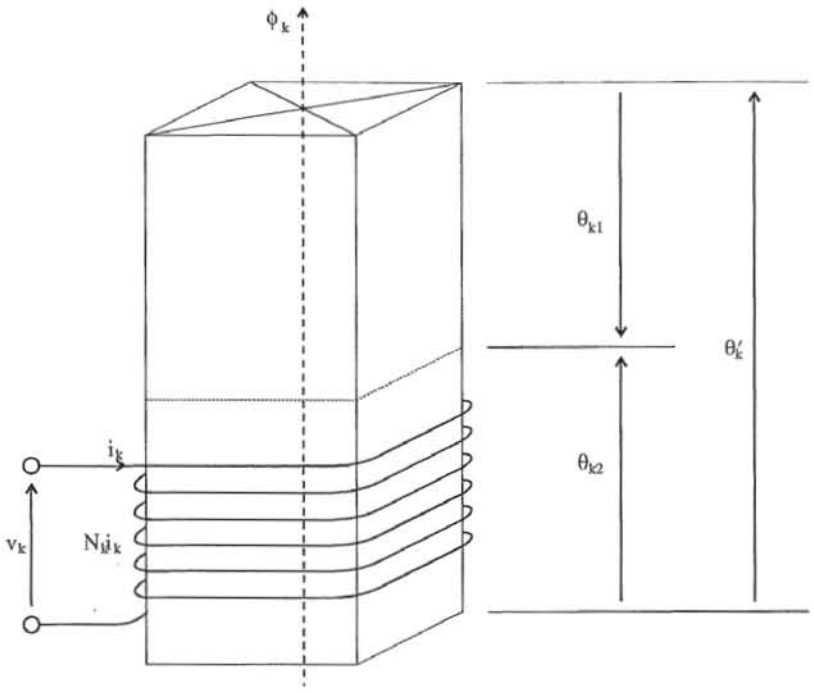

Figure 2.4 Magnetic equivalent circuit branch.

Combining these two equations to give the resultant branch MMF θ'_k yields

$$\theta'_k = \theta_{k2} - \theta_{k1} \tag{2.11}$$

Linearising equation 2.9 about $(t - \Delta t)$ in the time domain gives

$$\theta_{k1}(t) - \theta_{k1}(t - \Delta t) = \mathcal{R}_k[\phi_k(t) - \phi_k(t - \Delta t)] \tag{2.12}$$

where

$$\Delta t \to 0$$

and

$$\mathcal{R}_k = \left.\frac{d\theta_{k1}}{d\phi_k}\right|_{\phi_k(t-\Delta t)}$$

Solving equation 2.12 for the branch reluctance at the present time step gives

$$\theta_{k1}(t) = \theta_{k1}(t - \Delta t) + \mathcal{R}_k[\phi_k(t) - \phi_k(t - \Delta t)] \tag{2.13}$$

Equation 2.13 allows the linearised relationship between winding current and branch flux to be formulated, it can be re-written as

$$\theta_{k1}(t) = \mathcal{R}_k\phi_k(t) + \theta_{nk} \tag{2.14}$$

where

$$\theta_{nk} = \theta_{k1}(t - \Delta t) - \mathcal{R}_k\phi_k(t - \Delta t) \tag{2.15}$$

Hysteresis or single valued magnetic characteristics can be represented with equation 2.14. Combining equation 2.15 with equations 2.10 and 2.11 gives

$$\theta'_k = N_k i_k - \mathcal{R}_k \phi_k - \theta_{nk} \tag{2.16}$$

or

$$\phi_k = \mathcal{P}_k [N_k i_k - \theta'_k - \theta_{nk}] \tag{2.17}$$

where the incremental branch permeance

$$\mathcal{P}_k = \frac{1}{\mathcal{R}_k} \tag{2.18}$$

The relationship in equation 2.17 is general and can be extended to any number of branches in a multi-limb transformer magnetic equivalent circuit.

$$\tilde{\phi} = [\mathcal{P}] \Big([N] \tilde{i} - \tilde{\theta}' - \tilde{\theta}_n \Big) \tag{2.19}$$

Diagonal matrix $[\mathcal{P}]$ has individual elements of branch incremental permeance and diagonal matrix $[N]$ elements of branch winding turns. Diagonal elements of $[N]$ are zero for branches with no windings.

The linearised relationship between winding current and branch flux can be extended to incorporate the magnetic equivalent circuit branch connections. Let the node-branch connection matrix of the magnetic circuit be $[A]^T$ and the vector of nodal magnetic drops be $\tilde{\theta}_{node}$. At each node the flux must sum to zero, stated as

$$[A]^T \tilde{\phi} = \tilde{0} \tag{2.20}$$

Application of the branch-node connection matrix to the vector of nodal magnetic drops gives the branch MMF.

$$[A] \tilde{\theta}_{node} = \tilde{\theta}' \tag{2.21}$$

Combining equations 2.19, 2.20 and 2.21 gives

$$[A]^T \tilde{\phi} = \tilde{0} = [A]^T [\mathcal{P}][N] \tilde{i} - [A]^T [\mathcal{P}][A] \tilde{\theta}_{node} - [A]^T [\mathcal{P}] \tilde{\theta}_n \tag{2.22}$$

Solving equation 2.22 for $\tilde{\theta}_{node}$ and writing $\tilde{\phi}_n = [\mathcal{P}] \tilde{\theta}_n$ gives

$$\tilde{\theta}_{node} = \Big([A]^T [\mathcal{P}][A] \Big)^{-1} \Big([A]^T [\mathcal{P}][N] \tilde{i} - [A]^T \tilde{\phi}_n \Big) \tag{2.23}$$

Substitution of equation 2.23 into 2.21 gives

$$\tilde{\theta}' = [A] \Big([A]^T [\mathcal{P}][A] \Big)^{-1} \Big[[A]^T [\mathcal{P}][N] \tilde{i} - [A]^T \tilde{\phi}_n \Big] \tag{2.24}$$

Equation 2.24 is combined with equation 2.19 to give

$$\begin{aligned}\tilde{\phi} &= [\mathcal{P}]\Big([N]\tilde{i} - [A]\Big([A]^T[\mathcal{P}][A]\Big)^{-1}\Big[[A]^T[\mathcal{P}][N]\tilde{i} - [A]^T\tilde{\phi}_n\Big] - \tilde{\theta}_n\Big) \\ &= \Big([I] - [\mathcal{P}][A]\Big([A]^T[\mathcal{P}][A]\Big)^{-1}[A]^T\Big)\Big([\mathcal{P}][N]\tilde{i} - \tilde{\phi}_n\Big) \\ &= [M]\Big([\mathcal{P}][N]\tilde{i} - \tilde{\phi}_n\Big) \qquad (2.25)\end{aligned}$$

where

$$[M] = [I] - [\mathcal{P}][A]\Big([A]^T[\mathcal{P}][A]\Big)^{-1}[A]^T$$

If the branch connections of the magnetic circuit are such that two branches carry the same flux, the matrix $[M]$ is singular. If set of branches are partitioned into two sets, one with the MMF sources $\tilde{\phi}_s$ and another with pure reluctance paths $\tilde{\phi}_r$, then equation 2.25 can be rewritten

$$\begin{bmatrix}\tilde{\phi}_s \\ \tilde{\phi}_r\end{bmatrix} = \begin{bmatrix}[M_{ss}] & [M_{sr}] \\ [M_{rs}] & [M_{rr}]\end{bmatrix}\left(\begin{bmatrix}[\mathcal{P}_s] & [0] \\ [0] & [\mathcal{P}_r]\end{bmatrix}\begin{bmatrix}[N_s]\tilde{i}_s \\ \tilde{0}\end{bmatrix} - \begin{bmatrix}\tilde{\phi}_{ns} \\ \tilde{\phi}_{nr}\end{bmatrix}\right) \qquad (2.26)$$

The problem of possible $[M]$ matrix singularity may be removed by inverting only matrix partition $[M_{ss}]$. Utilizing matrix partitioning equation 2.26 gives

$$\tilde{\phi}_s = [M_{ss}]\Big([\mathcal{P}_s][N_s]\tilde{i}_s - \tilde{\phi}_{ns}\Big) - [M_{sr}]\tilde{\phi}_{nr} \qquad (2.27)$$

Equation 2.27 relates winding current to branch flux, what is required next is to relate branch flux to winding voltage. Winding voltage v_k is related to branch flux ϕ_k by Faraday's law of magnetic flux

$$v_k = N_k\frac{d\phi_k}{dt} \qquad (2.28)$$

Discretizing equation 2.28 with trapezoidal integration and generalising for magnetic branches with an MMF source gives

$$\tilde{\phi}_s(t) = \tilde{\phi}_s(t - \Delta t) + \frac{\Delta t}{2}[N_s]^{-1}\Big[\tilde{v}_s(t) + \tilde{v}_s(t - \Delta t)\Big] \qquad (2.29)$$

The number of first order differential equation solutions required is equal to the number of winding-limb branches. Residual flux can be simply included by setting each branch flux to the residual value desired at time zero. Finally, combining equation 2.27 and 2.29, and solving for winding current $\tilde{i}_s$ gives the Norton equivalent

$$\tilde{i}_s(t) = [Y_{ss}]\tilde{v}_s(t) + \tilde{i}_{ns} \qquad (2.30)$$

where

$$[Y_{ss}] = \Big([M_{ss}][\mathcal{P}_s][N_s]\Big)^{-1} \frac{\Delta t}{2}[N_s]^{-1}$$

and

$$\tilde{i}_{ns} = \Big([M_{ss}][\mathcal{P}_s][N_s]\Big)^{-1} \Big(\frac{\Delta t}{2}[N_s]^{-1}\tilde{v}_s(t-\Delta t) + \tilde{\phi}_s(t-\Delta t) + [M_{ss}]\tilde{\phi}_{ns} + [M_{sr}]\tilde{\phi}_{nr}\Big)$$

The Norton equivalent representation is a vector extension of the scalar inductor equation 2.2, it is in an ideal form for PSCAD-EMTDC implementation. The symmetric admittance matrix $[Y_{ss}]$ is non-diagonal and thus represents mutual couplings.[1] Equations 2.9 to 2.30 are general and apply to any magnetic equivalent circuit consisting of a finite number of branches as shown in figure 2.4.

Air as well as iron path magnetic characteristics can be applied to magnetic equivalent circuit branches. Historically the transformer has been represented with shunt magnetising and series leakage reactances [Steinmetz 1895]. This approximation leads to difficulties in division of the transformer magnetising current up amongst the excited windings [Dommel 1975]. A unified magnetic equivalent circuit will be described in chapter 4 which overcomes this problem.

Winding copper loss representation can be included by placing series resistances at the terminals of the Norton equivalent. Alternatively each individual transformer winding can be modeled on a turn to turn basis with many individual magnetic equivalent circuit branches, this provides a more precise copper loss representation than the lumped winding resistance.

The above formulation is based directly on a magnetic equivalent circuit; it is specifically concerned with the simulation of transients resulting from saturation of the magnetic core and thus winding capacitance is not represented.

The formulation calculates operating flux within each branch of the magnetic equivalent circuit at each time step. This flux is utilized to accurately determine an equivalent resistance [Slemon 1966] that is added as a shunt across the terminals of the Norton equivalent to represent magnetic core losses.

2.5 CONCLUSIONS

Although the need for suitable electromagnetic transient models of ac and ac/dc components has intensified, the effort spent on transformer models relative to other non-linear elements (such as HVdc converters) has been small. The PSCAD-EMTDC version of the electromagnetic transient program has been selected to implement the proposed transformer models because the main application intended relates to HVdc transmission. The present phase independent PSCAD-EMTDC transformer models are suited

[1] The matrix $[Y_{ss}]$ is implemented in PSCAD-EMTDC as a network of admittances. Proof of matrix symmetry is essential, and is given in appendix A.

to represent multi-phase banks of single-phase transformers, but not the multi-phase multi-limb core construction.

An incremental permeance formulation of the non-linear behaviour of multi-phase multi-limb transformers for use with an electromagnetic transient program has been presented. The non-linear relationship between winding mmf and saturated branch flux is linearised in the time-domain. The formulation utilizes direct analysis of a magnetic equivalent circuit to provide a Norton equivalent electrical interface at the transformer terminals. The Norton equivalent is easily implementable in the PSCAD-EMTDC program. The transformer magnetic equivalent circuit is constructed from a finite number of branches incorporating individual magnetic characteristics and windings.

Chapter 3

THE LINEAR AND LINEARISED TRANSFORMER

In this chapter the magnetic equivalent circuit (MEC) transformer model interphase magnetic coupling representation is verified with laboratory results. The transient behaviour of equivalent PSCAD-EMTDC three-phase bank and three-limb three-phase transformer models are compared.

Single-phase and three-limb three-phase MEC Time Domain equivalents to existing Harmonic Domain transformer representations are derived. The new models are used to intervalidate the Harmonic Domain Analysis (HDA) and PSCAD-EMTDC programs.

Finally, Newton's technique is applied to solve the non-linear three-limb three-phase MEC at each time step. Iterative and non-iterative MEC models are compared for steady-state over-voltage operation.

3.1 INCORPORATING A LINEAR MEC IN PSCAD-EMTDC

The flow diagram of figure 3.1 describes the implementation of a linear MEC in PSCAD-EMTDC simulation and forms the basis for the transformer models presented in this thesis; it is placed in operation (ii) of the PSCAD-EMTDC main program shown in figure 2.2.

The transformer core is divided into segments of length L_k and area A_k. The incremental permeance of each MEC steel branch is constant and can be calculated from

$$\mathcal{P}_k = \frac{\mu_o \mu_{rk} A_k}{L_k} \tag{3.1}$$

The relative permeability μ_{rk}, which is fixed in a linear transformer model, is derived from the core B-H characteristics; typical μ_{rk} values for unsaturated grain-oriented silicon-steel range from 2,000 to 70,000 [Turner 1977]. Once path permeances are known, the admittance matrix $[Y_{ss}]$ can be calculated and placed in the nodal admittance matrix $[Y]$ of equation 2.5. In this case the admittance matrix is constant and need only be calculated once during simulation. The current injections $\tilde{i}_{ns}$ however

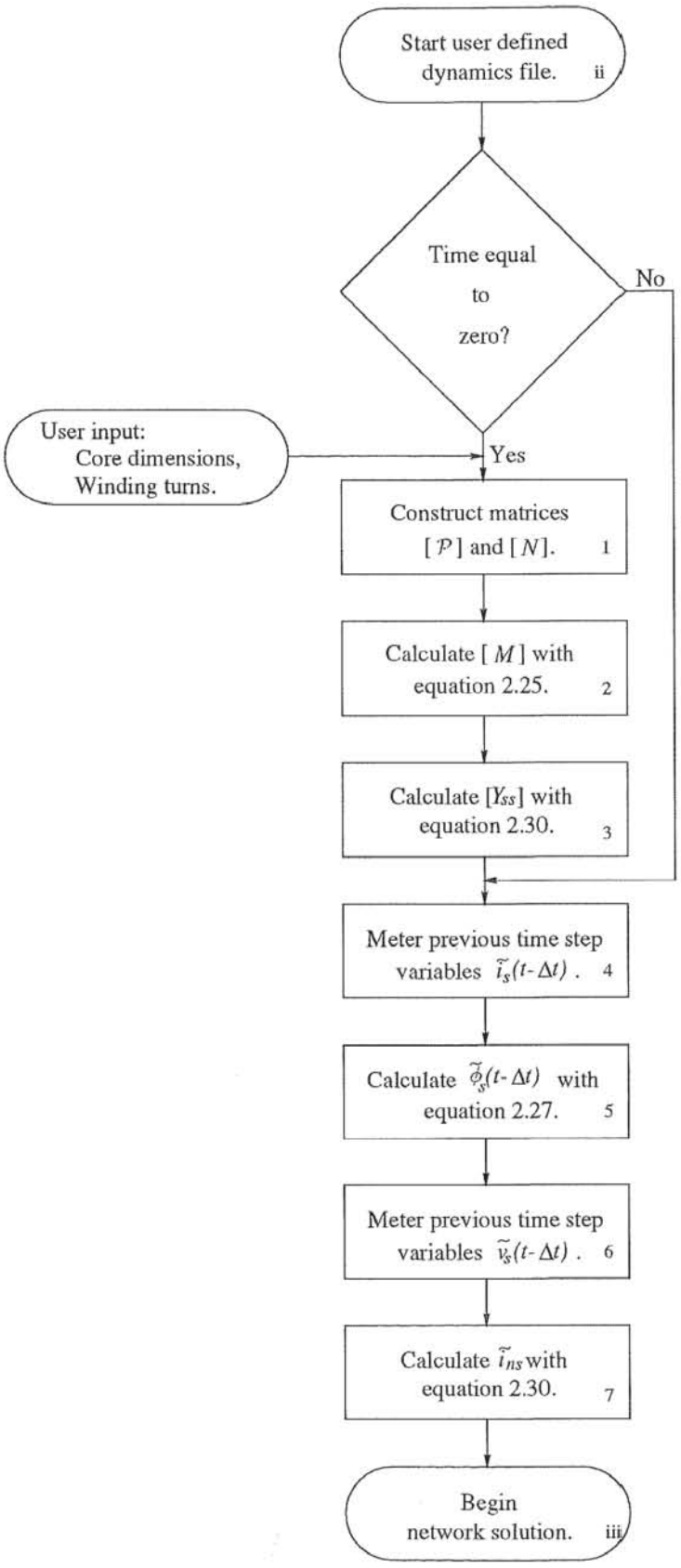

Figure 3.1 Linear formulation implementation in PSCAD-EMTDC.

must be recalculated at each time step and applied to the current source vector $\tilde{I}$ of equation 2.5.

3.1.1 Interphase magnetic coupling verification

Before discussions are complicated by the addition of core non-linearity, the verification of interphase magnetic coupling representation can be achieved with the linear implementation strategy. A three-limb three-phase transformer model was derived from the laboratory transformer parameters of table 3.1, and the MEC of figure 3.2(b).[1]

Electric circuit parameters		Magnetic circuit parameters	
Rating	40 kVA	$A_{winding\ limb}$	0.0122 (m^2)
Configuration	delta-star	$L_{winding\ limb}$	0.350 (m)
Frequency	50 (Hz)	A_{yoke}	0.0122 (m^2)
$V_{primary}$	440 (V)	L_{yoke}	0.180 (m)
$V_{secondary}$	220 (V)	μ_r	2000
		$N_{primary}$	108 $(turns)$
		$N_{secondary}$	31 $(turns)$

Table 3.1 Laboratory transformer parameters.

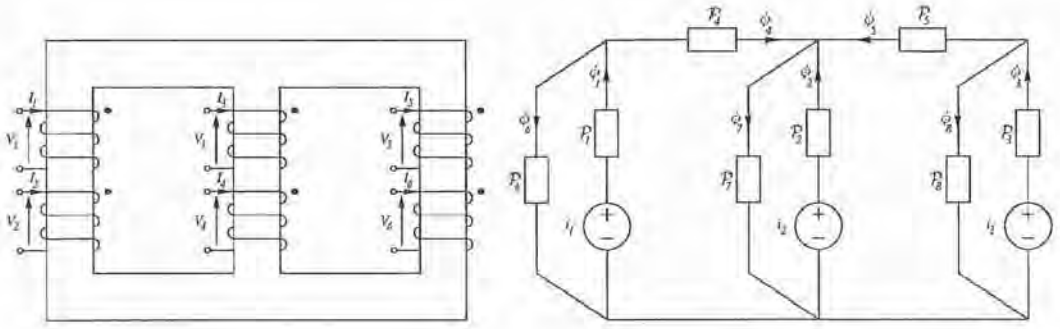

(a) (b)

Figure 3.2 Laboratory transformer: (a) Three-limb three-phase core type, (b) Magnetic equivalent circuit.

In this open-circuit transformer model, leakage flux paths are ignored. The MEC represents the core and zero-sequence magnetising component of transformer winding current alone. Permeances $\mathcal{P}_1$ to $\mathcal{P}_3$ represent the transformer winding limbs, $\mathcal{P}_4$ and $\mathcal{P}_5$ represent the yokes, and $\mathcal{P}_6$ to $\mathcal{P}_8$ represent the transformer zero-sequence flux paths. MMF sources i_{m1} to i_{m3} represent the transformer magnetising current.

Single-phase excitation of the three-limb transformer clearly demonstrates interphase magnetic coupling. In figure 3.3 the transformer red-phase primary winding

[1] To examine interphase magnetic coupling the laboratory transformer is operated below rated voltage, the effects of core saturation are removed. Under these conditions the zero-sequence flux paths do not greatly influence experimental results, therefore $\mathcal{P}_{zero\ sequence}$ has been arbitrarily set to $0.0005\mathcal{P}_{winding\ limb}$.

is energised. When a voltage $V_{coupling}$ is applied to only one transformer winding the magnetic flux from the energised limb returns via the remaining two limbs.

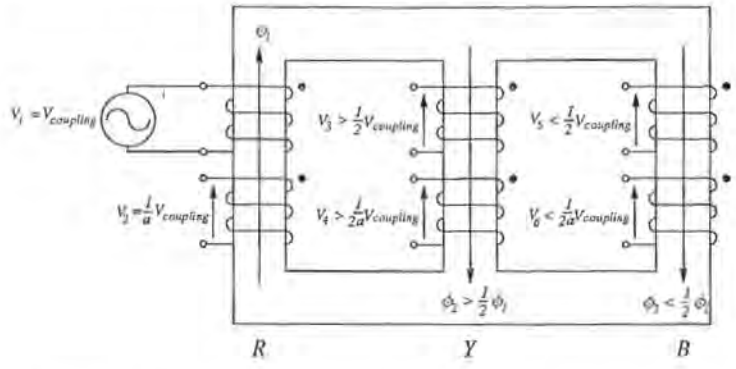

Figure 3.3 Laboratory transformer single-phase excitation.

The return path reluctance for red-phase flux ϕ_1 via the yellow winding-limb is less than via the blue winding-limb. The yellow-phase flux ϕ_2 is thus slightly greater than $\frac{1}{2}\phi_1$, and the blue-phase flux ϕ_3 is slightly less than $\frac{1}{2}\phi_1$. The magnitudes of primary and secondary yellow-phase induced voltages are slightly greater than $\frac{1}{2}V_{coupling}$, and $\frac{1}{2a}V_{coupling}$ respectively. The magnitudes of primary and secondary blue-phase voltages are slightly less than $\frac{1}{2}V_{coupling}$ and $\frac{1}{2a}V_{coupling}$ respectively. Orientation of the yellow and blue-phase windings phase shifts primary and secondary voltages by 180^o.

Experimental and simulated results for a 240V excitation of the laboratory transformer red-phase primary winding are displayed in figure 3.4. As predicted, the yellow and blue-phase voltages are phase shifted 180^o and each of them is approximately half the magnitude of the red-phase.

The magnitude unbalance which exists between yellow and blue-phase voltages is not obvious from the simulated results. In this linear model the constant relative permeability μ_r=2000 results in a high branch permeance. The large winding-limb and yoke permeances give only a small flux unbalance between the yellow and blue winding limbs.

3.2 INCORPORATING A NON-LINEAR MEC IN PSCAD-EMTDC

In the linear model, the matrix $[Y_{ss}]$ was calculated once only. This is not the case for the non-linear model. Each incremental permeance $\mathcal{P}_k$ changes as the magnetic branch moves around its saturation characteristic.

3.2.1 MEC branch saturation characteristics

Hysteresis will not be included in the transformer models proposed in this work. The effect of hysteresis is only apparent in the magnetising currents of small VA rated labo-

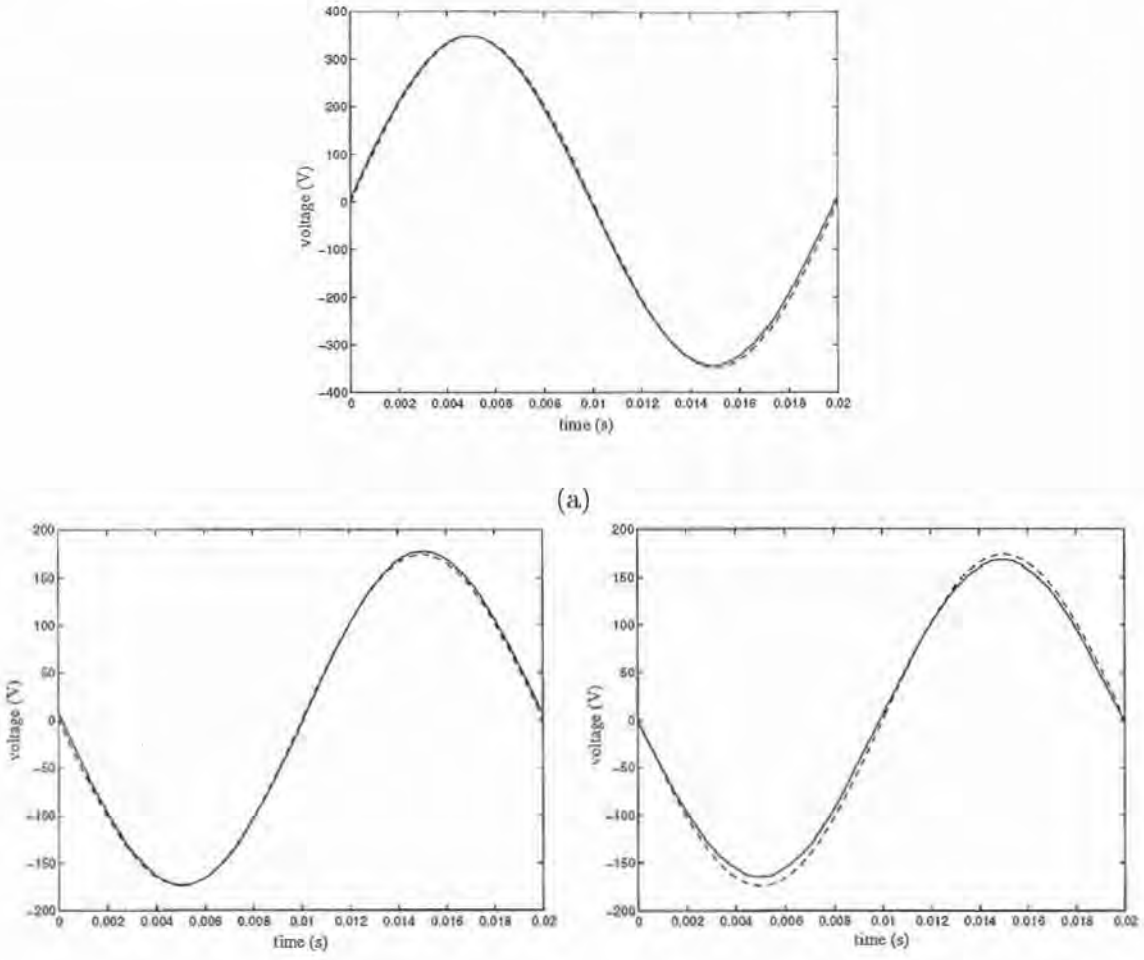

Figure 3.4 Single-phase excitation, primary winding voltages; Solid=recorded, Dash-dash=simulation: (a) Red-phase V_1, (b) Yellow-phase V_3, (c) Blue-phase V_5.

ratory transformers. Moreover it has been shown that the effects of detailed hysteresis loop representation in HVdc converter transformers have little effect on the converter behaviour during disturbances [Joosten *et al.* 1990].

During transient conditions the transformer branches may enter very high and different levels of saturation. To accurately represent the transformer behaviour during such transients, precise representation of the branch magnetising characteristics is required. The hyperbola equation 3.2 provides a preferred match to experimental per-unit characteristics in both the saturated and unsaturated regions [Medina and Arrillaga 1992a].

$$\mathcal{E}\phi_k = (m_1 i_k + b_1 - \phi_k)(m_2 i_k + b_2 - \phi_k) - b_1 b_2 \tag{3.2}$$

where

m_1 = slope of unsaturated region

m_2 = slope of saturated region

b_1 = ordinates to the origin of asymptote to m_1
b_2 = ordinates to the origin of asymptote to m_2
$\mathcal{E}$ = correction term

As correction term $\mathcal{E}$ is increased from zero, the knee point of the hyperbola saturation representation is made less sharp. Solving equation 3.2 for i_k and taking the positive root gives

$$i_k = -DA * (B - \Delta) \tag{3.3}$$

where

$A = m_1 m_2$
$B = m_1(b_2 - \phi_k) + m_2(b_1 - \phi_k)$
$C = \phi_k^2 - \phi_k(b_1 + b_2 + \mathcal{E})$
$\Delta = \sqrt{B^2 - 4AC}$
$DA = \frac{1}{2A}$

The incremental branch reluctance is derived from equation 3.2

$$\mathcal{R}_k = DA\left[m_1 + m_2 - \frac{B(m_1 + m_2) + 2A(2\phi_k - b_1 - b_2 - \mathcal{E})}{\Delta}\right] \tag{3.4}$$

Although equations 3.3 and 3.4 will not represent third quadrant operating points, the symmetrical nature of the saturation characteristic can be used for calculation in this quadrant. The incremental branch reluctance $\mathcal{R}_k$ never equates to zero, and at the origin it is equal to

$$\mathcal{R}_k = \frac{b_1 + b_2 + \mathcal{E}}{m_1 b_2 + m_2 b_1} \tag{3.5}$$

3.2.2 The linearised Norton equivalent

The flow diagram of figure 3.5 describes the per-unit implementation of a non-linear MEC in PSCAD-EMTDC. The incremental permeance formulation modifications required for per-unit implementation are listed in appendix B. The previous time step winding limb flux vector $\tilde{\phi}_s(t - \Delta t)$ can be calculated from the vector $\tilde{v}_s(t - \Delta t)$, and stored vectors $\tilde{\phi}_s(t - 2\Delta t)$ and $\tilde{v}_s(t - 2\Delta t)$ with the trapezoidal integration

$$\tilde{\phi}_s(t - \Delta t) = \tilde{\phi}_s(t - 2\Delta t) + \frac{\Delta t}{2}[N_s]^{-1}\left[\tilde{v}_s(t - \Delta t) + \tilde{v}_s(t - 2\Delta t)\right] \tag{3.6}$$

The per-unit form of equation 3.6 is given in appendix B. Calculation of the flux in yoke and zero-sequence paths $\tilde{\phi}_r(t - \Delta t)$ requires solving the non-linear MEC. [Medina 1992]

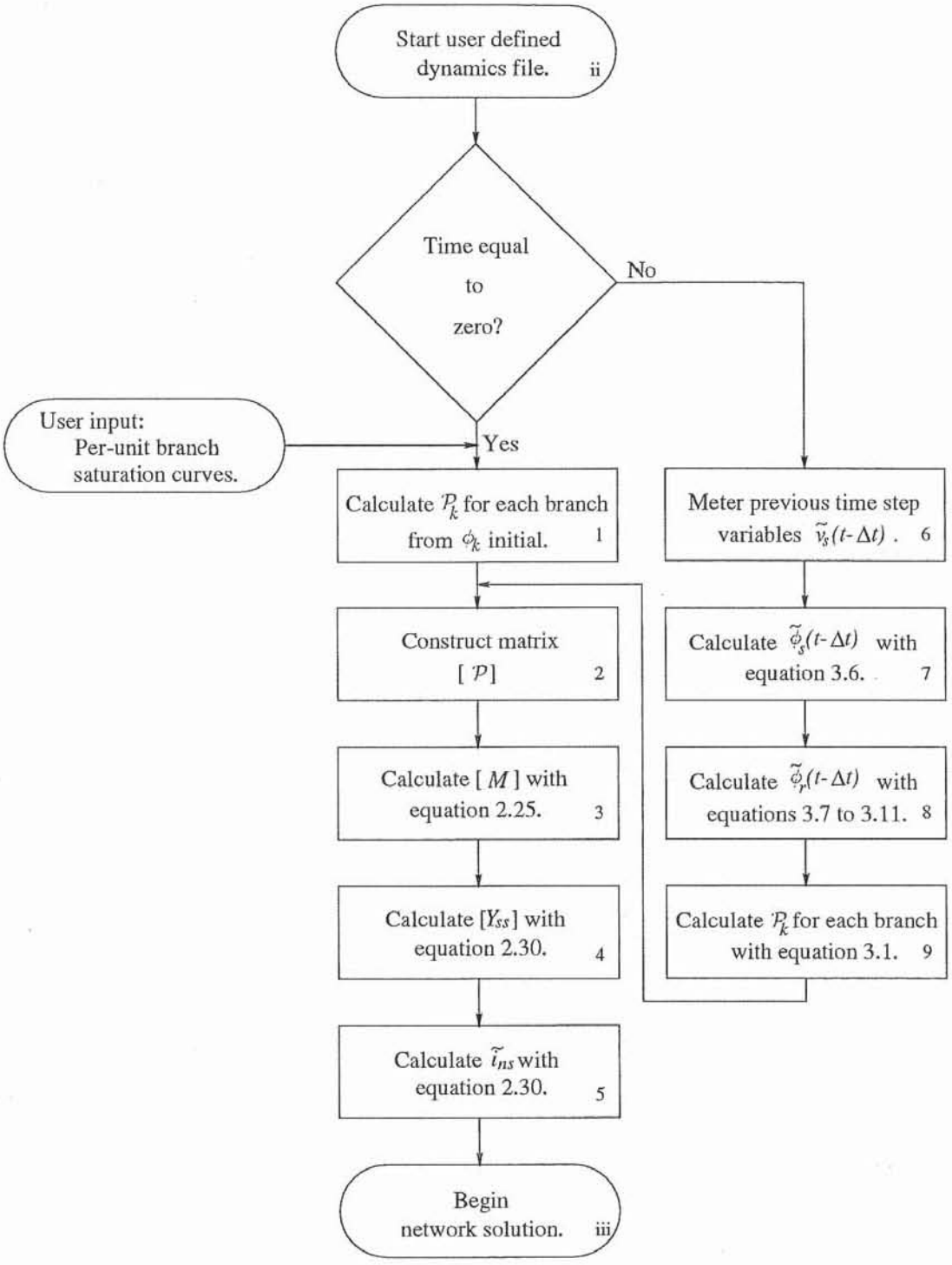

Figure 3.5 Non-linear formulation implementation in PSCAD-EMTDC.

proposes a linear approximation to the true solution

$$\phi_4(t-\Delta t) = k_1k_0\phi_1(t-\Delta t) - k_2k_0\phi_2(t-\Delta t) - k_3k_0\phi_3(t-\Delta t) \quad (3.7)$$

$$\phi_5(t-\Delta t) = -k_3k_0\phi_1(t-\Delta t) - k_2k_0\phi_2(t-\Delta t) + k_1k_0\phi_3(t-\Delta t) \quad (3.8)$$

$$\phi_6(t-\Delta t) = \phi_1(t-\Delta t) - \phi_4(t-\Delta t) \quad (3.9)$$

$$\phi_7(t-\Delta t) = \phi_4(t-\Delta t) + \phi_2(t-\Delta t) + \phi_5(t-\Delta t) \quad (3.10)$$

$$\phi_8(t-\Delta t) = \phi_3(t-\Delta t) - \phi_5(t-\Delta t) \quad (3.11)$$

where k_0=0.9, k_1=0.508, k_2=0.5 and k_3=0.492.

Using the solved branch flux $\phi_k(t-\Delta t)$ branch permeance $\mathcal{P}_k$ is calculated directly from the branch saturation characteristic . Once the branch permeance is known the per-unit admittance matrix $[Y_{ss}]$ and current source vector $\tilde{i}_{ns}$ can be calculated.

3.2.3 Comparing three-phase transformer representations

The circuit as shown in figure 3.6 and ideal circuit breaker action have been chosen to highlight the differences between the PSCAD-EMTDC three-phase bank and MEC three-limb three-phase transformer representations.

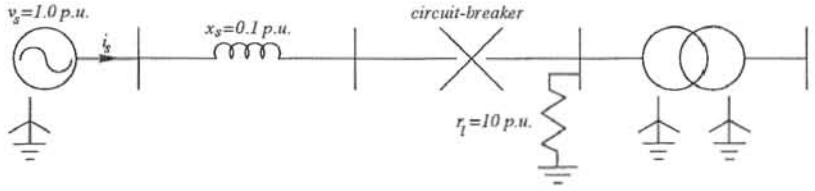

Figure 3.6 Transformer magnetic core test system.

The MEC of figure 3.2(b) is again utilized to represent the open-circuit three-limb transformer, but in this case all branches are non-linear. Table 3.2 lists the hyperbola constants for the per-unit characteristics. The saturation characteristics for the winding, yoke and zero-sequence paths are those suggested by [Medina 1992].

Branch	$m_{1(linear)}$	$m_{2(sat)}$	b_1	b_2	$\mathcal{E}$
Winding limb	292.38	0.67	0.0	1.03	0.0
Yoke	292.38	1.67	0.0	1.03	0.0
Zero-sequence	6.00	1.44	0.0	0.22	0.0

Table 3.2 Test transformer hyperbola parameters.

The three-limb three-phase model (3limb-oc) was compared with the present PSCAD-EMTDC model of the three-phase, two-winding transformer (xfmr-3p2w) [EMTDC user 1994] with saturation enabled. The circuit of figure 3.6 was subjected to three sequential operating conditions specially selected to emphasize the magnetic behaviour of the transformer. The resulting primary currents are shown in figure 3.7.

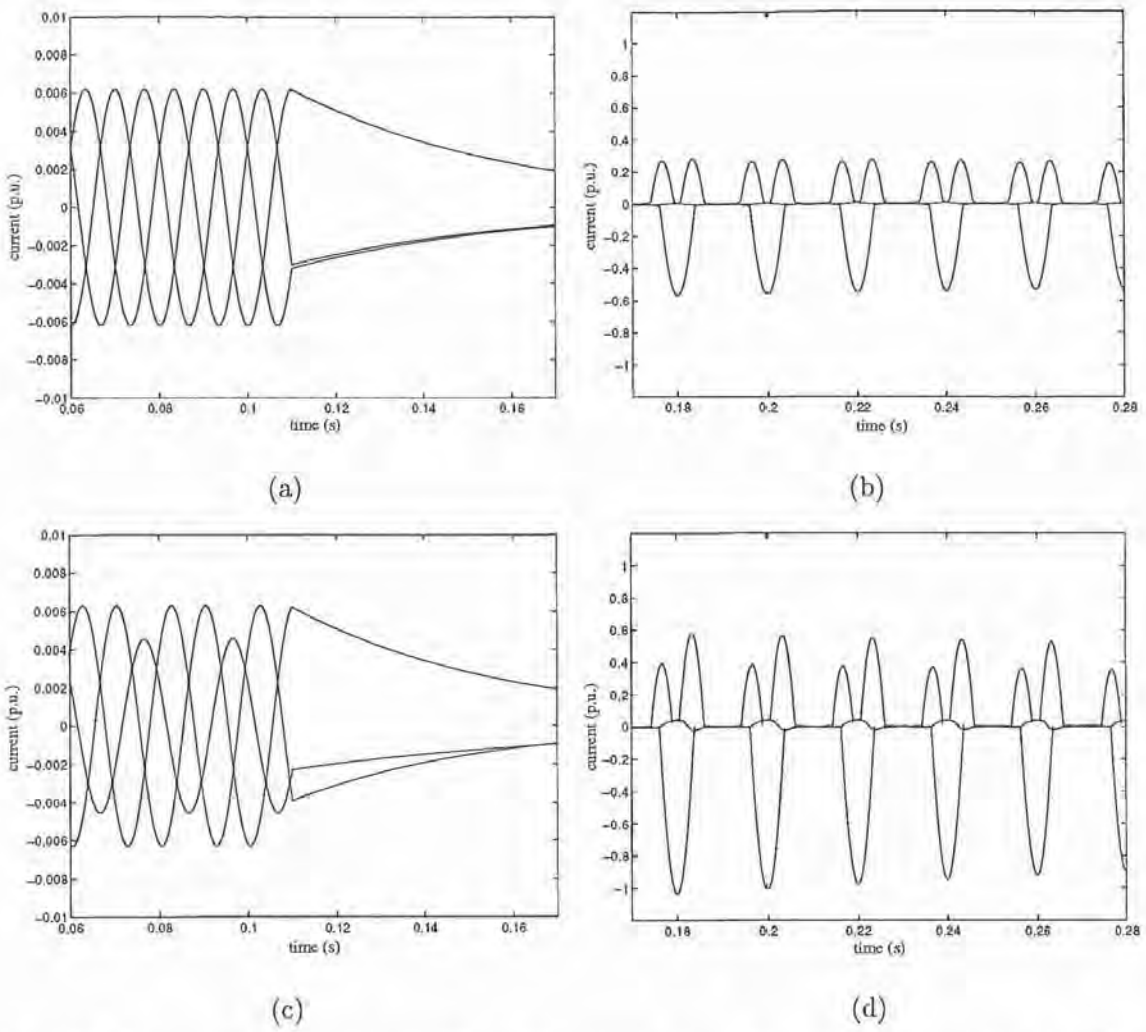

Figure 3.7 Three-phase transformers during transient operating conditions (top=three-phase bank [xfmr-3p2w], bottom=three-limb [3limb-oc]): (a) and (c) Steady state energisation and source removal, (b) and (d) Heavy saturation following source reconnection.

The first operating condition is the steady-state open-circuit energisation, which is achieved after a 0.06secs ramp up time. The resulting primary currents for the three-phase bank and three-limb three-phase models are shown in figure 3.7(a) and (c), for a two and a half cycle interval (time=0.06s-0.11secs). The three-limb magnetising currents show a substantial unbalance, whereas the three-phase bank fails to show this effect.

The second operating condition, of a two and a half cycle duration, started with the opening of the circuit breaker (time=0.11secs), the negative going zero crossing of the red-phase voltage. During this interval some of the energy stored in the magnetic circuit is dissipated in the primary load, with the primary currents decaying exponentially. In the case of the three-phase bank representation, due to the symmetry of the waveforms at the point of switching, the yellow and blue currents decay in an identical fashion. This is not the case however for the three-limb three-phase transformer.

At the negative-going zero crossing of the red-phase voltage (time=0.17secs) the

circuit breaker is reclosed giving rise to the third operating condition. As the core dc flux has not decayed to zero, this case forces the transformer into deep saturation. The phase currents are very large in comparison to the previous unsaturated state and the results need to be displayed separately (figure 3.7(b) and (d)). The three-limb three-phase model experiences deeper saturation than the three-phase bank. Differences appear also in the balance and shape of the saturated open-circuit current. Each cycle is distorted to a greater extent than the three-phase bank.

3.2.4 Field transformer saturation characteristics

Care must be exercised when equation 3.2 is applied to represent field transformer saturation characteristics. Magnetising currents at rated voltage are sensitive to small changes in the hyperbola parameters, and the experimental characteristics are often only available in graphical rather than tabular form.

The hyperbola constants selected for the transformer model comparisons of section 3.2.3 give a two slope piecewise linear saturation representation. With $\mathcal{E}$=0.0 and b_1=0.0 then the solutions of equation 3.2 are simplified to

$$\phi_k(t) = m_1 i_k(t) \tag{3.12}$$

in the unsaturated region, and

$$\phi_k(t) = m_2 i_k(t) + b_2 \tag{3.13}$$

in the saturated region. This simple representation is not accurate enough to match field transformer behaviour.

[Dick and Watson 1981] published per-unit saturation characteristics for the winding-limb, yoke and zero-sequence flux branches of a 25MVA, 110/44/4 kV three-limb transformer. The hyperbolas of figure 3.8(a) provide a reasonable match to this transformer's saturation characteristics. The curve parameters are given in table 3.3[2].

Branch	$m_{1(linear)}$	$m_{2(sat)}$	b_1	b_2	$\mathcal{E}$
Winding limb	292.38	0.076	0.0	1.280	0.850
Zero-sequence	292.38	1.670	0.0	1.200	0.652
Yoke	6.00	1.440	0.0	0.345	0.010

Table 3.3 Field transformer hyperbola parameters.

The non-zero correction factor rounds the hyperbola knee region, and affects the incremental permeance down to the origin. The transformer characteristics of figure

[2] [Dick and Watson 1981] tabulated saturated branch permeances only. The unsaturated permeances are assumed to be as given by [Medina 1992]

3.8(a) are used to show this effect. Setting the correction factors of the three curves each to zero gives the piecewise linear characteristics shown in figure 3.8(b). The incremental permeance of the figures 3.8(a) and 3.8(b) magnetic characteristics are shown in figures 3.8(c) and 3.8(d) respectively.

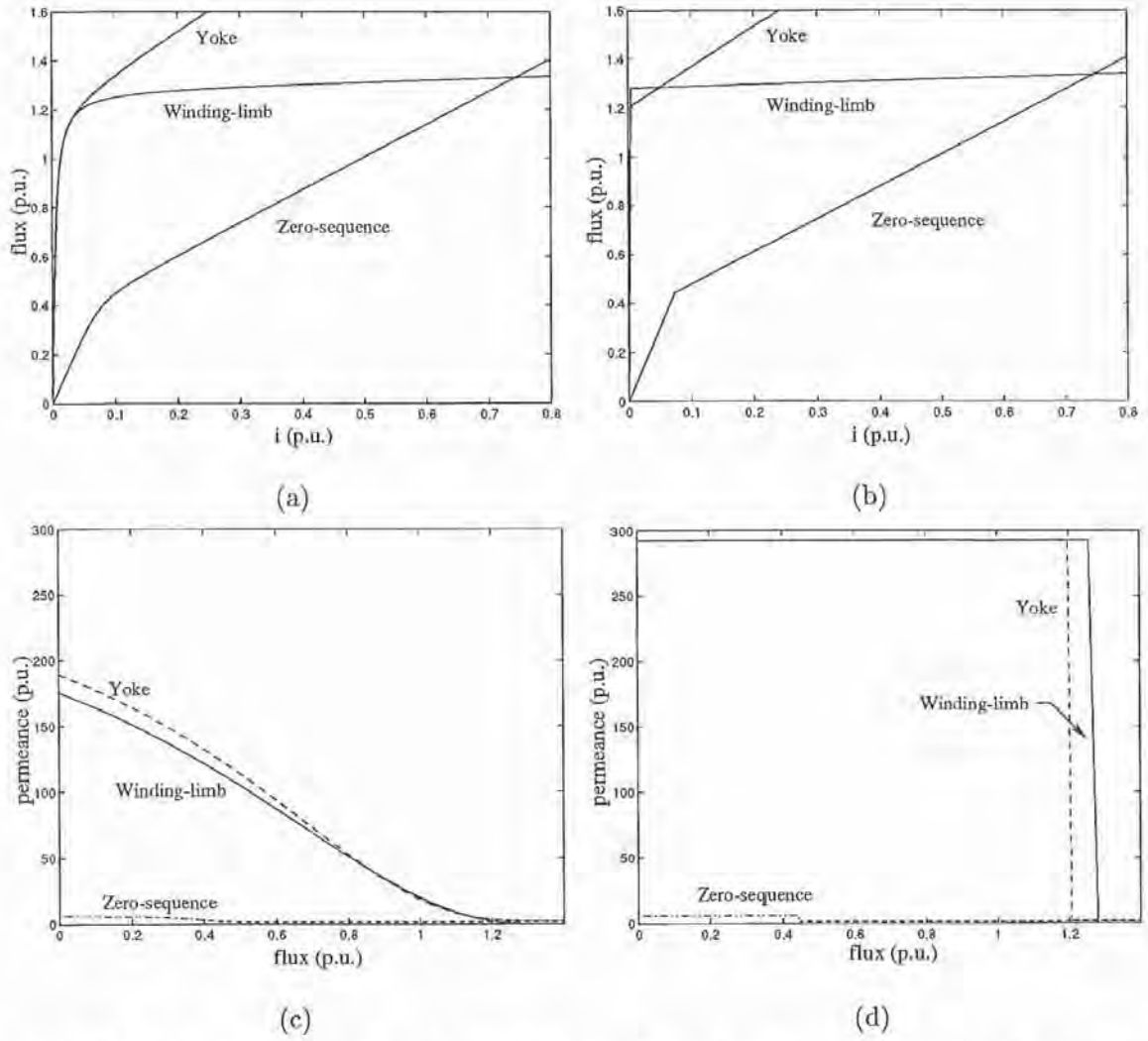

Figure 3.8 Field transformer core characteristics (left hand side=non-zero correction factor, right hand side=zero correction factor): (a) and (b) Saturation curve, (c) and (d) Core incremental permeance.

The field transformer piecewise linear ($\mathcal{E} = 0.0$) and smooth ($\mathcal{E} \neq 0.0$) saturation characteristics were each applied to the section 3.2.3 model (3limb-oc). The magnetising current spectra at rated voltage are given in table 3.4. The yellow-phase draws less current than the symmetrical red and blue-phases for both smooth and piecewise saturation representations. However, the current drawn when the saturation characteristic is smooth is ten times that with the piecewise characteristic. Moreover the piecewise representation open-circuit current is undistorted, even at rated voltage, and a perfect sinusoidal magnetising current is unrealistic.

	Harmonic number			
	1	3	5	7
Red-phase				
$\mathcal{E} = 0.0$	0.006	0.0	0.0	0.0
$\mathcal{E} \neq 0.0$	0.072	0.027	0.010	0.003
Yellow-phase				
$\mathcal{E} = 0.0$	0.005	0.0	0.0	0.0
$\mathcal{E} \neq 0.0$	0.058	0.016	0.009	0.003
Blue-phase				
$\mathcal{E} = 0.0$	0.006	0.0	0.0	0.0
$\mathcal{E} \neq 0.0$	0.072	0.027	0.010	0.003

Table 3.4 Magnetising current spectra (p.u.).

3.3 REPRESENTING WINDING FLUX LEAKAGE

3.3.1 Single-phase representation

Before describing the flux leakage in MEC three-limb three-phase transformer models a single-phase description is first given. In the Harmonic Domain a single-phase model has been proposed that superimposes the transformer linear leakage reactance network on a linearised magnetising current Norton equivalent representation [Acha *et al.* 1989].

A Time Domain version of this Harmonic Domain model can be derived for PSCAD-EMTDC. The formulation is applied to the calculation of the core magnetising current only. In the simple MEC of figure 3.9(b) the incremental permeance formulation reduces to the per-unit scalar form [Lisboa *et al.* 1995]

$$i_s(t) = y_{ss} v_s(t) + i_{ns} \tag{3.14}$$

where

$$y_{ss} = \mathcal{P}_c^{-1} \frac{\Delta t \omega_0}{2}$$

and

$$i_{ns} = \mathcal{P}_c^{-1} \frac{\Delta t \omega_0}{2} v_s(t - \Delta t) + i_s(t - \Delta t)$$

It has been suggested that the core flux $\phi_c(t)$ should be calculated using the voltage $v_s(t)$ from the winding closest to the core [Dommel 1975]. In the absence of construction details the primary and secondary voltage average $\frac{V_1+V_2}{2}$ is often used to calculate core flux. The magnetising current $i_s(t)$ is halved and placed on both sides of the transformer leakage admittance network. The resultant linear and linearised electromagnetic transient equivalent to the Harmonic Domain transformer model is shown in figure 3.9(c).

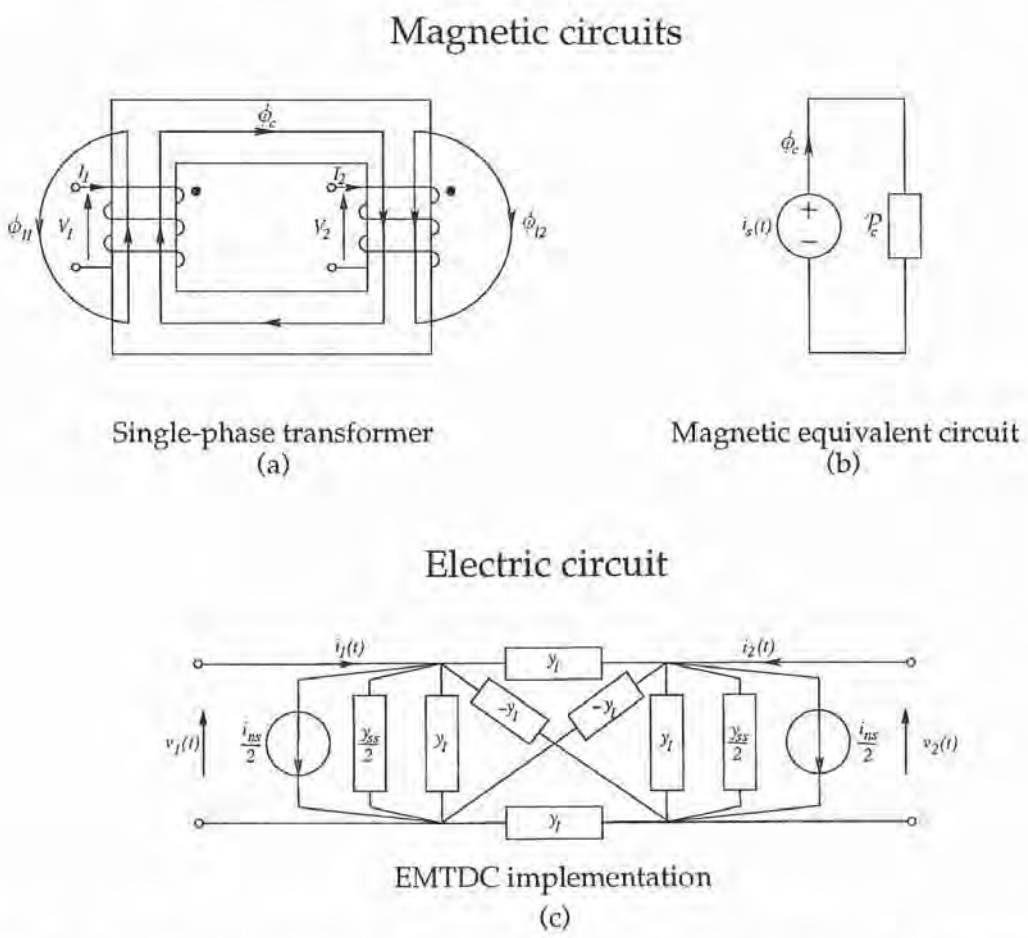

Figure 3.9 A linear and linearised PSCAD-EMTDC single-phase transformer model: (a) core flux paths, (b) magnetic equivalent circuit, (c) Norton equivalent.

3.3.2 HDA and PSCAD-EMTDC intervalidation: single-phase

Considerable progress in steady-state analysis of the non-linear power system has been achieved in the Harmonic Domain [Arrillaga *et al.* 1995]. Although highly efficient for harmonic analysis, the accuracy of the Harmonic Domain Analysis program (HDA) is yet to be rigorously validated. [Acha 1988] compared field data from the Jaguara-Tarquaril transmission circuit with early Harmonic Domain simulation. However the comparisons were presented as waveforms only, whereas spectra are required to gauge the accuracy of the harmonic solution.

The electromagnetic transient model presented in section 3.3.1 is an exact equivalent to the Harmonic Domain single-phase transformer model. If these two models are applied to the same test system, and simulated with PSCAD-EMTDC and HDA accordingly, then the Harmonic Domain solution can be compared with that of the well accepted electromagnetic transient technique. The test system of figure 3.10 was selected for this intervalidation.

The star-grounded/star-grounded three-phase bank of single-phase transformers is fed from an infinite busbar through an impedance $r_s = 1.0$ p.u. This large source

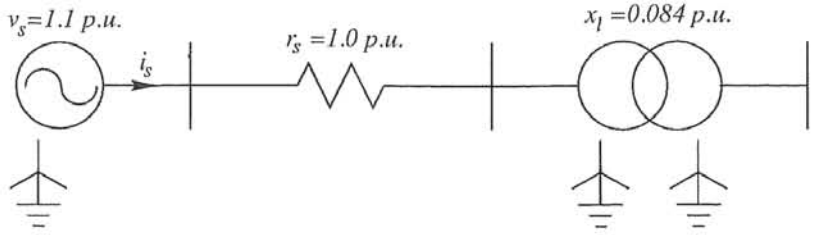

Figure 3.10 Single-phase validation test system.

impedance introduces voltage distortion at the transformer terminals. The source voltage is set to 1.1 p.u. to force the transformer into deep saturation. The transformer leakage reactance is x_l=0.084 p.u., and the saturation characteristic is represented with the winding-limb hyperbola of table 3.2.

Figure 3.11(a) illustrates a full period of the magnetising current derived with HDA and PSCAD-EMTDC simulations, and figure 3.11(c) the harmonic spectra. The results show good agreement, the maximum magnitude difference being 0.002 p.u. occurring at the third harmonic. The transformer primary voltage waveforms are illustrated in figure 3.11(b), the HDA and PSCAD-EMTDC waveforms almost match perfectly. The harmonic spectra illustrated in figure 3.11(d) indicate very close results, the maximum magnitude difference being 0.002 p.u. at the third harmonic.

3.3.3 Three-limb three-phase representation

[Medina and Arrillaga 1992b] extended the single-phase Harmonic Domain transformer models proposed by [Acha 1988] to represent three-limb three-phase core configurations. The MEC of figure 3.12(b) is linearised, converted into a Norton equivalent and superimposed on the [Chen and Dillon 1974] common core linear short-circuit admittance matrix. A Time Domain version of the Harmonic Domain three-limb three-phase linear and linearised model can also be derived for PSCAD-EMTDC.

The primitive electric parameters of figure 3.12(a) are represented by

$$\begin{bmatrix} I_1 \\ I_2 \\ I_3 \\ I_4 \\ I_5 \\ I_6 \end{bmatrix} = \begin{bmatrix} y_l & -y_l & y_l' & y_l'' & y_l' & y_l'' \\ -y_l & y_l & y_l'' & y_l''' & y_l'' & y_l''' \\ y_l' & y_l'' & y_l & -y_l & y_l' & y_l'' \\ y_l'' & y_l''' & -y_l & y_l & y_l'' & y_l''' \\ y_l' & y_l'' & y_l' & y_l'' & y_l & -y_l \\ y_l'' & y_l''' & y_l'' & y_l''' & -y_l & y_l \end{bmatrix} \begin{bmatrix} V_1 \\ V_2 \\ V_3 \\ V_4 \\ V_5 \\ V_6 \end{bmatrix} \tag{3.15}$$

where:

y_l = leakage admittance,
y_l' = mutual leakage between primary coils,
y_l'' = mutual leakage between primary and secondary coils on different limbs,
y_l''' = mutual leakage between secondary coils.

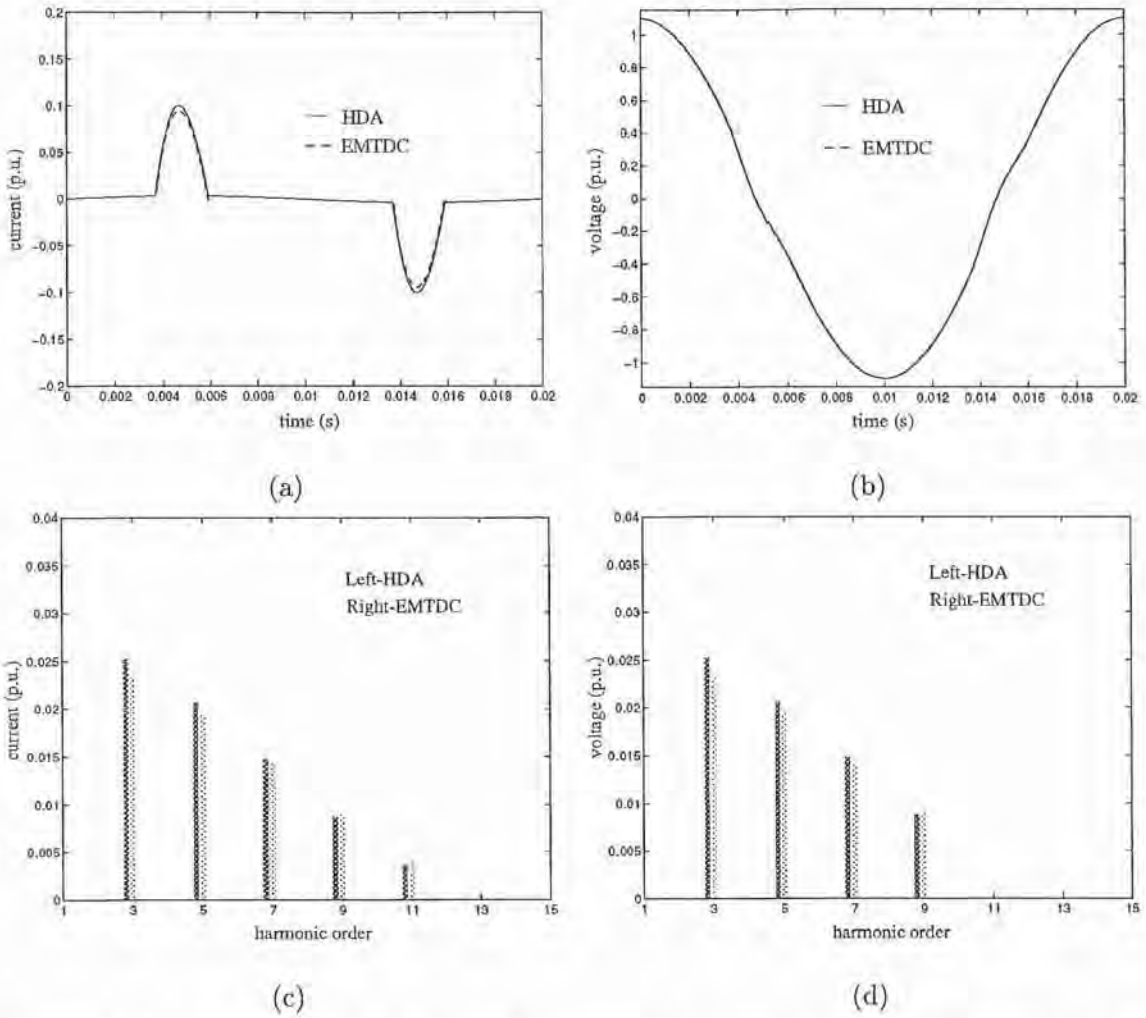

Figure 3.11 Single-phase bank intervalidation, red-phase comparison; Solid=HDA, Dash-dash=PSCAD-EMTDC: (a) primary current waveform, (b) primary voltage waveform, (c) primary current spectra, (d) primary voltage spectra.

In the MEC of figure 3.12(b) the flux in the primary and secondary windings on each transformer limb is the same. Therefore each limbs per-unit primary and secondary winding voltage is the same. The MEC Norton equivalent is thus

$$\begin{bmatrix} i_{sr}(t) \\ i_{sy}(t) \\ i_{sb}(t) \end{bmatrix} = \begin{bmatrix} y_{11} & y_{12} & y_{13} \\ y_{12} & y_{22} & y_{23} \\ y_{13} & y_{23} & y_{33} \end{bmatrix} \begin{bmatrix} v_1(t) \\ v_3(t) \\ v_5(t) \end{bmatrix} + \begin{bmatrix} i_{nsr} \\ i_{nsy} \\ i_{nsb} \end{bmatrix} \tag{3.16}$$

$$= \begin{bmatrix} y_{11} & y_{12} & y_{13} \\ y_{12} & y_{22} & y_{23} \\ y_{13} & y_{23} & y_{33} \end{bmatrix} \begin{bmatrix} v_2(t) \\ v_4(t) \\ v_6(t) \end{bmatrix} + \begin{bmatrix} i_{nsr} \\ i_{nsy} \\ i_{nsb} \end{bmatrix} \tag{3.17}$$

If the Norton equivalent is halved and placed on both sides of the leakage admittance matrix, the linear and linearised three-limb three-phase transformer representation is

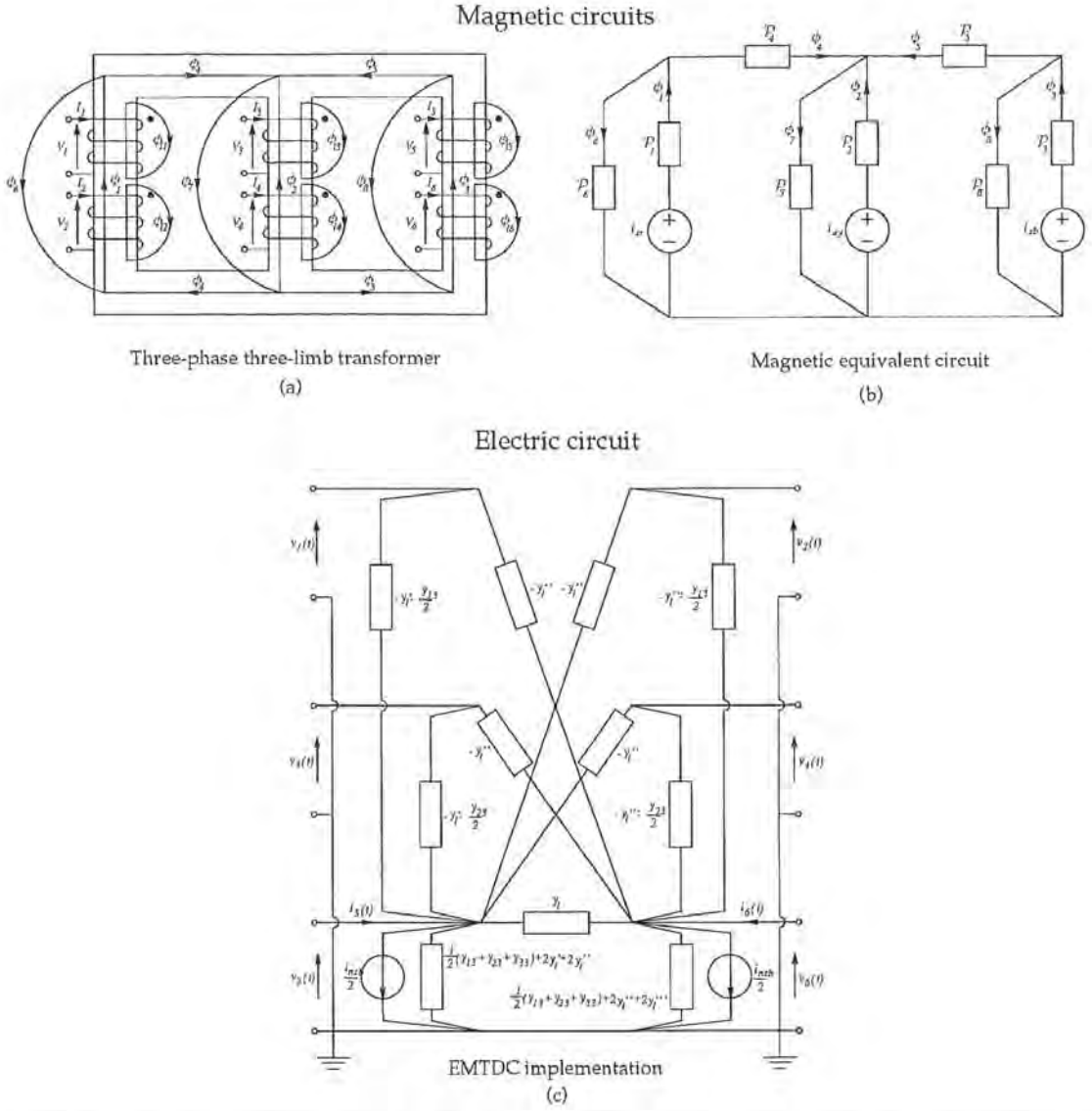

Figure 3.12 A linear and linearised PSCAD-EMTDC three-limb three-phase transformer model: (a) core flux paths, (b) magnetic equivalent circuit, (c) Norton equivalent (star-grounded/star-grounded, blue-phase only).

$$\begin{bmatrix} i_1(t) \\ i_2(t) \\ i_3(t) \\ i_4(t) \\ i_5(t) \\ i_6(t) \end{bmatrix} = [Y_t] \begin{bmatrix} v_1(t) \\ v_2(t) \\ v_3(t) \\ v_4(t) \\ v_5(t) \\ v_6(t) \end{bmatrix} + \begin{bmatrix} \frac{i_{nsr}}{2} \\ \frac{i_{nsr}}{2} \\ \frac{i_{nsy}}{2} \\ \frac{i_{nsy}}{2} \\ \frac{i_{nsb}}{2} \\ \frac{i_{nsb}}{2} \end{bmatrix} \tag{3.18}$$

where

$$[Y_l] = \begin{bmatrix} y_l + \frac{1}{2}y_{11} & -y_l & y_l' + \frac{1}{2}y_{12} & y_l'' & y_l' + \frac{1}{2}y_{13} & y_l'' \\ -y_l & y_l + \frac{1}{2}y_{11} & y_l'' & y_l''' + \frac{1}{2}y_{12} & y_l'' & y_l''' + \frac{1}{2}y_{13} \\ y_l' + \frac{1}{2}y_{12} & y_l'' & y_l + \frac{1}{2}y_{22} & -y_l & y_l' + \frac{1}{2}y_{23} & y_l'' \\ y_l'' & y_l''' + \frac{1}{2}y_{12} & -y_l & y_l + \frac{1}{2}y_{22} & y_l'' & y_l''' + \frac{1}{2}y_{23} \\ y_l' + \frac{1}{2}y_{13} & y_l'' & y_l' + \frac{1}{2}y_{23} & y_l'' & y_l + \frac{1}{2}y_{33} & -y_l \\ y_l'' & y_l''' + \frac{1}{2}y_{13} & y_l'' & y_l''' + \frac{1}{2}y_{23} & -y_l & y_l + \frac{1}{2}y_{33} \end{bmatrix}$$

The PSCAD-EMTDC circuit implementation of equation 3.18 for the blue-phase of a star-grounded/star-grounded transformer connection is shown in figure 3.12(c).

3.3.4 HDA and PSCAD-EMTDC intervalidation: three-limb three-phase

The intervalidation of the HDA program and PSCAD-EMTDC performed in section 3.3.2 showed acceptable agreement for a simple test system. The new Time Domain three-limb three-phase transformer model is again equivalent to a Harmonic Domain representation [Lisboa *et al.*]. A more detailed test system can be constructed with the three-limb models, and a more valuable intervalidation performed.

The test system of figure 3.13 has been selected to compare the HDA solution with that of the PSCAD-EMTDC program. In this example the star-grounded/star-grounded transformer is a three-limb three-phase unit. Unlike the previous three-phase bank case, the three-limb transformer magnetising current unbalance increases the complexity of the steady-state solution. The supply inductance and shunt capacitance are tuned to resonate at the third harmonic, the shunt resistance is added to provide damping. Any third harmonic current required to energise the transformer core must flow in the damping resistor and will significantly distort the transformer primary busbar. The inductance x_s, capacitance c_l and resistance r_s values are 0.1 p.u., 0.9

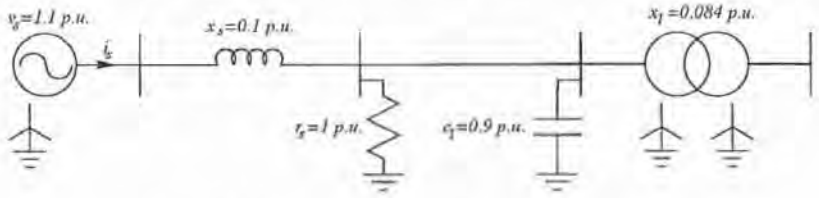

Figure 3.13 Three-limb validation test system.

p.u., and 1.0 p.u. respectively. The transformer hyperbola saturation characteristic parameters are given in table 3.2, leakage reactance x_l=0.084 p.u. and the mutual leakage terms are set to x_l'=x_l''=x_l'''=100 p.u.[3] The source voltage is set to 1.1 p.u. to force the transformer into deep saturation.

Figure 3.14(a) illustrates the source current obtained with HDA and PSCAD-EMTDC solutions, and 3.14(c) the harmonic content. The transformer primary side

[3]In the absence of further information the mutual leakage terms have been set as suggested by [Medina and Arrillaga 1992a]

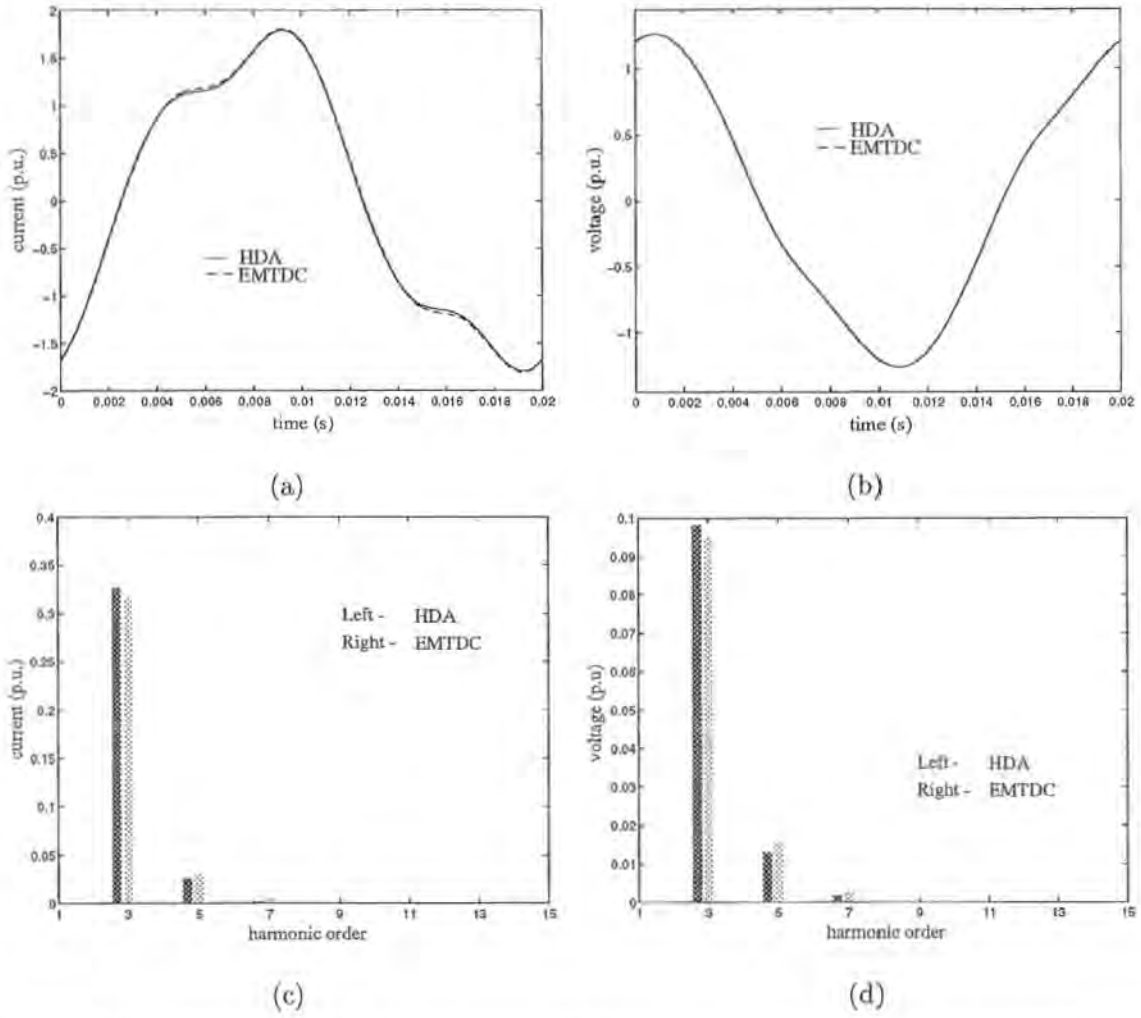

Figure 3.14 Three-limb three-phase bank intervalidation, red-phase comparison; Solid=HDA, Dash-dash=PSCAD-EMTDC: (a) primary current waveform, (b) primary voltage waveform, (c) primary current spectra, (d) primary voltage spectra.

voltage waveforms and harmonic content are shown in figures 3.14(b) and 3.14(d) (only red-phase results are shown). In this case, a significant level of voltage distortion is apparent (the third harmonic voltage amplitude is nearly 10%). An almost perfect match between the voltage waveforms is achieved. Considering the difficulties of the test system analysed, the results indicate very good agreement between the HDA and PSCAD-EMTDC solutions. The maximum magnitude differences are 0.003 p.u. for the voltages and 0.009 p.u. for the currents, both occurring at the third harmonic.

3.4 SOLVING THE NON-LINEAR MEC

The equations governing the MEC solution are non-linear and precise calculation of yoke and zero-sequence flux $\bar{\phi}_r(t - \Delta t)$ from winding-limb flux $\bar{\phi}_s(t - \Delta t)$ requires an iterative procedure. Newton's technique can be applied to the MEC model to iteratively find a true magnetic core solution at each time step. Figure 3.15 shows the

modifications required to place Newton's technique in operation box 8 of figure 3.5.

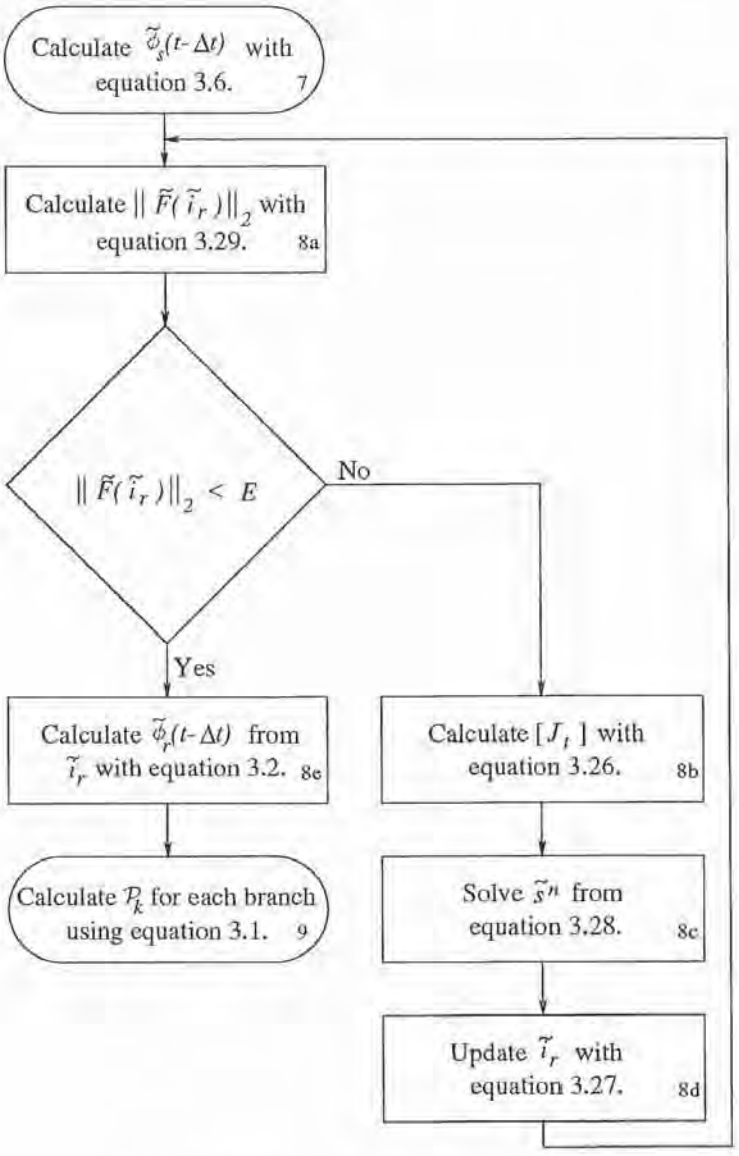

Figure 3.15 Newton solution implementation.

As discussed in section 3.2.2 the previous time step flux in the winding-limbs $\tilde{\phi}_s(t-\Delta t)$ is calculated with trapezoidal integration. Figure 3.16 presents the three-limb core MEC when the winding-limb fluxes $\tilde{\phi}_s(t-\Delta t)$ are known. Branch ampere-turns i_4 and i_5 represent the yokes, and i_6, i_7 and i_8 represent the zero sequence paths. If the saturation characteristic representing the yoke paths is expressed as

$$\phi_k = f(i_k) \tag{3.19}$$

and the zero-sequence paths as

$$\phi_k = g(i_k) \tag{3.20}$$

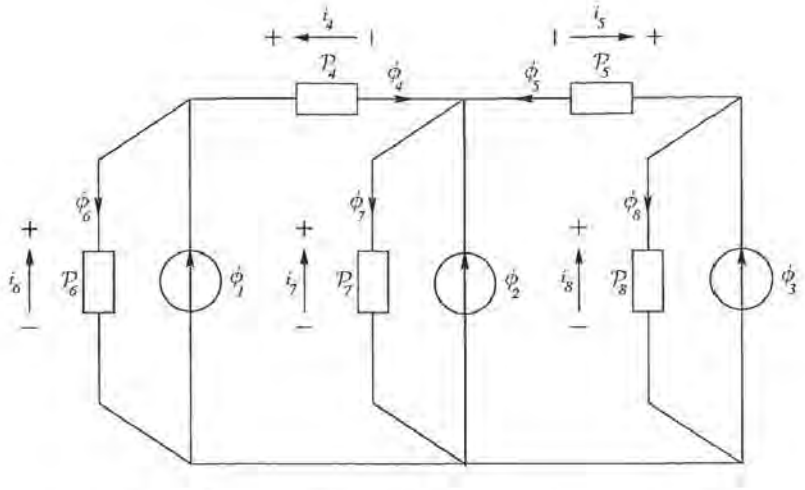

Figure 3.16 MEC with winding-limb flux known.

then the non-linear system of equations that describe the MEC are

$$F_1(i_4, i_5, i_6, i_7, i_8) = \phi_1 - f(i_4) - g(i_6) = 0 \tag{3.21}$$

$$F_2(i_4, i_5, i_6, i_7, i_8) = \phi_2 + f(i_4) + f(i_5) - g(i_7) = 0 \tag{3.22}$$

$$F_3(i_4, i_5, i_6, i_7, i_8) = \phi_3 - f(i_8) - g(i_5) = 0 \tag{3.23}$$

$$F_4(i_4, i_5, i_6, i_7, i_8) = i_4 - i_6 + i_7 = 0 \tag{3.24}$$

$$F_5(i_4, i_5, i_6, i_7, i_8) = i_5 - i_8 + i_7 = 0 \tag{3.25}$$

The Jacobian required to solve the five equations $\tilde{F}(\tilde{i}_r) = [F_1(\tilde{i}_r)\ F_2(\tilde{i}_r)\ F_3(\tilde{i}_r)\ F_4(\tilde{i}_r)\ F_5(\tilde{i}_r)]^T = \tilde{0}$ for the five unknowns $\tilde{i}_r = [i_4\ i_5\ i_6\ i_7\ i_8]^T$ is

$$[J_t] = \begin{bmatrix} \frac{-\delta f(i_4)}{\delta i_4} & 0 & \frac{-\delta g(i_6)}{\delta i_6} & 0 & 0 \\ \frac{-\delta f(i_4)}{\delta i_4} & \frac{-\delta f(i_5)}{\delta i_5} & 0 & \frac{-\delta g(i_7)}{\delta i_7} & 0 \\ 0 & \frac{-\delta f(i_5)}{\delta i_5} & 0 & 0 & \frac{-\delta g(i_8)}{\delta i_8} \\ 1 & 0 & -1 & 1 & 0 \\ 0 & 1 & 0 & 1 & -1 \end{bmatrix} \tag{3.26}$$

The previous time step solution is an appropriate starting point for the iterative procedure required to solve the unknown variables $\tilde{i}_r$. If the vector $\tilde{i}_r$ does not provide a suitable solution to the system of equations $\tilde{F}(\tilde{i}_r) = \tilde{0}$ then Newton's method states that

$$\tilde{i}_r^{n+1} = \tilde{i}_r^n - \tilde{s}^n \tag{3.27}$$

will be a better solution, where $\tilde{s}^n$ is obtained from

$$[J_t]\tilde{s}^n = \tilde{F}(\tilde{i}_r^n) \tag{3.28}$$

and n indicates the iteration number at each time step. The new solution is tested with the two norm error function $||\tilde{F}(\tilde{i}_r^n)||_2$ and iterations cease if the error is less than

the threshold E. The error function is written as

$$||\tilde{F}(\tilde{i}_r^n)||_2 = \sqrt{F_1^2(\tilde{i}_r^n) + F_2^2(\tilde{i}_r^n) + F_3^2(\tilde{i}_r^n) + F_4^2(\tilde{i}_r^n) + F_5^2(\tilde{i}_r^n)} \tag{3.29}$$

Figure 3.17 displays one cycle of yoke and zero-sequence flux for a three-limb three-phase transformer excited at 1.1 (p.u.) voltage. The winding-limb, yoke, and zero-sequence path hyperbola saturation characteristic parameters are given in table 3.5.[4]

Branch	$m_{1(linear)}$	$m_{2(sat)}$	b_1	b_2	$\mathcal{E}$
Winding limb	292.38	0.67	0.0	1.03	0.85
Yoke	292.38	1.67	0.0	1.03	0.001
Zero-sequence	6.00	1.44	0.0	0.22	0.001

Table 3.5 Transformer hyperbola parameters; Newton iteration and linear approximation comparison.

In the Newton solution the yoke limbs saturate, the permeance of the saturated yoke is less than that of the unsaturated zero-sequence path, and the winding limb flux returns via the zero-sequence path. Therefore less yoke flux is predicted by the linear approximation than by the Newton solution, this is shown in figures 3.17(a) and (b) respectively. The linear approximation also gives more zero-sequence flux than the Newton solution, as shown in figures 3.17(c) and (d) respectively. Inaccurate yoke and zero-sequence flux waveforms must eventually result in unacceptable transformer magnetising currents.

3.5 CONCLUSIONS

A magnetic equivalent circuit (MEC) of the three-limb three-phase transformer core type has been developed. The linear transformer model derived from this MEC has been validated with experimental results and the model interphase magnetic coupling has been verified.

Saturation has been incorporated using a hyperbola that matches experimentally obtained saturation characteristics. The steady-state energisation, flux decay, and in-rush behaviour of the conventional PSCAD-EMTDC single-phase bank and MEC three-limb three-phase transformers have been compared and considerable differences found, particularly in the simulation of in-rush transients.

Winding flux leakage has been added to a single-phase MEC model in a manner that is equivalent to the present Harmonic Domain single-phase representation. The

[4]The hyperbola parameters are those of table 3.2 with modified correction factors. The rounded winding-limb, and piecewise linear yoke and zero-sequence characteristics are useful in this example to clearly distinguish between each paths unsaturated and saturated regions.

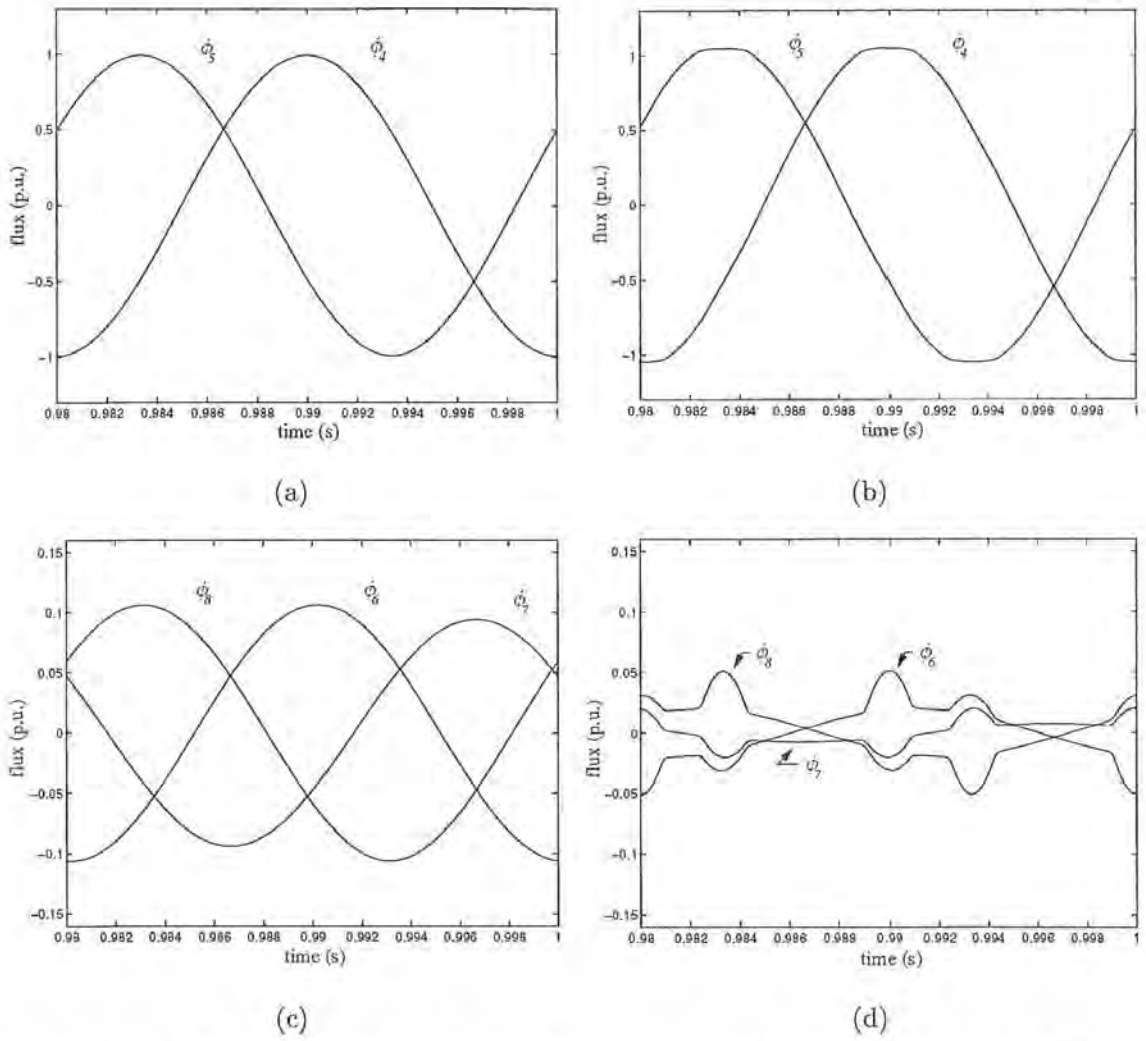

Figure 3.17 Magnetic equivalent circuit solutions (left hand side=non-iterative, right-hand-side=iterative); (a) and (b) Yoke flux, (c) and (d) Zero-sequence flux.

magnetising current has been linearised and the resultant Norton equivalent superimposed on the linear leakage admittance network. Intervalidation of the HDA and PSCAD-EMTDC programs has been carried out and an acceptable match obtained for over-voltage open-circuit transformer energisation.

The new formulation has also been applied to the calculation of the three-limb three-phase transformer magnetising current. In this case the resultant Norton equivalent was combined with a three-limb three-phase linear leakage network. This network superposition is equivalent to the present Harmonic Domain three-limb three-phase transformer model. A more challenging intervalidation was then presented using the three-limb three-phase transformer equivalents and a resonant test system. Again an acceptable match was achieved.

A MEC solution was obtained using Newton's technique and the linear solutions inaccuracies in predicted yoke and zero-sequence flux were presented. The linear approximation and Newton technique flux waveforms were dissimilar.

Chapter 4

THE UNIFIED MAGNETIC EQUIVALENT CIRCUIT

In this chapter the unified magnetic equivalent circuit (UMEC) is described. The UMEC branches represent winding flux leakage as well as core and zero-sequence flux paths. A linear two winding UMEC is applied to investigate the effect of core and flux leakage paths on open and short-circuit inductances respectively. Self and mutual inductances are expressed in terms of individual branch permeance in a similar manner.

The transformer Norton equivalent is rederived in terms of actual rather than incremental permeance. Non-linear UMEC iterative and non-iterative solutions are compared. The previous time step approximation of the present time step UMEC solution is shown to be acceptable.

The per-unit system is then removed and a model derived for the Benmore valve-group converter transformers. Model accuracy is verified with experimental data. A comparison is made between the harmonic flows predicted by PSCAD-EMTDC and UMEC transformer models for a test system derived from the New Zealand HVdc Benmore converter station. Finally the single-phase UMEC is extended to represent the three-limb three-phase core configuration. A model is derived for the Manapouri generator transformers and is verified with factory test data.

4.1 INCLUDING WINDING FLUX LEAKAGE IN THE MEC

A century has passed since Steinmetz presented the theory of the general alternating current transformer [Steinmetz 1895]. Now, text books describe transformers with the shunt magnetizing and series leakage reactances of the Steinmetz "exact", and "approximate" equivalent circuits [McPherson 1981]. The linear and linearised transformer models presented in this thesis so far are examples of the Steinmetz "approximate" equivalent circuit. For example, in the single-phase model, uniform flux throughout the core legs and yokes is assumed, individual winding leakages are combined and half of the magnetising current is placed on each side of the resultant series leakage reactance. Such arbitrary placement of magnetising current and lumped leakage representation was well suited to the open-circuit examples of sections 3.2.3, 3.3.2, and

3.3.4. However, transformer magnetising currents can play a large part in both power system transients and harmonic levels, under loaded as well as open-circuit conditions; UMEC transformer models will be shown to represent winding flux leakage and the division of magnetising current between windings with improved accuracy.

Often in power system modelling the open-circuit admittance of a linear single-phase transformer is split into two equal parts [Chen and Dillon 1974]. [Dommel 1975] raised the question that, if uniform flux throughout the core legs and yokes is assumed, which winding should be utilized to calculate core flux? In the absence of better information, a proposal was made for using the coil closest to the core. Considering the complexity of modern transformer designs, the proximity criterion, even when construction details are available, is difficult to implement in power system programs.

The most recent EMTP multi-limb transformer model derives an electric circuit dual from a magnetic circuit equivalent that includes air and steel flux paths [Stuehm 1993]. Although the core leg, yoke and zero-sequence paths are individually represented, the individual winding leakages are lumped together and the question of which side to place the magnetizing components is not answered.

The need for a proximity criterion, the arbitrary division of magnetising current as well as uniform core flux assumptions and lumped leakage reactance approximations are removed using the UMEC concept. The single-phase transformer, shown in figure 4.1(a), can be represented by the (UMEC) of figure 4.1(b). MMF sources $N_1 i_1(t)$ and $N_2 i_2(t)$ represent each winding individually. Winding voltages $v_1(t)$ and $v_2(t)$ are used to calculate winding limb flux $\phi_1(t)$ and $\phi_2(t)$ respectively. Winding-limb flux divides between leakage and yoke paths. Uniform core flux is not assumed.

Although single-phase transformer windings are not generally wound separately on different limbs, each winding can be separated in the UMEC. Permeances $\mathcal{P}_1$ and $\mathcal{P}_2$ represent the transformer winding limbs. If the total length of core surrounded by windings L_w has uniform cross-sectional area A_w, then UMEC branches 1 and 2 have length $L_1 = L_2 = \frac{L_w}{2}$ and cross-sectional area $A_1 = A_2 = A_w$. Permeance $\mathcal{P}_3$ represents the transformer yokes. The upper and lower yokes are assumed to have the same length L_y and cross-sectional area A_y. Both yokes are represented by the single UMEC branch 3 of length $L_3 = 2L_y$ and area $A_3 = A_y$. Leakage permeances are obtained from the open and short-circuit testing method described in appendix C and therefore the effective lengths and cross-sectional areas of leakage flux paths are not required to calculate leakage permeances $\mathcal{P}_4$ and $\mathcal{P}_5$.

Using the UMEC of figure 4.1(b) equation 2.30 becomes

$$\begin{bmatrix} i_1(t) \\ i_2(t) \end{bmatrix} = \begin{bmatrix} y_{11} & y_{12} \\ y_{21} & y_{22} \end{bmatrix} \begin{bmatrix} v_1(t) \\ v_2(t) \end{bmatrix} + \begin{bmatrix} i_{ns1} \\ i_{ns2} \end{bmatrix} \tag{4.1}$$

The matrix $[Y_{ss}]$ is symmetric and the Norton equivalent is implemented in PSCAD-

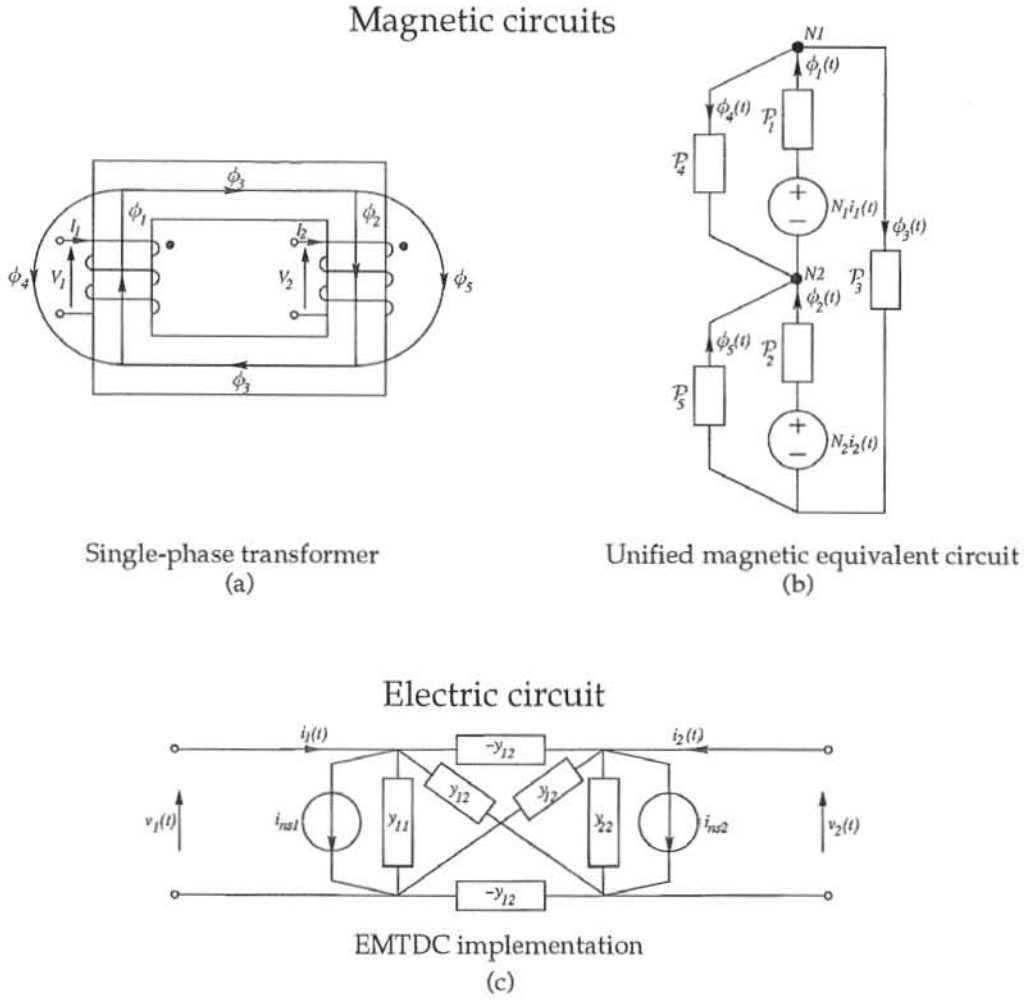

Figure 4.1 A UMEC PSCAD-EMTDC single-phase transformer model: (a) core flux paths, (b) unified magnetic equivalent circuit, (c) Norton equivalent.

EMTDC as shown in figure 4.1(c). Unlike the linear and linearised representation of chapter 3 all components of the transformer model are now derived from the UMEC.

4.2 ACTUAL PERMEANCE FORMULATION

For modern grain-oriented core steel, the $\phi - \theta$ characteristic becomes steeper below saturation, flatter above saturation, and the transition around the knee region becomes sharper. Presently, core non-linearity is represented in incremental permeance form. Equation 2.14 can be rearranged to

$$\phi_k(t) = \mathcal{P}_k \theta_{k1}(t) - \phi_{nk} \tag{4.2}$$

This magnetic operating point representation is displayed as line (a) of figure 4.2. As the transformer core moves around the knee region, the change in incremental permeance is much larger and more sudden (especially in the case of highly efficient cores) than the change in actual permeance. Although incremental permeance reliance is ac-

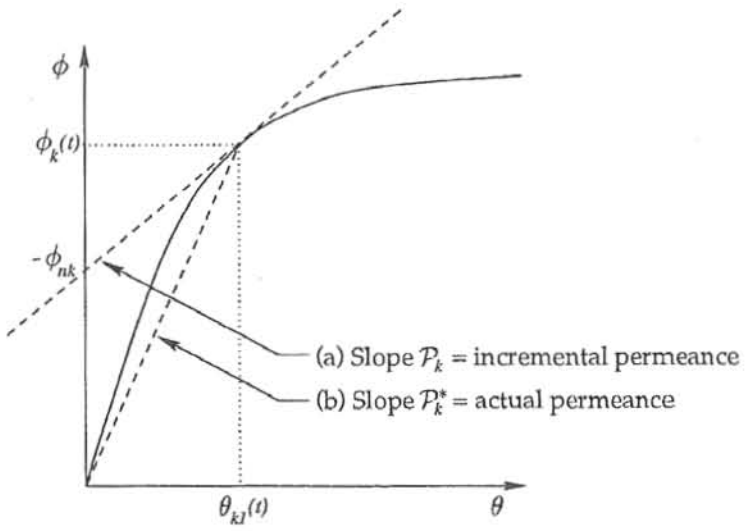

Figure 4.2 Incremental and actual permeance.

ceptable in the steady-state transformer models of the Harmonic Domain, [Chen and Neudorfer 1993] have recently shown modern transformer dynamic simulation requires actual permeance based magnetic circuit representations.

If the UMEC branch flux is expressed using actual permeance,

$$\phi_k(t) = \mathcal{P}_k^* \theta_{k1}(t) \tag{4.3}$$

as line (b) of figure 4.2, then equation 2.17 becomes

$$\phi_k = \mathcal{P}_k^*(N_k i_k - \theta_k') \tag{4.4}$$

which, in vector form,

$$\tilde{\phi} = [\mathcal{P}^*]([N]\tilde{i} - \tilde{\theta}') \tag{4.5}$$

represents all the branches of a UMEC. Applying the identical matrix manipulations that gave equations 2.20 through to 2.25, converts equation 4.5 into

$$\tilde{\phi} = [M^*][\mathcal{P}^*][N]\tilde{i} \tag{4.6}$$

where

$$[M^*] = [I] - [\mathcal{P}^*][A]\Big([A]^T[\mathcal{P}^*][A]\Big)^{-1}[A]^T$$

Partitioning the vector of branch flux $\tilde{\phi}$ into the set that contains the branches associated with each transformer winding $\tilde{\phi}_s$, and using trapezoidal integration (2.29), gives the Norton equivalent

$$\tilde{i}_s = [Y^*_{ss}]\tilde{v}_s(t) + \tilde{i}^*_{ns} \tag{4.7}$$

where

$$[Y^*_{ss}] = \left([M^*_{ss}][\mathcal{P}^*_s][N_s]\right)^{-1} \frac{\Delta t}{2}[N_s]^{-1}$$

and

$$\tilde{i}^*_{ns} = \left([M^*_{ss}][\mathcal{P}^*_s][N_s]\right)^{-1}\left(\frac{\Delta t}{2}[N_s]^{-1}\tilde{v}_s(t-\Delta t) + \tilde{\phi}_s(t-\Delta t)\right)$$

The admittance matrix is again symmetric. The structure of the $[Y^*_{ss}]$ and $[Y_{ss}]$ (equation 2.30) matrices is identical, only the permeance matrix element magnitudes $\mathcal{P}^*_{ii}$ and $\mathcal{P}_{ii}$ are dissimilar, and the appendix A symmetry proof can equally be applied to $[Y^*_{ss}]$.

4.2.1 The UMEC open and short-circuit inductances

The Steinmetz "approximate" equivalent circuit is based on the assumption that experimentally measured open-circuit, and short-circuit inductances result only from core flux paths, and leakage flux paths respectively. Before core non-linearity is added, the UMEC can be applied to derive open and short-circuit inductances taking into account both the core and leakage flux paths. Inductances are presented in either actual branch permeance $\mathcal{P}^*_k$ or reluctance $\mathcal{R}^*_k$ form depending upon which representation yields the simplest derivation.

Figure 4.3(a) displays the UMEC if the secondary winding is open-circuit. This magnetic network can be simplified to that of figure 4.3(b) which includes a single MMF $N_1 i_1(t)$ and an equivalent $\phi_1(t)$ path reluctance

$$\mathcal{R}^{*prim}_{oc} = \frac{(\mathcal{R}^*_1\mathcal{R}^*_4 + \mathcal{R}^*_1\mathcal{R}^*_3 + \mathcal{R}^*_3\mathcal{R}^*_4)(\mathcal{R}^*_2 + \mathcal{R}^*_5) + (\mathcal{R}^*_1 + \mathcal{R}^*_4)\mathcal{R}^*_2\mathcal{R}^*_5}{(\mathcal{R}^*_3 + \mathcal{R}^*_4)(\mathcal{R}^*_2 + \mathcal{R}^*_5) + \mathcal{R}^*_2\mathcal{R}^*_5} \tag{4.8}$$

Similarly, if the primary winding is open-circuit and the secondary winding energised, the UMEC can be reduced to a single MMF $N_2 i_2(t)$ and equivalent $\phi_2(t)$ path reluctance

$$\mathcal{R}^{*sec}_{oc} = \frac{(\mathcal{R}^*_2\mathcal{R}^*_5 + \mathcal{R}^*_2\mathcal{R}^*_3 + \mathcal{R}^*_3\mathcal{R}^*_5)(\mathcal{R}^*_1 + \mathcal{R}^*_4) + (\mathcal{R}^*_2 + \mathcal{R}^*_5)\mathcal{R}^*_1\mathcal{R}^*_4}{(\mathcal{R}^*_3 + \mathcal{R}^*_5)(\mathcal{R}^*_1 + \mathcal{R}^*_4) + \mathcal{R}^*_1\mathcal{R}^*_4} \tag{4.9}$$

Equations 4.8 and 4.9 are derived in appendix D, sections D.1 and D.2 respectively.

In so far the UMEC is linear and each path reluctance $\mathcal{R}^*_k$ is time invariant. The inductances measured from open-circuit primary and secondary open-circuit tests are

$$L^{prim}_{oc} = \frac{N_1^2}{\mathcal{R}^{*prim}_{oc}} \tag{4.10}$$

and

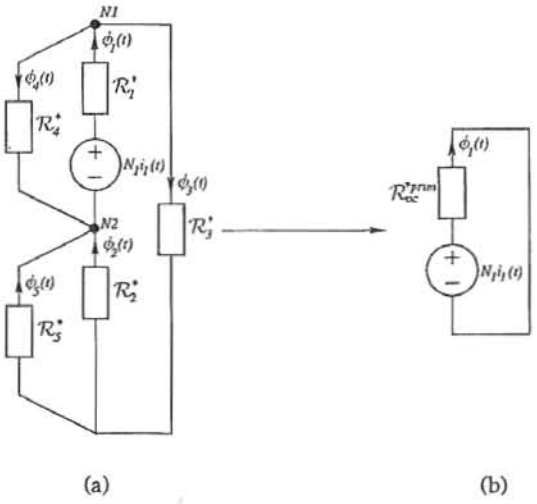

Figure 4.3 Linear UMEC reduction: (a) open-circuit secondary, (b) simplified open-circuit equivalent, (c) short-circuit secondary, (d) simplified short-circuit equivalent.

$$L_{oc}^{sec} = \frac{N_2^2}{\mathcal{R}_{oc}^{*sec}} \tag{4.11}$$

The linear single-phase UMEC winding-limb reluctances are assumed equal, $\mathcal{R}_1^* = \mathcal{R}_2^* = \mathcal{R}_w^*$. Although steel cored transformer leakage path reluctances may not be equal, they will be considerably larger than winding-limb and yoke path reluctances, $(\mathcal{R}_4^* \neq \mathcal{R}_5^*) >> (\mathcal{R}_w^*, \mathcal{R}_3^*)$. In a linear steel-cored single-phase transformer model, equations 4.8 and 4.9 can therefore be simplified to

$$\mathcal{R}_{oc}^{*prim} = \mathcal{R}_{oc}^{*sec} = 2\mathcal{R}_w^* + \mathcal{R}_3^* \tag{4.12}$$

The primary and secondary open-circuit equivalent reluctances are equal and thus the inductances L_{oc}^{prim} and L_{oc}^{sec} (referred correctly by the square of the transformer turns ratio) must also be the same.

In the case of air or partially cored transformers, dissimilar leakage path reluctances may be of the same order of magnitude as winding-limb and yoke path reluctance $(\mathcal{R}_4^* \neq \mathcal{R}_5^*) \simeq (\mathcal{R}_w^*, \mathcal{R}_3^*)$. Under these conditions, even if winding-limb reluctances equate $\mathcal{R}_1^* = \mathcal{R}_2^* = \mathcal{R}_w^*$, the open-circuit equivalent reluctances are not equal, $\mathcal{R}_{oc}^{*prim} \neq \mathcal{R}_{oc}^{*sec}$. In this case the leakage flux paths significantly influence the primary and secondary open-circuit tests. Inductances L_{oc}^{prim} and L_{oc}^{sec} (referred by the square of the transformer turns ratio) are different.

When the secondary winding is shorted, figures 4.3(c) and (d) display the resultant UMEC and simplified equivalent respectively. The simplified circuit contains MMF $N_1 i_1(t)$ and equivalent $\phi_1(t)$ path reluctance

$$\mathcal{R}_{ss}^{*prim} = \frac{\mathcal{R}_1^*(\mathcal{R}_3^* + \mathcal{R}_4^* + \mathcal{R}_5^*) + \mathcal{R}_4^*(\mathcal{R}_3^* + \mathcal{R}_5^*)}{\mathcal{R}_3^* + \mathcal{R}_4^* + \mathcal{R}_5^*} \tag{4.13}$$

Similarly, when the primary winding is shorted and the secondary energised, the UMEC can be reduced to the single MMF $N_2 i_2(t)$ and equivalent $\phi_2(t)$ path reluctance

$$\mathcal{R}_{ss}^{*sec} = \frac{\mathcal{R}_2^*(\mathcal{R}_3^* + \mathcal{R}_4^* + \mathcal{R}_5^*) + \mathcal{R}_5^*(\mathcal{R}_3^* + \mathcal{R}_4^*)}{\mathcal{R}_3^* + \mathcal{R}_4^* + \mathcal{R}_5^*} \tag{4.14}$$

Equations 4.13 and 4.14 are derived in appendix D, sections D.3 and D.4 respectively.

If the UMEC path reluctances are time invariant, the inductances measured from primary and secondary short-circuit tests are

$$L_{ss}^{prim} = \frac{N_1^2}{\mathcal{R}_{ss}^{*prim}} \tag{4.15}$$

and

$$L_{ss}^{sec} = \frac{N_2^2}{\mathcal{R}_{ss}^{*sec}} \tag{4.16}$$

In the linear steel cored transformer example, $\mathcal{R}_1^* = \mathcal{R}_2^* = \mathcal{R}_w^*$ and since $(\mathcal{R}_4^* \neq \mathcal{R}_5^*) >> (\mathcal{R}_w^*, \mathcal{R}_3^*)$, equations 4.13 and 4.14 can be simplified to

$$\mathcal{R}_{ss}^{*prim} = \mathcal{R}_{ss}^{*sec} = \frac{\mathcal{R}_4^* \mathcal{R}_5^*}{\mathcal{R}_4^* + \mathcal{R}_5^*} \tag{4.17}$$

The primary and secondary short-circuit equivalent reluctances are dependent upon leakage flux paths only, and are equal. The inductances L_{ss}^{prim} and L_{ss}^{sec} (referred correctly by the square of the transformer turns ratio) must also be the same.

In the case of air or partially cored transformers, the short-circuit path reluctance

core terms can not be neglected. However, provided the winding-limb reluctances equate, the primary and secondary equivalent reluctances remain equal.

4.2.2 The UMEC self and mutual inductances

The linear UMEC can also be applied to derive self and mutual terms of the inductance matrix transformer representation

$$\begin{bmatrix} v_1(t) \\ v_2(t) \end{bmatrix} = \begin{bmatrix} L_{11} & M_{12} \\ M_{21} & L_{22} \end{bmatrix} \begin{bmatrix} \frac{di_1(t)}{dt} \\ \frac{di_2(t)}{dt} \end{bmatrix} \tag{4.18}$$

Self inductance can be defined as the scaling factor that relates winding voltage to changes in winding current. The single-phase UMEC self inductances L_{11} and L_{22} are equal to the primary and secondary open-circuit inductances

$$L_{11} = L_{oc}^{prim} = \frac{N_1^2}{\mathcal{R}_{oc}^{*prim}} \tag{4.19}$$

and

$$L_{22} = L_{oc}^{sec} = \frac{N_2^2}{\mathcal{R}_{oc}^{*sec}} \tag{4.20}$$

Mutual inductance can be defined as the scaling factor that relates winding voltage to the change in current of another mutually coupled winding. The figure 4.3(a) open-circuit UMEC can be simplified to that of figure 4.4 which includes single MMF $N_1 i_1(t)$ and equivalent $\phi_2(t)$ path permeance

$$\mathcal{P}_{21}^* = \frac{\mathcal{P}_1^* \mathcal{P}_2^* \mathcal{P}_3^*}{(\mathcal{P}_2^* + \mathcal{P}_5^*)(\mathcal{P}_1^* + \mathcal{P}_3^* + \mathcal{P}_4^*) + \mathcal{P}_3^*(\mathcal{P}_1^* + \mathcal{P}_4^*)} \tag{4.21}$$

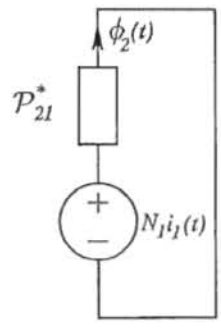

Figure 4.4 Mutual inductance equivalent circuit.

Similarly, if the primary winding is open-circuit and the secondary energised, the UMEC can be reduced to a single MMF $N_2 i_2(t)$ and equivalent $\phi_1(t)$ path permeance

$$\mathcal{P}_{12}^* = \frac{\mathcal{P}_1^* \mathcal{P}_2^* \mathcal{P}_3^*}{(\mathcal{P}_1^* + \mathcal{P}_4^*)(\mathcal{P}_2^* + \mathcal{P}_3^* + \mathcal{P}_5^*) + \mathcal{P}_3^*(\mathcal{P}_2^* + \mathcal{P}_5^*)} \tag{4.22}$$

Equations 4.21 and 4.22 are both derived in appendix D, section D.5.

If the UMEC is linear and time invariant then the mutual inductances are

$$M_{21} = N_1 N_2 \mathcal{P}^*_{21} \tag{4.23}$$

and

$$M_{12} = N_1 N_2 \mathcal{P}^*_{12} \tag{4.24}$$

The mutual inductances M_{12} and M_{21} always equate.

The transformer model parameters of open and short-circuit, or self and mutual inductance derived in sections 4.2.1 and 4.2.2 all assume time invariant path reluctance. Although the derivations are useful to gauge the contribution of individual UMEC branches upon each equivalent inductance, transformer models based solely upon these parameters do not include saturation. If saturation is considered even the short-circuit equivalent reluctances $\mathcal{R}^{*prim}_{ss}$ and $\mathcal{R}^{*sec}_{ss}$ are time variant; [Turner 1977] experimentally measured the non-linear relationship between leakage flux and winding MMF. Therefore core non-linearity must be added to the UMEC to improve transformer representation.

4.3 INCORPORATING A NON-LINEAR UMEC IN PSCAD-EMTDC

The flow diagram of figure 4.5 describes the per-unit implementation of a non-linear UMEC in PSCAD-EMTDC. If leakage flux path permeances are converted to per-unit, the winding-limb and yoke branch saturation characteristics given in section 3.2.1 can be applied to the UMEC.

The shape of leakage and winding-limb flux waveforms are dissimilar, since leakage flux is proportional to winding current while winding-limb flux is proportional to the integral of winding voltage. The section 3.2.2 linear division of the winding-limb flux $\tilde{\phi}_s$ into outer branches $\tilde{\phi}_r$ is now unacceptable. Calculation of UMEC branch flux ϕ_k requires the expansion of linearised equation 4.6.

$$\begin{bmatrix} \tilde{\phi}_s \\ \tilde{\phi}_r \end{bmatrix} = \begin{bmatrix} [M^*_{ss}] & [M^*_{sr}] \\ [M^*_{rs}] & [M^*_{rr}] \end{bmatrix} \begin{bmatrix} [\mathcal{P}^*_s] & [0] \\ [0] & [\mathcal{P}^*_r] \end{bmatrix} \begin{bmatrix} [N_s]\tilde{i}_s \\ \tilde{0} \end{bmatrix} \tag{4.25}$$

Winding-limb flux $\tilde{\phi}_s(t - \Delta t)$ is calculated from winding current using the upper partition of equation 4.25

$$\tilde{\phi}_s = [M^*_{ss}][\mathcal{P}^*_s][N_s]\tilde{i}_s \tag{4.26}$$

Yoke and leakage path flux $\tilde{\phi}_r(t - \Delta t)$ is calculated from winding current using the

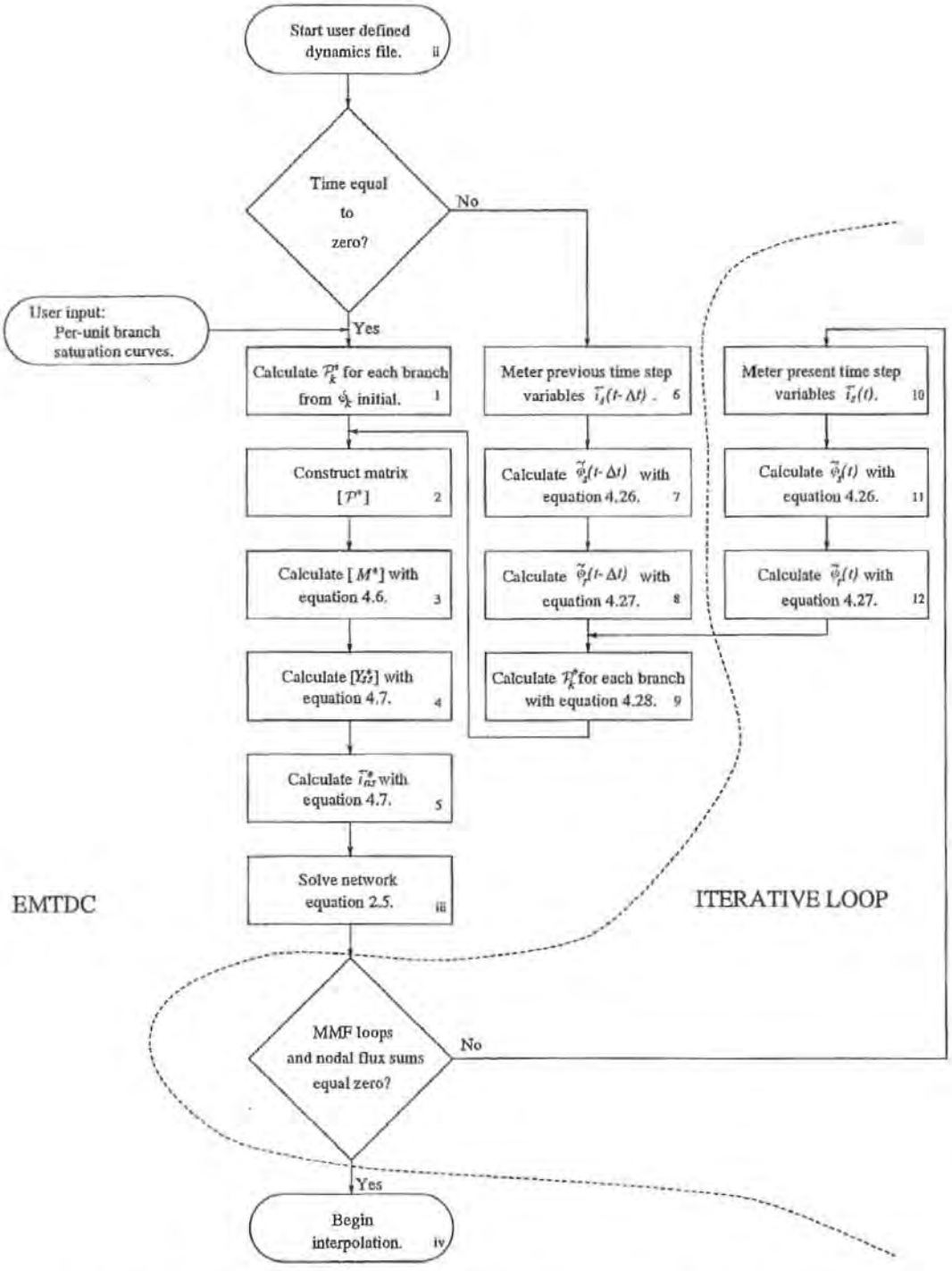

Figure 4.5 Actual permeance formulation UMEC implementation in PSCAD-EMTDC.

lower partition of equation 4.25

$$\tilde{\phi}_r = [M^*_{rs}][\mathcal{P}^*_s][N_s]\tilde{i}_s \tag{4.27}$$

Branch actual permeance $\mathcal{P}^*_k$ is calculated directly from the hyperbola saturation approximation using solved branch flux $\phi_k(t - \Delta t)$. Once $[\mathcal{P}^*]$ is known the per-unit admittance matrix $[Y^*_{ss}]$ and current source vector $\tilde{i}^*_{ns}$ can be obtained.

4.3.1 Time step delay validation

The Norton admittance matrix and current source vector are both derived from previous time step parameters. A time step delay is present between the winding current vector $\tilde{i}_s$, and UMEC branch flux vectors $\tilde{\phi}_s$ and $\tilde{\phi}_r$. With this delay a true solution to the UMEC can not be found; the flux sums at each node and MMF sums around each loop will not equate to zero. Although the typical PSCAD-EMTDC time step is small (50 μs) the error resulting from the time step delay has not yet been gauged.

The iterative loop shown in figure 4.5 is required to obtain a simultaneous non-linear UMEC and PSCAD-EMTDC electric circuit solution at each time t. Each iteration takes the electric network solution, uses the winding current $\tilde{i}_s$ to update the UMEC parameters $\tilde{\phi}_s$ and $\tilde{\phi}_r$, and recalculates the Norton equivalent. Unlike the iterative technique of section 3.4 this loop includes the electric circuit solution. Iteration ceases when the UMEC flux sums at each node and MMF sums around each loop are below specified tolerances.

Iteration at each time step modifies the original electromagnetic transient program proposed by [Dommel 1969], and the PSCAD-EMTDC main program structure shown in figure 2.2. Modifications are required when the electromagnetic transient program is applied to non-linear systems. For instance PSCAD-EMTDC modifies the electromagnetic transient technique with the addition of interpolation to accurately determine HVdc converter valve switching instants.

In order to quantify the effect of the previous time step approximation, comparisons were made between the non-iterative and iterative UMEC implementation techniques. To ensure that only the iterative loop differed in each technique, two electromagnetic transient programs were written from the flow diagrams of figures 2.2 and 4.5. Each program was written to model only the figure 4.6 single-phase transformer test system.[1]

Comparisons were made for open-circuit, short-circuit and in-rush operating conditions. Table 4.1 lists the test system electric circuit parameters for the three scenarios, a 50 μs time step was applied in each case. The single-phase transformer

[1]Insertion of the iterative technique in PSCAD-EMTDC requires alteration of the complex main program structure. Valid technique comparisons are more easily achieved with the simplier case specific programs.

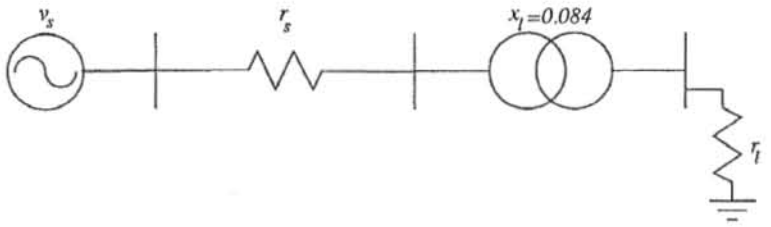

Figure 4.6 Iteration comparison test system.

UMEC winding-limb and yoke hyperbola saturation characteristic parameters, and leakage reactance are as listed in sections 3.4, and 3.3.2 respectively. The leakage permeances $\mathcal{P}_4$ and $\mathcal{P}_5$ were set at 4.12e-2 (p.u.) to give the 0.084 p.u. short-circuit impedance.

	v_s (peak p.u.)	r_s (p.u.)	r_l (p.u.)
Open-circuit	1.0	0.001	1.0e+6
Short-circuit	0.1	0.001	1.0e-6
In-rush	1.0	0.001	1.0e+6

Table 4.1 Non-iterative and iterative test-system electric parameters.

Iterative and non-iterative UMEC solutions are compared in figure 4.7. In all three scenarios the iterative and non-iterative solutions were indistinguishable. Moreover the open-circuit waveforms shown in figures 4.7(a) and (b) verify that UMEC winding leakage flux is proportional to winding current. Figures 4.7(c) and (d) reinforce that the short-circuit condition restricts flux from flowing in the secondary winding-limb; the primary winding-limb flux (10% rated) halves and flows in each leakage path. Figures 4.7(e) and (f) show that a linear division of the winding-limb flux into outer branches is not acceptable; the winding leakage waveform is not a scaled version of the winding-limb flux.

With a 50μs time step the non-iterative UMEC solution errors are small, and the previous time step approximation is satisfactory. For example, figure 4.8 displays the level of error introduced by this technique for the open-circuit test case. The MMF sum around the primary winding-limb and leakage path loop is shown in figure 4.8(a), and the flux sum at the top UMEC node (labeled $N1$ in figure 4.1(b)) is shown in figure 4.8(b).

4.3.2 Removal of per-unit representation

The UMEC based PSCAD-EMTDC transformer models can be further simplified if the reliance upon per-unit representation is removed. Although the per-unit system was well suited to the linear and linearised models, a requirement of the HDA interval-idation, the PSCAD-EMTDC convention is to set node voltages in kV, node current

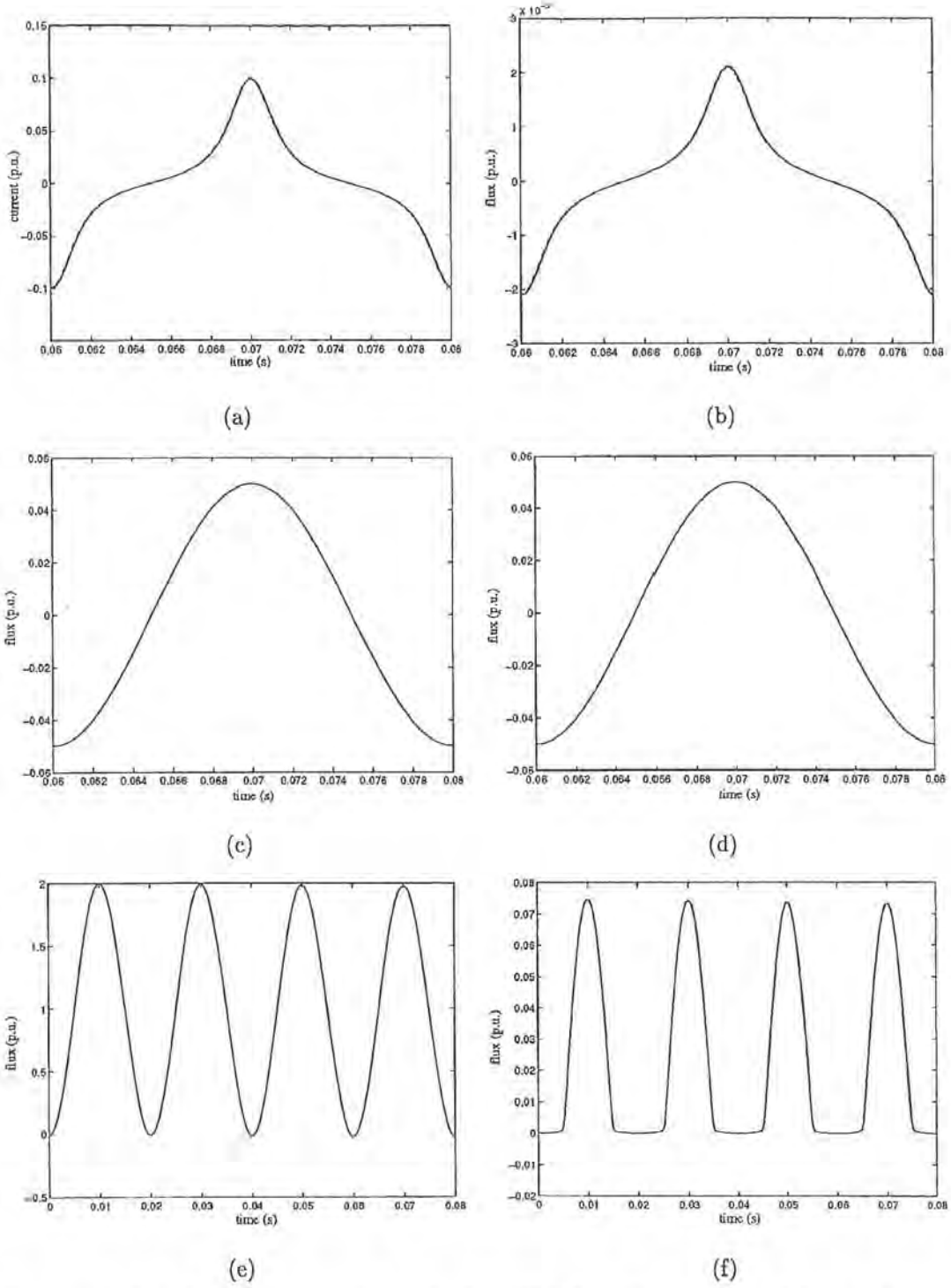

Figure 4.7 Iterative and non-iterative single-phase UMEC model comparison; Solid=non-iterative, Dash-dot=iterative: (a) open-circuit current, (b) open-circuit leakage flux (primary), (c) short-circuit leakage flux (primary), (d) short-circuit leakage flux (secondary), (e) in-rush primary winding-limb, (f) in-rush primary leakage flux.

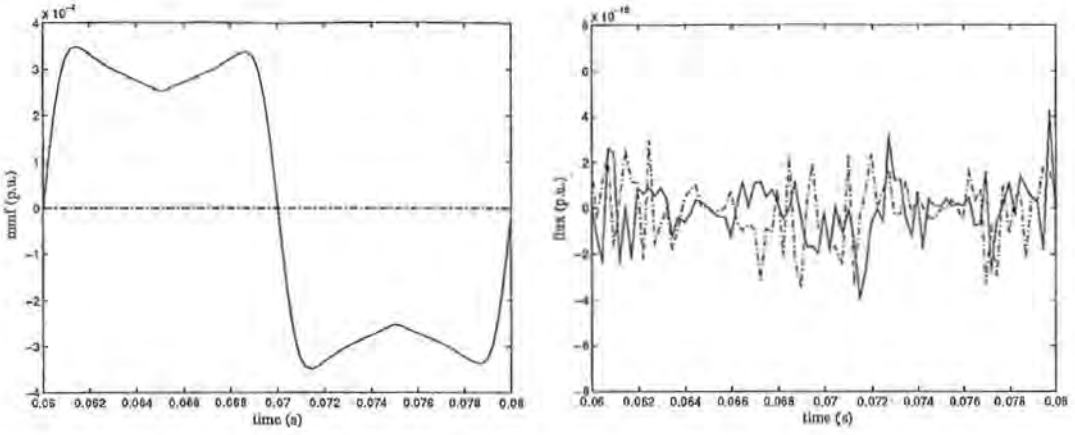

(a) (b)

Figure 4.8 Open-circuit single-phase UMEC solution comparison; Solid=non-iterative technique, Dash-dot=iterative technique: (a) mmf loop sum, (b) node flux sum.

in kA, and admittances in mhos. As a direct interface with other PSCAD-EMTDC components the Norton equivalent of figure 4.1 must also be scaled to this convention.

Figure 4.9 presents the new UMEC implementation strategy. The leakage flux branch permeances are constant (described in section 4.1), and the core branch saturation characteristic is the steel flux density-magnetising force (B-H) curve. If requested, manufacturers will provide the B-H characteristic for a transformer core, individual branch per-unit ϕ-i characteristics are not a conventional specification.[2]

Core dimensions, branch length L_k and cross-sectional area A_k, are required to calculate real value permeances

$$\mathcal{P}_k^* = \frac{\mu_o \mu_{rk} A_k}{L_k} \tag{4.28}$$

Branch flux $\phi_k(t - \Delta t)$ is converted to branch flux density

$$B_k(t - \Delta t) = \frac{\phi_k(t - \Delta t)}{A_k} \tag{4.29}$$

The hyperbola can be applied to represent the core B-H characteristic; branch permeability $\mu_o \mu_{rk}$ is calculated from flux density $B_k(t - \Delta t)$ using

$$\mathcal{E} B_k = (m_1 H_k + b_1 - B_k)(m_2 H_k + b_2 - B_k) - b_1 b_2 \tag{4.30}$$

Figure 4.9 also shows that winding-limb flux $\tilde{\phi}_s(t - \Delta t)$ is now calculated with trapezoidal integration (3.6) rather than linearised equation 4.26. Trapezoidal integration requires storage of vectors $\tilde{\phi}_s(t - 2\Delta t)$ and $\bar{v}_s(t - 2\Delta t)$. Matrices $[M_{ss}^*]$ and $[P_{ss}^*]$

[2] Appendix E details the relationship between B-H and per-unit ϕ-i characteristics for the UMEC winding-limb and yoke branches.

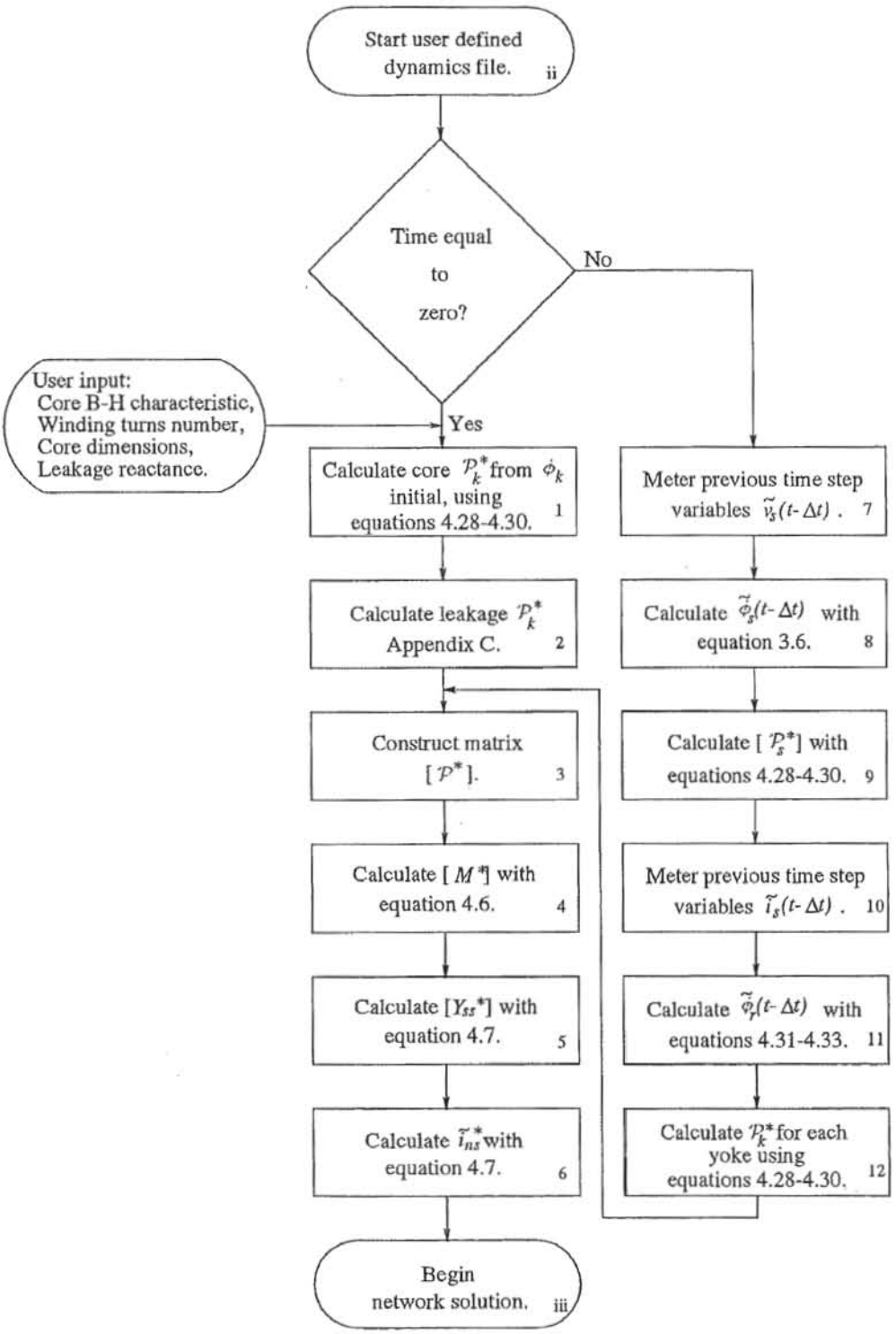

Figure 4.9 Real value UMEC implementation in PSCAD-EMTDC.

must be stored to apply equation 4.26. Although $[P^*_{ss}]$ is diagonal, $[M^*_{ss}]$ is full and therefore, in the latter method, element storage increases with the square of the UMEC winding-limb branch number.

The elements of $\tilde{\phi}_r(t-\Delta t)$ can be calculated using magnetic circuit theory. The MMF around the primary winding-limb and leakage branch loop must sum to zero, stated as

$$\phi_4(t-\Delta t) = \mathcal{P}^*_4\Big(N_1 i_1(t-\Delta t) - \phi_1(t-\Delta t)\mathcal{R}^*_1\Big) \tag{4.31}$$

The MMF around the secondary winding-limb and leakage branch loop must sum to zero, stated as

$$\phi_5(t-\Delta t) = \mathcal{P}^*_5\Big(N_2 i_2(t-\Delta t) - \phi_2(t-\Delta t)\mathcal{R}^*_2\Big) \tag{4.32}$$

Finally, the flux at node $N1$ must sum to zero, stated as

$$\phi_3(t-\Delta t) = \phi_1(t-\Delta t) - \phi_4(t-\Delta t) \tag{4.33}$$

Yoke branch actual permeance $\mathcal{P}^*_k$ is calculated directly from solved branch flux $\phi_k(t-\Delta t)$ using equations 4.28 to 4.30. Once $[\mathcal{P}^*]$ is known, the real valued admittance matrix $[Y^*_{ss}]$ and current source vector $\tilde{i}^*_{ns}$ can be obtained.

4.3.3 The Benmore converter transformers

The final UMEC implementation strategy, presented in the previous section, can be applied to create practical transformer models. Figure 4.10 displays the core dimensions, and table 4.2 gives the name-plate data, for the Benmore valve-group converter transformers. This information was supplied by Trans Power New Zealand Ltd, the transformer owners. In this section, single-phase transformer parameters have been given for a star-grounded/star-grounded connection.

Electric circuit parameters	
Rating	62.5 MVA
Configuration	single-phase
Frequency	50 (Hz)
V_1	$\frac{16}{\sqrt{3}}$ (kV)
V_2	$\frac{110}{\sqrt{3}}$ (kV)
$X_{leakage}$	0.113 (p.u.)

Table 4.2 Benmore transformer name-plate data.

Winding turns number, core dimensions and B-H characteristics are seldom specified as part of a transformer purchase. This example is no exception and also there is not sufficient information to calculate individual winding leakage permeances. This

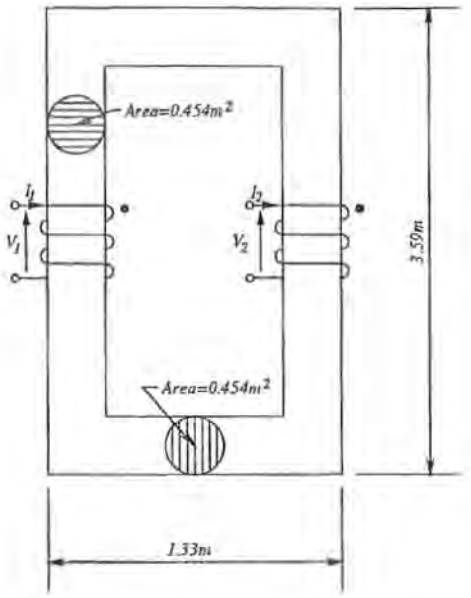

Figure 4.10 Benmore transformer core dimensions.

problem of insufficient data must be solved either with acceptable assumptions applied at the modeller's discretion or by obtaining a satisfactory parameter schedule from the transformer manufacturer. Further in this chapter, for the case of a three-limb three-phase field transformer, the latter option is exercised. In this case the former is applied because the problem of insufficient data is common, and the assumptions required can be presented.

In the absence of better information the core saturation curve is represented with the general B-H characteristics [Say 1983] presented in figure 4.11. Table 4.3 gives hyperbola constants.

m1	m2	b1	b2	$\mathcal{E}$
0.021	3.0e-5	0.0	1.63	1.9

Table 4.3 Assumed B-H curve hyperbola parameters.

The peak flux density that the transformer winding-limbs experience under steady-state rated conditions is

$$B_k^{peak} = \frac{\sqrt{2}V_1}{A_1 N_1 \omega_o} = \frac{\sqrt{2}V_2}{A_2 N_2 \omega_o} \tag{4.34}$$

where ω_o is the base angular frequency. In this example winding turns number must be calculated assuming a reasonable peak flux density. The transformer manufacturer must trade off the winding volt-per-turn design and core cross-sectional area, against the position of B_k^{peak} with respect to the saturation curve knee region. As the available transformer data gives only the core cross-sectional area, a reasonable peak operating

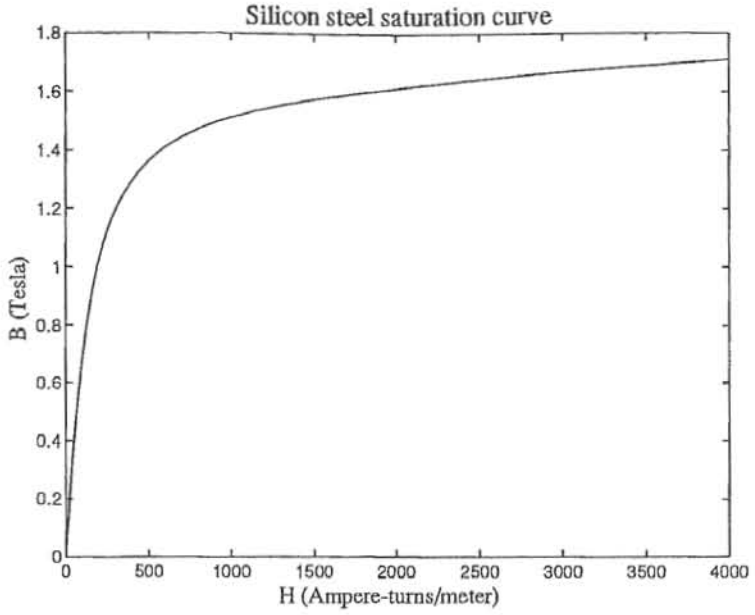

Figure 4.11 Assumed B-H saturation characteristic.

flux of 1.4T has been selected; the winding turn numbers are thus 65 and 450 turns for the $\frac{16}{\sqrt{3}}$ and $\frac{110}{\sqrt{3}}$ kV windings respectively. Finally, the name-plate data does not specify primary and secondary open-circuit current, the flux leakage path permeance is assumed to be equally divided amongst the primary and secondary windings. This assumption allows leakage path permeances $\mathcal{P}_4^*$ and $\mathcal{P}_5^*$ to be calculated in accordance with appendix C. The specified and assumed parameters required to model the Benmore transformer are summarised in table 4.4.

Electric circuit parameters		Magnetic circuit parameters	
Rating	62.5 MVA	$A_{winding\ limb}$	0.454 (m^2)
Configuration	single-phase	$L_{winding\ limb}$	3.59 (m)
Frequency	50 (Hz)	A_{yoke}	0.454 (m^2)
$V_{primary}$	$\frac{16}{\sqrt{3}}$ (kV)	L_{yoke}	2.66 (m)
$V_{secondary}$	$\frac{110}{\sqrt{3}}$ (kV)	$N_{primary}$	65 $(turns)$
$X_{leakage}$	0.113 (p.u.)	$N_{secondary}$	450 $(turns)$
		$\mathcal{P}_4$	5.85e-8
		$\mathcal{P}_5$	5.85e-8

Table 4.4 Single-phase UMEC model parameters.

An PSCAD-EMTDC transformer model was created from the table 4.4 parameters, placed in the figure 4.12 test system, and subjected to open-circuit energisation at full rated voltage, short-circuit energisation at 10% rated voltage, and full rated load operation at unity power factor. Table 4.5 lists the test system electric circuit parameters for the three scenarios, a 50μs time step was applied in each case. Figure

4.13 displays a select few simulation waveforms produced from the three scenarios.

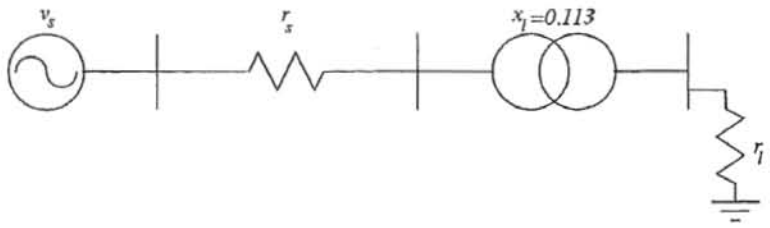

Figure 4.12 Single-phase field transformer test system.

	V_s (kV)	r_s (Ω)	r_l (Ω)
Open-circuit	$\frac{16}{\sqrt{3}}$	0.107	1.00e+6
Short-circuit	$\frac{1.6}{\sqrt{3}}$	8.00e-3	7.50e-3
Rated-load	$\frac{16}{\sqrt{3}}$	8.00e-3	64.5

Table 4.5 Single-phase field transformer test-system electric parameters.

The open-circuit current, shown in figure 4.13(a), exhibits the typical non-sinusoidal magnetising waveform that lags the terminal voltage by 90^o.[3] The magnetising current magnitude appears reasonable, it equates to 0.047kA, and when normalised by the rated transformer base current I_{base}=6.77kA, equals 0.0069 p.u. The open-circuit yoke flux, shown in figure 4.13(b), is correctly in phase with the magnetising current at a peak flux level ϕ_3=0.639Wb. The corresponding yoke flux density B_3=1.4T is in accordance with the previously described winding turns design at rated voltage.

Figures 4.13(c) and (d) present short-circuit primary voltage and current respectively. The short-circuit voltage v_1^{peak}=1.31kV and current i_1^{peak}=8.42kA, give a leakage impedance $X_{leakage}$=0.156Ω. When normalised by the impedance base Z_{base}=1.37Ω, $X_{leakage}$=0.114 p.u., which agrees with the name-plate leakage specification. Finally, figure 4.13(e) displays the primary current when a 1.0 p.u. (64.5Ω) resistive load is placed at the transformer secondary terminals. The simulated primary current I_1=6.80kA matches the rated primary current I_{base}. The small phase shift between primary voltage and current results from the combined transformer leakage reactance and winding resistance.

The single-phase Norton equivalent provides a reasonable representation of the Benmore valve-group converter transformers. However assumptions were required to derive model saturation curve, winding turns design and individual winding leakage permeance, therefore further validations are required to certify the performance of UMEC based transformer models.

[3] In all three cases the reference source voltage positive going zero-crossing occurs at time 0.08 secs.

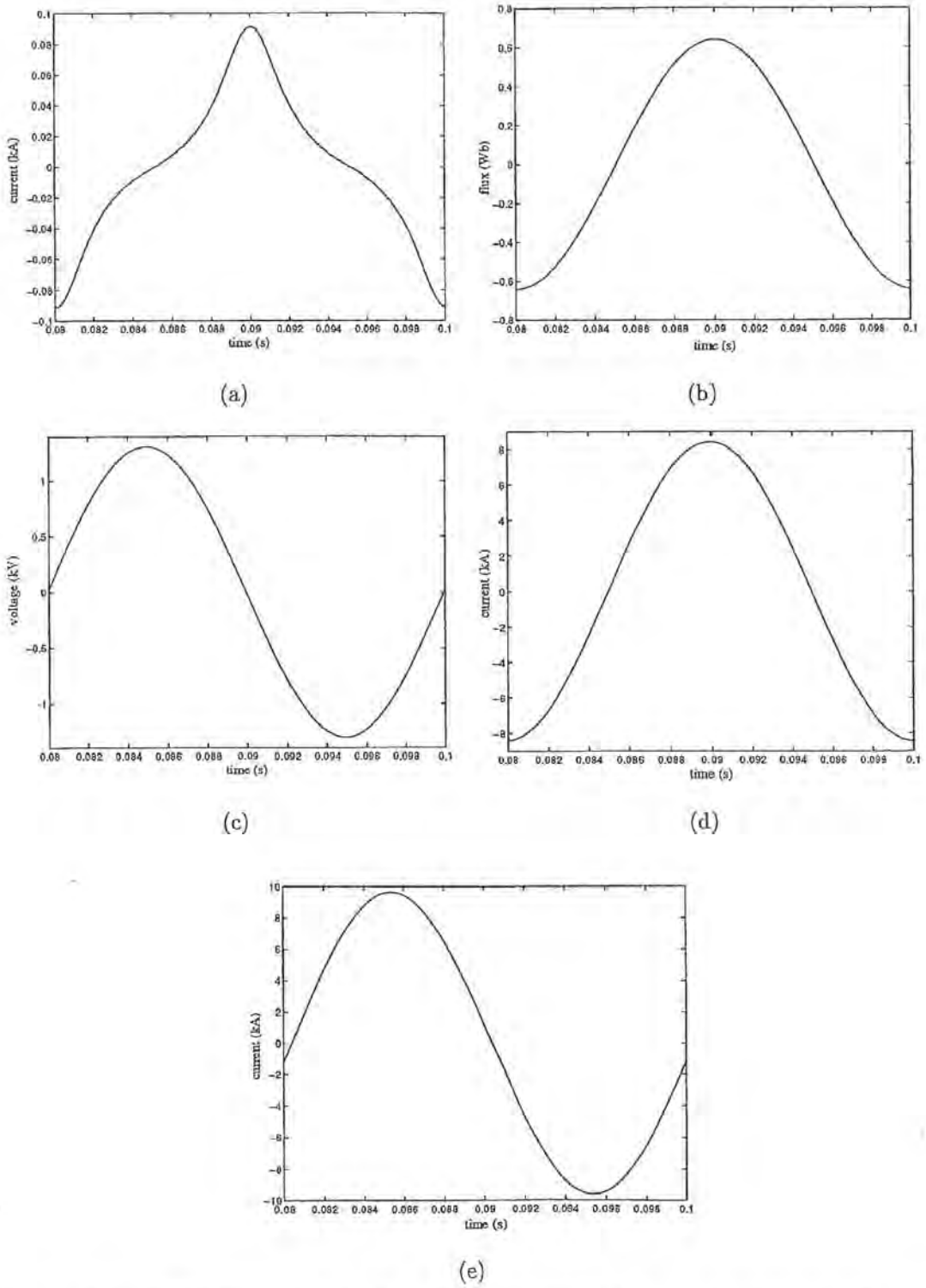

Figure 4.13 UMEC Benmore single-phase transformer model: (a) open-circuit current, (b) open-circuit yoke flux, (c) short-circuit voltage, (d) short-circuit current, (e) rated-load current.

4.4 UMEC AND PSCAD-EMTDC TRANSFORMER MODEL COMPARISON

Present HDA and PSCAD-EMTDC transformer models separate leakage, and core flux into electric circuit series leakage reactance, and shunt magnetising branches respectively. In HDA the single-phase two winding transformer magnetising current is halved and placed on either side of the lumped primary and secondary leakage reactance. The present non-linear PSCAD-EMTDC transformer model implements the magnetizing current as a source across one winding of an "ideal" transformer, as shown in figure 4.14. In this context an "ideal" transformer is one that exhibits a leakage reactance but zero magnetizing current. With reference to HVdc converter transformers, and considering the relatively large impedances as seen from the converter side windings, it can be acceptable to place the magnetizing currents on the ac system side of the transformer leakage reactance.

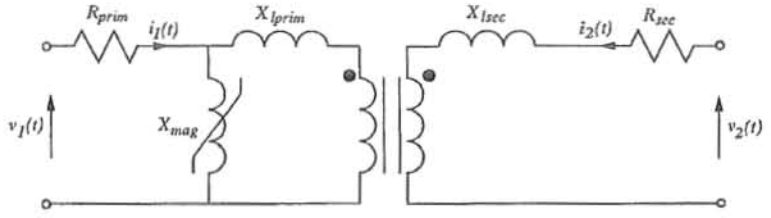

Steinmetz "approximate" equivalent

(a)

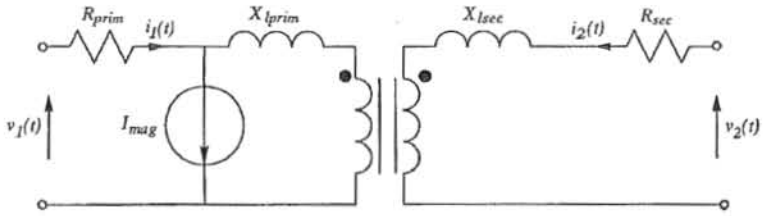

Conventional EMTDC non-linear transformer equivalent

(b)

Figure 4.14 The PSCAD-EMTDC model and Steinmetz "approximate" circuit: (a) Steinmetz "approximated" equivalent, (b) PSCAD-EMTDC representation.

The UMEC single-phase model can be applied to examine the consequences of the conventional representation. If the core loss component of transformer magnetizing current is neglected the single-phase transformer can be represented by the Steinmetz "exact" equivalent circuit shown in figure 4.15(a) and (c). Alternatively, the single-phase transformer can be redrawn as the UMEC shown in figure 4.15(b). The Norton equivalent implemented as shown in figure 4.15(d), is a model for the Steinmetz "exact" equivalent circuit.

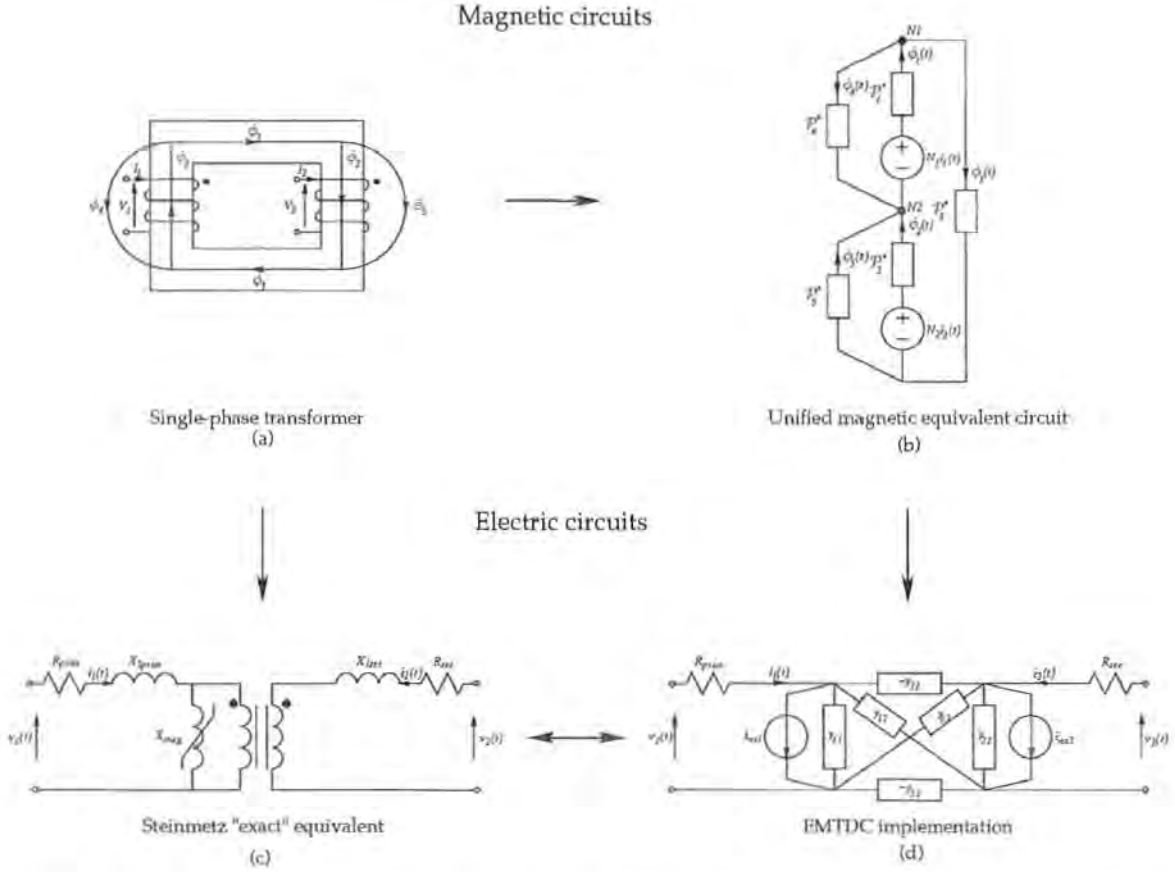

Figure 4.15 The single-phase Norton equivalent and Steinmetz "exact" circuit: (a) core flux paths, (b) unified magnetic equivalent circuit, (c) Steinmetz, equivalent (d) Norton equivalent.

4.4.1 Laboratory verification

To highlight the effect of the UMEC model on transformer magnetising current harmonic distribution, the laboratory set up of figure 4.16 was utilised. An undistorted sine-wave generator supplied the test transformer loaded with a series resonant circuit; the resonant point was tuned to the fifth harmonic. The sine-wave generator, test transformer, and series resonant load parameters are given in appendix F. The magnetising current distribution is dependent on the transformer individual leakage reactances, winding resistances and the system impedance at each frequency.

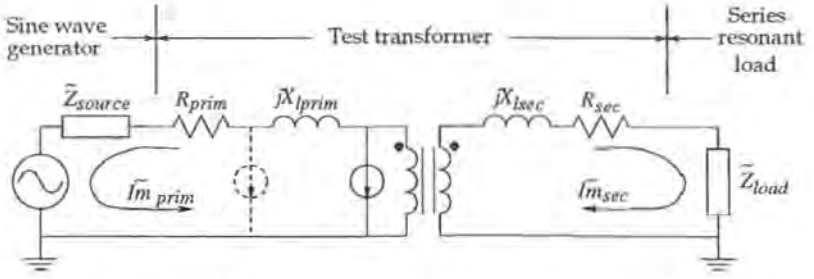

Figure 4.16 Laboratory experimental set up.

The primary and secondary impedances of the Steinmetz "exact" equivalent

circuit are

$$\tilde{Z}_{prim}^{exact} = \tilde{Z}_{source} + R_{prim} + jX_{lprim} \tag{4.35}$$

$$\tilde{Z}_{sec}^{exact*} = a^2(jX_{lsec} + R_{sec} + \tilde{Z}_{load}) \tag{4.36}$$

where the * is used to indicate parameters referred to the generator (primary) side.

The magnetising current injection (drawn as the solid line current source of figure 4.16) will divide up between primary and secondary windings according to

$$K^{Stmz(exact)} = \frac{|\tilde{Im}_{sec}^{*}|}{|\tilde{Im}_{prim}|} = \frac{|\tilde{Z}_{prim}^{exact}|}{|\tilde{Z}_{sec}^{exact*}|} \tag{4.37}$$

Similarly Steinmetz "approximate" equivalent circuit impedances are

$$\tilde{Z}_{prim}^{approx} = \tilde{Z}_{source} + R_{prim} \tag{4.38}$$

$$\tilde{Z}_{sec}^{approx*} = jX_{lprim} + a^2(jX_{lsec} + R_{sec} + \tilde{Z}_{load}) \tag{4.39}$$

Thus the magnetising current (drawn as the dashed line current source of figure 4.16) will divide up according to

$$K^{Stmz(approx)} = \frac{|\tilde{Im}_{sec}^{*}|}{|\tilde{Im}_{prim}|} = \frac{|\tilde{Z}_{prim}^{approx}|}{|\tilde{Z}_{sec}^{approx*}|} \tag{4.40}$$

Table 4.6 displays the laboratory measured and simulated fifth harmonic using the UMEC and conventional transformer models. Placing the circuit parameters of

	Experimental	UMEC	Conventional
$\lvert\tilde{Im}_{prim}\rvert$	4.00 (mA)	2.42 (mA)	1.11 (mA)
$\lvert\tilde{Im}_{sec}^{*}\rvert$	48.0 (mA)	27.0 (mA)	5.54 (mA)
$\frac{\lvert\tilde{Im}_{sec}^{*}\rvert}{\lvert\tilde{Im}_{prim}\rvert}$	12.0	11.2	4.98

Table 4.6 Measured and simulated primary and secondary 5th harmonic magnetising current.

Appendix F into equations 4.37 and 4.40 gives $K^{Stmz(exact)} = 11.2$ and $K^{Stmz(approx)} = 4.97$ respectively.

The UMEC model predicts the same current division as the Steinmetz "exact" equivalent and the current division ratio is similar to that of the experimental test results. The conventional transformer model predicts a magnetising current division ratio equal to that of the Steinmetz "approximate" equivalent and does not match

the experimental results. Because hysteresis and core loss has not been included, the actual levels of fifth harmonic predicted by the UMEC model do not exactly match the experimental results.

4.4.2 Harmonic comparison

In the previous example the ratios $K^{Stmz(exact)}$ and $K^{Stmz(approx)}$ are dissimilar. In many practical cases, where the transformer individual leakage reactances are much less than the system impedance at each frequency, the ratios will be similar. However, when transformers are connected to generators, transmission lines or filter banks the system impedance at each frequency may vary widely.

Recently a PSCAD-EMTDC model for the Benmore converter station was verified with field data [Macdonald *et al.* 1995]; this will be discussed in greater depth in chapter 5. In this system three 112.5 MVA generators are connected to a 270MW twelve-pulse mercury-arc valve converter, via two 187.5MVA, 16/110kV converter transformer banks. The 16kV bus-bar is connected to the South Island ac system via a three-winding 200MVA, 16/33/220kV interconnecting transformer bank. The converter filters are connected to the 33kV windings of the interconnecting transformer bank, and each filter includes individual circuits tuned at the 5th, 7th, 9th, 11th and 13th harmonic. These filters provide a low impedance path to the respective transformer magnetising currents as well as the converter harmonics.

Occasionally the converters are operated with the generators disconnected from the South Island ac system and the filters left in service. In this mode, if the mercury-arc valves and converter transformers are removed from service the generators can not absorb the capacitive VAR flow from the 33kV filter banks, and the 16kV bus-bar voltage rises. The voltage rise ceases when the transformer magnetization balances the extra capacitive VAR flow. Under such load rejection the generator bus-bar may rise to 1.46p,u [Arrillaga 1983]. Figure 4.17 illustrates this scenario, the parameters for the generators, transformer and filters are given in appendix G.

Table 4.7 presents the magnetising current division ratios for this test system calculated from equations 4.37 and 4.40.

	Harmonic				
	5	7	9	11	13
$K^{Stmz(exact)}$	3.9	4.5	9.7	4.7	4.2
$K^{Stmz(approx)}$	1.8	1.9	3.0	1.8	1.7

Table 4.7 Benmore magnetising current division ratio.

The magnetising current division ratios for each harmonic are different. In this test system, the predicted level of harmonic load on the generators and filter banks is

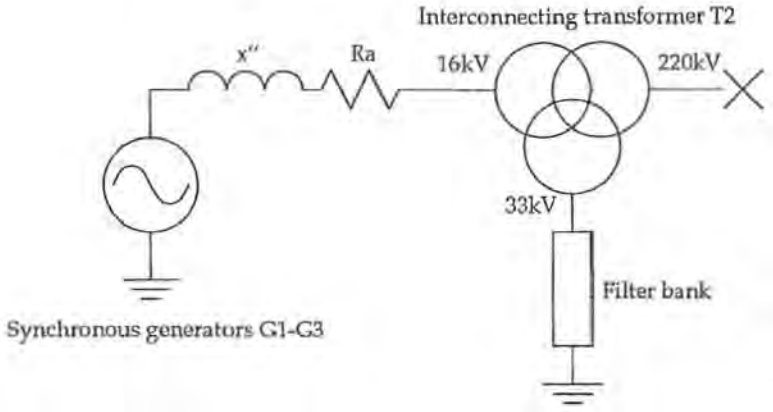

Figure 4.17 Benmore generators and interconnecting transformer bank.

dependent upon the equivalent circuit applied. Tables 4.8 and 4.9 present simulated current harmonic magnitudes and division ratios when a 1.46 p.u. overvoltage occurs on the 16kV bus-bar for the UMEC, and conventional transformer models respectively.

	Harmonic current (A_{RMS})				
	5	7	9	11	13
$\tilde{Im}_{prim}$	56.4	5.12	4.91	5.33	0.554
$\tilde{Im}^{*}_{sec}$	221	22.8	47.3	24.8	2.35
K^{UMEC}	3.92	4.45	9.63	4.65	4.24

Table 4.8 Magnetising current division; Transformer represented with UMEC model.

	Harmonic current (A_{RMS})				
	5	7	9	11	13
$\tilde{Im}_{prim}$	106	18.8	9.67	11.82	2.03
$\tilde{Im}^{*}_{sec}$	188	34.5	27.7	21.5	3.45
K^{CONV}	1.77	1.84	2.86	1.82	1.70

Table 4.9 Magnetising current division; Transformer represented with conventional model.

The levels of harmonic current predicted by each model are different. The conventional transformer model creates a harmonic load on the generator greater that that of the UMEC model. Again the UMEC model provides an excellent match to the Steinmetz "exact" equivalent and the conventional model an excellent match to the Steinmetz "approximate" equivalent.

4.5 THREE-LIMB THREE-PHASE UMEC

An extension of the single-phase UMEC concept to the three-phase transformer, shown in figure 4.18(a), leads to the UMEC of figure 4.18(b). Unlike the three-limb model,

presented in section 3.3.3, the magnetising current is not halved and placed on each side of the linear short-circuit admittance matrix. Instead there is no need to specify in advance the distribution of magnetising current components, which have been shown to be determined by the transformer internal and external circuit parameters.

MMF sources $N_1 i_1(t)$ to $N_6 i_6(t)$ represent each transformer winding individually, and winding voltages $v_1(t)$ to $v_6(t)$ are used to calculate winding-limb flux $\phi_1(t)$ to $\phi_6(t)$ respectively.

Permeances $\mathcal{P}_1^*$ to $\mathcal{P}_6^*$ represent the transformer winding limbs. If the total length of each phase winding limb L_w has uniform cross-sectional area A_w, the UMEC branches 1 to 6 have length $\frac{L_w}{2}$ and cross-sectional area A_w. Permeances $\mathcal{P}_{13}^*$ and $\mathcal{P}_{14}^*$ represent the transformer left and right hand yokes respectively. The upper and lower yokes are assumed to have the same length L_y and cross sectional area A_y. Both left and right hand yokes are represented by UMEC branches 13 and 14 of length $L_{13} = L_{14} = 2L_y$ and area $A_{13} = A_{14} = A_y$. Zero-sequence permeances $\mathcal{P}_{15}^*$ to $\mathcal{P}_{17}^*$ are obtained from in-phase excitation of all three primary or secondary windings [Stuehm 1993].[4]

Unlike the three-limb linear and linearised model, which required acquisition of non-conventional transformer parameters y_l, y_l', y_l'', and y_l''' (section 3.3.3), the UMEC can be derived from conventional transformer manufacturer specifications. Leakage permeances are obtained from open and short-circuit tests and therefore the effective length and cross-sectional areas of UMEC leakage branches 7 to 12 are not required to calculate $\mathcal{P}_7^*$ to $\mathcal{P}_{12}^*$.

The UMEC circuit of figure 4.18(b) places the actual permeance formulation in the real value form

$$\begin{bmatrix} i_1(t) \\ i_2(t) \\ i_3(t) \\ i_4(t) \\ i_5(t) \\ i_6(t) \end{bmatrix} = \begin{bmatrix} y_{11} & y_{12} & y_{13} & y_{14} & y_{15} & y_{16} \\ y_{21} & y_{22} & y_{23} & y_{24} & y_{25} & y_{26} \\ y_{31} & y_{32} & y_{33} & y_{34} & y_{35} & y_{36} \\ y_{41} & y_{42} & y_{43} & y_{44} & y_{45} & y_{46} \\ y_{51} & y_{52} & y_{53} & y_{54} & y_{55} & y_{56} \\ y_{61} & y_{62} & y_{63} & y_{64} & y_{65} & y_{66} \end{bmatrix} \begin{bmatrix} v_1(t) \\ v_2(t) \\ v_3(t) \\ v_4(t) \\ v_5(t) \\ v_6(t) \end{bmatrix} + \begin{bmatrix} i_{ns1} \\ i_{ns2} \\ i_{ns3} \\ i_{ns4} \\ i_{ns5} \\ i_{ns6} \end{bmatrix} \tag{4.41}$$

The matrix $[Y_{ss}]$ is symmetric and this Norton equivalent is implemented in PSCAD-EMTDC as shown in figure 4.19, only the blue phase network of a star-grounded/star-grounded transformer is shown.

The flow diagram of figure 4.9 describes the three-limb three-phase UMEC implementation in PSCAD-EMTDC with only slight modifications. The trapezoidal integration equation 3.6 is now applied to the six transformer windings to calculate the winding-limb flux vector $\tilde{\phi}_s(t - \Delta t)$. Equations 4.28 to 4.30 are utilized to calculate the permeances of the winding branches. Once the previous time step winding current

[4] If zero-sequence test data is not available, $\mathcal{P}_{15}^*$ to $\mathcal{P}_{17}^*$ can be set equal to leakage path permeance.

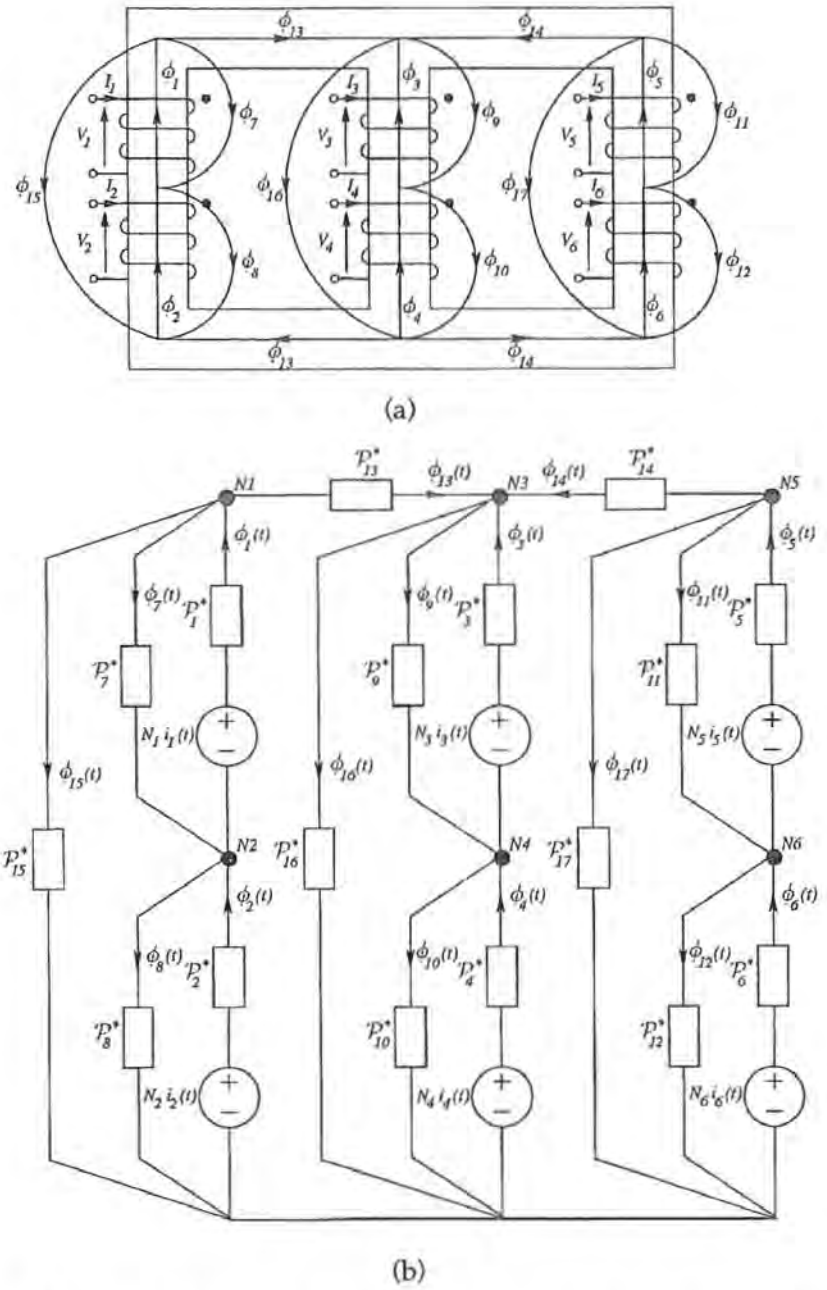

Figure 4.18 A UMEC PSCAD-EMTDC three-limb three-phase transformer model: (a) core flux paths, (b) unified magnetic equivalent circuit.

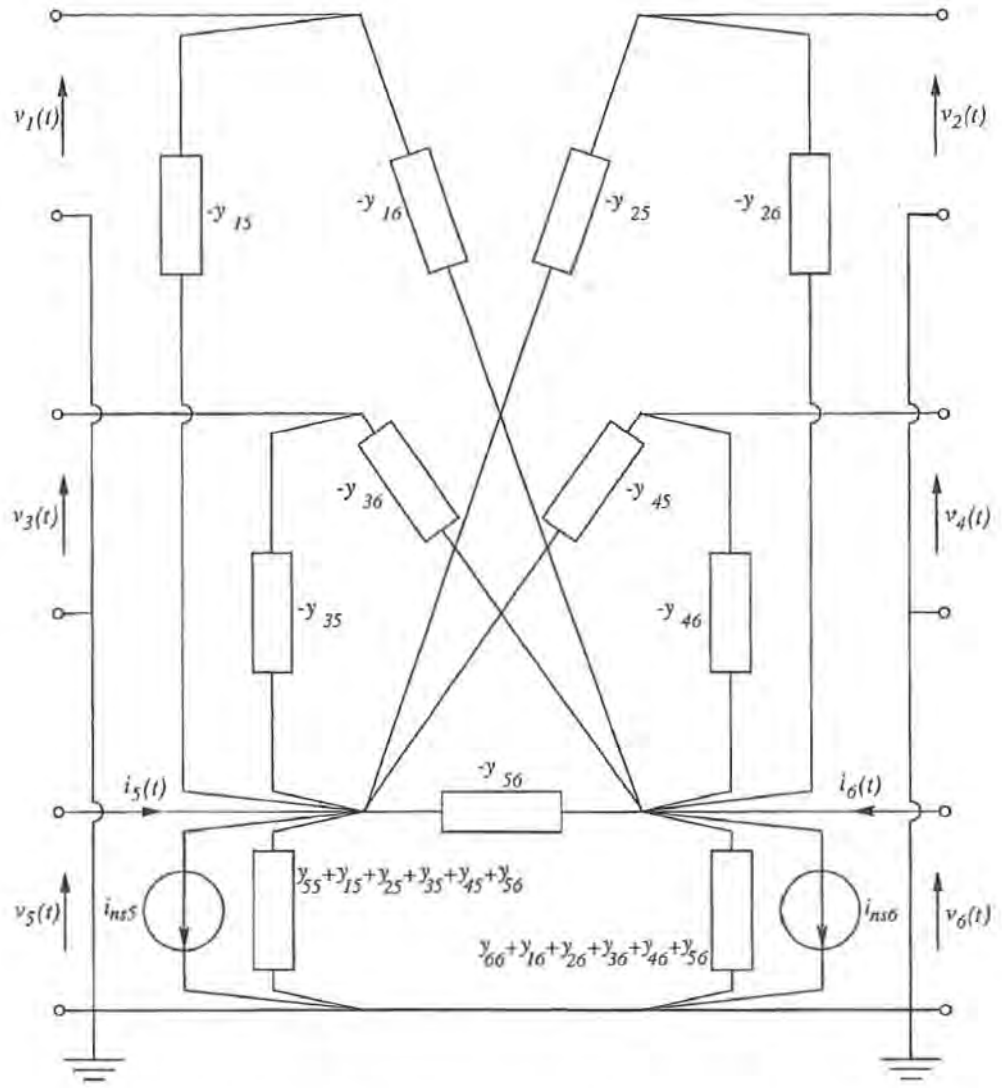

Figure 4.19 Three-limb three-phase Norton equivalent (blue-phase only, star-grounded/star-grounded).

vector $i_s(t-\Delta t)$ is formed, the flux leakage elements of $\tilde{\phi}_r(t-\Delta t)$ can be calculated using

$$\phi_7(t-\Delta t) = \mathcal{P}_7^*\Big(N_1 i_1(t-\Delta t) - \phi_1(t-\Delta t)\mathcal{R}_1^*\Big) \tag{4.42}$$

$$\phi_8(t-\Delta t) = \mathcal{P}_8^*\Big(N_2 i_2(t-\Delta t) - \phi_2(t-\Delta t)\mathcal{R}_2^*\Big) \tag{4.43}$$

$$\phi_9(t-\Delta t) = \mathcal{P}_9^*\Big(N_1 i_3(t-\Delta t) - \phi_3(t-\Delta t)\mathcal{R}_3^*\Big) \tag{4.44}$$

$$\phi_{10}(t-\Delta t) = \mathcal{P}_{10}^*\Big(N_2 i_4(t-\Delta t) - \phi_4(t-\Delta t)\mathcal{R}_4^*\Big) \tag{4.45}$$

$$\phi_{11}(t-\Delta t) = \mathcal{P}_{11}^*\Big(N_1 i_5(t-\Delta t) - \phi_5(t-\Delta t)\mathcal{R}_5^*\Big) \tag{4.46}$$

$$\phi_{12}(t-\Delta t) = \mathcal{P}^*_{12}\Big(N_2 i_6(t-\Delta t) - \phi_6(t-\Delta t)\mathcal{R}^*_6\Big) \tag{4.47}$$

The zero-sequence elements of $\tilde{\phi}_r(t-\Delta t)$ are calculated using the MMF loop sum around the primary to secondary winding-limb and zero-sequence branch, stated as

$$\begin{aligned}\phi_{15}(t-\Delta t) &= \mathcal{P}^*_{15}\Big(N_1 i_1(t-\Delta t) + N_2 i_2(t-\Delta t) - \phi_1(t-\Delta t)\mathcal{R}^*_1 \\ &\quad -\phi_2(t-\Delta t)\mathcal{R}^*_2\Big) \qquad (4.48)\\ \phi_{16}(t-\Delta t) &= \mathcal{P}^*_{16}\Big(N_1 i_3(t-\Delta t) + N_2 i_3(t-\Delta t) - \phi_3(t-\Delta t)\mathcal{R}^*_3 \\ &\quad -\phi_4(t-\Delta t)\mathcal{R}^*_4\Big) \qquad (4.49)\\ \phi_{17}(t-\Delta t) &= \mathcal{P}^*_{17}\Big(N_1 i_5(t-\Delta t) + N_2 i_6(t-\Delta t) - \phi_5(t-\Delta t)\mathcal{R}^*_5 \\ &\quad -\phi_6(t-\Delta t)\mathcal{R}^*_6\Big) \qquad (4.50)\end{aligned}$$

Finally the yoke flux is obtained using the flux summation at nodes $N1$ and $N2$, stated as

$$\phi_{13}(t-\Delta t) = \phi_1(t-\Delta t) - \phi_7(t-\Delta t) - \phi_{15}(t-\Delta t) \tag{4.51}$$

$$\phi_{14}(t-\Delta t) = \phi_5(t-\Delta t) - \phi_{11}(t-\Delta t) - \phi_{17}(t-\Delta t) \tag{4.52}$$

Yoke branch permeance $\mathcal{P}^*_{13}$ and $\mathcal{P}^*_{14}$ is again calculated directly from solved branch flux ϕ_{13} and ϕ_{14} using equations 4.28 to 4.30. Once $[\mathcal{P}^*]$ is known the real valued admittance matrix $[Y_{ss}]$ can be obtained.

4.5.1 UMEC factory data validation

A model for the Manapouri 105MVA, 13.8/220kV three-limb three-phase generator transformer was constructed to validate the extended UMEC representation. The core B-H characteristic, winding turns number, core dimensions and leakage reactance parameters were obtained directly from the transformer manufacturer, Savigliano. The connection matrix for the Dy11 transformer winding connection, and the complete technical documentation provided by Savigliano are given in appendix H. The parameters required to model the Manapouri transformer are summarised in table 4.10. The core B-H characteristics, presented in figure 4.20, is constructed from the hyperbola constants of table 4.11.

A PSCAD-EMTDC three-limb three-phase transformer model was created from the parameters of tables 4.10 and 4.11, placed in the figure 4.21 test systems. Table 4.12 lists the test system electric circuit parameters for each test system, a 50μs time step was applied in each case.

Electric circuit parameters		Magnetic circuit parameters	
Rating	105 MVA	$A_{winding\ limb}$	0.5555 (m^2)
Configuration	delta-star	$L_{winding\ limb}$	1.932 (m)
Frequency	50 (Hz)	A_{yoke}	0.5635 (m^2)
$V_{primary}$	13.8 (kV)	L_{yoke}	4.001 (m)
$V_{secondary}$	220 (kV)	$N_{primary}$	78 $(turns)$
$X_{leakage}$	0.1126 (p.u.)	$N_{secondary}$	718 $(turns)$
		$\mathcal{P}_{7,9,11}$	1.67e-7
		$\mathcal{P}_{8,10,12}$	1.67e-7
		$\mathcal{P}_{15,16,17}$	1.67e-7

Table 4.10 Manapouri three-limb transformer UMEC model parameters.

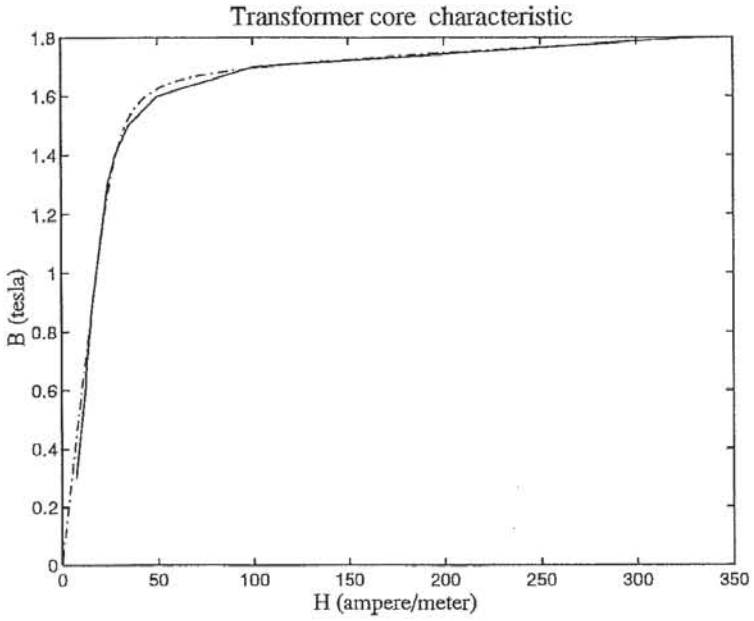

Figure 4.20 Manapouri transformer B-H saturation characteristic; Solid=Savigliano data, Dash-Dash=Hyperbola approximation.

The factory test data is given in tabular form (appendix H), table 4.13 no-load ratio, open-circuit, and short-circuit factory test results with simulation. Under these steady-state operating conditions the three-limb three-phase UMEC provides an acceptable match with the factory data.

4.6 CONCLUSIONS

Winding leakage flux representation has been shifted from the transformer electric network to the unified magnetic equivalent circuit (UMEC). Each UMEC MMF source now represents total winding current, rather than the magnetising current alone.

The PSCAD-EMTDC non-linear transformer model is based on the Steinmetz "approximate" equivalent circuit. A uniform flux density is assumed throughout the

m1	m2	b1	b2	$\mathcal{E}$
0.0616	3.8e-4	0.0	1.69	0.750

Table 4.11 Manapouri transformer B-H curve hyperbola parameters.

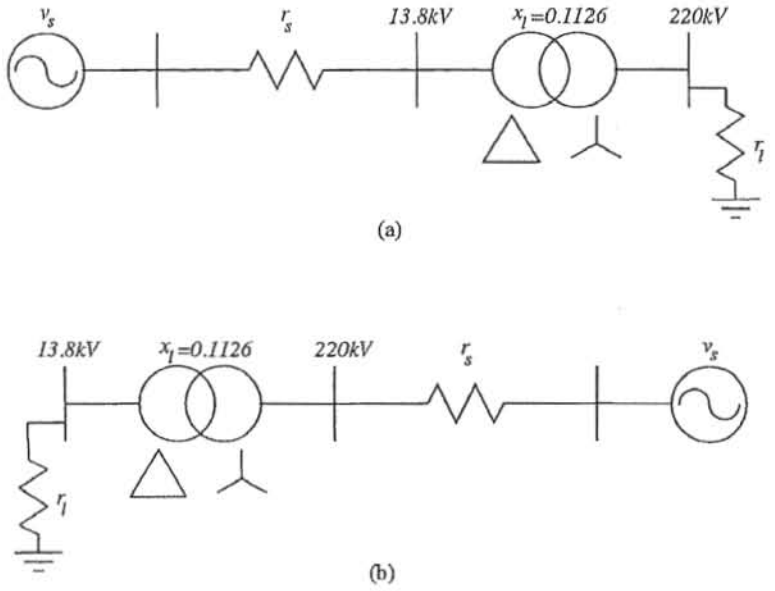

Figure 4.21 UMEC Manapouri three-limb three-phase transformer model test system: (a) open-circuit, (b) short-circuit.

core legs and yokes, individual winding flux leakage reactances are combined and the magnetising current is placed on one side of the resultant series leakage reactance. The core flux is calculated using the voltage of only one transformer winding. Laboratory and simulation results were used to show that this representation will produce inaccurate division of magnetising current between the transformer windings.

The dependence of core flux on a single transformer winding, the arbitrary placement of magnetising current, the uniform core flux assumption, and lumped leakage reactance approximations can be eliminated with the use of the UMEC. The single-phase UMEC model has been shown to be representative of the Steinmetz "exact" equivalent circuit. The simulated division of magnetising current between the UMEC transformer model windings was verified with the laboratory results.

A test system derived for the New Zealand HVdc converter station was used to

	$V_s^{linetolinerms}$ (kV)	r_s (Ω)	r_l (Ω)
No load ratio	13.8	0.00458	1.00e+7
No load	13.8	0.00458	1.00e7
Short-circuit	20.16	3.00e-3	3.00e-3

Table 4.12 Manapouri three-limb transformer test system electric parameters.

	Factory measurement	UMEC PSCAD-EMTDC simulation
No load ratio	9.218 $(\frac{V_2}{\sqrt{(3)}V_1})$	9.215
No load red-phase current	23.8 (A)	23.2 (A)
Short-circuit leakage reactance	11.3 (p.u.)	11.7 (p.u.)

Table 4.13 Simulation and factory data comparison.

compare the steady-state behaviour of the PSCAD-EMTDC and UMEC single-phase models. In this practical test system the PSCAD-EMTDC model led to significant errors in predicting the magnetising current distribution between transformer windings.

A model for the Benmore single-phase converter transformers has been presented and verified with name-plate specifications. The single-phase UMEC model was extended to represent three-limb three-phase transformers. A model for the Manapouri 105MVA, 13.8/220kV three-limb three-phase transformers was created and validated with factory test data.

Chapter 5

THE GROUP CONNECTION; MEASUREMENT AND SIMULATION

A recent CIGRE document published in ELECTRA has described the potential benefits of a direct connection of generators to HVdc converters [Arrillaga *et al.* 1993a]. While many theoretical contributions have been made, no practical test data has become available so far. This chapter reports on harmonic tests carried out at the Benmore end of the New Zealand HVdc link operating as a group connected scheme. The field data obtained provides an excellent bench-mark to further validate the UMEC transformer model.

5.1 DIRECT CONNECTED GENERATOR HVDC CONVERSION

The direct connection of generators to HVdc converters was first proposed a little over 20 years ago [Calverley *et al.* 1973]. It is envisaged that direct connection schemes could be strong contenders where generating stations exclusively feed HVDC converter terminals [CIGRE Joint Working Group 11/14-09 1993]. The main attraction is a great simplification of the sending end system, as illustrated in figure 5.1 where the intermediary filtered ac bus bar is removed. Feasibility studies have shown that the exclusion of generator transformers, ac filters and associated switchyards would reduce the station cost by about one third [Ingram 1988]. As well as the initial capital saving further savings accrue as the low number of components should reduce maintenance costs and improve reliability. The generators are completely independent and variable turbine speed operation is possible to maximize overall generation efficiency [Arrillaga *et al.* 1992],[Naidu and Mathur 1989]. Furthermore, generator self excitation, sub harmonic oscillations and transient overvoltage phenomena are eliminated.

It has been suggested [Arrillaga *et al.* 1991] that, while the unit connection can be designed to provide any specified nominal power, the absence of filters may limit the operational capability at larger currents levels and thus reduce the ability of the link to provide temporary power increases. In the absence of filters the generator must supply all the reactive power of the converter. Other disadvantages are that characteristic

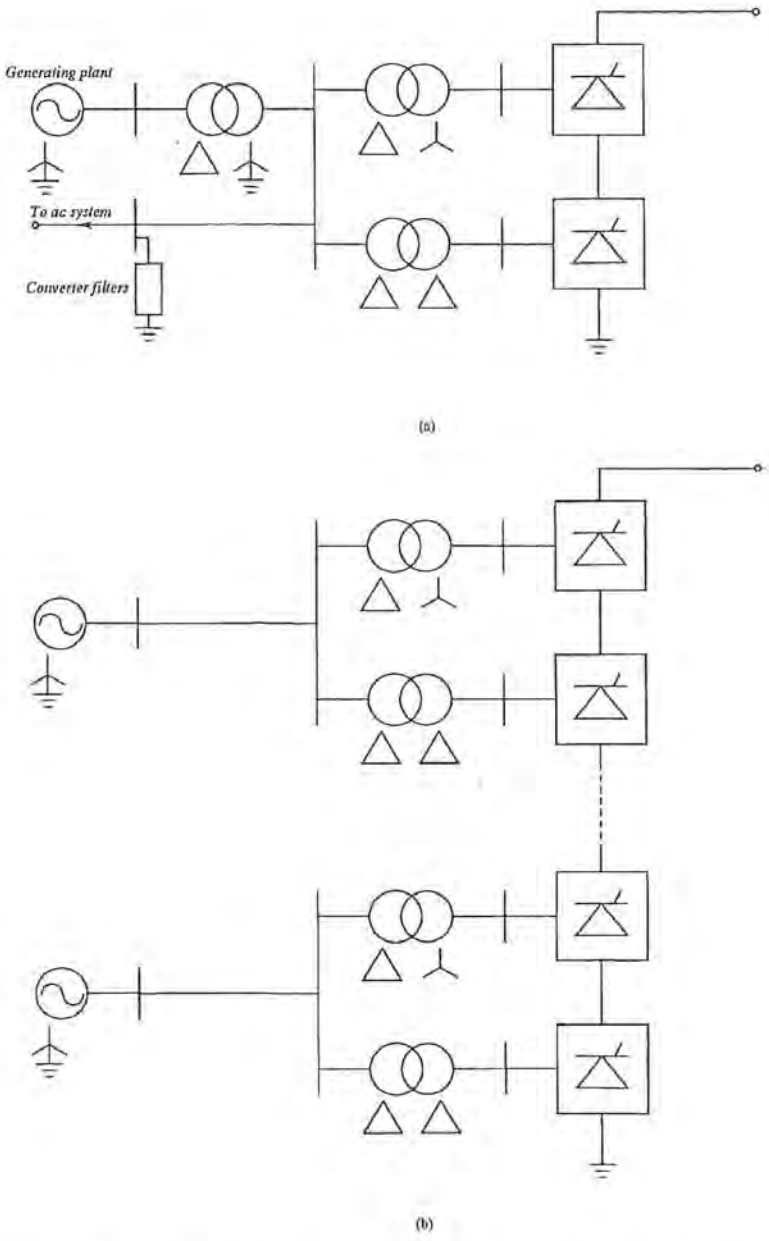

Figure 5.1 HVdc conversion: (a) conventional scheme, (b) unit connection.

harmonic currents flow in the generator stator windings causing additional losses and parasitic torques, and the harmonic voltages impressed upon the stator windings cause extra insulation stresses.

Issues relating to the design and rating of generators are becoming increasingly the focus of unit connection studies. Hence while the steady state capability, operational aspects and transient behaviour are well documented from a theoretical point of view, there is no practical information on the operation of such schemes and particularly the harmonic content and required ratings of the generator units involved.

This chapter reports on recent harmonic tests carried out at the Benmore end of the New Zealand HVdc link operating in the group connected mode. The field data obtained is used to show that the UMEC Norton equivalent representation is an ideal interface to realistic synchronous generator and valve group models. So far the UMEC transformer models have only been validated in test systems with linear idealised source and load representations.

5.2 GROUP VERSUS UNIT CONNECTION

One possible variation of the conventional unit connection concept is the group connection and there are important operational differences between these two schemes. In the unit connection each machine is directly connected to a 12 pulse converter, forming a unit, and the dc line voltage is raised by adding a number of these units in series. Reduced dc power levels may dictate the removal of generating units and this will reduce the dc line voltage and therefore the transmission efficiency. Moreover, the inverter end will then operate with larger value of γ, increasing the reactive power requirements [Arrillaga *et al.* 1993c].

In the group connection the generators are connected to a common bus and therefore the disconnection of generators does not affect the dc line voltage. The generators require some form of joint speed control and circuit breakers are also necessary to take machines in and out of service.

Regarding generator design there is practically no difference between the unit and group connections and, therefore, the group connected harmonic test results should also be applicable to unit connection schemes.

5.3 HARMONIC TESTS

The New Zealand HVdc link transmits surplus hydro-power from the South Island to major load centres in the North Island. The recently upgraded link consists of a parallel arrangement of two 12-pulse mercury-arc valve converters on pole 1 and a new thyristor-valve 12-pulse converter on pole 2. The older pole 1 mercury-arc valve equipment and the new thyristor pole 2 are rated for 270kV and 350kV respectively.

The nominal line current is 2kA and hence the overall maximum continuous power transfer is 1240MW from South to North.

5.3.1 The Benmore HVdc Terminal

Figure 5.2 extends the figure 4.17 test system to display the Benmore pole 1 terminal. When either of the interconnecting transformers, T2 or T5, are removed from service poles 1A or 1B can operate in group connected mode.

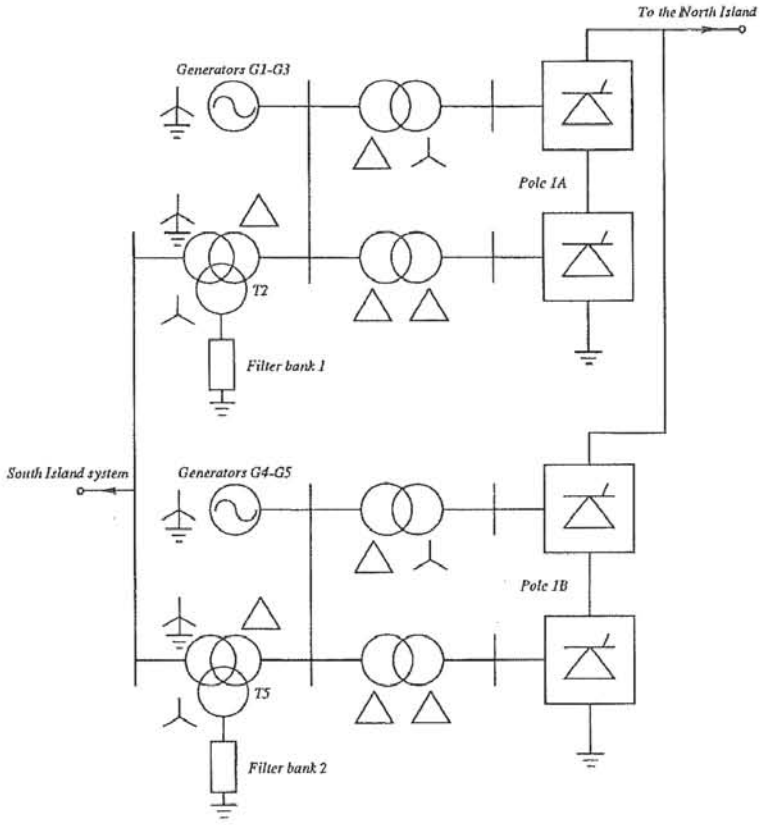

Figure 5.2 Pole 1 of the New Zealand HVdc link.

By arrangement with Trans Power New Zealand Ltd the system was available for harmonic tests in the group connection (i.e. with no filters and the ac system disconnected) during a recent period of maintenance for transformer T2. The maximum power transmitted under this condition was 212 MW (80 % of full power) with three generator units (G1-G3) connected on pole 1A.

5.3.2 Measurement Equipment

The harmonic measurements were made with a Hewlett Packard data aquisition unit HP-3565 (DAQ) which forms part of the Benmore instrumentation to capture system

transients. The usual DAQ traces are derived from filtered control system waveforms and are consequently of no use for harmonic studies.

In the group connection the voltage and current waveforms at the generator 16kV bus-bar are severely distorted. This bus-bar is the most effective point in the Benmore test system to compare simulated and measured waveforms. Three extra channels were installed to record the generator terminal voltage in one phase and the corresponding currents in each of the two transformers of the 12-pulse converter; these two currents were subsequently added to derive the total generator stator current.

It was assumed that the three phase waveforms were balanced. A thorough harmonic analysis would entail measuring the three phase generator voltage and current quantities; however this option was expensive in terms of technician cost and computer storage of all the sampled data. Other existing channels of interest were the dc voltage, the pole 1A dc current and the converter firing angle.

5.3.3 Experimental Procedure

The pole 1A mercury-arc valve converter was deblocked and a steady operating point of 350 Amps, 260kV at 15^o firing angle was achieved. Each waveform was sampled at 8192 samples per second for a 5 second interval. Further half-pole dc current increments were performed, and after allowing sometime for the system to stabilise, the waveforms were again sampled. In practice it was difficult to fix the frequency at 50Hz especially if the machines were lightly loaded. Small frequency deviations were experienced over the sampling period and consequently care was exercised when the spectra of the waveforms were computed. In future tests it is recommended to use a higher sampling rate and more accurate FFT processing taking into account the variation of the fundamental frequency during the test, such as provided by the CHART hardware [Miller 1992].

The dc current range varied from 350 to 785 amps. In all cases the uncharacteristic harmonic levels were insignificant. Moreover, the presence of dc side filters also made the dc voltage harmonics negligible. This chapter therefore discusses only the generator characteristic harmonic content.

5.4 GENERATOR RATING

The possibility of a direct connection was envisaged in the design of the Benmore generators although restrictions were imposed on the nominal power rating (lowered to 102.5 MVA) and the current harmonic content under such operating conditions. The ratings are listed in table 5.1 together with the actual maximum current harmonics monitored during the tests. Clearly none of the specified maximum limits were exceeded at the power levels involved. The maximum total harmonic distortion (THD) of the generator current was determined to be 5.4%.

Harmonic	rating (pu)	recorded (@212 MW)
11th	0.0744	0.0422
13th	0.0595	0.0267
23rd	0.0193	0.0067
25th	0.0154	0.0037

Table 5.1 Machine stator current harmonics.

If the dynamic simulation results are extrapolated in the high current region to the rated half–pole power of 270 MW, the rated harmonic currents are still not exceeded.

Conventional generators normally have extra thermal capacity to sustain 10% of negative sequence loading [Uhlman 1975]; however negative sequence is practically absent in the unit connected mode and the extra capacity compensates for the harmonic loading. This was verified for the Benmore generators after the original commissioning in the mid 1960's, when the rated machine power output (90MW) was confirmed for group connected 12-pulse operation.

5.5 GROUP CONNECTION SIMULATION AND FIELD DATA COMPARISON

The ability of dynamic simulation to predict the harmonic content of the group connection was assessed by comparison with the experimental results. Each converter transformer within the delta-delta and delta-star three-phase banks were represented with the new single-phase UMEC model. The simulation parameters of the UMEC transformer, synchronous generator, and converter models are given in appendix I. Simulations were run for sufficient time to reach the steady state. The resulting voltage and current waveforms were then processed, using the FFT, to derive their harmonic spectra.

Figures 5.3 and 5.4 display the machine current and voltage harmonic level comparisons. Overall the harmonic current levels are quite close to the test results, as they are less influenced by the generator operating conditions and more by the dc link firing and current control (which were fixed during the tests). The experimental and simulated voltage trends are consistent, their magnitude discrepancies being sensitive to uncertainties in the available generator parameters.

To give some perspective to the difference between the harmonic estimations, for a dc line current of 405A, figures 5.5(a) and (b) compare a single cycle of simulated generator current and voltage respectively with the measured data. Although there are differences in the plotted per-unit values of figures 5.3 and 5.4, the time domain waveforms seem to be in reasonable agreement.

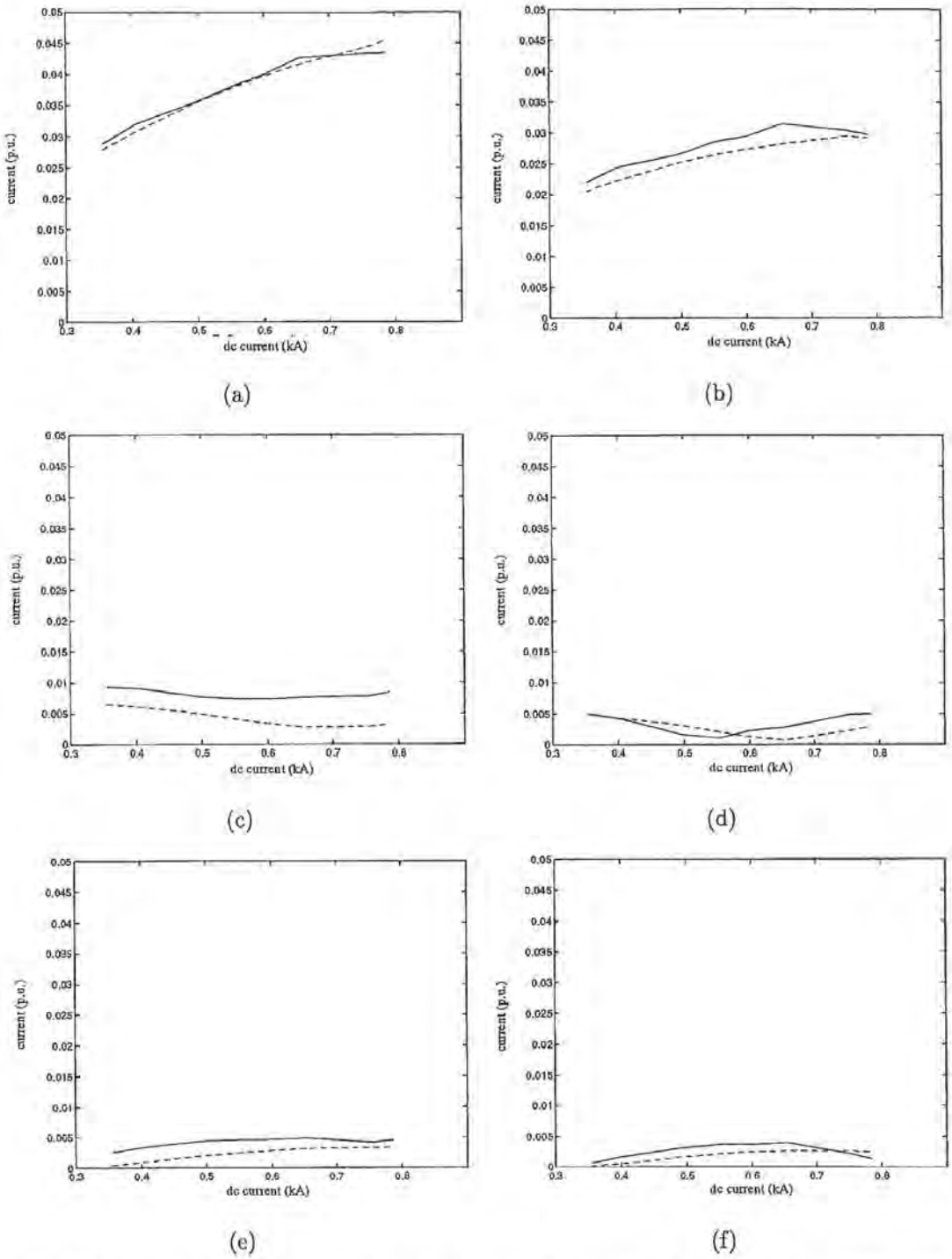

Figure 5.3 Harmonic comparison of recorded generator current with steady state and dynamic simulation; Solid=recorded data, Dash-dash=simulation: (a) 11th harmonic, (b) 13th harmonic, (c) 23rd harmonic, (d) 25th harmonic, (e) 35th harmonic, (f) 37th harmonic.

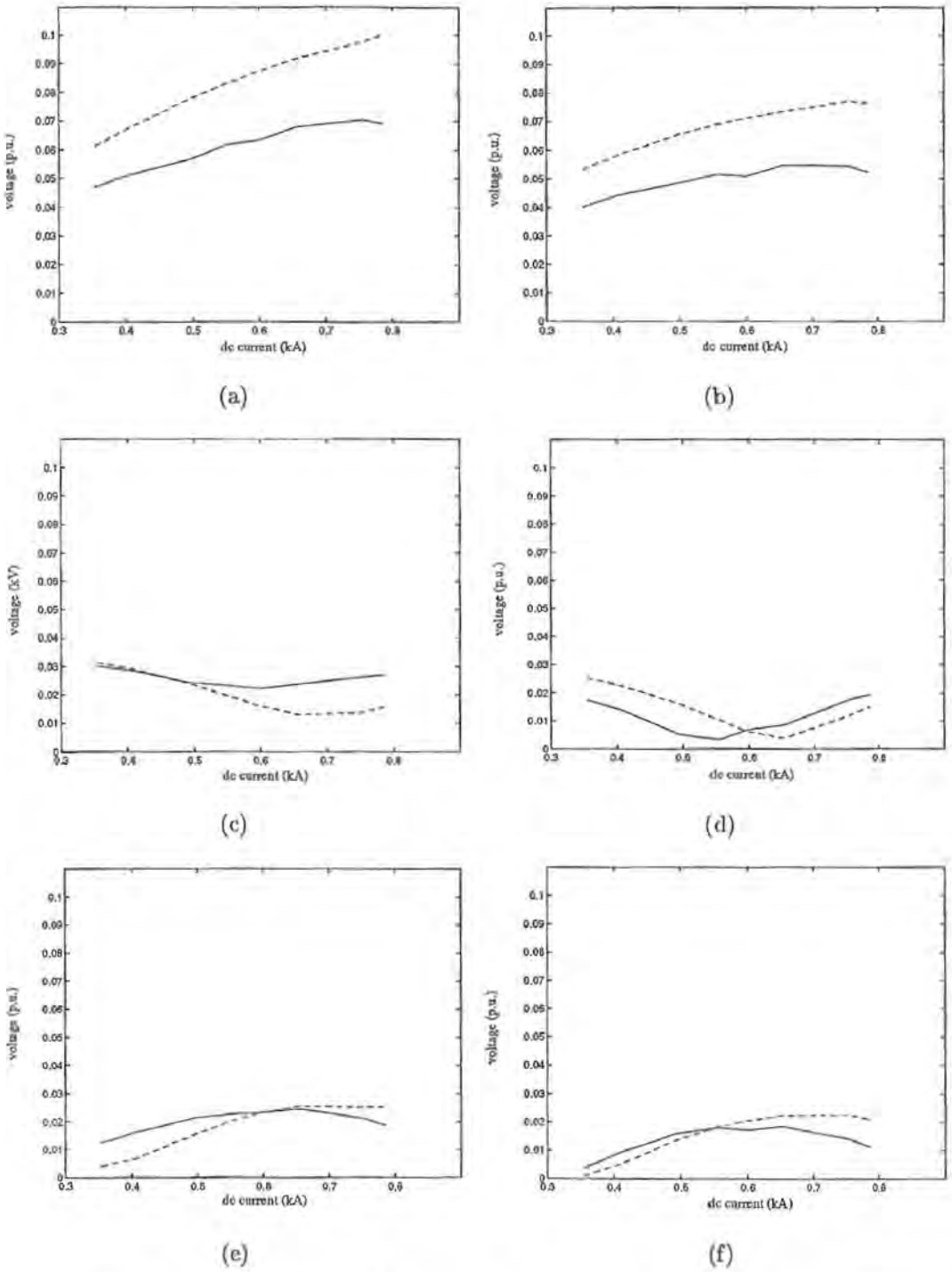

Figure 5.4 Harmonic comparison of recorded generator voltage with dynamic simulation; Solid=recorded data, Dash-dash=simulation: (a) 11th harmonic, (b) 13th harmonic, (c) 23rd harmonic, (d) 25th harmonic, (e) 35th harmonic, (f) 37th harmonic.

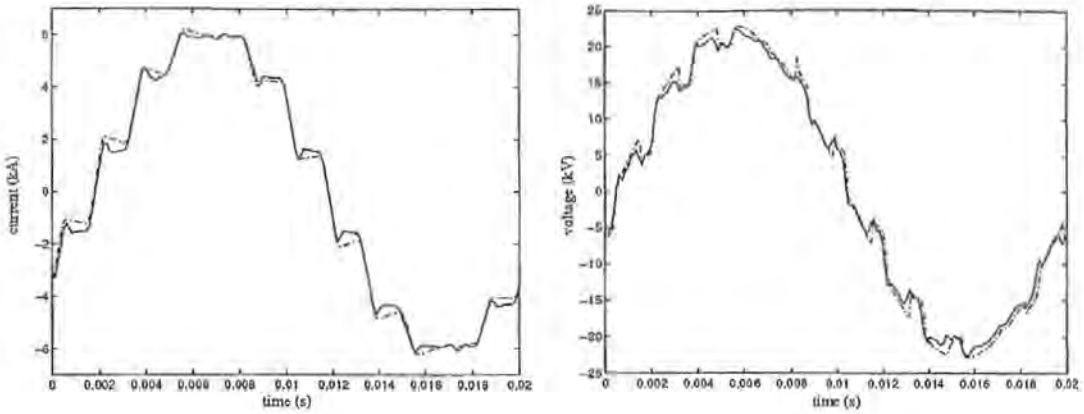

(a) (b)

Figure 5.5 Group connected generator waveforms (3 machines, Idc=405A); Solid=field measurement, Dash-dot=simulation: (a) current, (b) voltage.

5.6 CONCLUSIONS

The first set of harmonic measurements ever available of a direct connected generator HVdc converter scheme have been collected and discussed in this chapter. The harmonic current levels derived from the tests were all well below the specified maximum ratings of the generators and therefore the results provide the much needed evidence of the feasibility of the unit connection.

The test results were also used to investigate the performance of the UMEC transformer model when connected to the PSCAD-EMTDC synchronous machine and converter representations. Even in the highly distorted case of the group connection the simulated test system, inclusive of the UMEC transformer model, provides realistic generator busbar waveforms. The Norton equivalent representation correctly phase shifts and scales the non-sinusoidal converter ac currents to the transformer primary windings.

The experience gained with these tests will be extremely useful when the next opportunity to operate Benmore in group connection mode arises. In future tests it is recommended to use a higher sampling rate and more accurate FFT processing taking into account the variation of the fundamental frequency during the test.

Chapter 6

THE SMOOTHING TRANSFORMER

This chapter describes an alternative concept to conventional dc filters for reducing the voltage harmonic content on the dc side of an HVdc converter. The scheme uses a transformer instead of a smoothing reactor, but the connection is such that the conventional transformer model of the PSCAD-EMTDC program can not be used to simulate the schemes performance. Instead the UMEC model developed in chapter 4 had to be used to simulate the iron core saturation.

6.1 HVDC CONVERTER DC SIDE FILTERS

Unlike ac filters, which provide reactive power compensation to the converter, dc filters are used exclusively to reduce the dc line harmonic content. Therefore the design of dc side filters, although a complex exercise [Testi 1994], permits greater flexibility in the selection of filter components to try and minimise the cost of the converter plant.

Compacting the HVdc terminal has been investigated as a means for cost reductions [Asplund *et al.*]. The outdoor valve [Astrom *et al.*] has been suggested to significantly reduce the dimensions of the valve housing, and active dc filters are proposed to decrease the area needed for the dc switchyard.

The direct connection offers the advantages of compact HVdc as well as variable generator operating frequency. If the ac frequency supplying the converter is variable then the effectiveness of tuned dc side filters reduces. Recently it has been shown that the variation of harmonic voltages in the dc system will cause the conventional filters to function ineffectively [Pang and Tarnawecky 1995] and that active or on-line tuning filters are required.

Active dc filters have been considered as an alternative to the conventional passive component design [Cheuksun *et al.* 1989]. The active filter injects harmonic current back into the converter to "neutralise" the harmonic currents produced by the converter. Active filters are more complex than passive filters and they require accurate detection of harmonic voltage magnitude and phase, at the transmission line

terminals. Also, the current rating of the active harmonic source must be large enough to compensate the harmonics produced by the converter.

This chapter presents the smoothing transformer principle and describes initial feasibility investigations. The primary aim of the smoothing transformer is a reduction of the dc side harmonic content at nominal and off nominal ac system frequencies in a compact configuration.

6.2 THE SMOOTHING TRANSFORMER PRINCIPLE

The smoothing transformer operation is easily described with reference to the circuit of figure 6.1, using ideal components. During steady-state the dc side capacitor C is charged to V_{dc}. If C is infinitely large then all harmonic voltages V_h produced by the converter are developed across the primary winding of the smoothing transformer (the capacitor winding). If the transformer ratio is set to unity and the coils connected oriented as shown, then the harmonic voltages V_h are developed across the secondary winding of the smoothing transformer (the dc line side winding). The resulting voltage at the terminal of the smoothing transformer is the dc component of the rectifier terminal voltage V_{dc}.

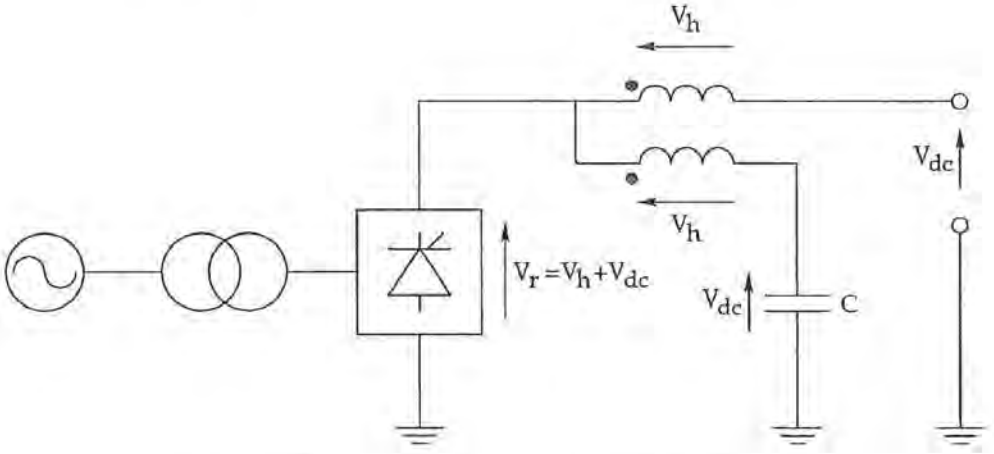

Figure 6.1 Ideal smoothing transformer operation.

If the smoothing transformer is ideal, with perfect coupling and no magnetising current, then no current will flow in the capacitor circuit and the Volt-Ampere rating of the primary winding and the capacitor is minimal. The converter harmonic voltages are cancelled out, rather than filtered from the transmission circuit. The ideal smoothing transformer will eliminate all dc side harmonics because, unlike conventional filters, it is not tuned to fixed frequencies.

6.3 SMOOTHING TRANSFORMER SATURATION

An unsaturated iron-cored smoothing transformer will exhibit the high level of coil coupling required for successful dc side harmonic voltage cancellation. However, the secondary winding of the smoothing transformer carries the full dc line current. Unless the transformer core cross-section is unrealistically large this current will force the iron core deep into saturation, and reduce the coil coupling severely.

The new UMEC transformer model is better suited than the PSCAD-EMTDC single-phase representation to determine the effects of smoothing transformer saturation. The magnetising component of the non-linear two-winding PSCAD-EMTDC transformer model must be injected across either the primary or secondary winding. However, in the case of the smoothing transformer, the magnetising current can not be injected across the capacitor winding because dc component present in the magnetising current will charge the dc blocking capacitor to an unrealistic voltage. The only remaining option is to inject the magnetising current across the dc line side winding. However, if the inverter and dc transmission line are represented by a constant dc current source (as was the case for the Benmore group connection validations) the ac components of the magnetising current can not flow in the dc line side winding. The use of the UMEC transformer model avoids these problems since the magnetising current will correctly distribute itself amongst the capacitor and dc line windings according to the system impedances at the transformer terminals.

The test system for the PSCAD-EMTDC solution consists of a three-phase ideal source directly connected to a six-pulse controlled converter feeding a purely resistive load. The non-linear UMEC transformer model (in the smoothing transformer configuration shown in figure 6.1) is connected between the converter and dc load. The source, converter, smoothing transformer and load parameters are given in appendix J.

The behaviour of a hypothetical linear iron-core smoothing transformer was first examined. Figure 6.2(a) displays the wall bushing, and dc line voltages for this test case. Without saturation, even when a dc current flows in the transformer winding, the coil coupling remains high and the smoothing transformer almost completely cancels the wall bushing voltage harmonics.

To asses the effect of saturation two extreme operating conditions were selected. In both examples the iron-core winding-limb saturation knee point resides at a flux level of 1.03 (p.u.). In the first case the converter firing angle is set to 15^o and the iron-core smoothing transformer is operated deep in saturation. Figures 6.2(b) and (c) present the dc harmonic voltage cancellation and winding-limb flux respectively. The voltage waveforms show that the smoothing transformer still significantly reduces the dc line harmonics, and the flux waveforms verify that this cancellation occurs entirely in the saturated region.

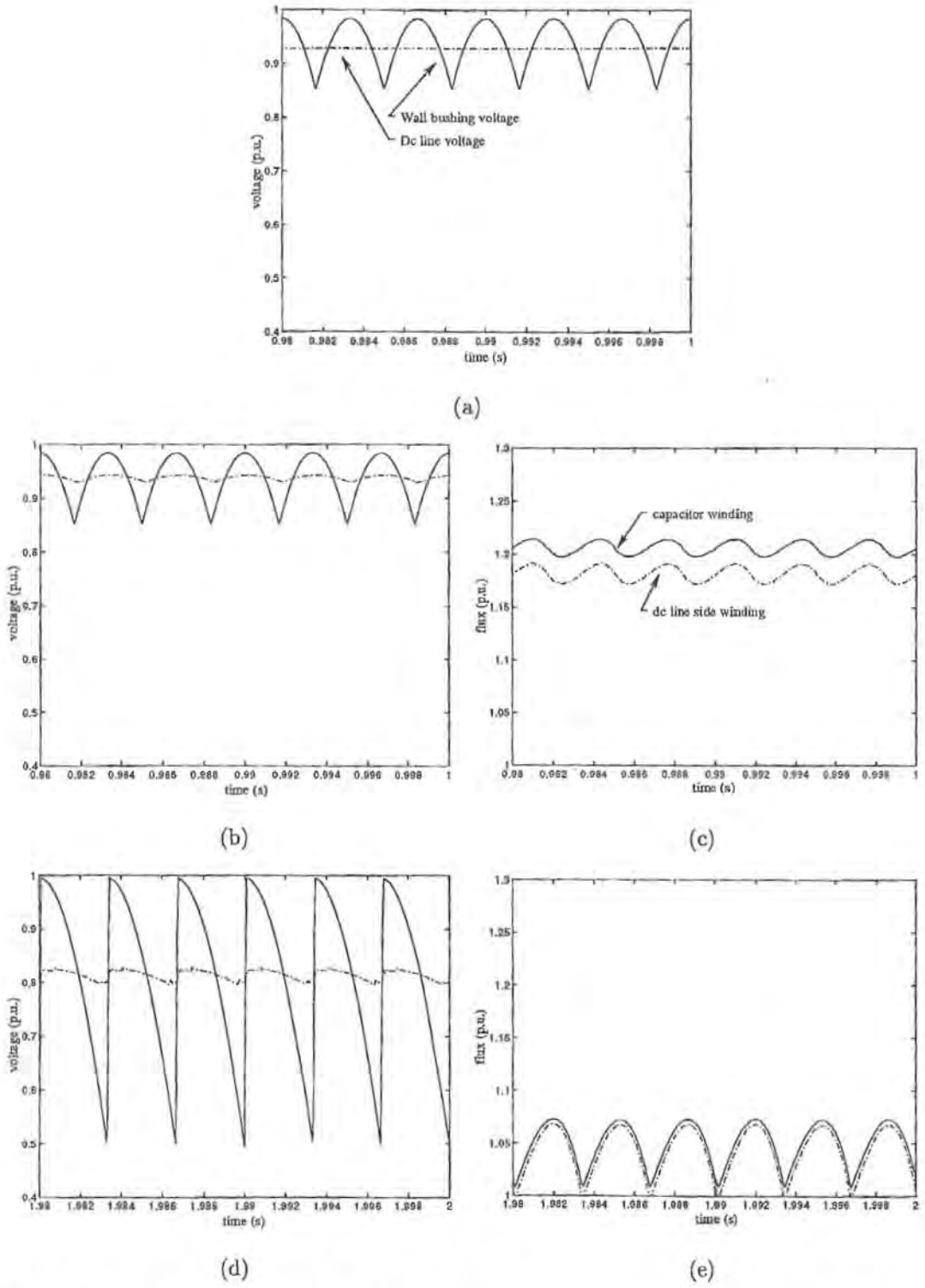

Figure 6.2 Iron-core smoothing transformer dc side harmonic voltage cancellation: (a) linear case, (b) and (c) non-linear case α=15°, (d) and (e) non-linear case α=60°.

Deep in saturation the smoothing transformer magnetising current is linearly proportional to winding voltage. Therefore, although a less likely operating condition, the second case investigates the level of cancellation for operation that traverses the saturation knee region. A 60^o converter firing angle was used to obtain a greater flux variation, and the dc current was lowered to 0.18 (p.u.) to bring operation below the knee region. Simulation time was lengthened to allow the dc side waveforms to stabilise under the lightly loaded conditions. Figures 6.2(d) and (e) display this operating condition. Again the smoothing transformer significantly reduced the wall bushing voltage harmonics.

The waveforms of figure 6.2 provide only a qualitative assessment of the performance of the smoothing transformer. They show that substantial voltage cancellation still occurs when saturation reduces coil coupling. Although the leakage paths separate the primary and secondary winding-limb flux by a significant dc component, the harmonic flux magnitudes are similar. Also, the primary and secondary winding voltages are similar even if the coil coupling reduces and the smoothing transformer experiences very little harmonic load.

If a saturated iron-core smoothing transformer provides reasonable voltage cancellation, an air-core design should also provide an effective solution. Since the air-core design is linear, the PSCAD-EMTDC mutually coupled coil representation is equally suitable as the UMEC model for linear smoothing transformer representation.

6.4 REALISTIC DESIGN CONSIDERATIONS

Figure 6.3 displays how the conventional air-core smoothing reactor may be modified with the addition of a low current primary winding to create the compact smoothing transformer.

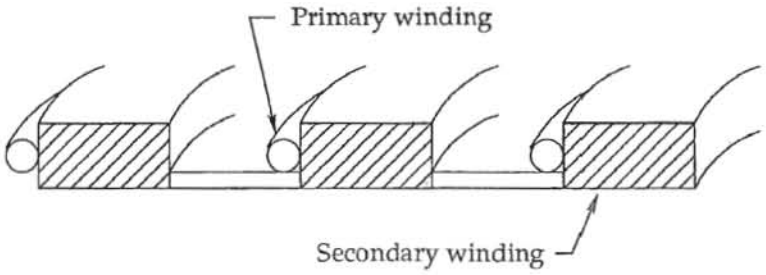

Figure 6.3 Impression of smoothing transformer section.

The viability of the smoothing transformer principle is dependent on its steady-state and transient performance using realistic components. Sizing the capacitor will affect performance. The capacitor is the most costly element of conventional dc side filters [Testi 1994] and is restricted in size. Even if the smoothing transformer capacitor can be designed to pass minimal harmonic current it is stressed by the total dc voltage

in the same manner as the conventional filter. In line with present HVdc filter designs the value of capacitance is limited to one micro-farad [Arrillaga 1983].

One coil of the smoothing transformer carries the full dc line current. As shown in the previous section this current would force a steel core transformer deep into saturation and may not provide suitable coil coupling for acceptable harmonic voltage cancellation. An air cored transformer will not saturate, but will offer poorer coil coupling. As the smoothing transformer essentially operates on no load, poorly coupled coils may be sufficient to provide harmonic voltage cancellation. For this example the self inductance of the coil carrying the dc line current is set to 0.16H, this is equal to the NZ HVdc Pole 2 smoothing reactor inductance.

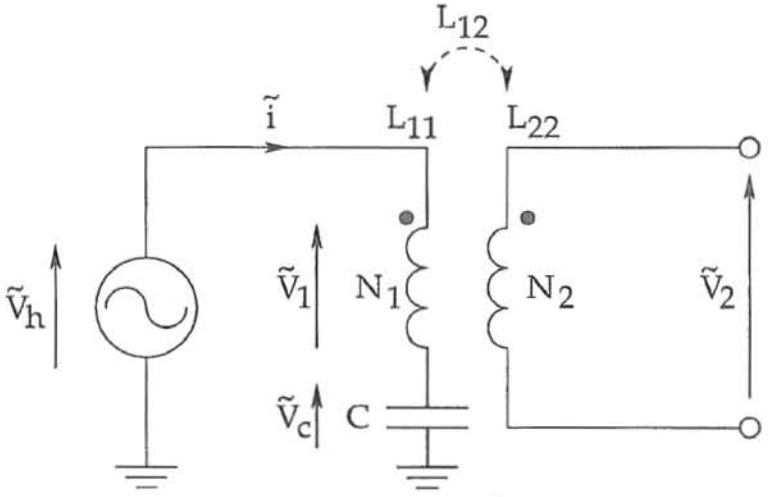

Figure 6.4 Harmonic voltage cancellation principle.

As the capacitor value is finite and restricted in size, the transformer ratio cannot be set to unity. The design for the capacitor winding is found from a steady-state analysis of the circuit of figure 6.4. The transformer secondary is open-circuit and applying Kirchoff's voltage law around the primary circuit gives

$$\tilde{V}_h = \tilde{i}j[\omega_h L_{11} - \frac{1}{\omega_h C}] \tag{6.1}$$

where ω_h is the angular frequency of the harmonic voltage source.

Under no load conditions, the transformer primary voltage is related to the secondary voltage by

$$\tilde{V}_1 = a\tilde{V}_2 \tag{6.2}$$

where a is the transformer turns ratio.

Rearranging equation 6.1 to solve for the capacitor circuit current and multiplying both sides by $j\omega_h L_{11}$ gives

$$\tilde{i}j\omega_h L_{11} = \frac{\tilde{V}_h j\omega_h L_{11}}{j\omega_h L_{11} - \frac{j}{\omega_h C}} \tag{6.3}$$

Utilizing $\tilde{V}_1 = \tilde{i}j\omega_h L_{11}$ and equation 6.2, equation 6.3 can be rewritten as

$$a\tilde{V}_2 = \frac{\tilde{V}_h j\omega_h L_{11}}{j\omega_h L_{11} - \frac{j}{\omega_h C}} \tag{6.4}$$

For harmonic voltage cancellation to occur

$$\tilde{V}_2 = \tilde{V}_h \tag{6.5}$$

Substitution of equation 6.5 into 6.4 gives

$$a\tilde{V}_h = \frac{\tilde{V}_h j\omega_h L_{11}}{j\omega_h L_{11} - \frac{j}{\omega_h C}} \tag{6.6}$$

The transformer turns ratio a can be defined in terms of primary and secondary self inductance.

$$a = \sqrt{\frac{L_{11}}{L_{22}}} \tag{6.7}$$

Substitution of equation 6.7 into equation 6.6 gives a quadratic equation in terms of the primary winding self inductance L_{11}

$$q = L_{11}^2 + [-L_{22} - \frac{2}{\omega_h^2 C}]L_{11} + \frac{1}{\omega_h^4 C^2} \tag{6.8}$$

where the two solutions of equation 6.8 (ie q=0 in figure 6.5) provide possible values for the self inductance of the smoothing transformer primary winding. With the self inductance of the secondary winding L_{22} set at 0.16H, the quadratic equation 6.8 is plotted in 6.5 for various capacitor values.

The two solutions for the quadratic equation 6.8 are given by

$$L_{11} = \frac{L_{22} + \frac{2}{\omega_h^2 C} \pm \sqrt{[L_{22} + \frac{2}{\omega_h^2 C}]^2 - \frac{4}{\omega_h^4 C^2}}}{2} \tag{6.9}$$

In the case of the positive root, $\frac{1}{\omega_h C} < \omega_h L_{11}$ and the current $\tilde{i}$ will lag the voltage $\tilde{V}_h$ by 90° (the inductive solution). The phasor diagram for this solution is shown in figure 6.6(a), L_{11} will always be greater than L_{22} and the transformer ratio a will be greater than unity. As $C \to 0$, it is simple to show that $L_{11} \to \infty$ and as $C \to \infty$, $L_{11} \to L_{22}$.

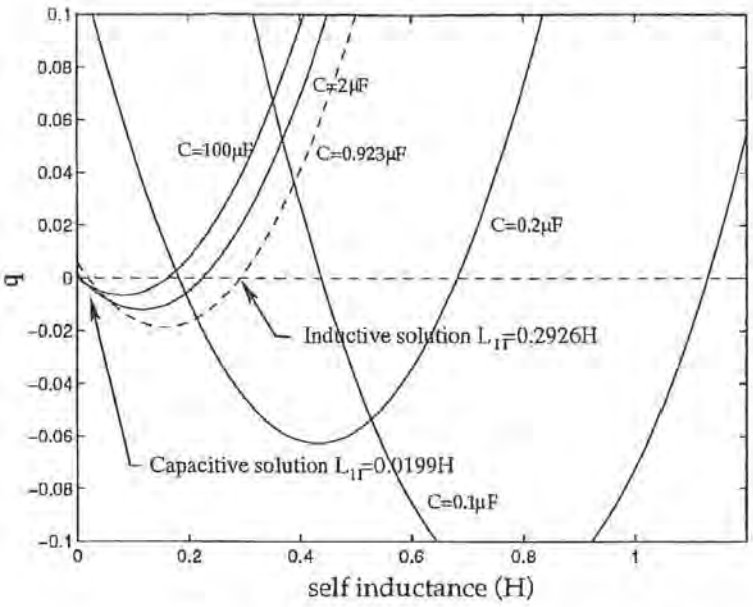

Figure 6.5 Primary winding self inductance; Dash-dash=NZ HVdc Pole 2 dc line filter capacitor.

In the case of the negative root, $\frac{1}{\omega_h C} > \omega_h L_{11}$ and the current $\tilde{i}$ will lead the voltage $\tilde{V}_h$ by 90° (the capacitive solution). The phasor diagram for this solution is shown in figure 6.6(b), as $C \to 0, L_{11} \to \infty$ and as $C \to \infty$, $L_{11} \to 0$.

Utilizing the parameters C=0.923μF, L_{22}=0.16H and ω_h set to the angular frequency of the NZ HVdc link 12th harmonic (50Hz=rated frequency), the inductive solution gives L_{11}=0.2926H $> L_{22}$, and a=1.35 > 1; the capacitive solution gives L_{11}=0.0199H $< L_{22}$, and a=0.353 < 1.

Once the capacitor and the self inductance of the secondary winding are selected, the choice remains between the capacitive or inductive solution. Both solutions provide total cancellation of a single harmonic voltage at angular frequency ω_h. Rearranging equation 6.4 gives

$$\frac{\tilde{V}_2}{\tilde{V}_h} = \frac{1}{a} \frac{j\omega_h L_{11}}{j\omega_h L_{11} - \frac{j}{\omega_h C}} \tag{6.10}$$

For harmonic voltage cancellation to occur the gain of equation 6.10 $|\frac{\tilde{V}_2}{\tilde{V}_h}|$ must be unity and the phase 0° or 180°, depending on the orientation of the secondary coil. The solutions of quadratic equation 6.8 guarantee the correct gain and phase for a single harmonic voltage at angular frequency ω_h. Consideration must be given to the smoothing transformer operation at other frequencies; reinforcement of characteristic converter voltage harmonics would be unacceptable. Figures 6.7(a) and 6.7(b) display the gain and phase plots for the inductive and capacitive designs using the NZ HVdc Pole 2 parameters. The angular frequency ω_h is set at the 12th harmonic.

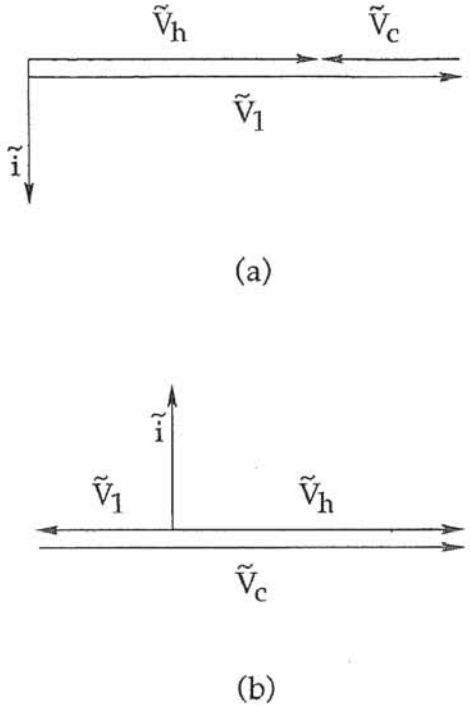

Figure 6.6 Inductive and capacitive harmonic cancellation solutions; (a) the positive root, (b) the negative root.

Although in both cases at the 12th harmonic the gain is unity and the phase either 0° or 180°, the characteristics are very different. In both solutions equation 6.10 shows that as $\omega_h \rightarrow \infty$ the gain approaches $\frac{1}{a}$. For the parameters used to create figure 6.7, $\frac{1}{a}$=0.74 and 2.83 for the inductive and capacitive solutions respectively. In this example, the capacitive solution is clearly not an acceptable design.

The gain of the inductive solution for harmonics above the 12th remains close to unity, and at worst becomes equal to the inverse of turns ratio, 0.74. This implies that a smoothing transformer with this design would remove 74-100% of the harmonic voltage content above the 12th.

Both cases exhibit a resonance point. In the inductive solution resonance occurs at a non-characteristic frequency just above the sixth harmonic (300Hz). The angular resonant frequency is calculated from

$$\omega_R = \frac{1}{\sqrt{L_{11}C}} \tag{6.11}$$

Combining equation 6.9 with 6.11 shows that as $C \rightarrow 0$ the resonant frequency $\omega_R \rightarrow \omega_h$. Figure 6.8 displays the variation in inductive solution resonant frequency with different values of capacitance.

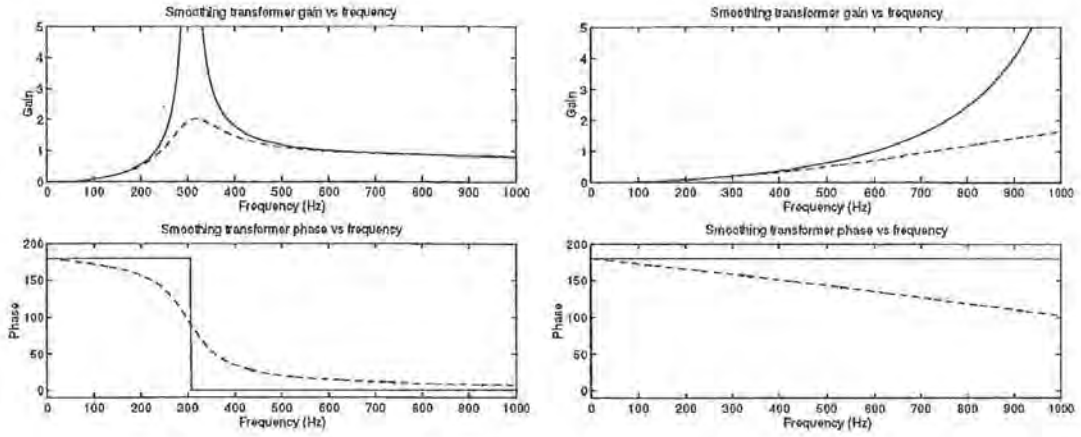

Figure 6.7 Smoothing transformer gain and phase; (a) Inductive solution, (b) Capacitive solution.

The resonant frequency can be altered with small variations in dc blocking capacitance. If the resonant point of the smoothing transformer excites a non-characteristic harmonic to an unsatisfactory level a series resistance R_s can be added to the primary circuit to alter the gain of the smoothing transformer. Equation 6.10 is then replaced by

$$\frac{\tilde{V}_2}{\tilde{V}_h} = \frac{1}{a} \frac{j\omega_h L_{11}}{j\omega_h L_{11} - \frac{j}{\omega_h C} + R_s} \tag{6.12}$$

The gain and phase plots for the smoothing transformer with $R_s = 210\Omega$ are shown by the dash-dash line of figure 6.7. This gain reduction ensures that harmonic reinforcement will not occur, but the harmonic voltages on the secondary side of the smoothing transformer are phase shifted and harmonic cancellation at frequencies of interest is less effective.

6.4.1 Test system

Resonance and coil coupling effects are best quantified with simulation of a smoothing transformer in a realistic HVdc test system. The chapter 5 field data verified PSCAD-EMTDC model for group connected operation of the New Zealand HVdc link has been selected for analysis of the smoothing transformer principle; all example solutions presented above are relevant to NZ HVdc link parameters and the group connection offers variable frequency operation. The dc filters operating on Pole 1A and Pole 2 are identical. The Pole 1A smoothing reactor is of the old iron-cored type and the Pole 2 reactor the newer air-cored design. This feasibility study aims to include the latest component designs and for this reason the Pole 2 smoothing reactor has been included in the Pole 1A test system. The section 5.5 synchronous generator and converter model parameters are re-applied, the PSCAD-EMTDC converter-transformer

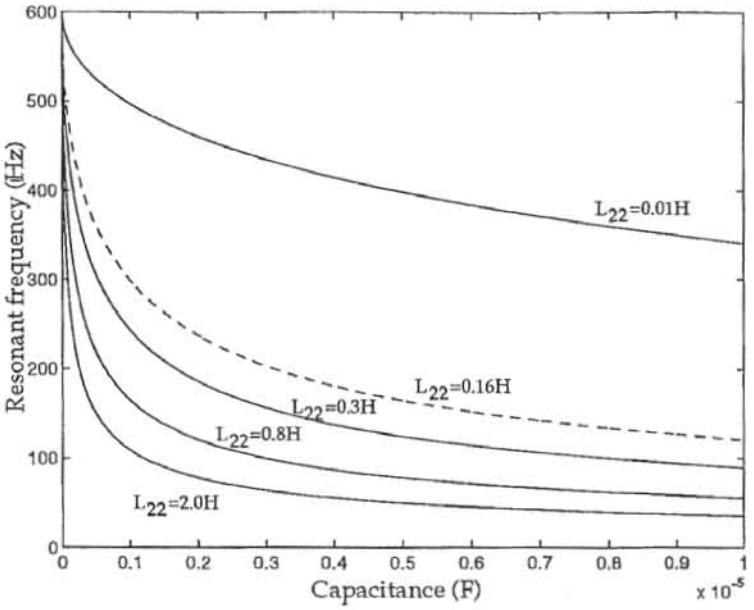

Figure 6.8 Resonant frequency variation; Dash-dash=L_{22} equal to the NZ HVdc Pole 2 smoothing reactor inductance.

and transmission line parameters are given in appendix K.

The smoothing transformer design selected in the previous section is used with the test system, that is L_{11}=0.2926H, L_{22}=0.16H and C=0.923 μF. The ideal coupling factor (k=1.0) used for best harmonic cancellation is unrealistic for a transformer with an air core. The coupling factor selected at k=0.96 uses as a basis an air cored laboratory transformer that was tested to exhibit a coupling factor of this order.

6.4.2 Steady-state performance

The Benmore test system was run to steady-state at full Pole 1A dc line voltage (270kV) and current (1000A) using PSCAD-EMTDC. Harmonic voltages were calculated at the rectifier wall bushing and at the start of the dc transmission line for two cases. Case A contains the Benmore smoothing reactor and the dc side filters (the design for the Benmore Pole 1A dc line filters are given in appendix K). Case B utilizes the smoothing transformer design selected above with the coil coupling factor k=0.96. Table 6.1 presents the conventional filter and smoothing transformer performance for Cases A and B at 35Hz, 50Hz (rated frequency) and 55Hz generator frequency. The performance measure for each harmonic is given by

$$\%\ harmonic\ reduction\ =\ 100(1-\frac{V_{dcl}}{V_{wbv}}) \tag{6.13}$$

where

V_{dcl} = The harmonic voltage present at the start of the dc transmission line

V_{wbv} = The harmonic voltage present at the converter wall bushing

	35Hz		50Hz		55Hz	
	Case A (%)	Case B (%)	Case A (%)	Case B (%)	Case A (%)	Case B (%)
V_{12}	-55	43	97	97	85	92
V_{24}	83	78	95	75	93	73
V_{36}	95	76	93	79	87	73

Table 6.1 Harmonic reduction at variable frequency.

The smoothing transformer has reduced the characteristic voltage harmonics produced at the rectifier wall bushing. At the 12th harmonic for 35Hz operation (420Hz) the smoothing transformer cancellation falls to 43%. This operating condition is near the primary circuit resonance point (306Hz) and in this example primary circuit resistance R_s has not been implemented to control the smoothing transformer gain. In comparison at this operating point the conventional filter results in a 155% reinforcement due to its own resonance between the smoothing reactor and dc blocking capacitor.

Over all operating frequencies examined the performance of the smoothing transformer is either equal or superior at the 12th harmonic and slightly poorer at the 24th and 36th as compared with the conventional filter. However the 12th harmonic is by far the dominant dc side component of HVdc converters at all generator operating frequencies.

As postulated previously, the harmonic current ratings of the smoothing transformer components can be less than that of the conventional filter. Table 6.2 presents the rms current flowing in the conventional filter and smoothing transformer primary circuit for the variable frequency operation.

	Conventional filter current (A_{rms})	Smoothing transformer primary current (A_{rms})
35 (Hz)	12.21	10.05
50 (Hz)	9.05	8.73
55 (Hz)	10.30	9.71

Table 6.2 Conventional filter and smoothing transformer harmonic current.

6.4.3 Transient performance

The inclusion of the smoothing transformer on the dc side of a converter must not impair the transient performance of the HVdc link. A dc line-to-ground fault and restart has been selected to examine this performance. Dc faults occur due to broken or contaminated insulators, icing insulators, failure of cables and flashover due to lightning strike and internal over voltages [Hingorani 1961].

The fault is applied at the dc line side of the smoothing reactor or smoothing transformer of the NZ HVdc model. This scenario provides the worst case disturbance, the highest level of fault current in the rectifier terminal [Peterson *et al.* 1969]. The resulting fault current is larger than an ac line fault or an internal converter fault [Ando *et al.* 1985].

The time to extinguish this fault and restart the link is dependent upon the energy stored in the conventional smoothing reactor [Turner 1980] or smoothing transformer. The dc line to ground fault is initiated at time 3.0s. The fault resistance affects the fault current decay and damping. A zero impedance fault is unrealistic. Although an accurate fault representation must include the tower footing resistance (typically 20Ω [Hingorani 1970]) and complex arc resistance, for this comparison a fault resistance of 50Ω has been selected [Heffernan *et al.* 1981].

Utilizing a similar fault detection delay to that of [Heffernan *et al.* 1981] the fault control begins at 3.02s, one cycle after the fault initiation. In typical control action [Arrillaga *et al.* 1993b] the rectifier firing angle is advanced to 120° and the inverter left on constant current control, with a 100° limit to the firing angle advance.

At time 3.5s a restart is ordered to the rated prefault conditions. Figures 6.9 and 6.10 display the simulated rectifier end dc line voltage and current respectively.

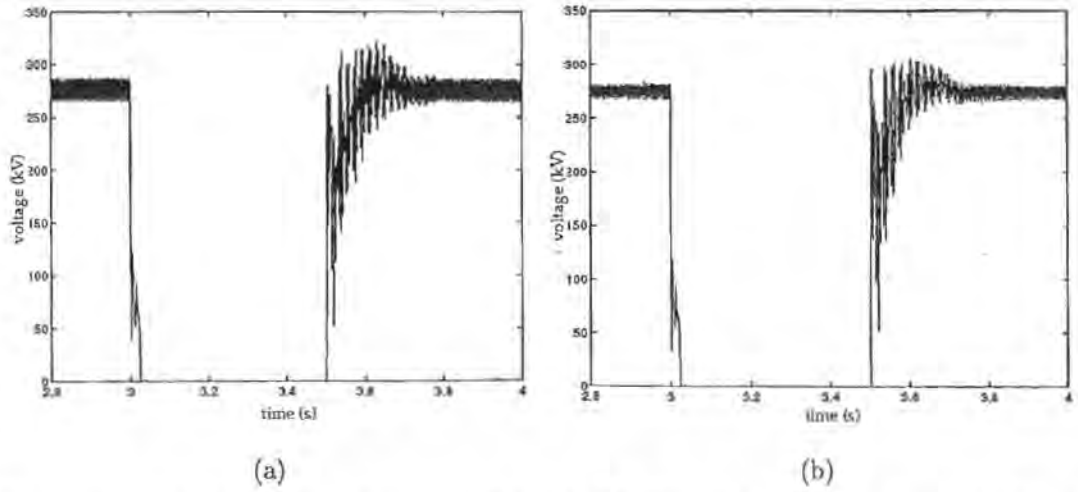

Figure 6.9 Fault initiation and recovery, Pole 1A, NZ HVdc link DC line voltage; (a) Case A, conventional system, (b) Case B, smoothing transformer (k=0.96).

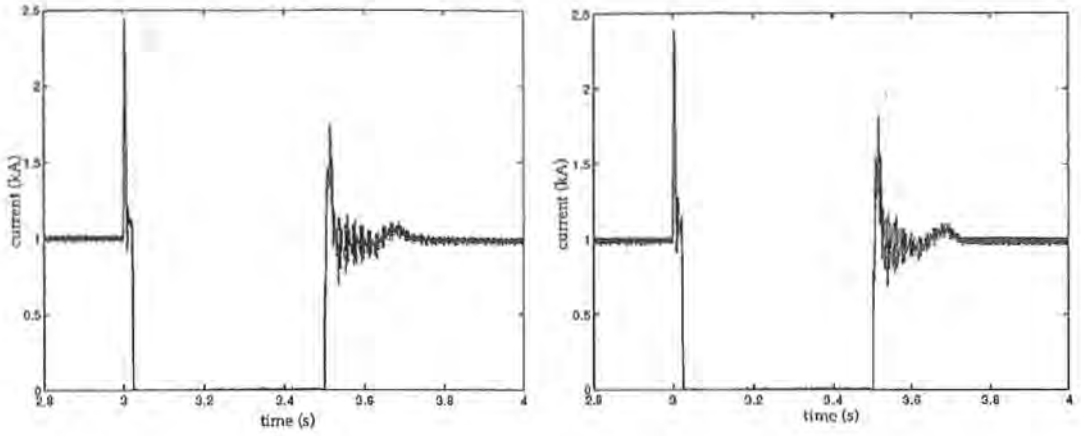

(a) (b)

Figure 6.10 Fault initiation and recovery, Pole 1A, NZ HVdc link DC line current; (a) Case A, conventional system, (b) Case B, smoothing transformer (k=0.96).

The replacement of the smoothing reactor and conventional dc filters with the smoothing transformer does not degrade the transient performance of the dc link under a dc line-to-ground fault. In each simulation peak fault currents and decay times are almost identical. The link restart to rated conditions is not slowed by the presence of the smoothing transformer. Moreover the smoothing transformer does not induce overvoltages or oscillations that are dissimilar from the conventional system at the converter wall bushing or on the dc line.

6.5 CONCLUSIONS

The UMEC transformer model has been used in a preliminary investigation of a new design concept, the smoothing transformer, as a means to reduce cost and increase the operational flexibility of an HVdc terminal. In this design the smoothing reactor and conventional filters are replaced by a single smoothing transformer and dc blocking capacitor. Unlike the conventional filters, the smoothing transformer achieves substantial harmonic cancellation at off nominal fundamental frequencies, an essential requirement in the direct connected schemes with adjustable speed. The UMEC representation was required to asses the feasibility of an iron-core smoothing transformer because the conventional non-linear PSCAD-EMTDC transformer model could not be applied to such an investigation. Investigations show that even smoothing transformer operation entirely in the core saturated region provides acceptable dc side harmonic reduction. The iron-core can therefore be removed and a linear air-core smoothing transformer design postulated.

Steady-state simulation studies using the NZ HVdc group connected test system have shown satisfactory performance of the air-core smoothing transformer. These

studies also indicate that the current harmonic ratings of the smoothing transformer dc blocking capacitor are less than those of the capacitor of a conventional filter.

The transient response of the dc link to a dc short-circuit, both in terms of peak fault current and recovery voltage, have been shown to be practically the same as those of a conventional scheme.

Chapter 7

HVDC CONVERTER TRANSFORMER COMPARISONS

Unlike transmission lines, where the interphase mutual coupling is often incorporated in fault studies, the strong mutual coupling between three-limb transformer phases has been largely neglected. The literature reports on the effect of such coupling in relation to the overvoltages present on disconnected phases when three-limb transformers are energised by asynchronous circuit-breaker closing [Smith *et al.* 1975] [German and Davies 1981] [Dijk 1986] [Lin *et al.* 1995].

In HVdc transmission studies, transformers are normally represented with magnetically independent single-phase units. However the response of a three-phase converter transformer bank to a single phase to ground fault is expected to be different to that of the three-limb three-phase transformer. A single phase to ground fault is used in this chapter to compare the transient behaviour of HVdc converter transformers.

7.1 A THREE-LIMB CONVERTER TRANSFORMER

To demonstrate the importance of incorporating core construction details in PSCAD-EMTDC transformer models, the proposed UMEC representation is used to compare the behaviour of equivalent three-phase bank and three-limb three-phase converter transformers. For a fair comparison, it is important that the transformer types draw similar magnetising currents in the steady-state. Unfortunately, it is difficult to achieve a perfect match, because three-limb transformers require less core steel and each phase is energised in an unbalanced manner.

The parameters of an equivalent Benmore three-limb UMEC transformer model have been selected to achieve steady-state magnetising currents very close to those of the single-phase model described in section 4.3.3.

Initially the windings are assumed connected in star-grounded/star-grounded configuration. Primary and secondary winding turns number are set to limit the maximum core flux density to 1.4T, at rated voltage. The hyperbola constants for the three-limb transformer core B-H characteristics are as given in table 4.3.

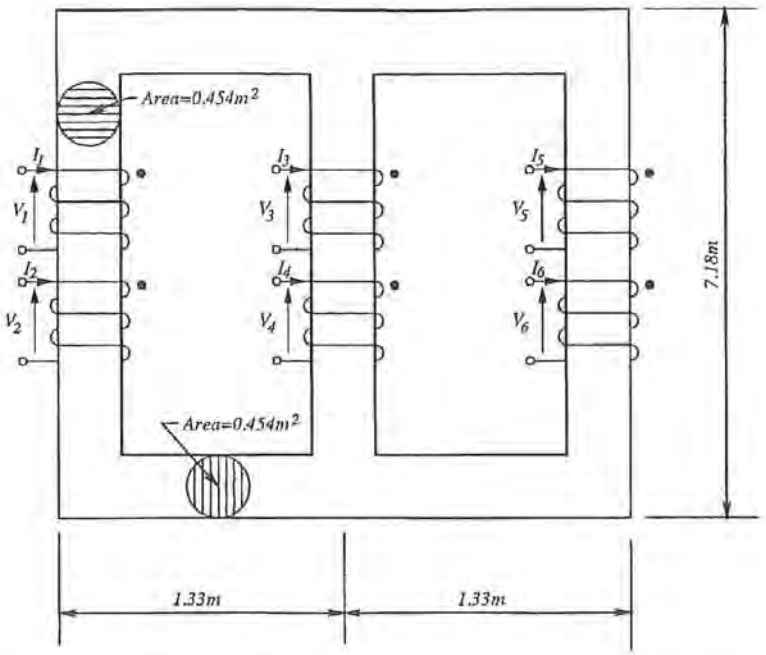

Figure 7.1 Benmore three-limb converter transformer core dimensions.

Figure 7.1 displays the three-limb UMEC model core dimensions[1] and table 7.1 gives the UMEC parameters. The primary and secondary winding leakage permeances are set equal to those of the Benmore single-phase units. In a similar manner to the Manapouri three-limb UMEC models (chapter 4), the permeances of the zero-sequence paths are set equal to the leakage path permeances.

Electric circuit parameters		Magnetic circuit parameters	
Rating	187.5 MVA	$A_{winding\ limb}$	0.454 (m^2)
Configuration	star-star	$L_{winding\ limb}$	3.59 (m)
Frequency	50 (Hz)	A_{yoke}	0.454 (m^2)
$V_{primary}$	$\frac{16}{\sqrt{3}}$ (kV)	L_{yoke}	2.66 (m)
$V_{secondary}$	$\frac{110}{\sqrt{3}}$ (kV)	$N_{primary}$	65 $(turns)$
$X_{leakage}$	0.113 (p.u.)	$N_{secondary}$	450 $(turns)$
		$\mathcal{P}_{7,9,11}$	5.85e-8
		$\mathcal{P}_{8,10,12}$	5.85e-8
		$\mathcal{P}_{15,16,17}$	5.85e-8

Table 7.1 Benmore three-limb UMEC transformer model parameters.

7.1.1 Steady-state performance

A three-limb three-phase UMEC transformer model was created from the table 7.1 parameters. To verify the close similarity of the three-phase bank and three-limb

[1]The three-limb core is twice as high as the single-phase core of figure 4.10. Although such construction is unrealistic, it must be applied in this example for a close magnetising current match.

three-phase UMEC models under steady-state operating conditions the two alternative constructions were subjected to open-circuit, short-circuit and over-voltage comparisons. The test system is shown in figure 7.2 and the circuit parameters are listed in table 7.2 for the three test cases.[2]

	$V_s^{line\ to\ ground\ rms}$ (kV)	r_s (Ω)	r_l (Ω)
Open-circuit	$\frac{16}{\sqrt{3}}$	0.107	1.00e+6
Short-circuit	$\frac{1.6}{\sqrt{3}}$	8.00e-3	7.50e-3
Over-voltage	$\frac{16*1.1}{\sqrt{3}}$	0.107	1.00e+6

Table 7.2 Benmore three-limb transformer test system electric parameters.

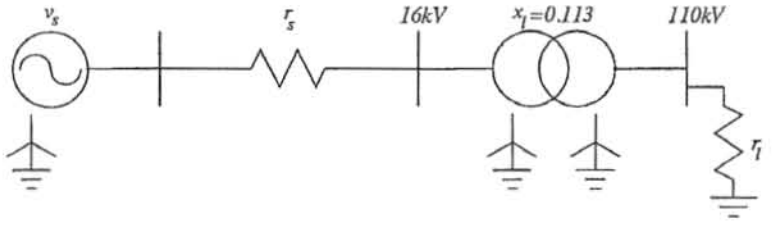

Figure 7.2 Benmore HVdc converter transformer steady-state test system.

Figures 7.3(a) and (b) display the three-limb UMEC open-circuit magnetising current and primary winding-limb flux waveforms respectively. As expected the magnetising current of the yellow-phase in the three-limb core is lower than those of the red and blue phases. The red, yellow and blue currents reach rms magnitudes of 0.043kA, 0.037kA and 0.043kA respectively; these currents are close to the matched red, yellow and blue three-phase bank magnetising currents of 0.047kA. The three-phase magnetising currents and winding-limb flux waveforms are in phase, and correctly lag the winding voltage by 90^o.[3]

The short-circuit three-phase primary winding voltage and current waveforms are shown in figure 7.3(c) and (d) respectively. The three-limb transformer red, yellow, and blue-phase leakage reactances equate to 0.153Ω, 0.156Ω, and 0.153Ω respectively. The short-circuit results compare favourably with the single-phase leakage reactance of 0.156Ω. The three-phase short-circuit currents all correctly lag the winding voltages by 90^o.

The three-limb short-circuit reactances are slightly unbalanced. The yellow-phase is slightly greater than the equal red and blue-phases. Such a result supports the section 4.2.1 conclusion (although explicit formula were only derived for the single-phase linear case) that short-circuit inductances are dependent upon core as well as

[2]For the single-phase UMEC tests only the over-voltage scenario required simulation; the open-circuit and short-circuit simulations were performed in section 4.3.3

[3]In all three scenarios the reference red phase to ground voltage positive going zero crossing occurs at time 0.08secs.

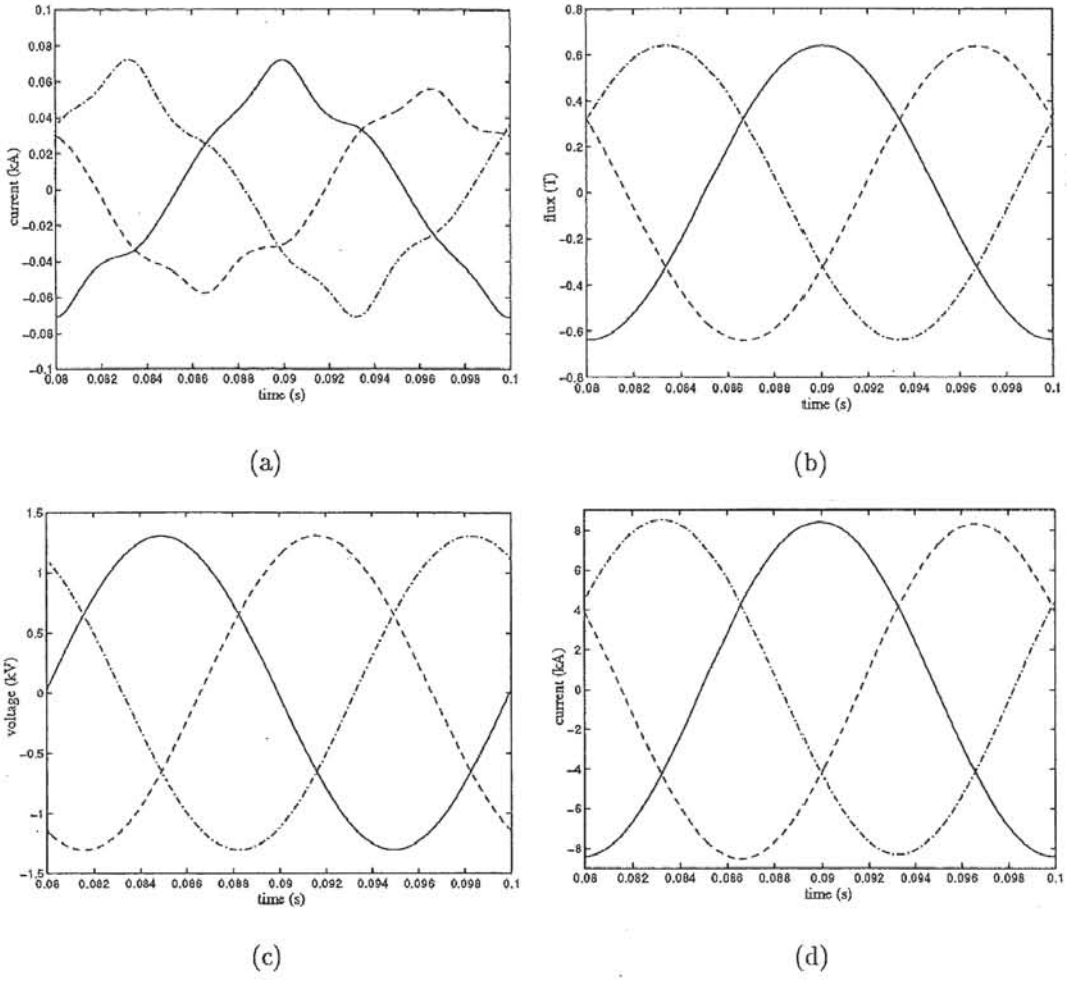

Figure 7.3 Benmore three-limb three-phase transformer steady-state tests; Solid=red-phase, Dash-dash=yellow-phase, Dash-dot=blue-phase: (a) open-circuit, primary winding current, (b) open-circuit, primary winding-limb flux, (c) short-circuit primary winding voltage, (d) short-circuit, primary winding current.

flux leakage paths.

The over-voltage test results for both the three-limb and three-phase bank UMEC models are shown in figures 7.4(a) and (b) respectively. The three-limb red, yellow and blue magnetising currents are 0.078kA, 0.067kA and 0.078kA respectively as compared with 0.086kA for the three phases of the independent transformer banks. This is considered sufficiently close for such excursion into saturation.

7.1.2 Transient comparison

The waveforms produced by the three-phase bank and three-limb three-phase transformer models in the previous section are similar under open-circuit and short-circuit operating conditions. Such similarity, however, is not sufficient to justify the common practice of ignoring the complexities involved in modelling the three-limb core. This

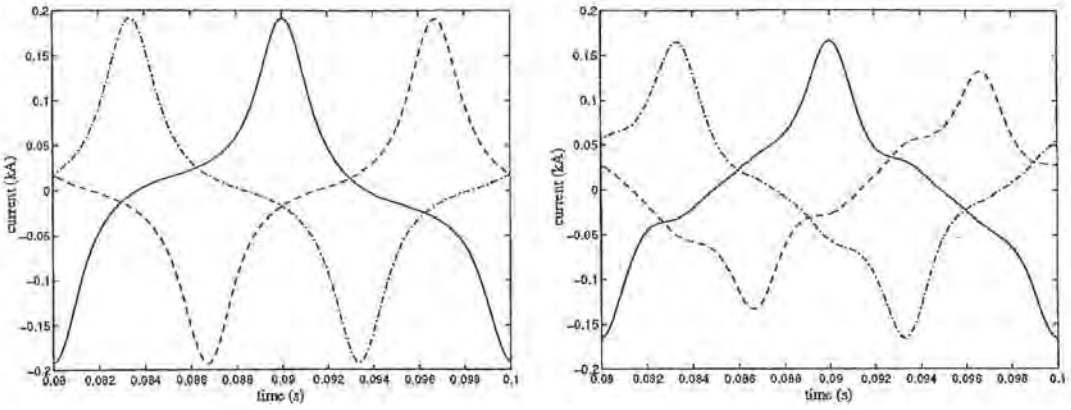

(a) (b)

Figure 7.4 Benmore steady-state over-voltage transformer energisation; Solid=red-phase, Dash-dash=yellow-phase, Dash-dot=blue-phase: (a) three-phase bank primary winding current, (b) three-limb three-phase primary winding current.

section shows the errors that such an assumption can cause.

The fictitious system of figure 7.5 has been selected to highlight the differences between three-phase bank and three-limb converter transformers during transient conditions. It consists of a synchronous generator, represented as an ideal source of impedance equal to the machine subtransient reactance x'' [Arrillaga and Arnold 1990] and armature resistance r_a. The generator parameters are given in appendix G. The star-grounded/star-grounded (Yy0) converter transformer configuration has been selected. The use of a delta winding connection would complicate presentation of the three-limb core interphase magnetic coupling effects during unbalanced operating conditions. The six-pulse mercury-arc valve converter parameters are as given in appendix I.

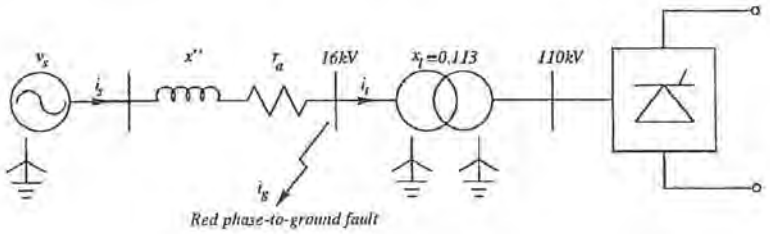

Figure 7.5 HVdc converter transformer transient test system.

A single-phase fault-to-ground is applied to the test system 16kV red-phase bus-bar at a negative going zero-crossing of the primary winding red-phase voltage (time=0.83secs). The 0.01Ω purely resistive fault is removed (reset to 1.00MΩ) after three-cycles, at the next occurring fault current zero-crossing.

A generator circuit-breaker has not been included; this is common practice with ac connected generator-transformer units where circuit-breakers are only present at

the high voltage transformer terminals. In the latter case, opening of the high voltage circuit-breaker during a fault on the generator bus-bar will give operating conditions similar to that presented in figure 7.5 (once the converter has blocked).

At the onset of the fault the dc line current is ramped down to zero in one quarter of a cycle [Joosten *et al.* 1990]. In order to highlight the behaviour of each transformer type the converter is not restarted after the fault is cleared.

The generator currents for the three-phase bank and three-limb converter transformer test cases are shown in figures 7.6(a) and (b) respectively. Although the peak magnitude of red-phase generator current (82.7 kA) is identical for both converter transformer types, in the three-limb example the generator feeds yellow and blue fault currents as well. In both cases the generator red-phase supplies the fault through the mainly inductive generator internal impedance; the generator red-phase current lags the internal emf by 90^o.[4]

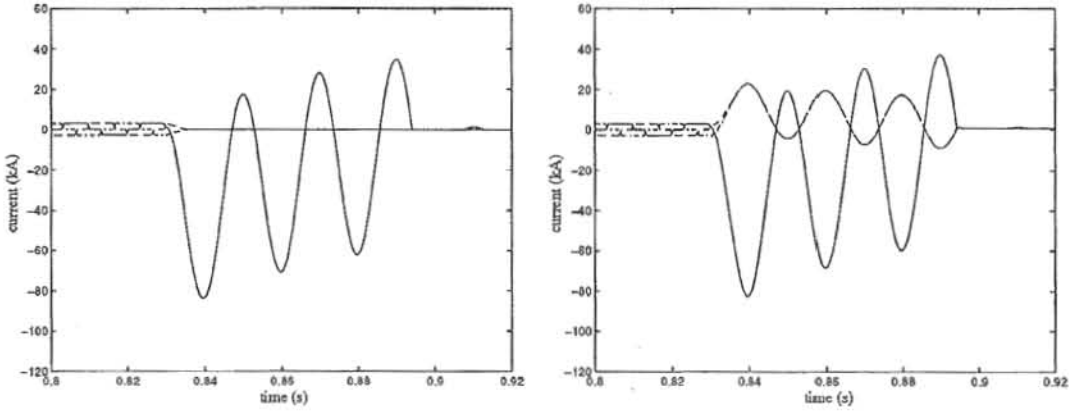

(a) (b)

Figure 7.6 Generator currents, 16kV red phase to ground fault, star-grounded/star-grounded converter transformer; Solid=red-phase, Dash-dash=yellow-phase, Dash-dot=blue-phase: (a) three-phase bank test system, (b) three-limb three-phase test system.

The primary winding currents for the three-phase bank and three-limb three-phase UMEC models are shown in figures 7.7(a) and (b) respectively. At the onset of the fault the three-phase bank primary current ramps to zero through the conducting phases. In the three-limb case this ramp is superimposed upon significant fault current (of peak 23.0kA) on all three transformer windings.

Once the converter currents have ramped to zero the transformer is effectively open-circuit. Consider only the transformer primary windings shown in figure 7.8(a) and the phasor diagram of figure 7.8(b). The reference phasor diagram is the three-limb transformer primary red-phase voltage $\tilde{V}_1$ prior to the fault. During the fault instead of the nominal flux $\tilde{\phi}_1$ in the red-phase winding-limb, the shorted red-phase

[4]The reference red phase to ground generator internal emf positive going zero crossing occurs at time 0.8secs.

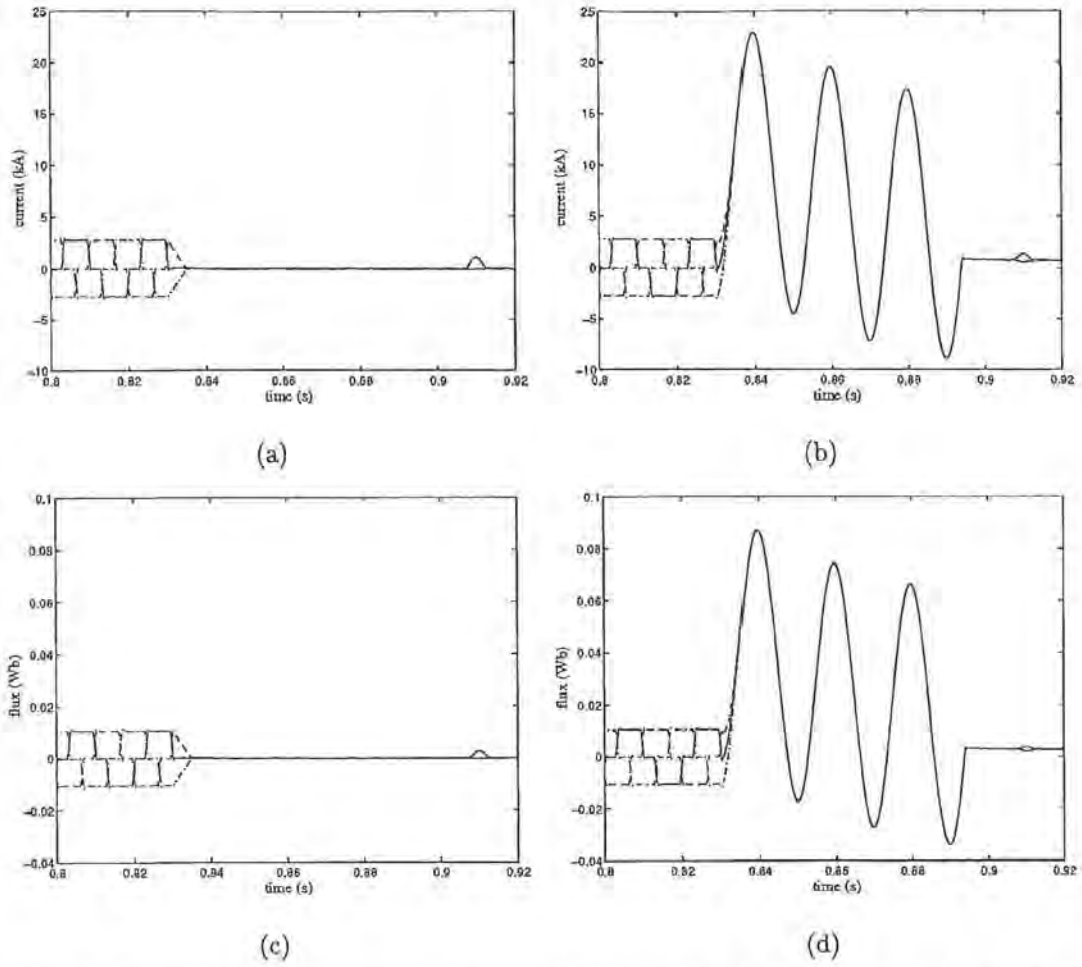

Figure 7.7 Star-grounded/star-grounded converter transformer red phase to ground fault (left hand side=three-phase bank, right hand side=three-limb three-phase); Solid=red-phase, Dash-dash=yellow-phase, Dash-dot=blue-phase: (a) and (b) primary winding current, (c) and (d) primary winding leakage flux.

phase causes the sum of the yellow and blue-phase flux $\tilde{\phi}_3$ and $\tilde{\phi}_5$ respectively to pass into the red-phase winding-limb. This flux $\tilde{\phi}_1^*$ is equal in magnitude, and 180^o out of phase, to the nominal flux $\tilde{\phi}_1$. Near rated voltage $\tilde{V}_1^*$ is induced in the red-phase winding during the fault, and the fault current $\tilde{I}_1^*$ flows from the generator yellow and blue phases through the mainly inductive transformer primary winding short-circuit impedance. The transformer red-phase fault current lags the induced voltage by 90^o and is in-phase with the fault current in the generator red-phase.

The mmf sum around each loop of the three-limb core must balance. The fault currents in the three-limb transformer yellow and blue-phases are therefore in phase with the red-phase current. Moreover the core flux levels are not increased by the over-current in the transformer primary windings. The in-phase nature of the primary fault currents cause the transformer zero-sequence and primary flux-leakage path flux levels to significantly increase. The primary leakage path flux waveforms are displayed in

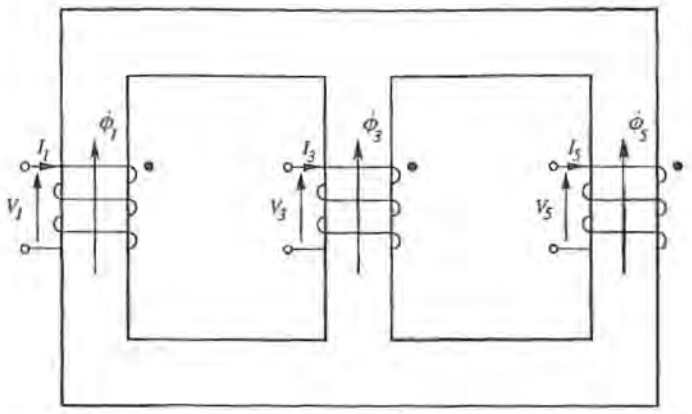

(a)

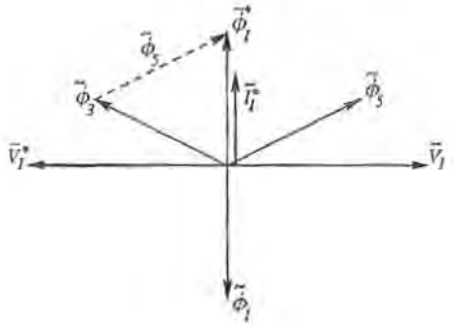

(b)

Figure 7.8 Star-grounded three-limb transformer flux distribution, red phase to ground fault: (a) open-circuit core flux, (b) voltage, current and flux phasor diagram.

figures 7.7(c) and (d) for the three-phase bank and three-limb transformers respectively.

Figures 7.9(a) and (b) display the three-phase bank and three-limb three-phase transformer primary winding currents for five complete cycles following fault removal. In both transformer types, the fault is removed but the red-phase winding-limb fluxes, shown in figure 7.9(c) and (d), have not decayed to zero. The resultant dc flux offset causes in-rush current to flow in the red-phase windings.

Upon fault removal each transformer type again exhibits dissimilar behaviour. In the three-limb test case the red-phase fault current i_g (figure 7.5) is not exactly in phase with the red-phase primary winding current i_t. Therefore at the fault removal, fault current zero crossing, a significant current (point A) is present in all the three-limb primary windings. The in-rush current is superimposed upon this zero-sequence current, and a maximum current of 2.46kA flows in the transformer neutral. The zero-sequence winding current does not affect three-limb winding-limb flux waveforms (figure 7.9(d)). Instead the zero-sequence and primary leakage path fluxes increase.

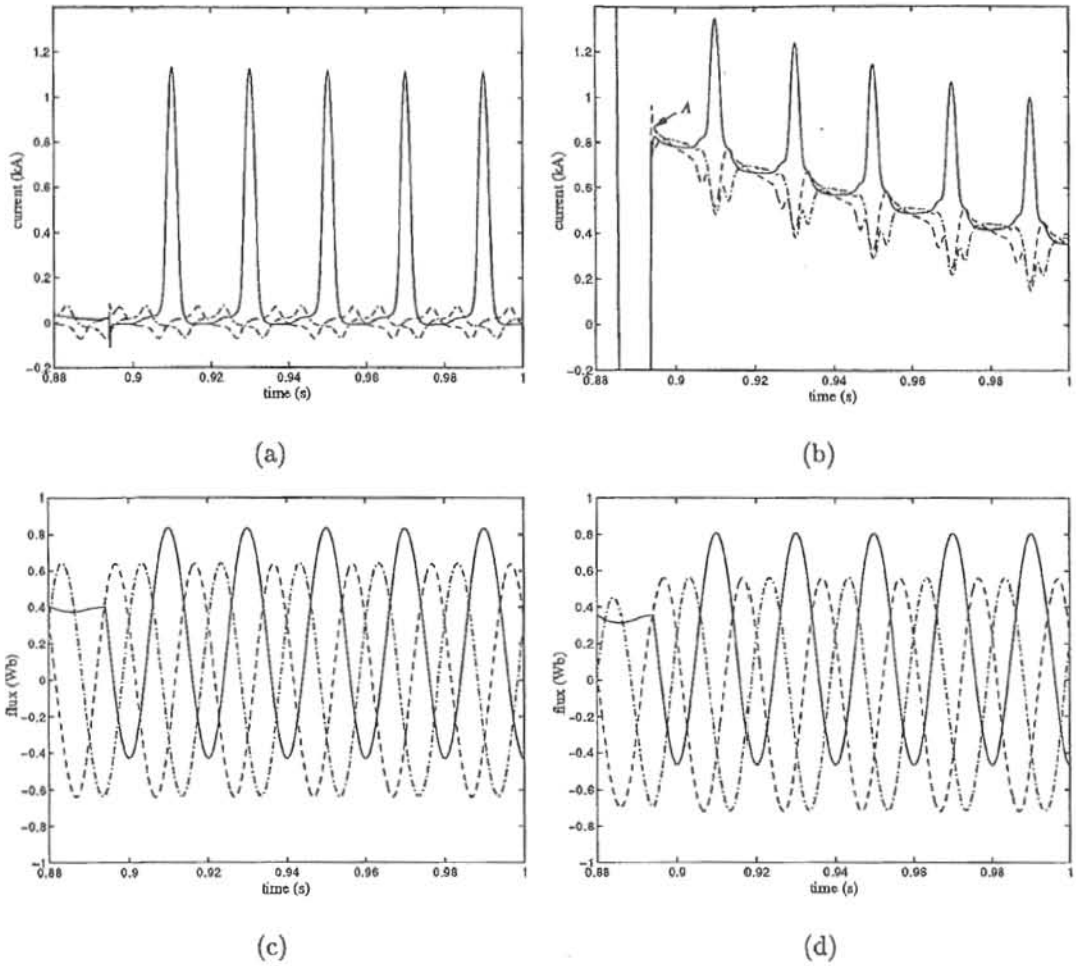

Figure 7.9 Star-grounded/star-grounded converter transformer fault recovery (left hand side=three-phase bank, right hand side=three-limb three-phase); Solid=red-phase, Dash-dash=yellow-phase, Dash-dot=blue-phase: (a) and (b) primary winding current, (c) and (d) primary winding-limb flux.

7.2 BENMORE CONVERTER TRANSFORMER COMPARISONS

The previous section has clearly shown the different behaviour of three-phase bank and three-limb three-phase transformers. However the results are not applicable to HVdc converters, which do not include a star-grounded/star-grounded transformer.

In chapter 5 a PSCAD-EMTDC model of the Benmore group connected HVdc converter station was verified with field data. In this practical test system the converter transformers were represented adequately with single-phase UMEC models connected in the delta/delta (Dd0), delta/star (Dy11) configuration. For a realistic HVdc test system, the Benmore transformer connections are used in this section together with the three-limb three-phase UMEC transformer of section 7.1, and the transient behaviour is compared with corresponding results from the three-phase bank transformer model.

7.2.1 Steady-state performance

Open and short-circuit tests of the UMEC single-phase and three-limb Benmore converter transformer models have already been presented in sections 4.3.3 and 7.1.1 respectively. The purpose of this section is to verify that the three-limb core configuration does not alter the steady-state operation of the HVdc converter.

Figures 7.10 (a), and (b) compare field data with the simulated three-limb three-phase converter transformer Benmore test system. The simulated and measured time-domain waveforms are in close agreement. The generator and converter parameters are as applied in section 7.1.2. The parameters of the Dd0 and Dy11 three-limb three-phase converter transformers are given in appendix I, and the Benmore converter is operating on group connection with a dc line current of 405A.

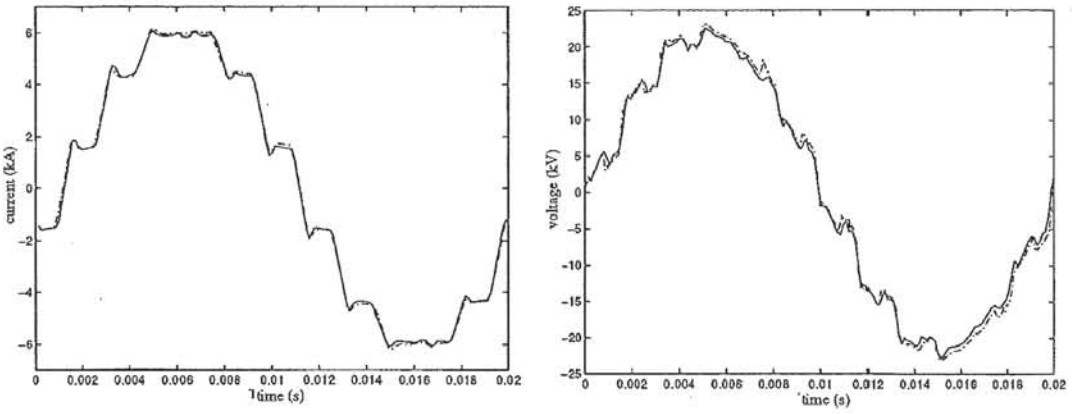

(a) (b)

Figure 7.10 Benmore group connection generator waveforms, Dd0 and Dy11 three-limb converter transformers, I_{dc}=405A; Solid=field measurement, Dash-dot=simulation: (a) generator current, 3 machines, (b) generator voltage.

7.2.2 Transient comparison

A red phase to ground fault has been selected to investigate the transient behaviour of the Benmore converter transformers. The fault is applied to the 110kV side of the Dd0 converter transformer (time=1.0secs), and the converter is blocked and the bypass valves fired two cycles later (time=1.04secs). The circuit-breaker opens two and a half cycles after the fault (time=1.05secs). The circuit-breaker recloses after 0.03secs and the converter is deblocked three cycles after the reclose (time=1.14secs).

Figure 7.11 displays the test system. The Pole 1 Benmore converter transformers are situated at the generator power-house, and connected to the synchronous machines by a 16kV enclosed bus network. Therefore the fault is more likely to occur on the 110kV overhead line connecting a converter transformer to the valves. The fault is

placed on the Dd0, rather than the Dy11 converter transformer. This selection simplifies the test system transient behaviour by ensuring that fault current flows only through one of the six pulse valve groups.

The parameters for the generator, converter transformers, and converter are the same as in section 7.2.1. The circuit-breaker, bypass valve, and fault parameters are given in appendix I.

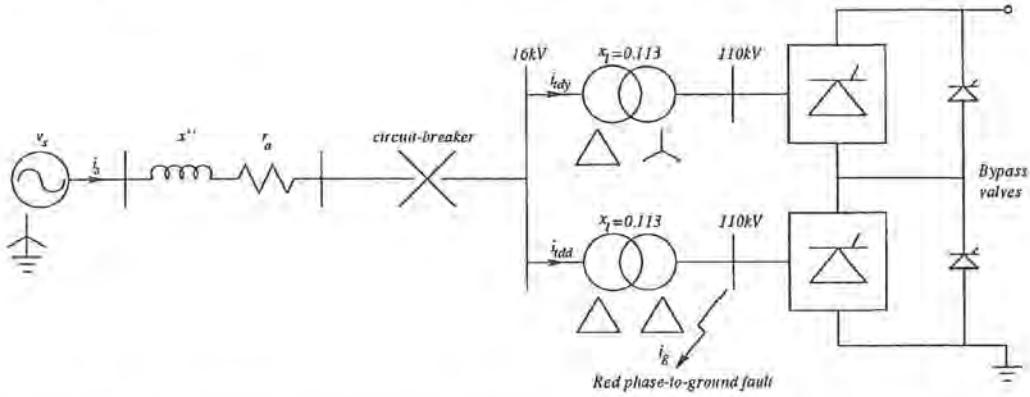

Figure 7.11 Benmore group connected HVdc converter transformer transient test system.

Figures 7.12(a) and (b) present the three-phase bank and three-limb three-phase converter transformer primary line currents respectively for the Dd0 connection prior to the circuit-breaker reclose. Both transformer representations produce similar waveforms. The secondary windings of the Dd0 converter transformer are all electrically connected to the fault and the interphase magnetic coupling of the three-limb three-phase transformer has little effect.

Between the fault initiation and converter block the unidirectional fault currents are superimposed on the converter currents. Once converter blocking is ordered and the bypass valve fired, the blue-phase current naturally commutates off (point A) whereas conduction of the red and yellow-phases is extended until the fault current passes through zero (point B).

Figures 7.13(a) and (b) compare the three-phase bank and three-limb three-phase primary line currents respectively for the Dd0 converter transformer. The same comparison is made for the Dy11 converter transformer in figures 7.13(c) and (d). These waveforms display operation following the circuit-breaker reclose (time=1.08secs) and in-rush follows.

The three-phase bank and three-limb three-phase converter transformer fault recovery waveforms are almost indistinguishable. However the maximum in-rush current peaks of the three-phase banks (points A and B) are slightly smaller than the three-limb three-phase transformer (points C and D).

When the generator circuit-breaker opens (time=1.05secs) the converter transformer primary windings are open-circuit. The converter snubber capacitance dis-

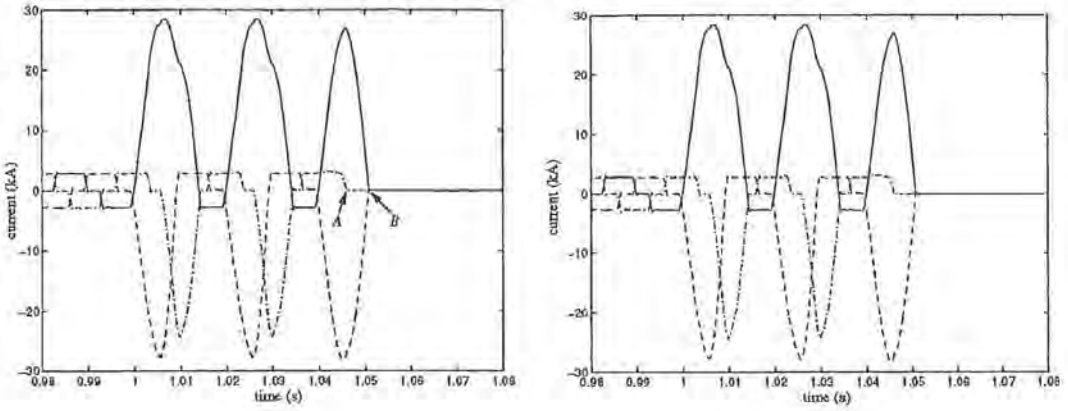

Figure 7.12 Dd0 converter transformer, 110kV red phase to ground fault; Solid=red-phase, Dash-dash=yellow-phase, Dash-dot=blue-phase: (a) Three-phase bank primary line current, (b) Three-limb three-phase primary line current.

charges through the large non-linear magnetising inductance of the transformer secondary windings. Figures 7.14(a) and (b) compare the three-phase bank and three-limb three-phase primary winding-limb flux respectively for the Dd0 converter transformer; the Dy11 transformer is connected to the same busbar, the primary winding-limb flux waveforms are therefore identical to the Dd0. Snubber circuit discharge occurs in the period time=1.05-1.08secs. The three-phase bank and three-limb snubber discharge waveforms are dissimilar because the magnetising inductances of each core type are not identical. At the circuit-breaker reclose, the resulting three-limb red-phase winding-limb flux magnitude is slightly greater than that of the three-phase bank.

7.3 CONVENTIONAL CONVERTER TRANSFORMER COMPARISONS

The Benmore Dd0, Dy11 converter transformers are not typical of conventional HVdc configurations. The assessment of converter transformer transient behaviour must therefore be extended to include the more common star-grounded/star, star-grounded/delta converter transformer configuration.

7.3.1 Steady-state performance

The three-phase bank and three-limb three-phase converter transformers are now reconnected in the star-grounded/star (Yy0), star-grounded/delta (Yd11) configuration. The reconnected transformer parameters are given in appendix I, the dc line current is set to 405A.

Figures 7.15 (a), and (b) compare the field test waveforms with the results of the simulation using the three-limb three-phase converter transformer equivalent of the

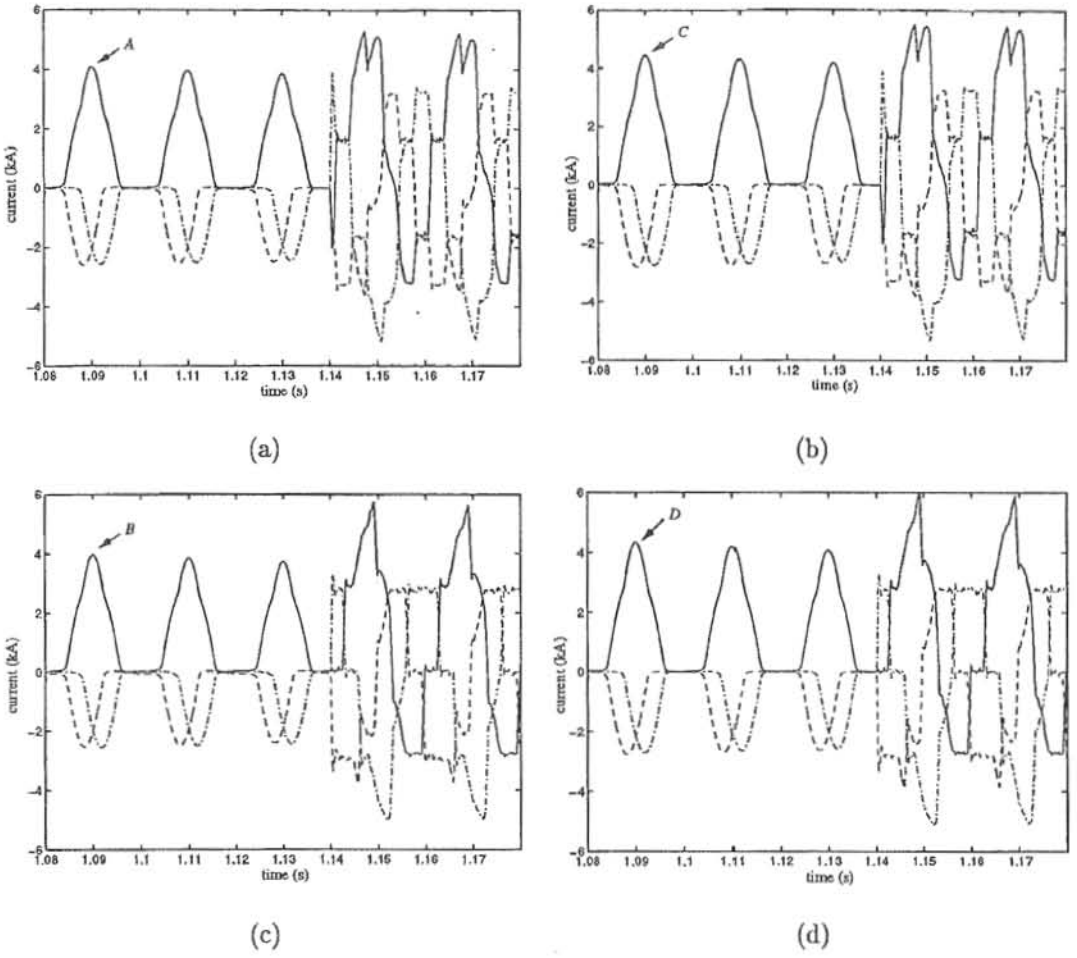

Figure 7.13 Converter transformer line currents, fault recovery (left hand side=three-phase bank, right hand side=three-limb three-phase); Solid=red-phase, Dash-dash=yellow-phase, Dash-dot=blue-phase: (a) and (b) Dd0 primary current, (c) and (d) Dy11 primary current.

Benmore units. As expected, reconnection of the transformer windings in the Yy0 and Yd11 configuration does not affect the steady-state waveforms of the Benmore group connected scheme, measured and simulated time domain steady-state waveforms are shown to be in close agreement.

7.3.2 Transient comparison

In conventional HVdc terminals the converter transformers are positioned with the secondary transformer bushings extending into the enclosed valve-hall and a fault to ground on the secondary side the converter transformers is unlikely. A phase to ground fault is most likely to occur on the converter transformer primary side; these windings are commonly connected to an outdoor ac switchyard. Therefore the transient behaviour of the three-phase bank and three-limb three-phase converter transformers is again compared, this time using a red phase to ground fault on the 16kV bus-bar.

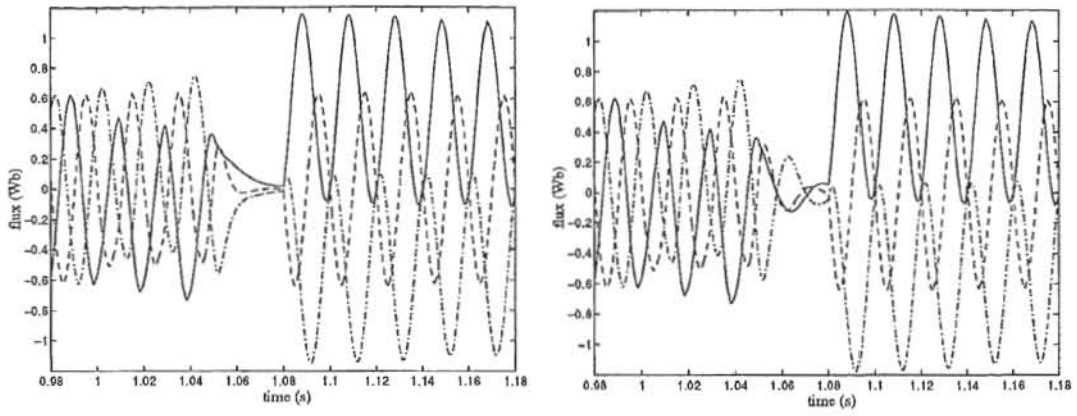

(a) (b)

Figure 7.14 Dd0 converter transformer, 110kV red phase to ground fault and recovery; Solid=red-phase, Dash-dash=yellow-phase, Dash-dot=blue-phase: (a) Three-phase bank primary winding-limb flux, (b) Three-limb three-phase primary winding-limb flux.

Figure 7.16 displays the new HVdc converter transformer test system configuration. The parameters for the generator, converter transformers, and valve groups are as applied in the previous steady-state field data verification (section 7.2). Details of the circuit-breaker, bypass valve, and fault parameters are given in appendix I. The sequence and timing of the fault, circuit-breaker, and converter controls are identical to those of the previous 110kV red phase to ground fault study (section 7.2.2).

Figures 7.17(a), and (b) present the generator current in the three-phase bank, and three-limb three-phase converter transformer test systems respectively, prior to the circuit-breaker reclose. The red-phase generator fault currents are similar, but the yellow and blue-phase currents of the three-limb converter transformer test system exceed those of the three-phase bank.

The three-phase bank and three-limb three-phase Yy0 converter transformer primary currents i_{tyy} are shown in figures 7.18(a), and (b) respectively. In this winding configuration the single-phase bank is not affected by the presence of the fault. However significant fault currents flow in the primary winding of the three-limb three-phase converter transformer. The Yy0 three-limb converter transformer transient behaviour is similar to that of the star-grounded/star-grounded unit explained in section 7.1.2.

Fault currents flow in both the three-phase bank, and three-limb three-phase Yd11 transformer primary currents i_{tyd}, shown in figures 7.18(c), and (d) respectively. This behaviour is caused by the delta secondary winding connection. Although the red-phase primary is shorted, the three secondary windings are energised (due to the delta connection) and fault current flows in all the transformer windings.

Between fault initiation and converter blocking the fault current is superimposed on the converter currents. Once the blocking is ordered, the bypass valve is fired, and

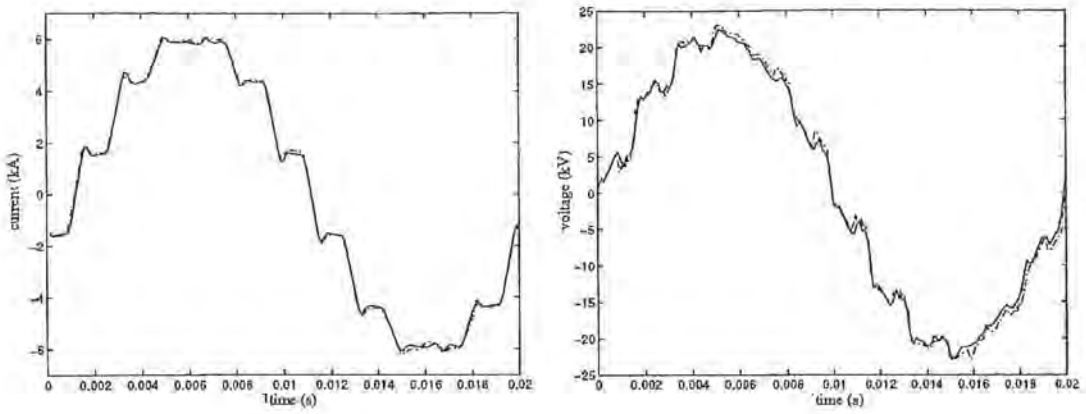

(a) (b)

Figure 7.15 Benmore group connection generator waveforms, Yy0 and Yd11 three-limb converter transformers, I_{dc}=405A; Solid=field measurement, Dash-dot=simulation: (a) generator current, 3 machines, (b) generator voltage.

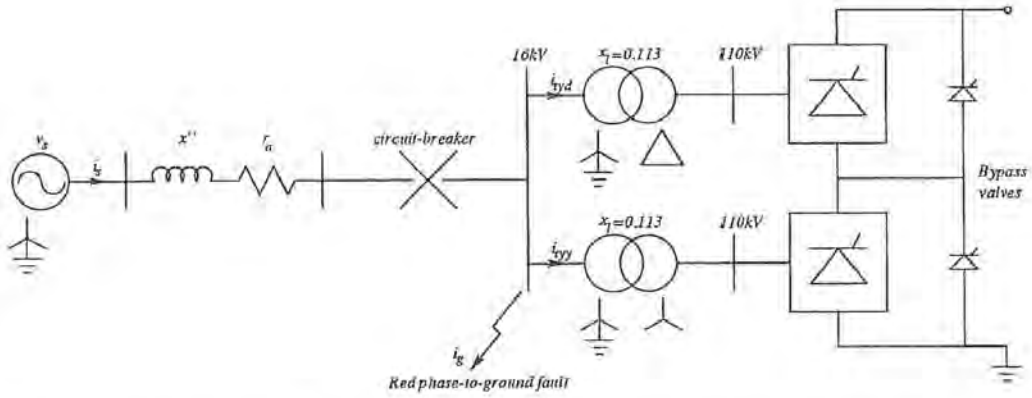

Figure 7.16 Conventional converter transformer configuration transient test system.

the red, yellow, and blue valves commutate off. After the circuit-breaker is opened conduction does not cease until the fault current in each phase passes through zero.

The waveforms of figure 7.18 are continued in figure 7.19 for the period following the circuit-breaker reclose. Again the three-phase bank and three-limb three-phase converter fault recovery waveforms are almost indistinguishable. The maximum in-rush current peak of the Yy0 three-phase bank (point A) is greater than that of the three-limb three-phase equivalent (point B). The maximum in-rush current peak of the Yd11 three-phase bank (point C) is less than that of the three-limb three-phase equivalent (point D). When the converter is deblocked (time=1.14secs) the in-rush currents are super-imposed on the converter currents.

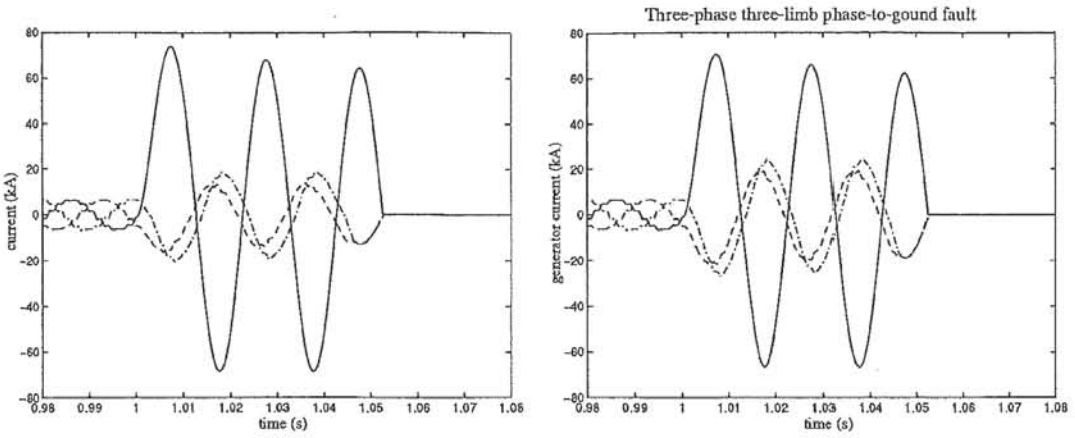

(a) (b)

Figure 7.17 Generator currents, 16kV red phase to ground fault; Solid=red-phase, Dash-dash=yellow-phase, Dash-dot=blue-phase: (a) three-phase bank test system, (b) three-limb three-phase test system.

7.4 CONCLUSIONS

In this chapter equivalent UMEC three-phase bank and three-limb three-phase HVdc converter transformer models have been compared under steady-state and transient operating conditions. Under steady-state open-circuit, short-circuit and over-voltage conditions both transformer types produced acceptably similar waveforms. A single phase to ground fault was applied to the primary bus-bar of a star-grounded/star-grounded converter transformer. This test system included a single six-pulse HVdc valve group. Significant fault currents flowed in all primary phases of the three-limb three-phase converter transformer, yet no fault currents flowed in the three-phase bank. The behaviour of each converter transformer type was also dissimilar after the fault was cleared.

Assessment of three-phase bank and three-limb three-phase converter transformer behaviour was made in a practical test system. A red phase to ground fault was applied to the converter side of the delta/delta converter transformer of the Benmore group connected test system. In this example the behaviour of the three-phase bank and three-limb three-phase converter transformers were almost indistinguishable. The faulted delta winding electrically, rather than magnetically, connected all phases to the fault.

Finally, three-phase bank and three-limb three-phase pairs of star-grounded/star-grounded, star-grounded/delta converter transformers were placed in the Benmore test system and again verified with steady-state field data. A red phase to ground fault was applied to the converter transformer primary side. In this typical winding configuration fault currents were present on all three-phases of the three-limb star-grounded/star converter transformer. The single-phase equivalent failed to show this effect.

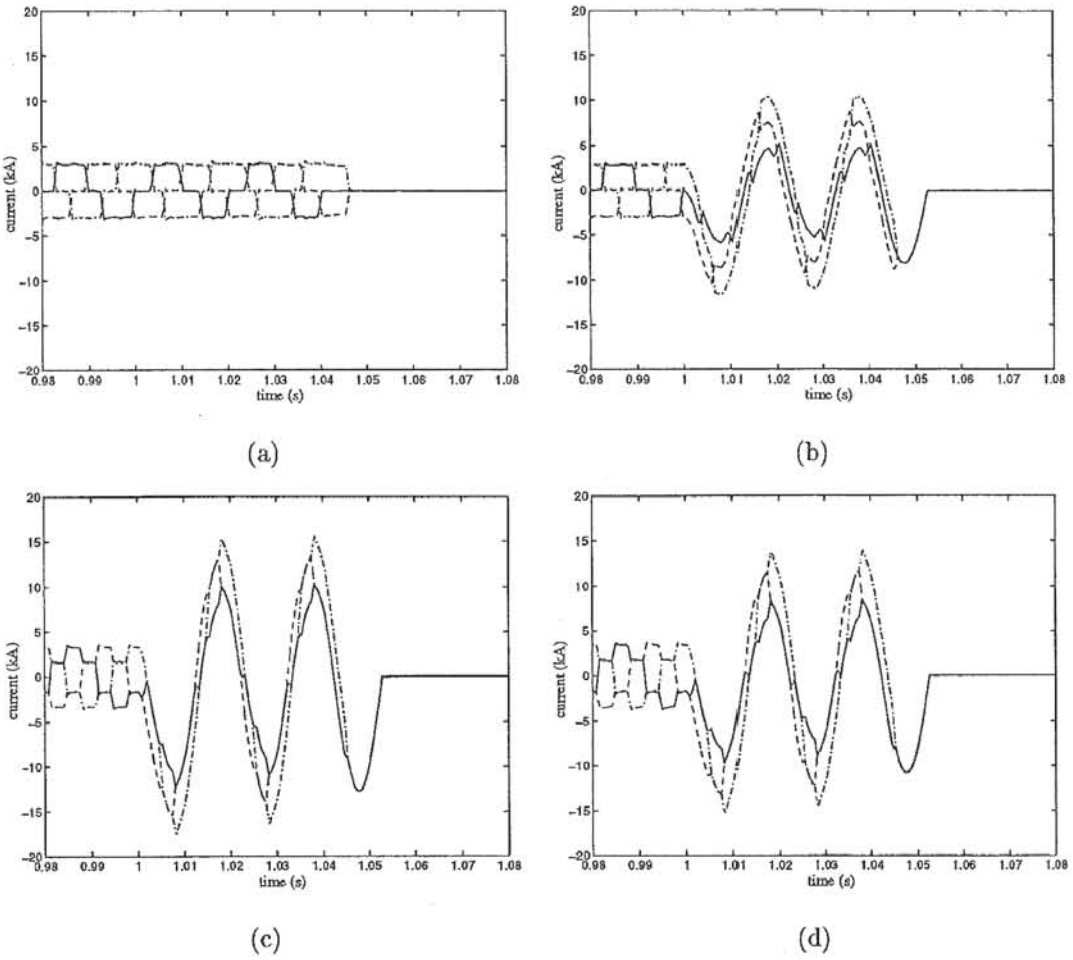

Figure 7.18 Converter transformer winding currents, 16kV red phase to ground fault (left hand side=three-phase bank, right hand side=three-limb three-phase); Solid=red-phase, Dash-dash=yellow-phase, Dash-dot=blue-phase: (a) and (b) Yy0 primary current, (c) and (d) Yd11 primary current.

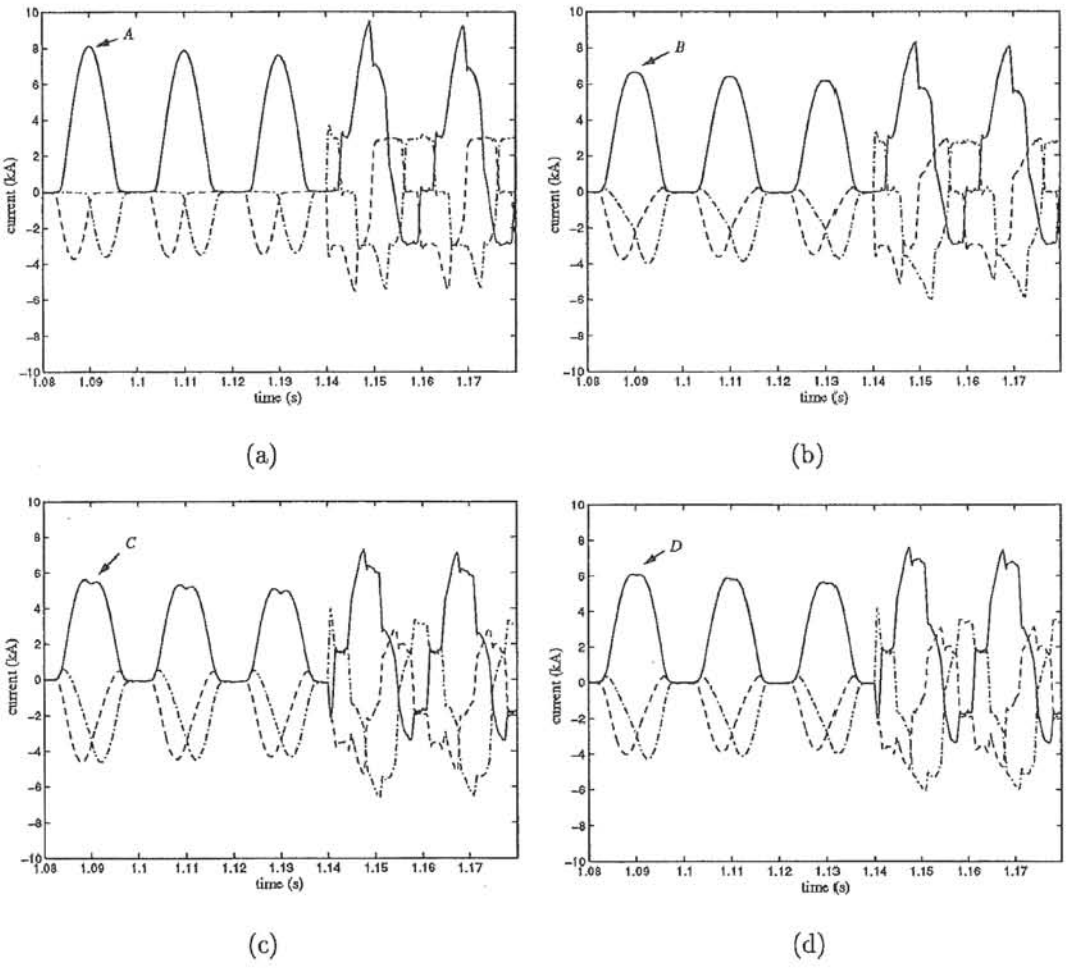

Figure 7.19 Converter transformer winding currents, fault recovery (left hand side=three-phase bank, right hand side=three-limb three-phase); Solid=red-phase, Dash-dash=yellow-phase, Dash-dot=blue-phase: (a) and (b) Yy0 primary current, (c) and (d) Yd11 primary current.

Chapter 8

FUTURE WORK AND CONCLUSIONS

In this thesis magnetic circuits have been used to model single-phase and three-limb three-phase transformers. The proposed magnetic equivalent circuit (MEC) concept has been implemented in an electromagnetic transient program as a Norton equivalent. Since the transformer model applications presented in this thesis are specific to HVdc improvements, the PSCAD-EMTDC package has been used to incorporate the proposed models. Moreover the effort spent on the PSCAD-EMTDC program transformer models, relative to other HVdc components, has been small.

The MEC model has been used to intervalidate the Harmonic Domain Analysis (HDA) and PSCAD-EMTDC programs. Intervalidations have been performed for overvoltage excitation of single-phase and three-limb transformers with the test system supply impedance being purely resistive, and series resonant respectively. Acceptable matches in Time Domain waveforms and Harmonic Domain spectra were achieved in each case.

The interphase magnetic coupling representation of the three-limb three-phase MEC model was verified with experimental data. Currently PSCAD-EMTDC uses magnetically independent phase models. Comparisons between equivalent PSCAD-EMTDC three-phase bank and MEC three-limb three-phase models under steady-state energisation, flux decay and in-rush operating conditions showed considerable differences in the behaviour of each model.

The present PSCAD-EMTDC transformer model core flux is calculated from the voltage of only one winding, a uniform flux density is assumed throughout the core legs and yokes. The non-linear magnetising current is injected across the terminals of one transformer winding. The unified magnetic equivalent circuit (UMEC) transformer model does not apply any of these approximations.

Laboratory results were used to show that the UMEC representation provides an accurate division of magnetising current between transformer windings. To demonstrate the effects of the PSCAD-EMTDC transformer approximations in a practical test system, the New Zealand HVdc system was used. For the case of load rejection, the results showed that the PSCAD-EMTDC model lead to significant errors in predicting

the magnetising current harmonics in the Benmore interconnecting bank windings.

The first set of group connected generator HVdc converter scheme harmonic measurements are presented. The field data provides evidence to support the feasibility of the group connection, and is useful for verification of the UMEC transformer model. Benmore three-phase bank converter transformer UMEC models were derived and placed in a PSCAD-EMTDC model of the Benmore group connection. The simulated generator voltage and current provided an acceptable match to the field data.

A new means to reduce cost and increase the operational flexibility of the HVdc terminal was investigated. It consists of the smoothing transformer and dc blocking capacitor as a replacement for the HVdc smoothing reactor and conventional filtering arrangement. The PSCAD-EMTDC model of the Benmore group connection, and single-phase UMEC transformer model have also been used to investigate the smoothing transformer concept. Dc side harmonic cancellation was achieved with the smoothing transformer at characteristic and non-characteristic harmonic frequencies. Satisfactory dc side harmonic cancellation was verified for a range of synchronous generator operating speeds. Moreover, during a dc line fault the transient behaviour of the smoothing transformer was shown to be similar to that of the conventional filter arrangement.

The single-phase UMEC was extended to represent three-limb three-phase transformers and a model of the Manapouri 105MVA, 13.8/220kV transformers was validated with factory test data. Three-phase bank and three-limb three-phase HVdc converter transformers comparisons were also made. UMEC three-limb three-phase models, equivalent to the single-phase Benmore converter transformers, were developed and model equivalence in the steady-state was verified with the field data. In the conventional star-grounded/star, star-grounded/delta winding configuration, the response of the single-phase bank and three-limb three-phase converter transformers to a primary phase-to-ground fault are dissimilar. Significant fault currents flow in all phases of the three-limb three-phase star-grounded/delta transformer while no fault current flows in the corresponding three-phase bank.

The transformer models developed in this thesis will be incorporated in version 3 of PSCAD-EMTDC (for release to all users in 1996). To place the UMEC model in this program further work is required to fix the Norton equivalent admittance matrix at each time step, or remove it completely. When the time step is small ($50\mu s$), the UMEC admittance matrix has little effect on the winding current as the Norton equivalent current source dominates. Updating the transformer admittance network significantly slows the PSCAD-EMTDC main program loop. Alternatively, the MEC models could be applied to calculate transformer magnetising current. The MEC Norton equivalent current source would then be injected across a six winding inductance transformer representation.

The models proposed in this thesis should be extended to include hysteresis.

Branch permeance should be calculated using hysteresis loops. The addition of hysteresis representation would be useful to verify models with small VA rating (laboratory transformers). Winding resistance and core loss representation could also be added.

The addition of tank and winding capacitances would extend the capacitor electromagnetic representation to a Norton equivalent electric field formulation. The UMEC magnetic and electric field Norton equivalents could then be superimposed to give a transformer more suitable for simulating fast transients.

It would be beneficial if more widespread use of accurate models could prompt manufacturers to release improved transformer specifications. Core design, winding turns numbers, and core steel characteristics are essential parameters of detailed transformer models. These parameters are rarely all listed in individual transformer technical documentation.

Only simple single-phase and three-limb three-phase transformer magnetic equivalent circuits have been proposed in this thesis. The Norton equivalent formulation may be used to interface more complex magnetic circuits in PSCAD-EMTDC. Individual transformer windings can be represented with multiple magnetic circuit branches, such a representation would be useful for studying turn to turn short-circuits. Zero-sequence or winding-leakage flux paths may be broken into multiple magnetic branches. Small magnetic networks may be applied to represent the core clamps, bolts, frames, or the transformer tank; this detail would be useful for examining localised saturation. Extensive three-dimensional magnetic equivalent circuits could be applied.

Core configurations other than single-phase and three-limb three-phase types are yet to be examined. Four and five-limb, single and multi-phase transformers can be modelled with magnetic equivalent circuits. Saturable reactor and dc measuring transformer models would also benefit from accurate core and winding representation, these devices have not been addressed in this thesis.

A magnetic equivalent circuit similar to the UMEC transformer representation can be proposed for the salient pole synchronous generator. Figure 8.1 displays a single-phase example. The permeance of the rotor path $\mathcal{P}_2$ and the field mmf $N_2 i_2$ would be time varying according to pole saliency and rotor speed. The superscript $\#$ is used in the figure to indicate variables scaled according to the field windings rotating frame of reference. Leakage paths $\mathcal{P}_4$ and $\mathcal{P}_5$ are associated with the armature and field windings respectively, the flux return path is represented with $\mathcal{P}_3$. It would be useful to create a UMEC model for the Benmore synchronous generators using the practical magnetic circuit design. Such a model could then be placed in the Benmore group connected test system to try and improve the chapter 5 voltage harmonic match.

The UMEC transformer model should be implemented in the Harmonic Domain Analysis (HDA) program to provide an accurate prediction of magnetising current harmonic distribution between transformer windings. To make the UMEC model more

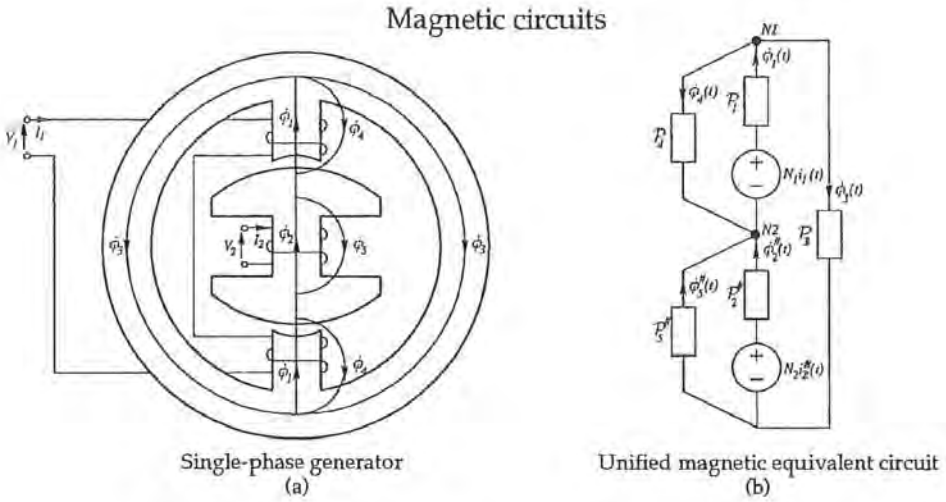

Figure 8.1 Synchronous generator magnetic equivalent circuit.

generally available, it should also be placed in the EMTP program and comparisons made with the existing three-limb three-phase duality based EMTP representation.

Appendix A

NORTON EQUIVALENT ADMITTANCE MATRIX SYMMETRY

To prove the symmetry of the Norton admittance matrix $[Y_{ss}]$, it must be shown that the product $[M][P]$ (see equation 2.25) is symmetric.

$$[M][P] = [P] - [P][A]([A]^T[P][A])^{-1}[A]^T[P] \tag{A.1}$$

Now

$$\Big([M][P]\Big)^T = [P]^T - [P]^T[A]([A]^T[P][A])^{-T}[A]^T[P]^T \tag{A.2}$$

Since the permeance matrix $[P]$ is diagonal $[P]^T = [P]$, and therefore $[A]^T[P][A]$ is obviously symmetric. The inverse of a symmetric matrix is also symmetric, thus $\Big([A]^T[P][A]\Big)^{-T} = \Big([A]^T[P][A]\Big)^{-1}$. Therefore

$$\Big([M][P]\Big)^T = [P] - [P][A]([A]^T[P][A])^{-1}[A]^T[P] \tag{A.3}$$

and the product $[M][P] = \Big([M][P]\Big)^T$.

If $[M][P]$ is symmetric the upper left-hand partition $[M_{ss}][P_s]$ is also symmetric. Now

$$[Y_{ss}] = \Big([M_{ss}][\mathcal{P}_s][N_s]\Big)^{-1}\frac{\Delta t}{2}[N_s]^{-1} \tag{A.4}$$

and the scaler $\frac{\Delta t}{2}$ does not affect $[Y_{ss}]$ matrix symmetry. Using $[A]^{-1}[B]^{-1} = ([B][A])^{-1}$ leads to

$$\Big([M_{ss}][\mathcal{P}_s][N_s]\Big)^{-1}[N_s]^{-1} = \Big([N_s][M_{ss}][\mathcal{P}_s][N_s]\Big)^{-1} \tag{A.5}$$

Also

$$\Big([N_s][M_{ss}][\mathcal{P}_s][N_s]\Big)^T = [N_s]^T\Big([M_{ss}][\mathcal{P}_s]\Big)^T[N_s]^T \tag{A.6}$$

But $[N_s]$ is diagonal and the product $[M_{ss}][\mathcal{P}_s] = \Big([M_{ss}][\mathcal{P}_s]\Big)^T$. Therefore

$$[N_s][M_{ss}][\mathcal{P}_s][N_s] = \Big([N_s][M_{ss}][\mathcal{P}_s][N_s]\Big)^T \tag{A.7}$$

and

$$\Big([N_s][M_{ss}][\mathcal{P}_s][N_s]\Big)^{-1} = \Big([N_s][M_{ss}][\mathcal{P}_s][N_s]\Big)^{-T} \tag{A.8}$$

Now

$$[Y_{ss}] = \Big([N_s][M_{ss}][\mathcal{P}_s][N_s]\Big)^{-1}\frac{\Delta t}{2} \tag{A.9}$$

$$= \Big([N_s][M_{ss}][\mathcal{P}_s][N_s]\Big)^{-T}\frac{\Delta t}{2} \tag{A.10}$$

$$= [Y_{ss}]^T \tag{A.11}$$

and the symmetry of $[Y_{ss}]$ is shown.

Appendix B

PER-UNIT DYNAMIC SIMULATION

With all variables in per-unit form, generalised equation 2.10 becomes B.1 and equation 2.29 becomes B.2, where ω_0 is the base angular frequency. In the per-unit examples of this thesis angular frequency is not normalised.

$$\tilde{\theta}_2 = \tilde{i} \tag{B.1}$$

$$\tilde{\phi}_s(t) = \tilde{\phi}_s(t - \Delta t) + \frac{\Delta t}{2}\omega_0 \left[\tilde{v}_s(t) + \tilde{v}_s(t - \Delta t)\right] \tag{B.2}$$

In the per-unit system the elements of equation 2.30 become

$$[Y_{ss}] = \left([M_{ss}][\mathcal{P}_s]\right)^{-1} \frac{\Delta t \omega_0}{2}$$

and

$$\tilde{i}_{ns} = \left([M_{ss}][\mathcal{P}_s]\right)^{-1} \left(\frac{\Delta t \omega_0}{2}\tilde{v}_s(t - \Delta t) + \tilde{\phi}_s(t - \Delta t) + [M_{ss}]\tilde{\phi}_{ns} + [M_{sr}]\tilde{\phi}_{nr}\right)$$

Appendix C

LEAKAGE PERMEANCE CALCULATION

Theory

Consider two mutually coupled windings having primary and secondary self inductances L_{11} and L_{22} respectively. The mutual inductance M_{12} between the two windings can be defined by the relationship

$$M_{12} = k\sqrt{L_{11}L_{22}} \tag{C.1}$$

where k is the coil coupling factor.

Mutually coupled coils can be represented with the electrical equivalent circuit of figure C.1.

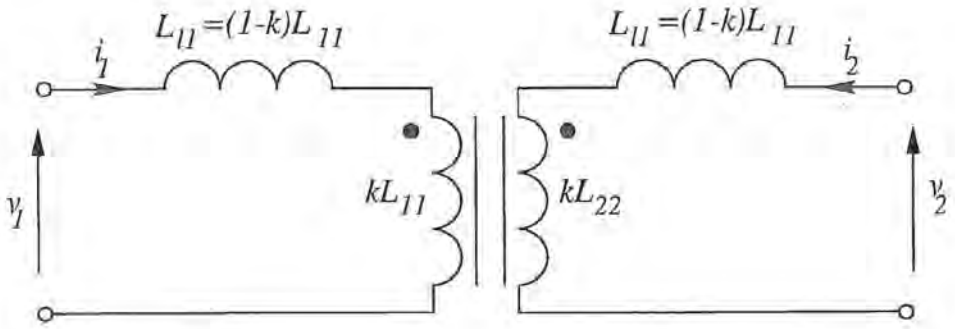

Figure C.1 Mutually coupled coil equivalent circuit.

Calculation of transformer coupling factor k, and self inductances L_{11} and L_{22} gives the primary and secondary winding leakage reactance L_{l1} and L_{l2} respectively.

Measurement

Energise the transformer primary with the secondary open-circuit. Measure the primary voltage v_1, primary current i_1, primary power W_1, and secondary voltage v_2. Calculate L_{11}, M_{21} using

$$i_{ro} = \frac{W_1}{v_1} \tag{C.2}$$

$$i_{xo} = \sqrt{i_1^2 - i_{ro}^2} \tag{C.3}$$

$$L_{11} = \frac{v_1}{i_{xo}\omega_o} \tag{C.4}$$

$$M_{21} = \frac{v_2}{i_{xo}\omega_o} \tag{C.5}$$

where ω_o is the supply angular frequency.

Now energise the transformer secondary with the primary open-circuit. Measure the secondary voltage v_2, secondary current i_2, secondary power W_2, and primary voltage v_1. Calculate L_{22}, M_{12} using

$$i_{ro} = \frac{W_2}{v_2} \tag{C.6}$$

$$i_{xo} = \sqrt{i_2^2 - i_{ro}^2} \tag{C.7}$$

$$L_{22} = \frac{v_2}{i_{xo}\omega_o} \tag{C.8}$$

$$M_{12} = \frac{v_1}{i_{xo}\omega_o} \tag{C.9}$$

Check that $M_{12} = M_{21}$, and if they agree calculate the coupling factor using equation C.1. The primary and secondary winding leakage inductances L_{l1} and L_{l2} are then calculated with

$$L_{l1} = (1-k)L_{11} \tag{C.10}$$

$$L_{l2} = (1-k)L_{22} \tag{C.11}$$

Single-phase UMEC leakage path permeances $\mathcal{P}_4$ and $\mathcal{P}_5$ are obtained from

$$\mathcal{P}_4 = \frac{L_{l1}}{N_1^2} \tag{C.12}$$

$$\mathcal{P}_5 = \frac{L_{l2}}{N_2^2} \tag{C.13}$$

where N_1 and N_2 are the primary and secondary winding turns number respectively.

If only the total transformer leakage reactance is given, for example X_l=0.10p.u., and the above tests can not be performed, then the modeller must approximate. One approximation is to halve the given leakage inductance between the transformer primary and secondary windings, and then apply equations C.12 and C.13.

Appendix D

TRANSFORMER RELUCTANCE/PERMEANCE PATHS

D.1 PRIMARY OPEN-CIRCUIT RELUCTANCE

If a single-phase transformer primary winding is energised and the secondary is open-circuit, the effective flux path reluctance $\mathcal{R}_{oc}^{*prim}$ is derived from the magnetic equivalent circuit of figure 4.3(a).

$$\mathcal{R}_{oc}^{*prim} = \mathcal{R}_1^* + \mathcal{R}_4^* // (\mathcal{R}_3^* + \mathcal{R}_2^* // \mathcal{R}_5^*) \tag{D.1}$$

$$= \mathcal{R}_1^* + \mathcal{R}_4^* // (\mathcal{R}_3^* + \frac{\mathcal{R}_2^* \mathcal{R}_5^*}{\mathcal{R}_2^* + \mathcal{R}_5^*}) \tag{D.2}$$

$$= \mathcal{R}_1^* + \frac{\mathcal{R}_4^* \mathcal{R}_3^* (\mathcal{R}_2^* + \mathcal{R}_5^*) + \mathcal{R}_4^* \mathcal{R}_2^* \mathcal{R}_5^*}{\mathcal{R}_4^* (\mathcal{R}_2^* + \mathcal{R}_5^*) + \mathcal{R}_3^* (\mathcal{R}_2^* + \mathcal{R}_5^*) + \mathcal{R}_2^* \mathcal{R}_5^*} \tag{D.3}$$

$$= \frac{(\mathcal{R}_1^* \mathcal{R}_4^* + \mathcal{R}_1^* \mathcal{R}_3^* + \mathcal{R}_3^* \mathcal{R}_4^*)(\mathcal{R}_2^* + \mathcal{R}_5^*) + (\mathcal{R}_1^* + \mathcal{R}_4^*) \mathcal{R}_2^* \mathcal{R}_5^*}{(\mathcal{R}_3^* + \mathcal{R}_4^*)(\mathcal{R}_2^* + \mathcal{R}_5^*) + \mathcal{R}_2^* \mathcal{R}_5^*} \tag{D.4}$$

D.2 SECONDARY OPEN-CIRCUIT RELUCTANCE

Similarly, if the transformer secondary winding is energised and the primary is open-circuit the effective flux path reluctance $\mathcal{R}_{oc}^{*sec}$ is derived from

$$\mathcal{R}_{oc}^{*sec} = \mathcal{R}_2^* + \mathcal{R}_5^* // (\mathcal{R}_3^* + \mathcal{R}_1^* // \mathcal{R}_4^*) \tag{D.5}$$

$$= \mathcal{R}_2^* + \mathcal{R}_5^* // (\mathcal{R}_3^* + \frac{\mathcal{R}_1^* \mathcal{R}_4^*}{\mathcal{R}_1^* + \mathcal{R}_4^*}) \tag{D.6}$$

$$= \mathcal{R}_2^* + \frac{\mathcal{R}_5^* \mathcal{R}_3^* (\mathcal{R}_1^* + \mathcal{R}_4^*) + \mathcal{R}_5^* \mathcal{R}_1^* \mathcal{R}_4^*}{\mathcal{R}_5^* (\mathcal{R}_1^* + \mathcal{R}_4^*) + \mathcal{R}_3^* (\mathcal{R}_1^* + \mathcal{R}_4^*) + \mathcal{R}_1^* \mathcal{R}_4^*} \tag{D.7}$$

$$= \frac{(\mathcal{R}_2^* \mathcal{R}_5^* + \mathcal{R}_2^* \mathcal{R}_3^* + \mathcal{R}_3^* \mathcal{R}_5^*)(\mathcal{R}_1^* + \mathcal{R}_4^*) + (\mathcal{R}_1^* + \mathcal{R}_4^*) \mathcal{R}_2^* \mathcal{R}_5^*}{(\mathcal{R}_3^* + \mathcal{R}_5^*)(\mathcal{R}_1^* + \mathcal{R}_4^*) + \mathcal{R}_1^* \mathcal{R}_4^*} \tag{D.8}$$

D.3 PRIMARY SHORT-CIRCUIT RELUCTANCE

If a single-phase transformer primary is energised and the secondary winding shorted, the effective flux path reluctance $\mathcal{R}_{ss}^{*prim}$ is derived from the magnetic equivalent circuit of figure 4.3(b).

$$\mathcal{R}_{ss}^{*prim} = \mathcal{R}_1^* + \mathcal{R}_4^* // (\mathcal{R}_3^* + \mathcal{R}_5^*) \tag{D.9}$$

$$= \mathcal{R}_1^* + \frac{\mathcal{R}_4^*(\mathcal{R}_3^* + \mathcal{R}_5^*)}{\mathcal{R}_3^* + \mathcal{R}_4^* + \mathcal{R}_5^*} \tag{D.10}$$

$$= \frac{\mathcal{R}_1^*(\mathcal{R}_3^* + \mathcal{R}_4^* + \mathcal{R}_5^*) + \mathcal{R}_4^*(\mathcal{R}_3^* + \mathcal{R}_5^*)}{\mathcal{R}_3^* + \mathcal{R}_4^* + \mathcal{R}_5^*} \tag{D.11}$$

D.4 SECONDARY SHORT-CIRCUIT RELUCTANCE

If the transformer secondary winding is energised and the primary is shorted, the effective flux path reluctance $\mathcal{R}_{oc}^{*sec}$ is derived from

$$\mathcal{R}_{ss}^{*sec} = \mathcal{R}_2^* + \mathcal{R}_5^* // (\mathcal{R}_3^* + \mathcal{R}_4^*) \tag{D.12}$$

$$= \mathcal{R}_2^* + \frac{\mathcal{R}_5^*(\mathcal{R}_3^* + \mathcal{R}_4^*)}{\mathcal{R}_3^* + \mathcal{R}_4^* + \mathcal{R}_5^*} \tag{D.13}$$

$$= \frac{\mathcal{R}_2^*(\mathcal{R}_3^* + \mathcal{R}_4^* + \mathcal{R}_5^*) + \mathcal{R}_5^*(\mathcal{R}_3^* + \mathcal{R}_4^*)}{\mathcal{R}_3^* + \mathcal{R}_4^* + \mathcal{R}_5^*} \tag{D.14}$$

D.5 MUTUAL INDUCTANCE PATH PERMEANCE

The equivalent open-circuit reluctance network of figure 4.3(a) is redrawn as the equivalent permeance network shown in figure D.1(a), where

$$\phi_a = N_1 i_1 \mathcal{P}_1^* \tag{D.15}$$

$$\mathcal{P}_a^* = \mathcal{P}_1^* + \mathcal{P}_4^* \tag{D.16}$$

$$\mathcal{P}_b^* = \mathcal{P}_3^* \tag{D.17}$$

$$\mathcal{P}_c^* = \mathcal{P}_2^* \tag{D.18}$$

$$\mathcal{P}_d^* = \mathcal{P}_5^* \tag{D.19}$$

The permeance network of figure D.1(a) can be simplified to the reluctance network of figure D.1(b), where

$$\theta_a = \frac{N_1 i_1 \mathcal{P}_1^*}{\mathcal{P}_1^* + \mathcal{P}_4^*} \tag{D.20}$$

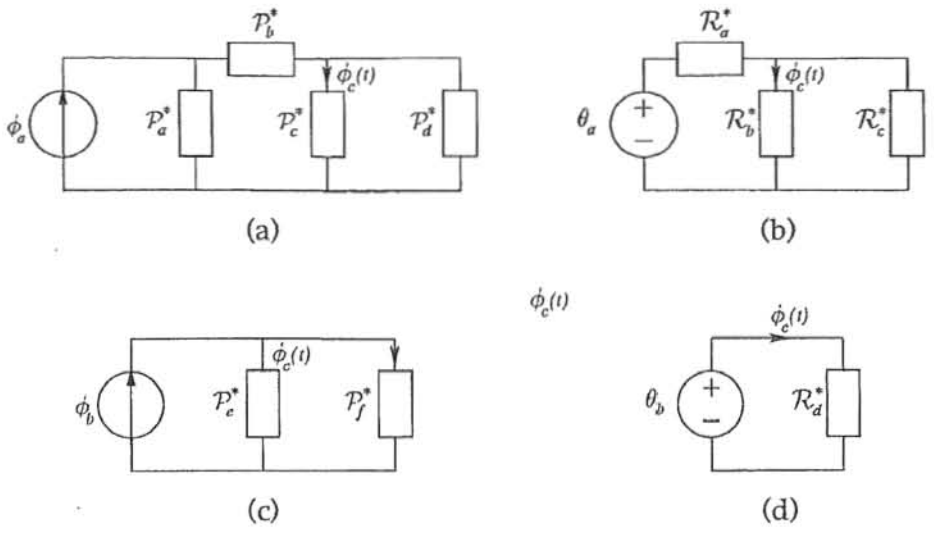

Figure D.1 Mutual inductance equivalent circuits.

$$\mathcal{R}_a^* = \frac{1}{\mathcal{P}_1^* + \mathcal{P}_4^*} + \frac{1}{\mathcal{P}_3^*} \tag{D.21}$$

$$\mathcal{R}_b^* = \frac{1}{\mathcal{P}_2^*} \tag{D.22}$$

$$\mathcal{R}_c^* = \frac{1}{\mathcal{P}_5^*} \tag{D.23}$$

The reluctance network can be converted back to the permeance form of figure D.1(c), where

$$\phi_b = \frac{N_1 i_1 \mathcal{P}_1^* \mathcal{P}_3^* (\mathcal{P}_1^* + \mathcal{P}_4^*)}{(\mathcal{P}_1^* + \mathcal{P}_4^*)(\mathcal{P}_3^* + \mathcal{P}_1^* + \mathcal{P}_4^*)} \tag{D.24}$$

$$\mathcal{P}_e^* = \mathcal{P}_5^* + \frac{\mathcal{P}_3^* (\mathcal{P}_1^* + \mathcal{P}_4^*)}{\mathcal{P}_3^* + \mathcal{P}_1^* + \mathcal{P}_4^*} \tag{D.25}$$

$$\mathcal{P}_f^* = \mathcal{P}_2^* \tag{D.26}$$

Finally the permeance network of figure D.1(c) can be placed in the thevenin form of figure D.1(d), where

$$\theta_b = \frac{N_1 i_1 \mathcal{P}_1^* \mathcal{P}_3^*}{\mathcal{P}_3^* (\mathcal{P}_1^* + \mathcal{P}_4^*) + \mathcal{P}_5^* (\mathcal{P}_3^* + \mathcal{P}_1^* + \mathcal{P}_4^*)} \tag{D.27}$$

$$\mathcal{R}_d^* = \frac{(\mathcal{P}_2^* + \mathcal{P}_5^*)(\mathcal{P}_3^* + \mathcal{P}_1^* + \mathcal{P}_4^*) + \mathcal{P}_3^* (\mathcal{P}_1^* + \mathcal{P}_4^*)}{\mathcal{P}_2^* (\mathcal{P}_3^* (\mathcal{P}_1^* + \mathcal{P}_4^*) + \mathcal{P}_5^* (\mathcal{P}_3^* + \mathcal{P}_1^* + \mathcal{P}_4^*))} \tag{D.28}$$

Solving for $\phi_c(t)$ in figure D.1(d) gives

$$\phi_c(t) = \frac{N_1 i_1 \mathcal{P}_1^* \mathcal{P}_2^* \mathcal{P}_3^*}{\mathcal{P}_2^* (\mathcal{P}_3^* + \mathcal{P}_1^* + \mathcal{P}_4^*) + \mathcal{P}_3^* (\mathcal{P}_1^* + \mathcal{P}_4^*) + \mathcal{P}_5^* (\mathcal{P}_3^* + \mathcal{P}_1^* + \mathcal{P}_4^*)} \tag{D.29}$$

Now $\phi_c(t) = \phi_2(t)$ and

$$v_2 = N_2 \frac{d\phi_2(t)}{dt} \tag{D.30}$$

$$= \frac{N_1 N_2 \mathcal{P}_1^* \mathcal{P}_2^* \mathcal{P}_3^*}{\mathcal{P}_2^*(\mathcal{P}_3^* + \mathcal{P}_1^* + \mathcal{P}_4^*) + \mathcal{P}_3^*(\mathcal{P}_1^* + \mathcal{P}_4^*) + \mathcal{P}_5^*(\mathcal{P}_3^* + \mathcal{P}_1^* + \mathcal{P}_4^*)} \frac{di_1}{dt} \tag{D.31}$$

Which gives the mutual inductance

$$M_{21} = N_1 N_2 \mathcal{P}_{21}^* \tag{D.32}$$

where

$$\mathcal{P}_{21}^* = \frac{\mathcal{P}_1^* \mathcal{P}_2^* \mathcal{P}_3^*}{(\mathcal{P}_2^* + \mathcal{P}_5^*)(\mathcal{P}_1^* + \mathcal{P}_3^* + \mathcal{P}_4^*) + \mathcal{P}_3^*(\mathcal{P}_1^* + \mathcal{P}_4^*)} \tag{D.33}$$

If the equivalent open-circuit reluctance network of figure 4.3(a) is drawn with the primary winding open-circuit and the secondary winding energised $\mathcal{P}_{12}^*$ can be derived. In this case

$$\phi_a = N_2 i_2 \mathcal{P}_2^* \tag{D.34}$$

$$\mathcal{P}_a^* = \mathcal{P}_2^* + \mathcal{P}_5^* \tag{D.35}$$

$$\mathcal{P}_b^* = \mathcal{P}_3^* \tag{D.36}$$

$$\mathcal{P}_c^* = \mathcal{P}_1^* \tag{D.37}$$

$$\mathcal{P}_d^* = \mathcal{P}_4^* \tag{D.38}$$

If the permeance network of figure D.1(a) is again simplified to the reluctance network of figure D.1(b)

$$\theta_a = \frac{N_2 i_2 \mathcal{P}_2^*}{\mathcal{P}_2^* + \mathcal{P}_5^*} \tag{D.39}$$

$$\mathcal{R}_a^* = \frac{1}{\mathcal{P}_2^* + \mathcal{P}_5^*} + \frac{1}{\mathcal{P}_3^*} \tag{D.40}$$

$$\mathcal{R}_b^* = \frac{1}{\mathcal{P}_1^*} \tag{D.41}$$

$$\mathcal{R}_c^* = \frac{1}{\mathcal{P}_4^*} \tag{D.42}$$

The permeance network of figure D.1(c) becomes

$$\phi_b = \frac{N_2 i_2 \mathcal{P}_2^* \mathcal{P}_3^* (\mathcal{P}_2^* + \mathcal{P}_5^*)}{(\mathcal{P}_2^* + \mathcal{P}_5^*)(\mathcal{P}_3^* + \mathcal{P}_2^* + \mathcal{P}_5^*)} \tag{D.43}$$

$$\mathcal{P}_e^* = \mathcal{P}_4^* + \frac{\mathcal{P}_3^*(\mathcal{P}_2^* + \mathcal{P}_5^*)}{\mathcal{P}_3^* + \mathcal{P}_2^* + \mathcal{P}_5^*} \tag{D.44}$$

$$\mathcal{P}_f^* = \mathcal{P}_1^* \tag{D.45}$$

The figure D.1(d) thevenin form becomes

$$\theta_b = \frac{N_2 i_2 \mathcal{P}_2^* \mathcal{P}_3^*}{\mathcal{P}_3^*(\mathcal{P}_2^* + \mathcal{P}_5^*) + \mathcal{P}_4^*(\mathcal{P}_3^* + \mathcal{P}_2^* + \mathcal{P}_5^*)} \tag{D.46}$$

$$\mathcal{R}_d^* = \frac{(\mathcal{P}_1^* + \mathcal{P}_4^*)(\mathcal{P}_3^* + \mathcal{P}_2^* + \mathcal{P}_5^*) + \mathcal{P}_3^*(\mathcal{P}_2^* + \mathcal{P}_5^*)}{\mathcal{P}_1^*(\mathcal{P}_3^*(\mathcal{P}_2^* + \mathcal{P}_5^*) + \mathcal{P}_4^*(\mathcal{P}_3^* + \mathcal{P}_2^* + \mathcal{P}_5^*))} \tag{D.47}$$

Solving for $\phi_c(t)$ now gives

$$\phi_c(t) = \frac{N_2 i_2 \mathcal{P}_1^* \mathcal{P}_2^* \mathcal{P}_3^*}{\mathcal{P}_1^*(\mathcal{P}_3^* + \mathcal{P}_2^* + \mathcal{P}_5^*) + \mathcal{P}_3^*(\mathcal{P}_2^* + \mathcal{P}_5^*) + \mathcal{P}_4^*(\mathcal{P}_3^* + \mathcal{P}_2^* + \mathcal{P}_5^*)} \tag{D.48}$$

Now $\phi_c(t) = \phi_1(t)$ and

$$v_1 = N_1 \frac{d\phi_1(t)}{dt} \tag{D.49}$$

$$= \frac{N_1 N_2 \mathcal{P}_1^* \mathcal{P}_2^* \mathcal{P}_3^*}{\mathcal{P}_1^*(\mathcal{P}_3^* + \mathcal{P}_2^* + \mathcal{P}_5^*) + \mathcal{P}_3^*(\mathcal{P}_2^* + \mathcal{P}_5^*) + \mathcal{P}_4^*(\mathcal{P}_3^* + \mathcal{P}_2^* + \mathcal{P}_5^*)} \frac{di_2}{dt} \tag{D.50}$$

Which gives the mutual inductance

$$M_{12} = N_1 N_2 \mathcal{P}_{12}^* \tag{D.51}$$

where

$$\mathcal{P}_{12}^* = \frac{\mathcal{P}_1^* \mathcal{P}_2^* \mathcal{P}_3^*}{(\mathcal{P}_1^* + \mathcal{P}_4^*)(\mathcal{P}_2^* + \mathcal{P}_3^* + \mathcal{P}_5^*) + \mathcal{P}_3^*(\mathcal{P}_2^* + \mathcal{P}_5^*)} \tag{D.52}$$

Appendix E

PER-UNIT ϕ-I AND B-H SATURATION REPRESENTATION

Although only a single B-H saturation characteristic is required to represent a transformer core, individual per-unit winding-limb and yoke saturation characteristics are applied in this thesis. The relationships shown in figure E.1: $F(B_k)$, between per-unit branch flux ϕ_k^{pu} and branch flux density B_k, and $G(H_k)$, between per-unit branch mmf i_k^{pu} and branch magnetising force H_k, are described in this appendix.

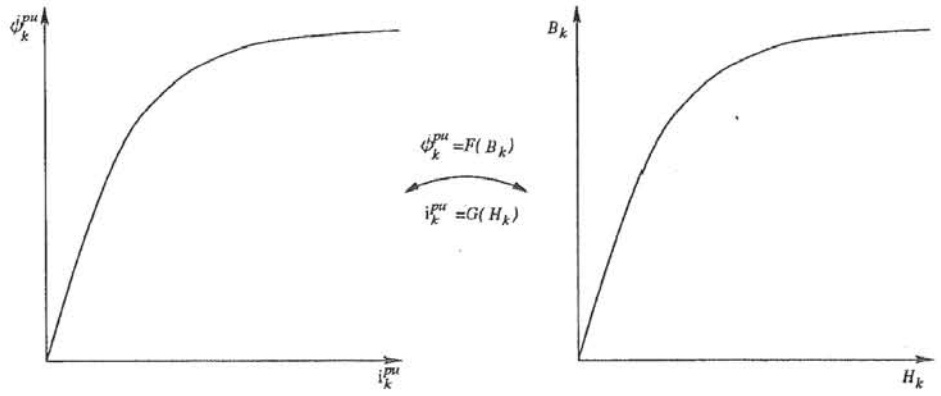

Figure E.1 Saturation characteristic conventions.

For each branch k of the magnetic equivalent circuit

$$\phi_k = B_k A_k \tag{E.1}$$

where: ϕ_k is the branch flux, B_k is the branch flux density of branch k, and A_k is the branch cross-sectional area. Now the transformer core flux base is defined as

$$\phi_b = \frac{\sqrt{2}V_{1b}}{N_1\omega_o} \tag{E.2}$$

$$= \frac{\sqrt{2}V_{2b}}{N_2\omega_o} \tag{E.3}$$

where: V_{1b} is the primary side base voltage, V_{2b} is the secondary side base voltage, N_1

is the primary winding turns number, N_2 is the secondary winding turns number, and ω_o is the rated angular frequency. Per-unit flux is written

$$\begin{aligned} \phi_k^{pu} &= F(B_k) && \text{(E.4)} \\ &= \frac{\phi_k}{\phi_b} && \text{(E.5)} \\ &= \frac{A_k N_1 \omega_o}{\sqrt{2} V_{1b}} B_k && \text{(E.6)} \\ &= \frac{A_k N_2 \omega_o}{\sqrt{2} V_{2b}} B_k && \text{(E.7)} \end{aligned}$$

Also, for branch k

$$\theta_k = H_k l_k \qquad \text{(E.8)}$$

where: θ_k is the branch mmf, H_k is the branch magnetising force, and l_k is the branch length. Now the tranformer branch mmf base is defined as

$$\begin{aligned} \theta_b &= \sqrt{2} N_1 I_{1b} && \text{(E.9)} \\ &= \sqrt{2} N_2 I_{2b} && \text{(E.10)} \end{aligned}$$

where: I_{1b} is the primary side base current, and I_{2b} is the secondary side base current. Per-unit mmf is written

$$\begin{aligned} i_k^{pu} &= \theta_k^{pu} && \text{(E.11)} \\ &= G(H_k) && \text{(E.12)} \\ &= \frac{\theta_k}{\theta_b} && \text{(E.13)} \\ &= \frac{l_k}{\sqrt{2} N_1 I_{1b}} H_k && \text{(E.14)} \\ &= \frac{l_k}{\sqrt{2} N_2 I_{2b}} H_k && \text{(E.15)} \end{aligned}$$

The transformer winding-limb length and cross-sectional area dimensions will not usually equal those of yoke. Dissimilar length l_k and cross-sectional area A_k dimensions produce dissimilar per-unit winding-limb and yoke ϕ_k^{pu}-i_k^{pu} saturation characteristics, from the one core steel $B - H$ curve.

Appendix F

LABORATORY AND SIMULATION PARAMETERS

Sine-wave generator

Rating	3.0 kVA
Voltage	230 V
Frequency	50 Hz
L_{source}	115 mH
R_{source}	0.3 Ω

Test transformer data

Type	Single-phase
Rating	2.0 kVA
Primary voltage	210 V
Secondary voltage	210 V
X_l	0.3362 p.u.
R_{prim}	0.5 Ω
R_{sec}	0.5 Ω

UMEC test transformer model parameters

Winding-limb length	0.0580 m
Winding-limb area	0.0049 m^2
Yoke length	0.2960 m
Yoke area	0.0049 m^2
Primary winding turns number	250 Turns
Secondary winding turns number	250 Turns
L_{l1}	11.8 mH
L_{l2}	11.8 mH
m_1	0.124
m_2	6.3e-4
b_1	0.0
b_2	0.77
$\mathcal{E}$	1.85

PSCAD-EMTDC test transformer model parameters

Rating	2.0 kVA
Frequency	50 Hz
X_L	0.3362 p.u.
No-load losses	0.0 p.u.
Ideal transformer?	Yes
Tap changer winding?	None
Primary winding voltage	210 V
Primary side magnetising current	1.66%
Secondary winding voltage	210 V
Secondary side magnetising current	1.66%
Saturation enabled?	Yes
Saturation placement	Primary
Air core reactance	6.27 p.u.
In-rush decay time constant	1e-3 secs
Knee voltage	1.0 p.u.
Time to release flux clipping	0.0 secs

Series resonant load

R_{load}	0.364 Ω
L_{load}	40 mH
C_{load}	10 μF

Appendix G

BENMORE GENERATOR AND INTERCONNECTING TRANSFORMER PARAMETERS

Generators G1-G3

Rating	112.5 MVA
Voltage	16.0 kV
Frequency	50 Hz
x''	0.1820 p.u.
R_a	0.0042 p.u.

Interconnecting transformer data

Type	Three-phase bank; Delta-Star-Star
Rating	200 MVA
Primary voltage	16 kV
Secondary voltage	220 kV
Tertiary voltage	33 kV
$X_{l(prim-ter)}$	0.0392 p.u. (66.67 MVA base)
R_{prim}	0.004 Ω
R_{ter}	0.016 Ω

UMEC per-phase interconnecting transformer model parameters

Winding limb length	1.0 m
Winding limb area	0.4536 m^2
Yoke length	9.836 m
Yoke area	0.4536 m^2
Primary winding turns number	113 Turns
Secondary winding turns number	897 Turns
Tertiary winding turns number	135 Turns
L_{l1}	0.243 mH
L_{l3}	0.345 mH

m_1	0.0145
m_2	1.59e-5
b_1	0.0
b_2	1.72
$\mathcal{E}$	1.90

The winding turns have been estimated assuming a peak operating flux density of 1.4T at rated voltage and frequency.

PSCAD-EMTDC per-phase interconnecting transformer model parameters

Rating	66.67 MVA
Frequency	50 Hz
X_L	0.0392 p.u.
No-load losses	0.0 p.u.
Ideal transformer?	Yes
Tap changer winding?	None
Primary winding voltage	16 kV
Primary side magnetising current	1.0%
Secondary winding voltage	19.0526 kV
Secondary side magnetising current	1.0%
Saturation enabled?	Yes
Saturation placement	Primary
Air core reactance	0.6667 p.u.
In-rush decay time constant	1.0 secs
Knee voltage	1.25 p.u.
Time to release flux clipping	0.0 secs

33kV Filters (Series RLC)

	Harmonic number				
	5	7	9	11	13
R_{filter} (Ω)	0.412	0.454	0.560	0.249	0.305
L_{filter} (mH)	13.1	10.3	10.0	3.60	3.75
C_{filter} (μF)	30.9	20.0	12.1	23.2	16.1

Appendix H

MANAPOURI TRANSFORMER TECHNICAL DOCUMENTATION

Delta-star Dy11, connection matrix

$$[C] = \begin{bmatrix} 1 & 0 & 0 & 0 & -1 & 0 \\ 0 & 1 & 0 & 0 & 0 & 0 \\ -1 & 0 & 1 & 0 & 0 & 0 \\ 0 & 0 & 0 & 1 & 0 & 0 \\ 0 & 0 & -1 & 0 & 1 & 0 \\ 0 & 0 & 0 & 0 & 0 & 1 \\ 0 & -1 & 0 & -1 & 0 & -1 \end{bmatrix} \tag{H.1}$$

savigliano
TEST DEPARTMENT

PURCHASER DOMINION OF NEW ZEALAND
MINISTRY OF WORKS

Report No 16143
Purchaser's Order No 7224-201 C
Mfr's References 111386

TRANSFORMER N. 60372 TYPE TRA kVA 105.000

H.V. kV A 262 - 270 - 276 - 283 - 290

L.V. On load kV A 4390

kV A

2x18 2x18

H.V. kV 231 - 225,5 - 220 - 214,5 - 209 Turns 754 .. 718 .. 682

L.V. At no-load kV 13,8 Turns 78

kV Turns

CONNECTIONS Y/Δ GROUP Yd1 PHASES 3 FREQ 50

RESISTANCES amb. temp. = °C - oil temp. = 29,5°C

H.V. Winding				H.V. Winding				L.V. Winding			
Tap-changer position Phases	V x0,01	I x0,02	R	Tap-changer position Phases	V x0,01	I x0,02	R	Tap-changer position Phases	V x0,0005	I x 0,1	R
1 - A_8N	139	102,3	0,6793	4 - A_8N	130,3	102,8	0,627	a_2b_2	83	117,1	0,003544
1 - B_8N	139,4	102,6	0,6793	4 - B_8N	130	102,6	0,6265	b_2c_2	83,8	116	0,003611
1 - C_8N	139,4	102,8	0,678	4 - C_8N	130,2	102,8	0,6265	a_2c_2	84	116,8	0,003535
		Avg.=	0,67886			Avg.=	0,6266			Avg.=	0,003583
At 75°C			0,7862	At 75°C			0,7342	At 75°C			0,004202
2-A_8N	136	102,4	0,664	5 - A_8N	127,4	103,2	0,6174				
2-B_8N	136,2	102,6	0,663	5 - B_8N	127,4	102,8	0,6196				
2-C_8N	136,5	102,8	0,664	5 - C_8N	127	102,9	0,6171				
		Avg.=	0,6636			Avg.=	0,61800				
At 75°C			0,778	At 75°C			0,7245				
3 - A_8N	133,2	102,6	0,64912								
3 - B_8N	133,2	102,7	0,64849								
3 - C_8N	133,1	102,8	0,64737								
		Avg.=	0,64833								
At 75°C			0,760								

Tested 30-31/7/1969 Inspected by Mr.Dover

Date, 15 OTT 1969 Signed

Us. Tip. Cassia - mod. 1181 - 12-64 - 1000

NO-LOAD RATIO TEST

Tap-changer pos.	Calculated t. r.				Measured t. r.								
	H.V. kV	L.V. kV	..... kV	K	V.....			V.....			K/√3		
											$\frac{A_8N}{a_2b_2}$	$\frac{B_8N}{b_2c_2}$	$\frac{C_8N}{c_2a_2}$
1	231	13,8		16,75							9,68	=	=
2	225,5	"		16,35							9,45	=	=
3	220	"		15,95							9,215	=	=
4	214,5	"		15,55							8,982	=	=
5	209	"		15,15							8,752	=	=

NO-LOAD TEST

Feeding from L.V. kV 13,8 — Frequency 50 Hz.

Vr.m.s. x160	Vm.x 1,11 x 160	I_1 x 5	I_2 x 5	I_3 x 5	W_1 x 400	W_2 x400	W_3 x 400	kVr.m.s.	kVmx1,11	I	kW	cosφ_0
76,1	76,5	2,77	2,32	1,95	83,6	10,6	69,9	12,18	12,24	11,73	65,64	
79,8	80,2	3,6	3	2,56	100,1	4,2	86,5	12,77	12,84	15,265	76,32	
83,6	83,9	4,67	3,95	3,38	120,7	-4,9	107,3	13,38	13,43	20	89,24	
		x10	x10	x10	x800	x800	x800					
87,9	87,6	3,18	2,69	2,34	73	-9,6	69	14,07	14,02	27,36	109,92	
90,5	90,4	3,94	3,38	3	88	-13,7	79,6	14,48	14,47	34,4	123,12	
		x20	x20	x20	x1600	x1600	x1600					
95,6	94,5	2,95	2,6	2,39	54,3	-9,9	50,9	15,3	15,12	52,93	152,48	
					See attached diagram			13,8	13,8	24,2	98,7	

Un. Tip. Cessio - Mod. 1646 - 9.44 - 1000

Test temperature 29,5 °C

Tap-changer position	V (kV)	I (A)	P (kW)	Reference temperature 75 °C: RI² losses (kW)	Stray load losses (kW)	Total losses (kW)	cos φ_{cc}
3	20,16	224,1	233,4				
	19,35	215,5	215,45				
	18,80	209,3	203,75				
	24,79	276	353,8	295,113	87	382,113	0,0323
	Esc % = $\frac{24,79}{220}$ ×100 = 11,27 %						
1	22,23	225,25	252,75				
	21,71	220,5	242,6				
	21,11	213,91	228,45				
	25,85	262	342,5	285,311	84,5	369,811	0,0315
	Esc% = $\frac{25,85}{231}$ 100 = 11,19 %						
5	18,48	224,3	225,6				
	17,98	218,75	213,55				
	17,41	211,3	200,55				
	23,87	290	376,5	304,200	99,8	404	0,0337
	Esc % = $\frac{23,87}{209}$ 100 = 11,42 %						

HIGH-VOLTAGE TESTS (oil temperature 29,5 °C)

(*) Induced voltage test: kV 395 Hz 160 time sec. 40

Applied voltage test: (H = mmHg — t = °C)

	Ø of spheres mm	Distance mm	Calibration at kV: correct	Calibration at kV: no correct	Voltmeter readings	Test at kV	Voltmeter readings	Time sec
H.V.	V.T. 40000/100 V					34	85	60
L.V.						38	95	60

(*) The H.V. terminals raised by induced voltage to 395 kV for 40" at 160 c.p.s. with neutral terminal earthed (B.S. 171 — Clause 1810).

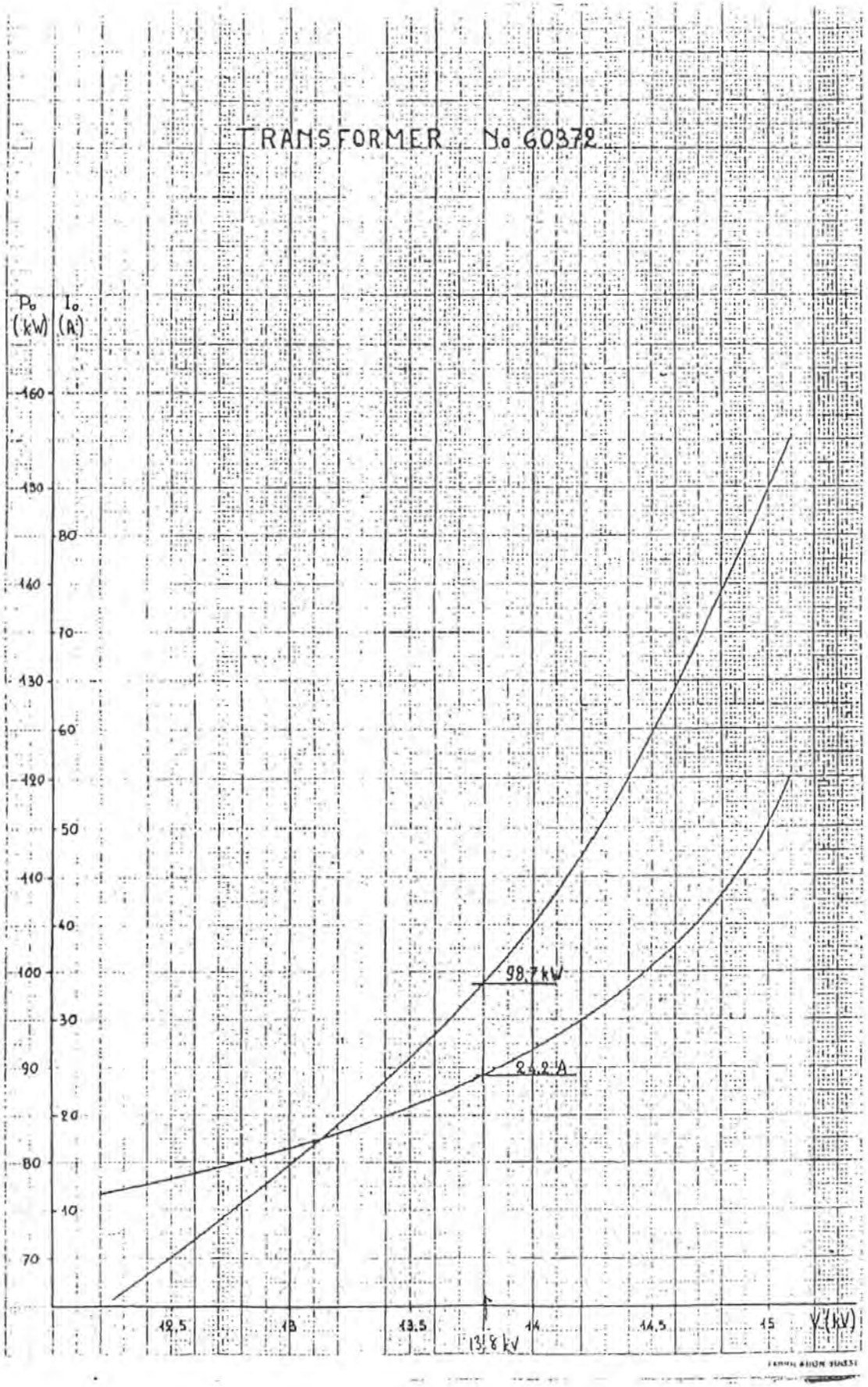
TRANSFORMER No 60372
Po (kW)
Io (A)
160
150
140
130
120
110
100
90
80
70
80
70
60
50
40
30
20
10
98,7 kW
82,2 A
12,5
13
13,5
13,8 kV
14
14,5
15
V (kV)

SHORT-CIRCUIT TEST

Feeding from H.V. I 276 Amps (p.3) Frequency 50 c.p.s.

	Tap changer position	Δ V x 160	Δ I x 50	Δ W x 1000	V (kV)	I (A)	P (kW)	tang φ	ε_A	ε_V	$(\varepsilon_A - \varepsilon_V)$ tang φ	Pcorr. (kW)
Phase C	3	126	4,47	87,9	20,16	223,5	87,9	29,59	0,228	0,08	9,11	79,9
		121	4,30	81,4	19,35	215	81,4	29,51	0,232	−0,083	9,30	73,85
		117,5	4,18	76,8	18,80	209	76,8	29,52	0,235	0,085	9,45	69,55
	1	139	4,49	94,7	22,23	224,5	94,7	30,42	0,228	−0,072	9,13	86,1
		136	4,39	91,2	21,77	219,5	91,2	30,22	0,230	−0,074	9,19	82,8
		132	4,27	86	21,11	213,5	86	30,24	0,233	−0,077	9,37	77,95
	5	115,5	4,47	84,6	18,48	223,5	84,6	28,13	0,228	−0,086	8,83	77,15
		112,4	4,36	80	17,98	218	80	28,23	0,230	−0,088	8,98	72,85
		108,8	4,22	74,8	17,41	211	74,8	28,32	0,234	−0,089	9,15	67,95
Phase B	3	126	4,49	85,2	20,16	224,5	85,2	30,66	0,198	−0,096	9,02	77,55
		121	4,32	78,8	19,35	216	78,8	30,60	0,201	−0,100	9,21	71,55
		117,5	4,19	74,7	18,80	209,5	74,7	30,43	0,204	−0,102	9,31	67,75
	1	139	4,515	92,1	22,23	225,75	92,1	31,45	0,197	−0,085	8,87	83,9
		136	4,42	88,4	21,77	221	88,4	31,39	0,199	−0,088	9,01	80,55
		132	4,285	83,6	21,11	214,25	83,6	31,22	0,202	−0,092	9,18	75,90
	5	115,5	4,50	82	18,48	225	82	29,25	0,198	−0,104	8,83	74,75
		112,4	4,385	77,8	17,98	219,25	77,8	29,23	0,200	−0,105	8,92	70,90
		108,8	4,23	72,9	17,41	211,5	72,9	29,13	0,203	−0,107	9,03	67,3
Phase A	3	126	4,49	84,3	20,16	224,5	84,3	30,99	0,222	−0,099	9,94	75,95
		121	4,31	78,1	19,35	215,5	78,1	30,83	0,226	−0,101	10,08	70,05
		117,5	4,19	74	18,80	209,5	74	30,71	0,23	−0,102	10,19	66,45
	1	139	4,51	91,7	22,23	225,5	91,7	31,58	0,222	−0,087	9,76	82,75
		136	4,42	88	21,77	221	88	31,53	0,225	−0,091	9,97	79,25
		132	4,28	83	21,11	214	83	31,41	0,228	−0,095	10,14	74,6
	5	115,5	4,49	81,6	18,48	224,5	81,6	29,32	0,222	−0,103	9,53	73,8
		112,4	4,38	77,3	17,98	219	77,3	29,39	0,225	−0,105	9,7	69,8
		108,8	4,23	72,4	17,41	211,5	72,4	29,35	0,229	−0,106	9,83	65,3

Transformer Serial No. 60372

savigliano

TEST PERFORMANCE

(Referred to Exhibit G of the contract)

Ref.		Unit	Measured	Guaranteed
G1.1				
(a)	Resistances (75°C)			
	Transformer resistance voltage percent on medium tap.	%	0,364	0,333
	High tension winding ohms per phase	ohm	0,760	0,79
	Low tension winding ohms per phase	"	0,00630	0,0064
(b)	Impedance			
	Transformer impedance percent, on medium tap.	%	11,27	12
	Zero sequence impedance percent	"	10,25	11
(c)	Transformer reactance voltage percent, on medium tap.	"	11,26	11,99
(d)	Exciting current (13,8 kV)	Amps	24,2	20
G.1.2				
(a)	No load losses at rated voltage	kW	98,70	96
(b)	Load losses			
	" " at 115 % rated kVA	"	506	463
	" " " 100 % " "	"	382,113	350
	" " " 75 % " "	"	215,0	196
	" " " 50 % " "	"	95,5	87,5
(c)	Regulation on medium tap			
	Regulation at 100 % rated kVA and.			
	100 % p.F.	%	0,998	1,05
	90 " "	"	5,73	6,08
	80 " "	"	7,442	7,90
(d)	Efficiency			
	Efficiency at 100 % power factor			
	at 115 % rated kVA	"	99,496	99,48
	at 100 " " "	"	99,541	99,53
	at 75 " " "	"	99,599	99,58
	at 50 " " "	"	99,626	99,60

savigliano	Nucleo magnetico a cornice n. 14 gradini	C.° 1606 TR 910669/A

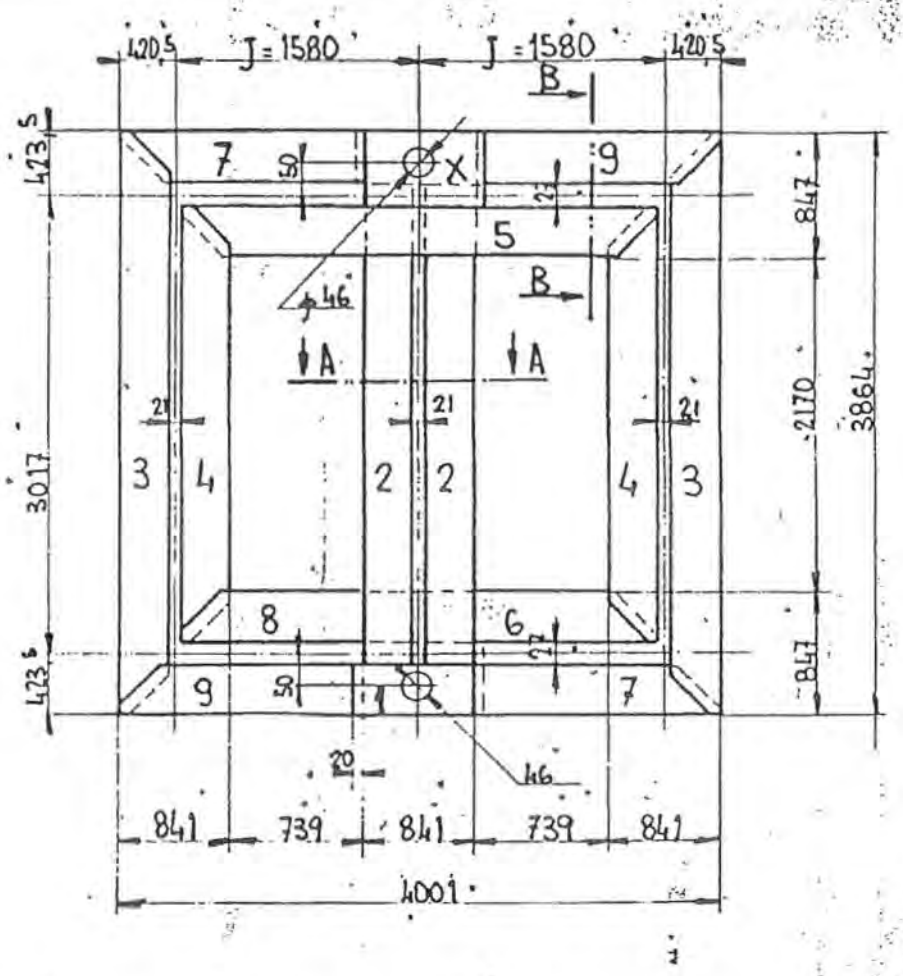

Diametro colonna: ϕ 850 mm - Peso tot. 54145 kg. - Sez. netta 4820 cm²

Impaginatura: n° 2 lamierini per strato

Strati dispari: linea unita (—) - Strati pari linea a tratti (- - -)

Materiale: lamierino a cristalli orientati - Tipo M6X - sp. nudo 0,35 - isol. 0,365

Isolanti pressopann sp. 0,2

Dopo il taglio e la punzonatura i lamierini dovranno essere ricotti alla temperatura di 800° C.

Torino: 21-3-66 - Firma Lattuada L. - Contr. Mariotti - Visto

Terni-M6T35 Magnetizzazione e permeabilità in c.c.

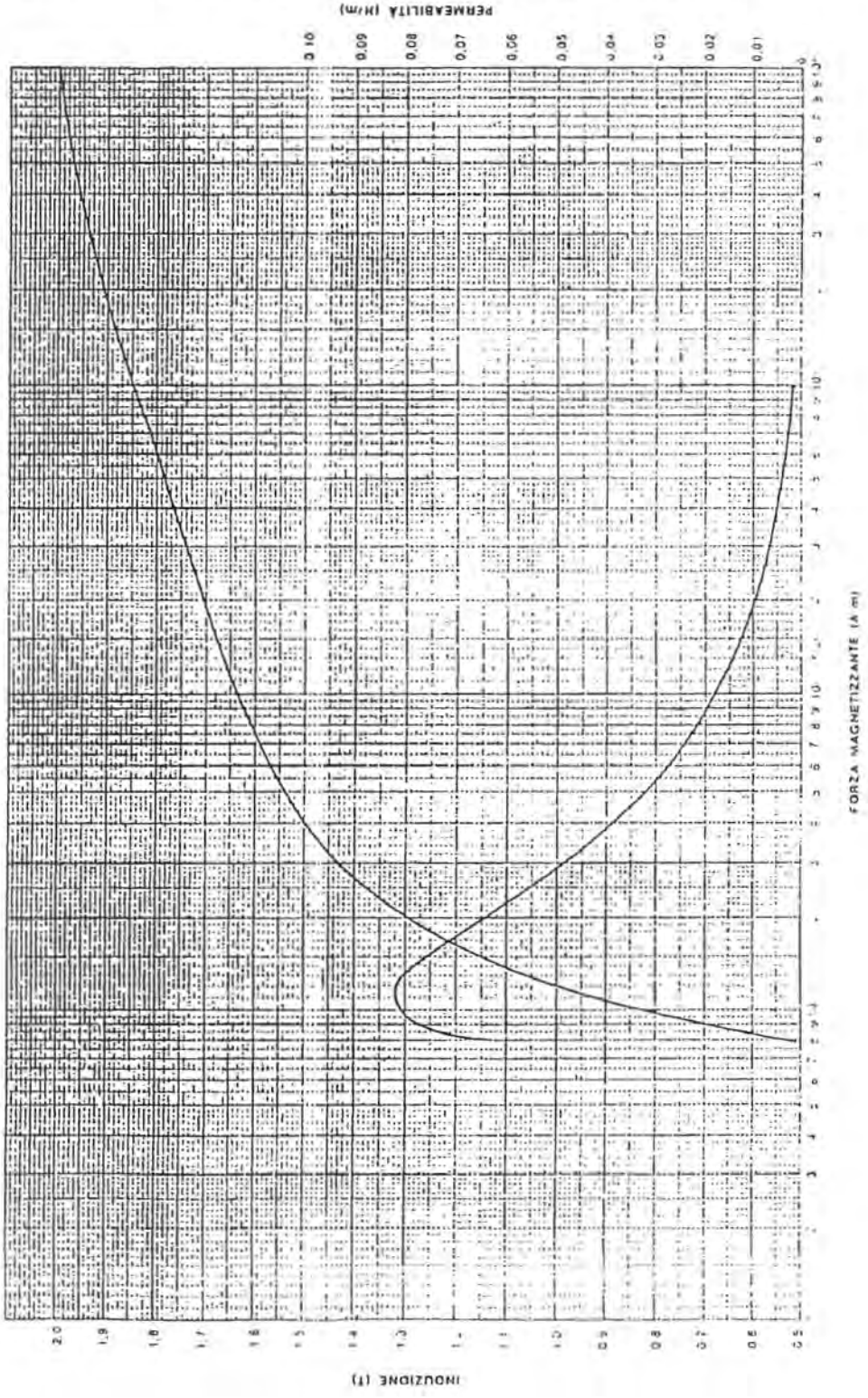

Montaggio a giunti doppiamente sovrapposti
Densità assunta 7650 kg/m³

Prove eseguite con apparecchio Epstein.
Provini ricavati nella direzione di laminazione e sottoposti a ricottura a 800° C (1472° F)

Forza di eccitazione Terni-M6T35

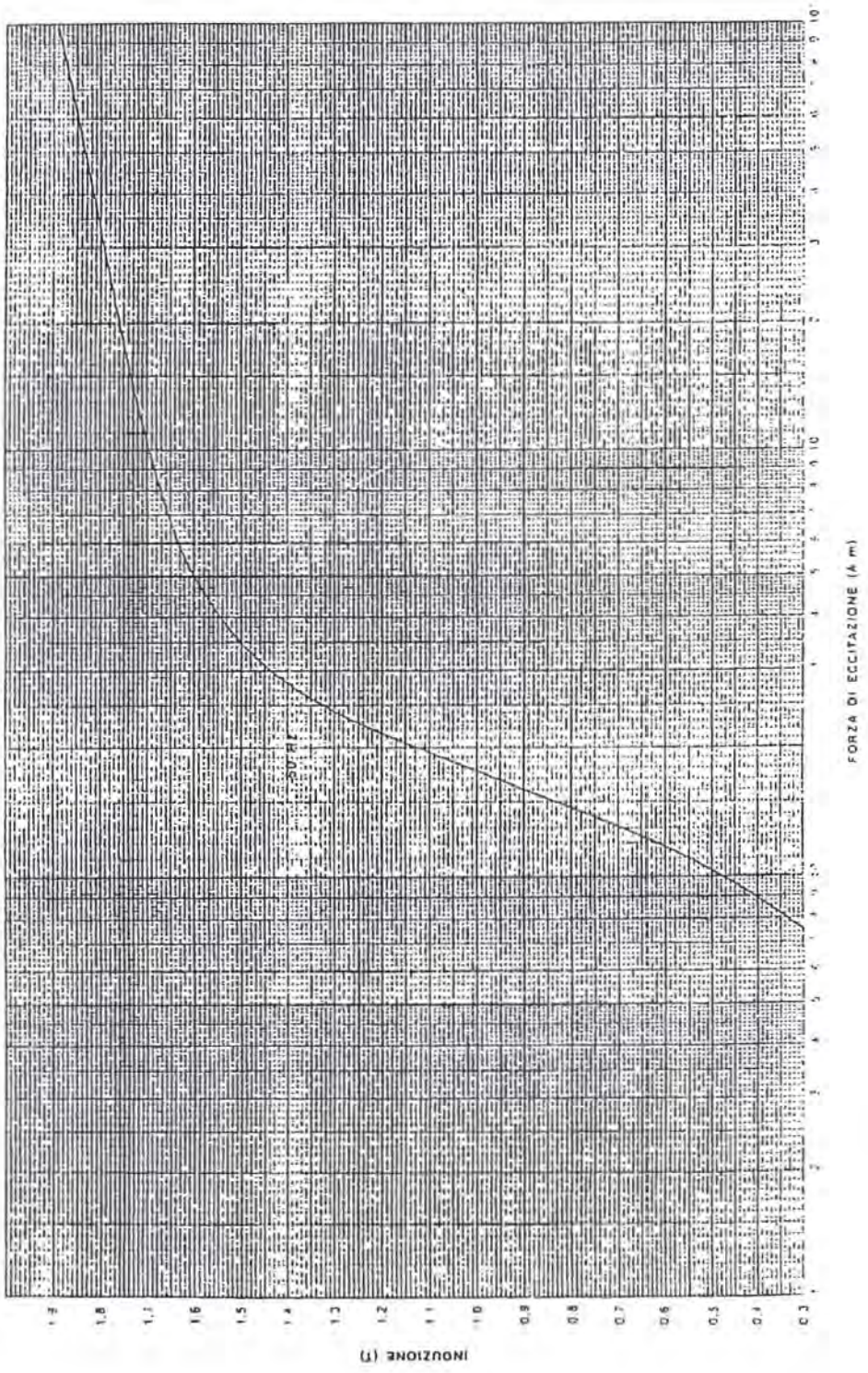

Perdita Terni-M6T35

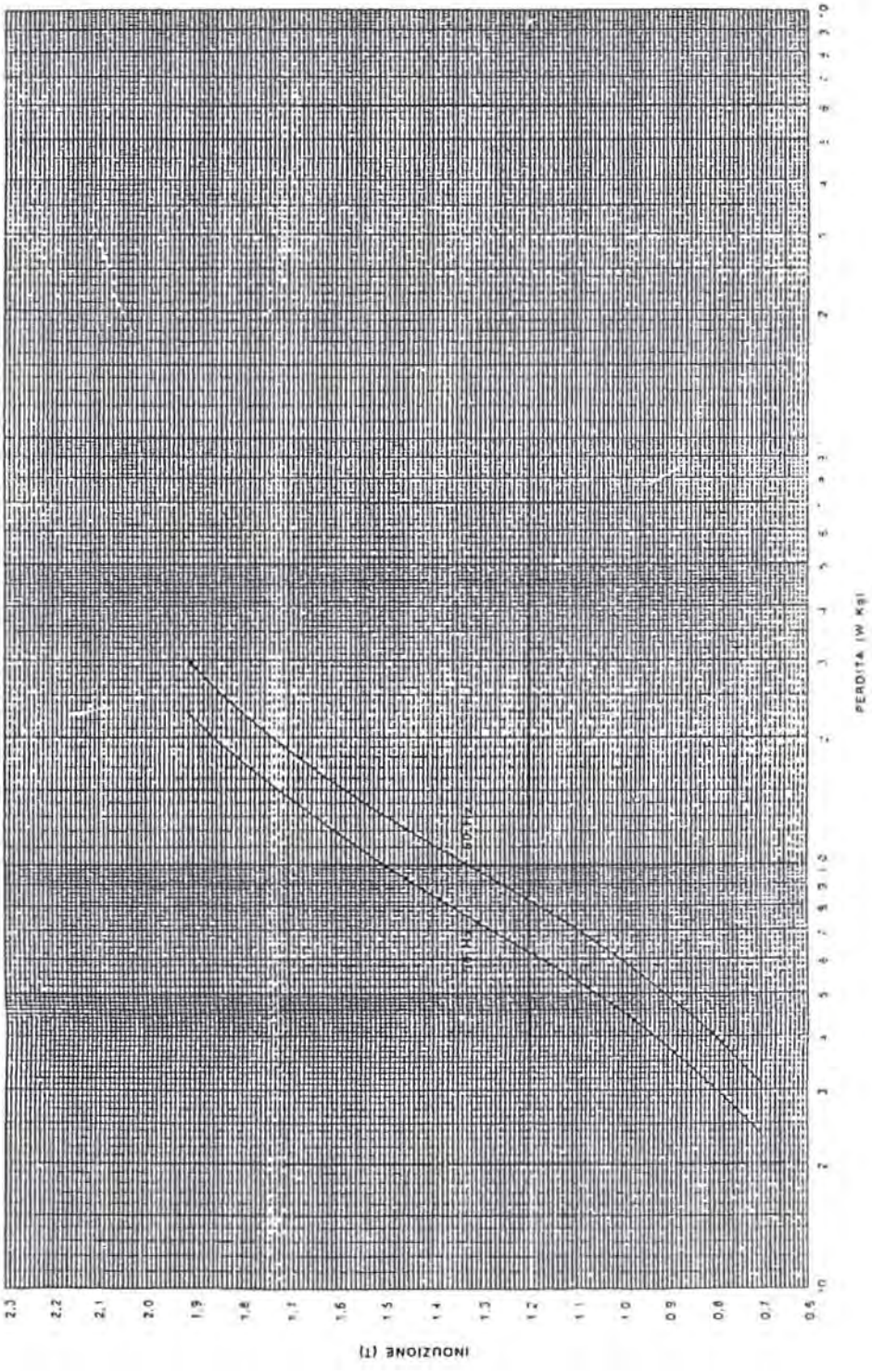

Terni-M6T35 Potenza di eccitazione

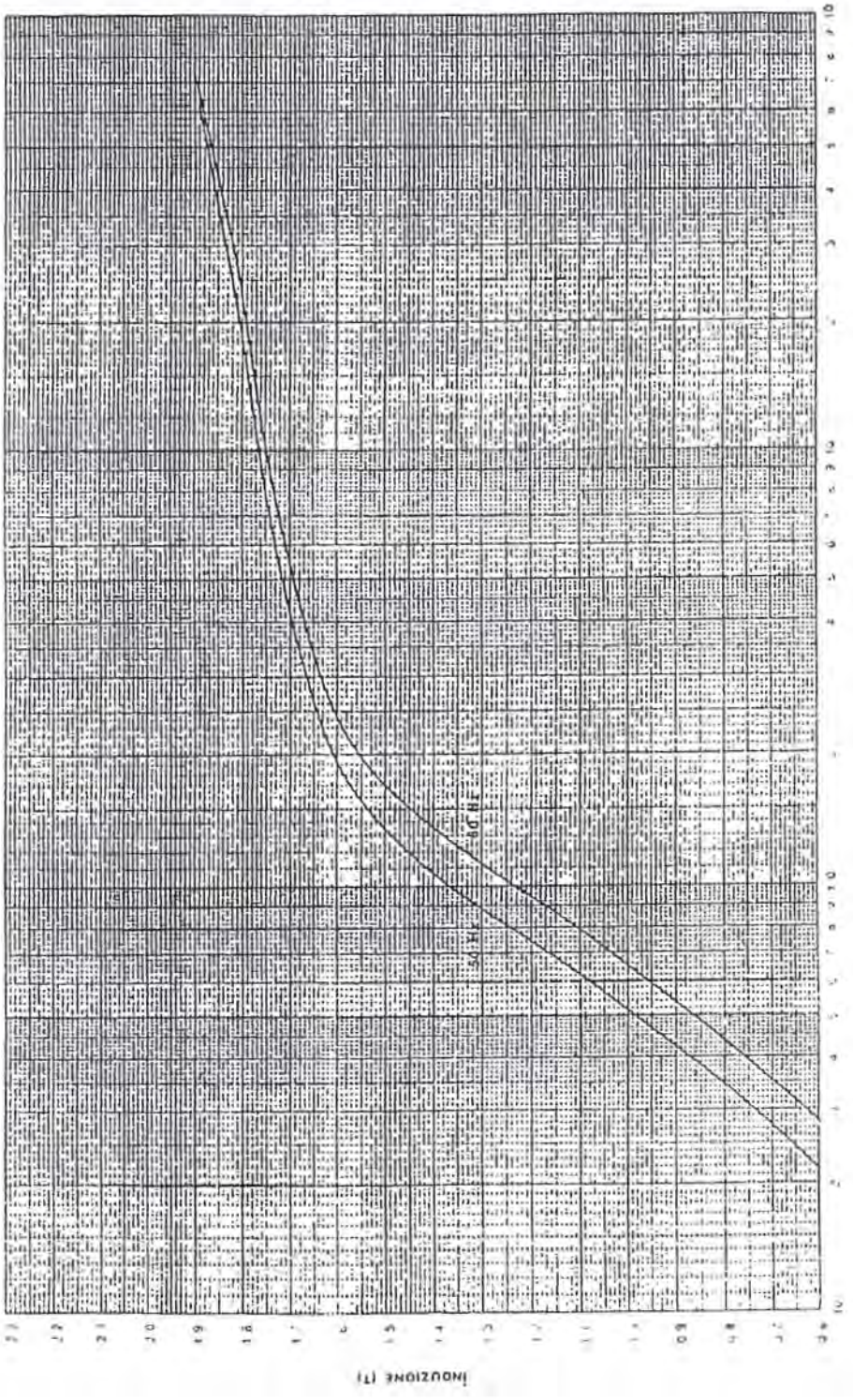

Isteresi in c.c. Terni-M6T35

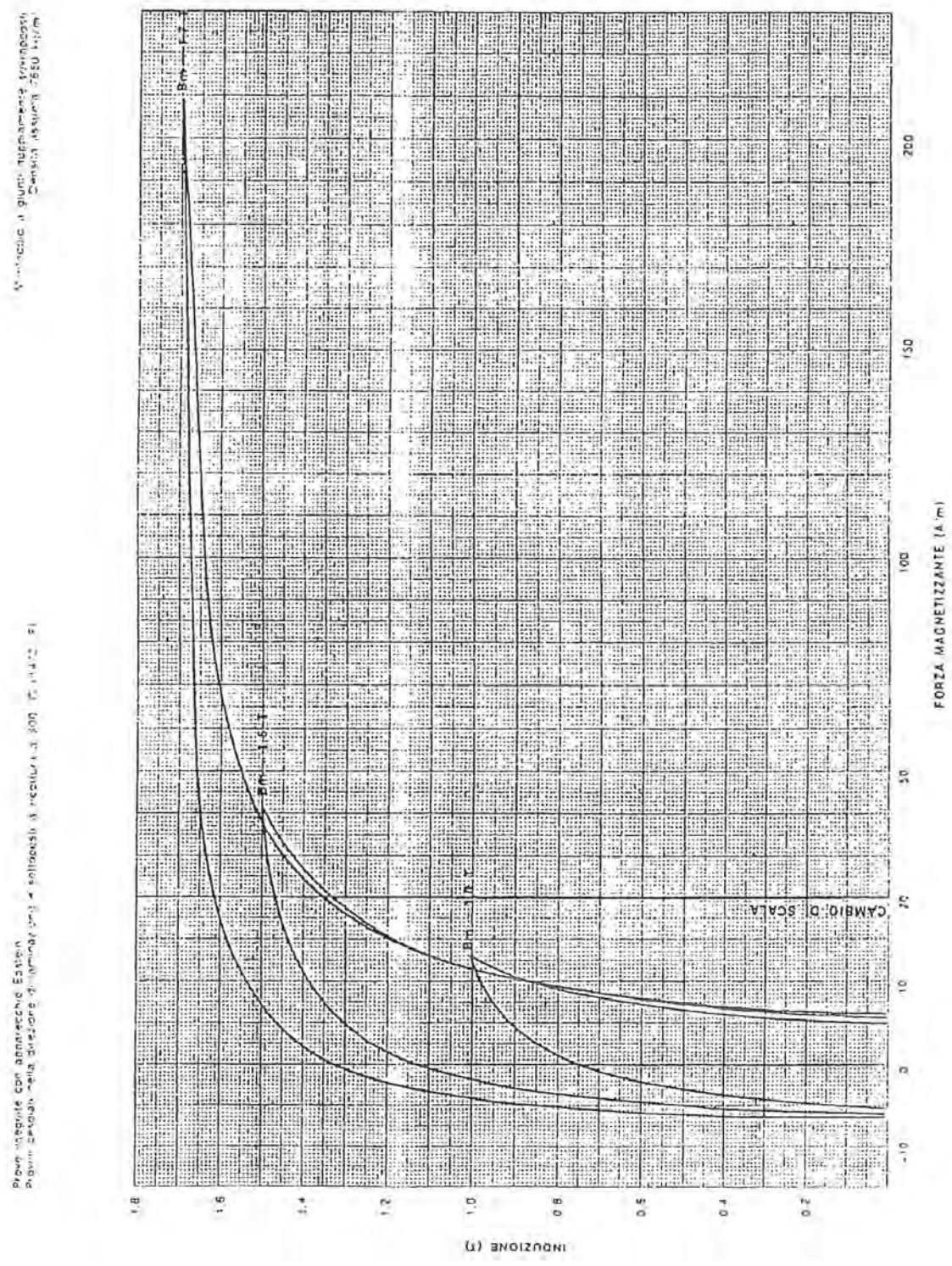

Appendix I

BENMORE POLE 1A PARAMETERS

I.1 UMEC SINGLE-PHASE VALIDATION DATA

chapter 5

Generators G1-G3 data

Rating	112.5 MVA
Voltage	16.0 kV
x_d	1.168 p.u.
x'_d	0.264 p.u.
x''_d	0.174 p.u.
x_q	0.672 p.u.
x''_q	0.19 p.u.
T'_{do}	8.7 secs
T''_{do}	0.087 secs
T''_{qo}	0.132 secs
X_l	0.15 p.u.
R_a	0.0042 p.u.

Converter transformer data

Type	Three-phase banks; Delta-Star, and Delta-Delta
Rating	187.5 MVA
Primary voltage	16 kV
Secondary voltage	110 kV
$X_{l(prim-ter)}$	0.113 p.u. (62.5 MVA base)

PSCAD-EMTDC generator model parameters

Inertia constant	3.42 MW/MVA
Base angular frequency	314.15926 rad/sec
Mechanical damping	1e-4 p.u.
Rated rms phase voltage	9.238 kV
Rated rms phase current	4.0595 kA

Terminal voltage magnitude at t-	0 p.u.
Terminal voltage phase at t-	0 rad
Real power at t-	0 MW
Reactive power at t-	0 MVAr
Number of coderant machines	3.0
Potier reactance	0.14587 p.u.
Direct-axis reactance	1.16775 p.u.
Direct-axis transient reactance	0.30814 p.u.
Direct-axis sub-transient reactance	0.19913 p.u.
Damper-field mutual reactance	0 p.u.
Quad-axis reactance	0.67163
Quad-axis sub-transient reactance	0.19913 p.u.
Armature resistance	0.00042 p.u.
Armature time constant	0.37127 secs
Direct-axis transient time constant	8.7 secs
Direct-axis subtransient time constant	0.087sec
Air-gap factor	0.8
X_1	0.0
Y_1	0.0
X_2	0.5
Y_2	0.5
X_3	0.8
Y_3	0.79
X_4	0.1
Y_4	0.947
X_5	1.2
Y_5	1.076
X_6	1.5
Y_6	1.2
X_7	1.8
Y_7	1.26
X_8	2.2
Y_8	1.32
X_9	3.2
Y_9	1.53
X_10	4.2
Y_10	1.74

UMEC per-phase converter transformer model parameters

Winding limb length	3.59 m
Winding limb area	0.4536 m^2
Yoke length	2.656 m
Yoke area	0.4536 m^2
Primary winding turns number (Delta-Star and Delta-Delta)	113 Turns
Secondary winding turns number (Delta-Star)	450 Turns
Secondary winding turns number (Delta-Delta)	780 Turns
L_{l1} (Delta-Star and Delta-Delta)	0.768 mH
L_{l2} (Delta-Star)	11.8 mH
L_{l2} (Delta-Delta)	35.6 mH
m_1	0.021
m_2	3.0e-5
b_1	0.0
b_2	1.63
$\mathcal{E}$	1.90

PSCAD-EMTDC converter model parameters

Rated frequency	50 Hz
Thyristor configuration variable (Delta-star)	0
Thyristor configuration variable (Delta-Delta)	-1
Firing pulses	PLO
PLO proportional gain	10.0
PLO integral gain	100.0
PLO input reference varaible	0
Snubber resistance	2400 Ω
Snubber capacitance	0.29 μF
Thyristor on resistance	0.01 Ω
Thyristor off resistance	1.0e6 Ω
Forward voltage drop	0.001 kV
Forward break-over voltage	1.0e5 kV
Minimum extinction time	0.0 μsecs

I.2 UMEC CONVERTER TRANSFORMER COMPARISON DATA

chapter 7

I.2.1 Delta-primary, 110kV fault

UMEC three-limb three-phase converter transformer Dd0

Winding-limb length	3.59 m
Winding-limb area	0.4536 m^2
Yoke length	2.656 m
Yoke area	0.4536 m^2
Primary winding turns number	113 Turns
Secondary winding turns number	780 Turns
$\mathcal{P}_{7,9,11}$	5.85e-8
$\mathcal{P}_{8,10,12}$	5.85e-8
$\mathcal{P}_{15,16,17}$	5.85e-8
m_1	0.021
m_2	3.0e-5
b_1	0.0
b_2	1.63
$\mathcal{E}$	1.90

Connection matrix

$$[C] = \begin{bmatrix} 1 & 0 & 0 & 0 & -1 & 0 \\ 0 & 1 & 0 & 0 & 0 & -1 \\ -1 & 0 & 1 & 0 & 0 & 0 \\ 0 & -1 & 0 & 1 & 0 & 0 \\ 0 & 0 & -1 & 0 & 1 & 0 \\ 0 & 0 & 0 & -1 & 0 & 1 \end{bmatrix} \tag{I.1}$$

UMEC three-limb three-phase converter transformer Dy11

Winding limb length	3.59 m
Winding limb area	0.4536 m^2
Yoke length	2.656 m
Yoke area	0.4536 m^2
Primary winding turns number	113 Turns
Secondary winding turns number	450 Turns
$\mathcal{P}_{7,9,11}$	5.85e-8
$\mathcal{P}_{8,10,12}$	5.85e-8
$\mathcal{P}_{15,16,17}$	5.85e-8
m_1	0.021
m_2	3.0e-5
b_1	0.0
b_2	1.63
$\mathcal{E}$	1.90

Connection matrix

$$[C] = \begin{bmatrix} 1 & 0 & 0 & 0 & -1 & 0 \\ 0 & 1 & 0 & 0 & 0 & 0 \\ -1 & 0 & 1 & 0 & 0 & 0 \\ 0 & 0 & 0 & 1 & 0 & 0 \\ 0 & 0 & -1 & 0 & 1 & 0 \\ 0 & 0 & 0 & 0 & 0 & 1 \\ 0 & -1 & 0 & -1 & 0 & -1 \end{bmatrix} \tag{I.2}$$

PSCAD-EMTDC circuit-breaker model

Initial state	Closed
Use pre-insertion resistances?	No
Breaker open resistance	1.0e6 Ω
Breaker closed resistance	0.005 Ω
Open possible if current flowing?	No
Time to open breaker	1.05 secs
Time to close breaker	1.08 secs
Repeat	No

PSCAD-EMTDC bypass valve model

Snubber resistance	2400 Ω
Snubber capacitance	0.01 μF
Thyristor on resistance	0.005 Ω
Thyristor off resistance	1.0e6 Ω
Forward voltage drop	0.001 kV
Forward break-over voltage	1.0e5 kV
Minimum extinction time	0.0 μsecs

PSCAD-EMTDC fault parameters

Fault on resistance	30 Ω
Fault off resistance	1.0e6 Ω
Is phase A in fault?	Yes
Is phase B in fault?	No
Is phase C in fault?	No
Is fault to ground?	Yes
Clear possible if current flowing	No
Time to apply fault	1.00 secs
Duration of fault	0.08 secs
Repeat	No

I.2.2 Star-primary, 16kV fault

UMEC three-limb three-phase converter transformer Yy0

All parameters the same as Dd0 except:

Primary winding turns number	65 Turns
Secondary winding turns number	450 Turns

Connection matrix

$$[C] = \begin{bmatrix} 1 & 0 & 0 & 0 & 0 & 0 \\ 0 & 1 & 0 & 0 & 0 & 0 \\ 0 & 0 & 1 & 0 & 0 & 0 \\ 0 & 0 & 0 & 1 & 0 & 0 \\ 0 & 0 & 0 & 0 & 1 & 0 \\ 0 & 0 & 0 & 0 & 0 & 1 \\ 0 & -1 & 0 & -1 & 0 & -1 \end{bmatrix} \tag{I.3}$$

UMEC three-limb three-phase converter transformer Yd11

All parameters the same as Dy11 except:

Primary winding turns number	65 Turns
Secondary winding turns number	780 Turns

Connection matrix

$$[C] = \begin{bmatrix} 1 & 0 & 0 & 0 & 0 & 0 \\ 0 & 1 & 0 & -1 & 0 & 0 \\ 0 & 0 & 1 & 0 & 0 & 0 \\ 0 & 0 & 0 & 1 & 0 & -1 \\ 0 & 0 & 0 & 0 & 1 & 0 \\ 0 & -1 & 0 & 0 & 0 & 1 \end{bmatrix} \tag{I.4}$$

PSCAD-EMTDC circuit-breaker, bypass valve and fault paramters for the 16kV fault are identical to the 110kV fault except the fault resistance is changed 0.1 Ω.

Appendix J

SMOOTHING TRANSFORMER TEST SYSTEM PARAMETERS

PSCAD-EMTDC three-phase source model parameters	
Type	resistive
External voltage control?	No
External frequency control?	No
Initial phase	0.0 deg
Impedance	1.0 Ω
Voltage magnitude (ac, L-L, rms)	0.707 kV
Ramp up time	0.2 sec
Frequency	50 Hz
PSCAD-EMTDC converter model parameters	
Rated frequency	50 Hz
Thyristor configuration variable	0
Firing pulses	PLO
PLO proportional gain	10.0
PLO integral gain	100.0
PLO input reference varaible	0
Snubber resistance	5000 Ω
Snubber capacitance	0.05 μF
Thyristor on resistance	0.01 Ω
Thyristor off resistance	1.0e6 Ω
Forward voltage drop	0.001 kV
Forward break-over voltage	1.0e5 kV
Minimum extinction time	0.0 μsecs

UMEC smoothing transformer model parameters

(a) Linear model.

Branch	$m_{1(linear)}$
Winding limb	292.38
Yoke	292.38
leak-path	4.17e-2

Table J.1 Per-unit smoothing transformer iron-core characteristics.

Base frequency 50 Hz

Dc blocking capacitor 10 mF

(a) Non-linear model.

Branch	$m_{1(linear)}$	$m_{2(sat)}$	b_1	b_2	$\mathcal{E}$
Winding limb	292.38	0.67	0.0	1.03	0.85
Yoke	292.38	1.67	0.0	1.03	0.0
leak-path	4.17e-2				

Table J.2 Per-unit smoothing transformer iron-core saturation characteristics.

Base frequency 50 Hz

Dc blocking capacitor 10 mF

Dc load parameters

Linear smoothing transformer I_{dc} 0.62 p.u.

Non-linear smoothing transformer (α=15^o) I_{dc} 0.75 p.u.

Non-linear smoothing transformer (α=60^o) I_{dc} 0.18 p.u.

Appendix K

CONVERTER TRANSFORMER MODEL PARAMETERS AND DC LINE DATA

PSCAD-EMTDC delta-star converter transformer model parameters

Transformer name	Delta-Star
Three-phase transformer MVA	187.5 MVA
Base operation frequency	50 Hz
Winding #1 Type	Delta
Winding #2 Type	Star
Delta leads of lags star?	Lags
Positive sequence leakage reactance	0.113 p.u.
Ideal transformer model ?	No
No-load losses	0.0 p.u.
Tap-changer winding	#2
Winding 1 line to line voltage	16 kV
Magnetising current	1.0 %
Winding 2 line to line voltage	110 kV
Magnetising current	1.0 %
Saturation enabled?	No

PSCAD-EMTDC delta-delta converter transformer model parameters

Transformer name	Delta-Delta
Three-phase transformer MVA	187.5 MVA
Base operation frequency	50 Hz
Winding #1 Type	Delta
Winding #2 Type	Delta
Positive sequence leakage reactance	0.113 p.u.
Ideal transformer model ?	No
No-load losses	0.0 p.u.
Tap-changer winding	#2
Winding 1 line to line voltage	16 kV
Magnetising current	1.0 %
Winding 2 line to line voltage	110 kV
Magnetising current	1.0 %
Saturation enabled?	No

Transmission line data

The data for the NZ HVdc transmission line was obtained from New Zealand Electricity. The per pole line resistance is made up of: Overhead line 10.95Ω per pole and submarine cable resistance 1.51Ω. The submarine cable capacitance is 0.333μF/km; a total capacitance of 13.3331μF. The series inductance for the overhead line is 1.33mH/km, and the shunt capacitance 0.012μF/km. The submarine cable divides the overhead line into two segments; the South Island and North Island partitions are 530km and 40km respectively.

Dc filter data

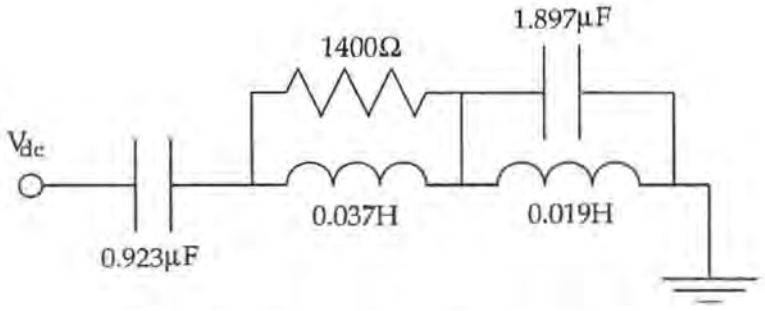

Figure K.1 Benmore P1A dc line filter design.

REFERENCES

ABU-NASSER, A.I. (1981), 'Transformer Inrush in Traction and HVdc Schemes', *PhD thesis, Victoria University of Manchester*, October, pp. 135–168.

ACHA, E. (1988), *Modelling of Power System Transformers in the Complex Conjugate Harmonic Space*, PhD thesis, University of Canterbury, Christchurch, New Zealand.

ACHA, E., ARRILLAGA, J., MEDINA, A. AND SEMLYEN, A. (1989), 'General frame of reference for analysis of harmonic distortion in systems with multiple transformer non-linearities', *IEE Proceedings Pt. C*, Vol. 136, No. 5, September, pp. 271–278.

ANDERSON, G.W.J. (1995), *Hybrid simulation of ac-dc power systems*, PhD thesis, University of Canterbury, Christchurch, New Zealand, April.

ANDO, M., SCHWEITZER, E.O. AND BAKER, R.A. (1985), 'Development and field-data evaluation of single-end fault locator for two-terminal hvdc transmission lines: Part I- data collection system and field data', *IEEE Transactions on Power Apparatus and Systems*, Vol. PAS-104, No. 12, December, pp. 3525–3537.

ARRILLAGA, J. (1983), *High Voltage Direct Current Transmission*, Peter Peregrinus, London.

ARRILLAGA, J. AND ARNOLD, C.P. (1990), *Computer Analysis of Power Systems*, John Wiley and Sons, Baffins Lane, Chichester, West Sussex PO19 1UD England.

ARRILLAGA, J., SANKAR, S., WATSON, N.R. AND ARNOLD, C.P. (1991), 'Operational Capability of generator HVDC Convertor Units', *IEEE Transactions on Power Delivery*, Vol. 6, No. 3, July, pp. 1171–1176.

ARRILLAGA, J., SANKAR, S., ARNOLD, C.P. AND WATSON, N.R. (1992), 'Characteristics of Unit—Connected HVDC Generator Convertors Operating at Variable Speeds', *Proceedings of the IEE, Part C*, Vol. 139, No. 3, May, pp. 295–299.

ARRILLAGA, J., BOWLES, J., BARROS, J.C., KANNGIESSER, K.W. AND INGRAM, L. (1993a), 'Direct connection of generators to HVdc converters: main characteristics and comparitive advantages', *ELECTRA*, Vol. 149, August, pp. 19–39.

ARRILLAGA, J., MACDONALD, S.J., WATSON, N.R. AND WATSON, S. (1993b), 'Direct connection of series self-excited generators and hvdc converters', *IEEE Transactions on Power Delivery*, Vol. 8, No. 4, October, pp. 1860–1866.

ARRILLAGA, J., CAMACHO, J.R., MACDONALD, S.J. AND ARNOLD, C.P. (1993c), 'Operating Characteristics of unit and group connected generator HVDC converter schemes', *Proceedings of the IEE, Part C*, Vol. 140, No. 6, November, pp. 503–508.

ARRILLAGA, J., MEDINA, A., LISBOA, M.L.V., CAVIA, M.A. AND SANCHEZ, P. (1995), 'The Harmonic Domain. A frame of reference for power system Harmonic Analysis', *IEEE Transactions on Power Systems*, Vol. 10, No. 1, February, pp. 433–440.

ARTURI, C.M. (1991), 'Transient Simulation and Analysis of a Three-Phase Five—Limb Step—Up Transformer Following Out—Of—Phase Synchronisation', *IEEE Transactions on Power Delivery*, Vol. 6, No. 1, January, pp. 196–207.

ASPLUND, G., ASTROM, U., CANALHAS, A., ABERG, M., PUR-RA, E. AND HEYMAN, O. 'A novel approach on UHVdc 800kV station and equipment design'. Paper presented at the CIGRE Study Committee 14 Meeting, Wellington, New Zealand, 29 September-1 October, 1993.

ASTROM, G., ASPLUND, G., CARLSSON, L., JONSSON, U. AND LOOF, O. 'Outdoor thyristor valve-A test installation in the Konti-Skan dc link at Stenkullen converter station'. Paper presented at the CIGRE Study Committee 14 Meeting, Wellington, New Zealand, 29 September-1 October, 1993.

BICKFORD, J.P. AND HEATON, A.G. (1986), 'Transient overvoltages on power systems', *IEE Proceedings*, Vol. Pt C, No. 4, May, pp. 201–225.

CALVERLEY, T.E., OTTAWAY, C.H. AND TUFNELL, D.H.A. (1973), 'Concept of a unit generator converter transmission system', *IEE Conference on High Voltage dc and ac Transmission, London.*

CHEN, M.S. AND DILLON, W.E. (1974), 'Power Systems Modeling', *Proceedings IEEE*, Vol. 62, No. 7, July, pp. 901–915.

CHEN, X.S. AND NEUDORFER, P. (1993), 'The Development of a Three-Phase Multi-Legged Transformer Model for Use With EMTP', *Department of Energy Contract #DE-AC79-92BP26702*, March.

CHEUKSUN, W., MOHAN, N., WRIGHT, S.E. AND MORTENSEN, K.N. (1989), 'Feasibility study of AC- and DC-side active filters for HVdc converter terminals', *IEEE Transactions on Power Delivery*, Vol. 4, No. 4, October, pp. 2067–2075.

CIGRE JOINT WORKING GROUP 11/14-09 (1993), 'Hvdc unit connected generators', *ELECTRA*, Vol. 149, August.

DICK, E.P. AND WATSON, W. (1981), 'Transformer Models for Transient Studies based on Field Measurements', *IEEE Transactions on Power Apparatus and Systems*, Vol. PAS-100, No. 1, January, pp. 409–419.

DIJK, H.E. (1986), 'Voltage jump at transformer terminals due to non-simultaneous switching', *IEEE Transactions on Power Delivery*, Vol. PWRD-1, No. 3, July, pp. 147–155.

DOMMEL, H.W. (1969), 'Digital Computer Simulation of Electromagnetic Transients in Single- and Multiphase Networks', *IEEE Transactions on Power Apparatus and Systems*, Vol. PAS-88, No. 4, April, pp. 388–399.

DOMMEL, H.W. (1975), 'Transformer Models in the Simulation of Electromagnetic Transients', *5th Power Systems Computation Conference, Cambridge, England*, Vol. 3.1/4, pp. 1–16.

DOMMELEN, D.V. (1987), *Alternative Transients Program Rule Book*, Leuven EMTP Center, July.

EMTDC MODELS (1994), *EMTDC V3 Custom models*, Manitoba HVdc Research Centre, 400-1619 Pembina Highway, Winnipeg, Manitoba, Canada R3T 2G5.

EMTDC USER (1994), *EMTDC V3 User's manual*, Manitoba HVdc Research Centre, 400-1619 Pembina Highway, Winnipeg, Manitoba, Canada R3T 2G5.

FLUX, R.W. (1971), 'The sealed windings site-assembled transformer-A cas study', *IEEE transactions of Power Apparatus and Systems*, Vol. PAS-90, No. 5, October, pp. 2002–2009.

GENERAL ELECTRIC COMPANY (1987), *Protective relays application guide*, GEC measurements, St. Leonards Works, Stafford ST174LX, England, third edition ed., June.

GERMAN, D.M. AND DAVIES, A.E. (1981), 'The simulation of transformer feeders following switching operations', *IEEE Transactions on Power Apparatus and Systems*, Vol. PAS-100, No. 11, November, pp. 4510–4514.

GIESNER, D.B. (1971), *The dynamic behaviour of ac/dc power systems under ac fault conditions*, PhD thesis, University of Canterbury, Christchurch, New Zealand.

HATZIARGYRIOU, N.D., PROUSALIDIS, J.M. AND PAPADIAS, B.C. (1993), 'Generalised Transformer Model Based on Analysis of its Magnetic Circuit', *IEE Proceedings—C*, Vol. 140, No. 4, July, pp. 269–278.

HEFFERNAN, M.D., ARRILLAGA, J. AND TURNER, K.S. (1981), 'Recovery from temporary HVdc line faults', *IEEE Transactions on Power Apparatus and Systems*, Vol. PAS-100, No. 4, April, pp. 1864–1870.

HINGORANI, N.G. (1961), *Control and protection of high voltage dc systems*, PhD thesis, The Victoria University of Manchester, January.

HINGORANI, N.G. (1970), 'Transient overvoltages on a bi-polar HVdc overhead line caused by dc line faults', *IEEE Transactions on Power Apparatus and Systems*, Vol. PAS-89, No. 4, April, pp. 592–610.

INGRAM, L. (1988), 'A practical design for an integrated HVDC unit connected Hydro Electric Power Station', *IEEE Transactions on Power Delivery*, Vol. 3, No. 4, October, pp. 1615–1621.

JOOSTEN, A.P.B., ARRILLAGA, J., ARNOLD, C.P. AND WATSON, N.R. (1990), 'Simulation of hvdc system disturbances with reference to the magnetizing history of the converter transformer', *IEEE Transactions on Power Delivery*, Vol. 5, No. 1, January, pp. 330–336.

LEON, F.D. AND SEMLYEN, A. (1994), 'Complete Transformer Model for ElectroMagnetic Transients', *IEEE Transactions on Power Delivery*, Vol. 9, No. 1, pp. 231–239.

LIN, C.E., YEH, J.C., HUANG, C.L. AND CHENG, C.L. (1995), 'Transient model and simulation in three-phase three-limb transformers', *IEEE Transactions on Power Delivery*, Vol. 10, No. 2, April, pp. 896–905.

LISBOA, M.L.V., ENRIGHT, W. AND ARRILLAGA, J. 'Improved repesentation of the magnetic non-linearities of multi-limb transformers for use in power system harmonic studies'. Paper accepted for presentation at the 12th PSCC conference, Dresden, Germany, 19-23 August 1996.

LISBOA, M.L.V., ENRIGHT, W. AND ARRILLAGA, J. (1995), 'Harmonic and time domain simulation of transformer magnetisation non-linearities', *Proceeedings IPENZ Annual Conference (Innovative Technology)*, Vol. 2, February, pp. 72–77.

MACDONALD, S.J., ENRIGHT, W., ARRILLAGA, J. AND O'BRIEN, M.T. (1995), 'Harmonic measurements from a group connected generator HVdc converter scheme', *IEEE Transactions on Power Delivery*, Vol. 10, No. 4, October, pp. 1937–1943.

MCPHERSON, G. (1981), *An Introduction to Electrical Machines and Transformers*, John Wiley and Sons.

MEDINA, A. (1992), *Power Systems Modelling in the Harmonic Domain*, PhD thesis, University of Canterbury.

MEDINA, A. AND ARRILLAGA, J. (1992a), 'Simulation of multilimb power transformers in the harmonic domain', *IEE Proceedings-C*, Vol. 139, No. 3, May, pp. 269–276.

MEDINA, A. AND ARRILLAGA, J. (1992b), 'Generalised modelling of power transformers in the Harmonic Domain', *IEEE Transactions on Power Delivery*, Vol. 7, No. 3, July, pp. 1458–1465.

MILLER, A.J.V. (1992), 'Multichannel continuous harmonic analysis in real time', *IEEE Transactions on Power Delivery*, Vol. 7, No. 4, October, pp. 1813–1819.

NAIDU, M. AND MATHUR, R.M. (1989), 'Evaluation of Unit Connected, Variable Speed Hydropower Station for HVDC Power Transmission', *IEEE Transactions on Power Systems*, Vol. 4, No. 2, May, pp. 668–676.

PANG, C.X. AND TARNAWECKY, M.Z. (1995), 'Generator winding I^2R losses and Harmonic Interference under variable frequency operation of a HVdc unit-connected scheme', *IEEE Transactions on Energy Conversion*, Vol. 10, No. 1, March, pp. 133–139.

PETERSON, H.A., PHADKE, A.G. AND REITAN, D.K. (1969), 'Transients in EHVDC power systems: Part I-Rectifier fault currents', *IEEE Transactions on Power Apparatus and Systems*, Vol. PAS-88, No. 7, July, pp. 981–989.

SAY, M.G. (1983), *Alternating current machines*, Longman scientific and technical, Longman house, Burnt Mill, Harlow, Essex CM20 2JE, England, fifth ed.

SLEMON, G. (1966), *Magnetoelectric Devices: Transducers, Transformers and Machines*, John Wiley and Sons, Inc.

SMITH, D.R., SWANSON, S.R. AND BORST, J.D. (1975), 'Overvoltages with remotely-switched cable-fed grounded wye-wye transformers', *IEEE Transactions on Power Apparatus and Systems*, Vol. PAS-94, No. 5, September/October, pp. 1843–1851.

STEINMETZ, C.P. (1895), 'Theory of the general Alternating Current transformer', *American Institute of Electrical Engineers*, Vol. xii, June, pp. 245 – 256.

STUEHM, D.L. (1993), *Three-phase Transformer Core Modeling*, Technical Report, North Dakota State University.

TAKASU, N., OSHI, T., MIYAWAKI, F., SAITO, S. AND FUJIWARA, Y. (1994), 'An experimental analysis of dc excitation of transformers by geomagnetically induced currents', *IEEE Transactions on Power Delivery*, Vol. 9, No. 2, April, pp. 1173–1182.

TESTI, G. (1994), *Dc side harmonics and filtering in HVdc transmission systems*, CIGRE Task Force 02, Working Group 14.03.

THE ELECTRICITY COUNCIL (1981), *Power system protection*, Vol. Principles and components, Peter Peregrinus Ltd, Stevenage UK and New York.

TURNER, S. (1977), *Modelling the Magnetic Characteristics of a Power Transformer*, PhD thesis, The Victoria University of Manchester.

TURNER, K.S. (1980), *Transient stability analysis of integrated ac and dc power systems*, PhD thesis, University of Canterbury.

UHLMAN, E. (1975), *Power Transmission by Direct Current*, Springer–Verlag.

WOODFORD, D.A. (1985), 'Validation of digital simulation of DC links', *IEEE Transactions on Power Apparatus and Systems*, Vol. PAS-104, No. 9, pp. 2588–2595.

WOODFORD, D.A., GOLE, A.M. AND MENZIES, R.W. (1983), 'Digital Simulation of DC Links', *IEEE Transactions on Power Apparatus and Systems*, Vol. PAS-102, No. 6, pp. 1616–1623.

ZAVAHIR, J.M. (1992), *Electromagnetic Transient Simulation with State Variable Representation of HVdc Conversion*, PhD thesis, University of Canterbury, Christchurch, New Zealand, June.